Enclosure 3

MHI Topical Report: MUAP-07008-NP, Rev.0

Mitsubishi Fuel Design Criteria and Methodology

May 2007
(Non-Proprietary Version)

This is a non-proprietary version of MHI Topical Report, MUAP-07008-NP, Rev.0, with all proprietary information removed.

Portions of the report where proprietary information has been removed are identified by the designation "[ ]".

Non-Proprietary

US-APWR Topical Report

Mitsubishi Fuel Design Criteria and Methodology

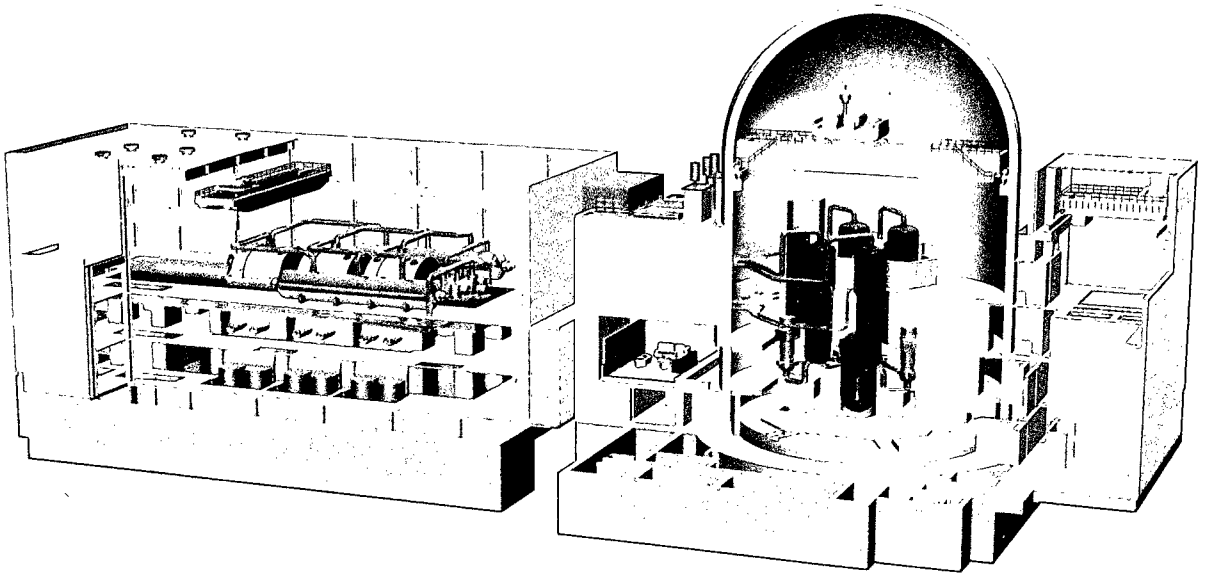

Doc. Number :
MUAP-07008-NP R0

May 2007

MITSUBISHI HEAVY INDUSTRIES, LTD.

Mitsubishi Fuel Design Criteria and Methodology

Non-Proprietary Version

May 2007

Abstract

Mitsubishi Heavy Industries, Ltd. (Mitsubishi) has substantial experience in the nuclear industry in Japan, having supplied more than 17,000 nuclear fuel assemblies to Japanese PWR utilities since 1969. The irradiation experience accumulated for Mitsubishi fuel assemblies has demonstrated excellent performance and high reliability.

The fuel design, fabrication, the associated analysis methods and criteria that have led to high reliability performance of Mitsubishi fuel in Japan will now be applied to the design and manufacture of US-APWR fuel, consistent with NRC regulations and standards. The US-APWR fuel incorporates the latest design such as ZIRLO™ cladding, higher density pellet of 97 % TD, 10 wt% gadolinia doped fuel and the features to reduce or eliminate debris fretting, grid fretting and incomplete rod insertion.

The fuel rod and fuel assembly design criteria to be applied to the US-APWR fuel design is in compliance with Title 10 of Code of Federal Regulations Part 50 (10CFR50), Regulatory Guide 1.70, and the NRC Standard Review Plan (NUREG-0800).

Based on an extensive fuel performance database, Mitsubishi has developed the Fuel rod Integrity Evaluation (FINE) code for use in performing fuel rod design and performance analysis. The FINE code has been reviewed and approved in Japan for application to all Mitsubishi designed fuel rods. The FINE code is also applicable to the Mitsubishi US-APWR fuel rod design, with rod average burnup of up to 62 GWd/t.

The FINE code is supported by significant irradiation data and also has been validated by comparison with the results of FRAPCON-3 using the benchmark cases for code verification that have been provided by Pacific Northwest National Laboratory (PNNL).

Additionally, the evaluation methodology for the ability of the fuel assembly to withstand earthquakes and LOCA events are also described, since the fuel assembly is an important structural component of the core and has the important functions of maintaining the coolable geometry of the core and the capability to allow the insertion of control rods for safe reactor shutdown during both seismic and LOCA events.

Revision History

Revision	Page	Description
0	All	Original issued

Mitsubishi Heavy Industries, Ltd.
16-5, Konan 2-chome, Minato-ku
Tokyo 108-8215 Japan

Table of Contents

List of Tables

List of Figures

Lists of Acronyms

AOOs	Anticipated Operating Occurrences
APWR	Advanced Pressurized Water Reactor
BA	Burnable Absorber
DF	Debris Filter
DFBN	Debris Filter Bottom Nozzle
DNB	Departure from Nucleate Boiling
DNBR	Departure from Nucleate Boiling Ratio
ECCS	Emergency Core Cooling System
ECR	Equivalent Cladding Reacted
FEM	Finite Element Method
FINE	Fuel rod INtegrity Evaluation
GDC	General Design Criterion
ICCC	In-Core Control Component
IRI	Incomplete Rod Insertion
LOCA	Loss Of Coolant Coolant Accident
LPBN	Low Pressure Bottom Nozzle
ITA	Lead Test Assembly
IUA	Lead Use Assembly
NO	Normal Operation
NRC	Nuclear Regulatory Commission
PA	Postulated Accident
PCI	Pellet Cladding Interaction
PCMI	Pellet Cladding Mechanical Interaction
PIE	Post Irradiation Examination
PNNL	Pacific Northwest National Laboratory
RCC	Rod Cluster Control
RCCA	Rod Cluster Control Assembly
RCS	Reactor Cooling System
RIA	Reactivity Initiated Accident
SAFDL	Specified Acceptance Fuel Design Limits
SAR	Safety Analysis Report
SRSS	Square Root of the Sum of the Squares

1.0 INTRODUCTION

Mitsubishi Heavy Industries, Ltd. (Mitsubishi) has substantial experience in the nuclear industry in Japan, having supplied more than 17,000 nuclear fuel assemblies to Japanese PWR utilities since 1969. The irradiation experience accumulated for Mitsubishi fuel assemblies has demonstrated excellent performance and high reliability.

The fuel design, fabrication, the associated analysis methods and criteria that have led to high reliability performance of Mitsubishi fuel in Japan will now be applied to the design and manufacture of US-APWR fuel, consistent with NRC regulations and standards.

Based on an extensive fuel performance database, Mitsubishi has developed the Fuel rod Integrity Evaluation (FINE) code for use in performing fuel rod design and performance analysis. The FINE code has been reviewed and approved in Japan for application to all Mitsubishi designed fuel rods with. The FINE code is also applicable to the Mitsubishi US-APWR fuel rod design with rod average burnup of up to 62 GWd/t.

Included in this report is:

1. A description of the Mitsubishi designed US-APWR fuel assembly;

2. The fuel rod and fuel assembly design criteria that is to be applied to the US-APWR fuel design (in accordance with Title 10 of Code of Federal Regulations Part 50 (10CFR50), Regulatory Guide 1.70, and the NRC Standard Review Plan (NUREG-0800); and

3. The validation of the Mitsubishi FINE code for use in the US-APWR fuel rod design.

2.0 MITSUBISHI FUEL ASSEMBLY

Mitsubishi has supplied more than 17,000 fuel assemblies to Japanese PWR utilities since the first region of Mitsubishi built fuel was supplied to Mihama Unit 1 in 1969. The irradiation experience for these fuel assemblies has confirmed very high reliability, as summarized in Appendix A.

The US-APWR fuel incorporates the latest design such as ZIRLO™ cladding, higher density pellet of 97 % TD, 10 wt% gadolinia doped fuel and the features to reduce or eliminate debris fretting, grid fretting and incomplete rod insertion.

2.1 Basic Fuel Assembly Structure

The Mitsubishi fuel assembly consists of fuel rods, top nozzle, bottom nozzle, control rod guide thimble tubes, the in-core instrumentation guide tube and grid spacers basically, as shown in Figure 2.1-1. The geometry and materials of the Mitsubishi fuel assembly are summarized as shown in the figure.

These structural components are discussed below.

2.2 Fuel Rods

The fuel rods have the functions of transferring the heat generated due to nuclear fission to the reactor coolant and containing the fission products inside the fuel rods.

The fuel rods consist of fuel cladding (referred to simply as "cladding" below) loaded with sintered uranium dioxide pellets or sintered uranium dioxide pellets doped with gadolinia, a coil spring (called a "pellet spring") situated above the fuel pellet stack and end plugs welded at the top and bottom ends to seal the rod as shown in Figure 2.1-1. To reduce pellet-cladding interaction, the fuel rods are also filled with pressurized helium through a pressurization hole provided in the top end plug which is then closed off by welding to yield a sealed structure.

The sintered uranium dioxide pellets and sintered gadolinia-uranium dioxide pellets are produced by compression molding powdered uranium dioxide and a powdered mixture of uranium dioxide and gadolinia, respectively, and then sintering in an atmosphere of hydrogen or a hydrogen/nitrogen mixture to yield cylindrical pellets with an indentation (called a "dish") at the center of each end surface. The edges of these end surfaces are chamfered.

The dishes accommodate the axial swelling and thermal expansion of the pellet stack during irradiation, and the chamfer acts to strengthen the pellet ends; to reduce the incidence of small defects close to the pellet surface and to suppress deformation of the end surfaces when the pellets expand.

Between the top of the pellet stack and the bottom of the top end plug, there is a plenum space to accommodate the increase in the internal gas content due to the release of gaseous fission products with burnup. The plenum acts as a gas reservoir and helps to reduce the buildup of the rod internal pressure.

The pellet spring placed in the plenum space, prevents the pellets from moving during shipping and handling of the fuel rods.

The US-APWR fuel rod design includes a bottom plenum to reduce internal pressure. A stainless steel spacer in the bottom plenum provides additional cladding support.

The radial gap between the pellets and cladding, and the cladding thickness, are determined so that the integrity of the fuel rod is fully maintained during AOOs, where the pellet thermal expansion exceeds that of the cladding.

The axial gaps between the fuel rod top end plug and the top nozzle and the fuel rod bottom end plug and the bottom nozzle are determined to allow for anticipated axial fuel rod growth and differential thermal expansion of the fuel rods and assembly in the axial direction during operation.

2.3 Top Nozzle and Bottom Nozzle

The top and bottom nozzles have the function of positioning the fuel assemblies inside the reactor core. To remove heat generated inside the fuel assembly, the top and bottom nozzles are provided with flow holes to guide the primary coolant flowing into the fuel rod from below into the fuel assembly and allow it to flow through, and out of the assembly. In the top and bottom nozzles, holes that engage with the guide pins attached to the upper and lower reactor core plates are provided in two corners in opposite positions on the top and bottom nozzles.

In order to prevent the fuel assembly from lifting off the lower core plate during normal operation due to the lift in force of the coolant, holddown springs are integrated into the top nozzle. They are attached by means of a spring screw and are compressed by the upper core plate to generate a sufficient force to keep the assembly seated on the bottom core plate. The holddown spring is designed to account for the changing fuel assembly length during irradiation.

Sleeves welded to the top nozzle assembly provide the means to attach the top nozzle to the fuel assembly. A sleeve is linked to a control rod guide thimble by a three-stage expansion tube, as shown in Figure 2.3-1. For the US-APWR, the top nozzle can be easily removed and replaced for repair, or maintenance.

2.4 Control Rod Guide Thimbles

The control rod guide thimble has the function of guiding In-core Control Components such as the control rods, burnable absorber rods and neutron source rods when they are inserted into the fuel assembly, and holding them in place.

The control rod guide thimble is given a narrower internal diameter at the bottom, called the dashpot to utilize the resistance of the primary coolant inside it to help reduce the impact that occurs when the control rod is dropped.

2.5 In-Core Instrumentation Guide Tube

The guide tube for in-core instrumentation has the function of guiding the in-core neutron detector and holding this detector in place. It is inserted into the fuel assembly from the lower surface of the bottom nozzle for conventional fuel type and from the upper surface of the top nozzle for US-APWR fuel.

The top and bottom ends of the in-core instrumentation guide tube are constructed so that they can be inserted into the flow holes provided in the top and bottom nozzles.

2.6 Grid Spacer

As shown in Figure 2.6-1, the grid spacer holds the fuel rods by means of grid spacer springs and dimples. It also has the function of keeping gaps between adjacent fuel rods and between the control rod guide thimble and the in-core instrumentation guide tube so as to maintain the nuclear and thermal hydraulic performance.

The grid spacer may be referred to as the upper grid spacer or lower grid spacer if it is attached at the uppermost or lowermost part of the fuel assembly, and is otherwise called an intermediate grid spacer.

The grid spacer is assembled from a lattice of thin strips in 17 rows and 17 columns. The upper and lower grid spacers are soldered, and the intermediate grid spacers have a welded structure, if the grid spacers are made of Zircaloy-4.

Sleeves are attached to the upper and intermediate grid spacers by soldering and welding respectively. The upper and intermediate grid spacers are both linked to the control rod guide thimble and the in-core instrumentation guide tube by a single stage expansion tube via a sleeve as previously shown in Figure 2.3-1.

Also, the intermediate grid spacers are provided with mixing vanes in order to assist mixing of the primary coolant and increase the heat removal efficiency.

For the lower grid spacer, an insert is welded to the grid spacer, and the control rod guide thimble is inserted via this insert, which is then linked to the bottom nozzle by a thimble screw from the lower surface of the nozzle.

2.7 Debris Mitigation Measures

For the US-APWR and a 14x14 fuel assembly, the bottom nozzle, as shown in Figure 2.7-1, has a plate on which other thin plates are placed and welded in grooved slits, providing a filter for debris passing through flow holes.

For conventional 17x17 and APWR fuel assemblies, the debris filter placed between the bottom nozzle and lower grid spacer has the function of preventing debris from flowing into the interior of the fuel assembly. The debris filter is assembled by welding together a lattice of thin strips in 17 rows and 17 columns, and is attached by welding to the bottom grid spacer, where it is positioned directly above the lower nozzle.

Table 2.1-1 Fuel Assembly Characteristics

Fuel Assemblies	14x14 / 15x15	17x17 APWR	US APWR
Fuel Rods Array	14x14 / 15x15	17x17	17 x 17
Number of Fuel Rods	179 / 204	264	264
Number of Control Rod Guide Thimbles	16 / 20	24	24
Number of In-core Instrumentation Guide Tube	1	1	1
Number of Grid Spacers	7 or 8 / 7	9	11
Measure for Trapping Debris	Anti-debris bottom nozzle with built-in filter	Addition of debris filter	Anti-debris bottom nozzle with built-in filter
Fuel Rods			
Outside Diameter	0.422 in. (10.72mm)	0.374 in. (9.50mm)	0.374 in. (9.50mm)
Cladding Thickness	0.0244 in. (0.62mm)	0.022 in. (0.57mm)	0.022 in. (0.57mm)
Active Fuel Length	143.4" (3,642mm)	143.6" (3,648mm)	165.4" (4,200mm)
Reload Fuel Enrichment	Max. 5 wt%	Max. 5 wt%	Max. 5 wt%
Gadolinia Content	Max. 10 wt%	Max. 10 wt%	Max. 10 wt%
Pellet Density	97 % TD	97 % TD	97 % TD
Plenum	Upper	17x17 : Upper APWR : Upper & Lower	Upper & Lower
Materials			
Cladding	ZIRLO™	ZIRLO™	ZIRLO™
Top & Bottom Grid Spacers	Inconel 718	Inconel 718	Inconel 718
Middle Grid Spacers	Inconel 718	Zircaloy-4	Zircaloy-4
Guide Thimbles	Zircaloy-4	Zircaloy-4	Zircaloy-4
Nozzles	Stainless Steel	Stainless Steel	Stainless Steel
Holddown Springs	Inconel 718	Inconel 718	Inconel 718

- ZIRLO™ is a registered trademark of the Westinghouse Electric Corporation.
- Inconel 718 is a nickel-chromium-iron Alloy 718.

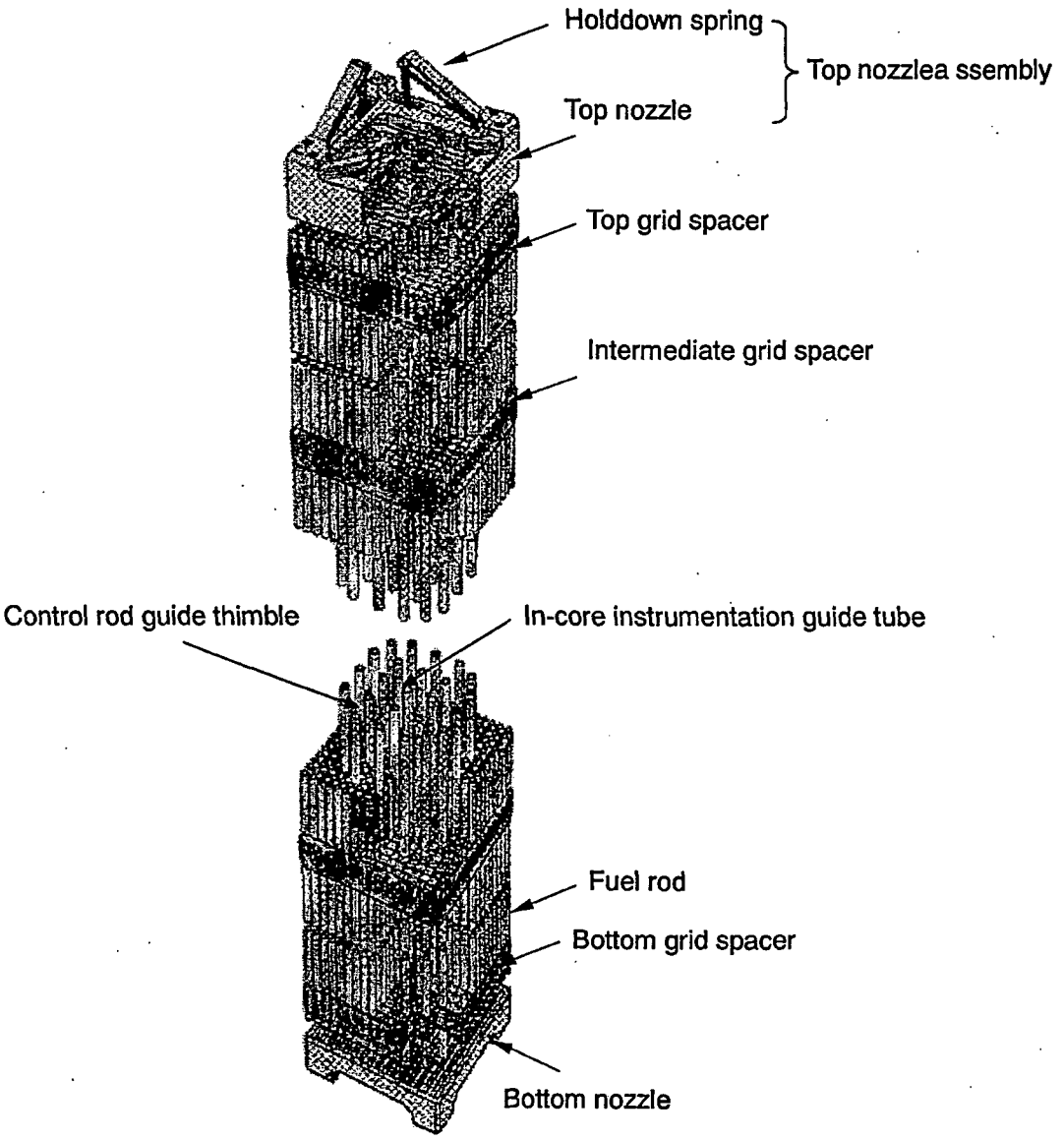

Figure 2.1-1 Schematic Mitsubishi Fuel Assembly

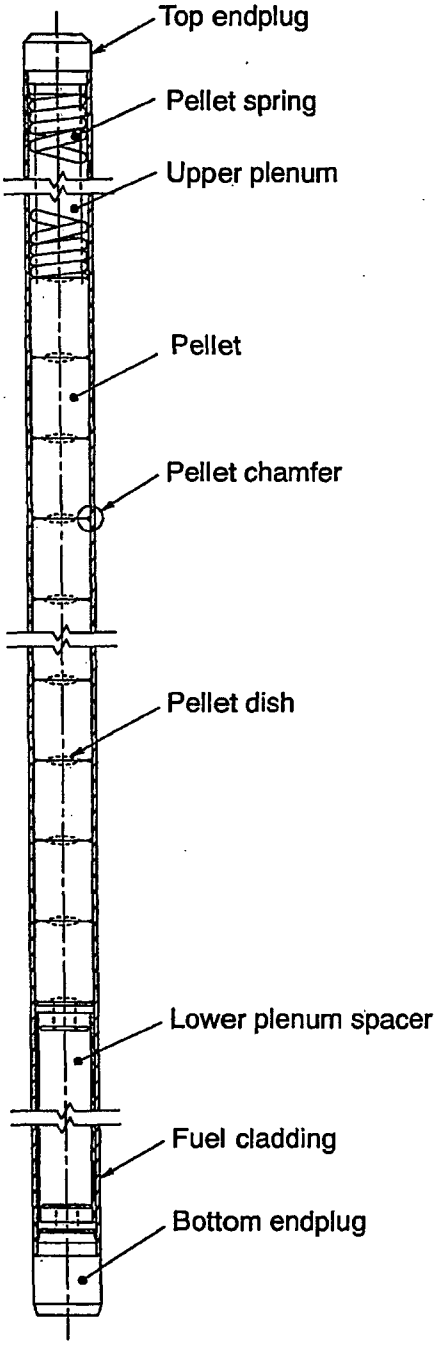

Figure 2.2-1 Schematic Fuel Rod

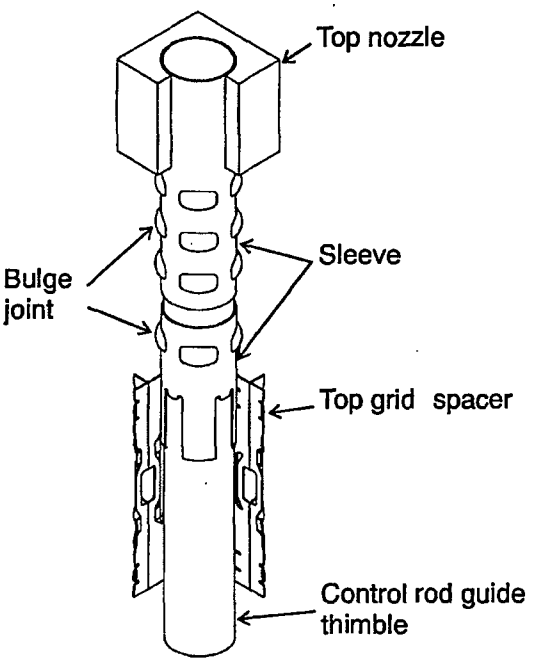

Figure 2.3-1 Connection between Top Nozzle and Sleeve

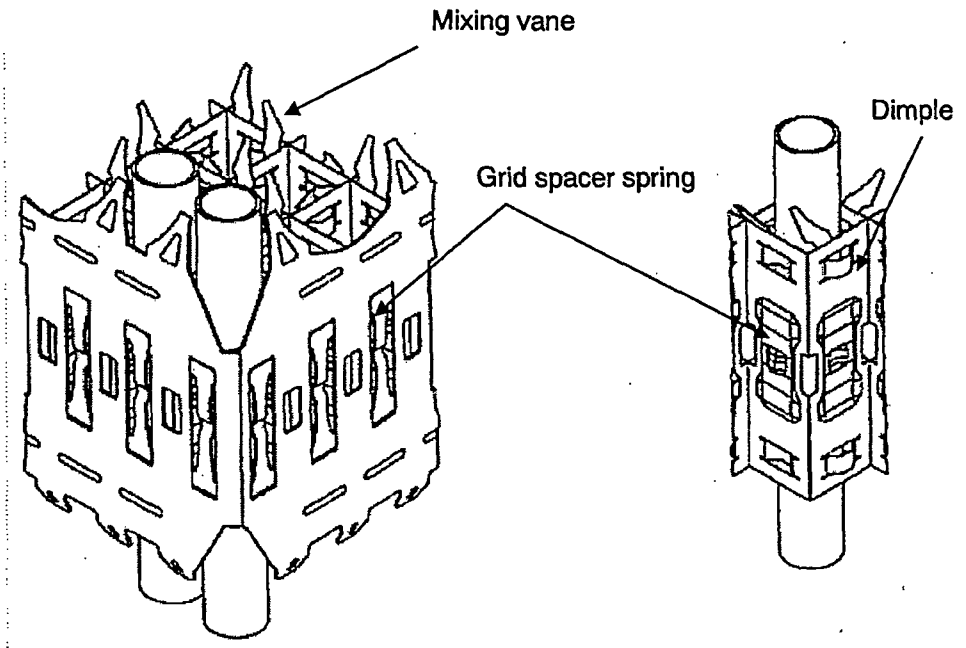

Figure 2.6-1 Schematic Grid Spacer

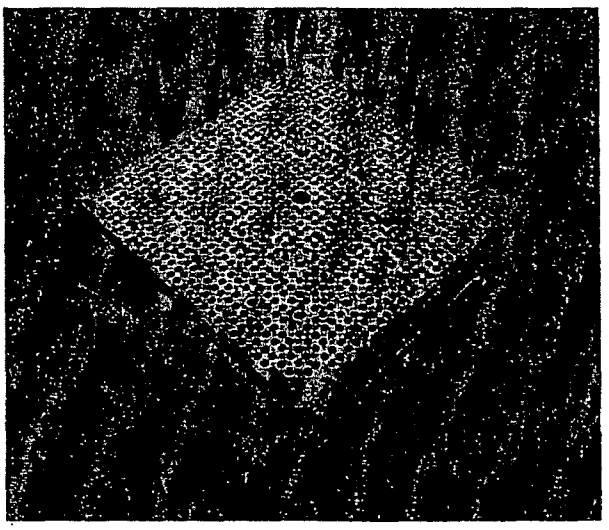

Figure 2.7-1 Anti-Debris Bottom Nozzle with Built-in Filter

3.0 DESIGN CRITERIA AND METHODOLOGY

3.1 Background

3.1.1 Design Requirement

Design requirements for the fuel system are described in the NRC Standard Review Plan (SRP) Section 4.2 (NUREG-0800)[1]. These requirements are in compliance with General Design Criteria (GDC) 10, 27 and 35 within 10CFR50 Appendix A[2] and 10CFR50.46[3] (and 10CFR100[4]). They are also consistent with Section 4.2 of Regulatory Guide 1.70[5].

The objectives of the fuel system design in safety analysis are to assure that;

(a) the fuel system is not damaged as a result of normal operation and anticipated operational occurrences (AOOs),
(b) fuel system damage is never so severe as to prevent control rod insertion when it is required,
(c) the number of fuel rod failures is not underestimated for postulated accidents, and
(d) coolability is always maintained.

GDC10 (Reactor design) "The reactor core and associated coolant, control, and protection systems shall be designed with appropriate margin to assure that specified acceptable fuel design limits are not exceeded during any condition of normal operation, including the effects of anticipated operational occurrences", within Appendix A to 10 CFR Part 50, also addresses item (a) above. Specifically, GDC 10 establishes Specified Acceptable Fuel Design Limits (SAFDLs) that should not be exceeded during any condition of normal operation, including the effects of AOOs. These SAFDLs are established to ensure that the fuel is not damaged.

With respect to the fuel system design, "Not damaged" means that fuel rods do not fail, that the fuel system remains within operational tolerances, and that the functional capabilities are not reduced below those assumed in the safety analysis.

"Fuel rod failure" means that the fuel rod leaks and that the first fission product barrier (the cladding) has been breached. This relates to 10CFR Part 100, dose analysis.

"Coolability" means that fuel assembly retains its rod-bundle geometry with adequate coolant channels to permit removal of residual heat even after a severe accident.

General requirements to maintain control rod insertability and core coolability appear repeatedly in GDC 27 (Combined reactivity control systems capability.) and 35 (Emergency core cooling). Specific coolability requirements for the loss-of-coolant accident (LOCA) are given in 10CFR part 50.46.

To satisfy these requirements, design criteria for the fuel system are categorized with respect to:

(A) fuel system damage,
(B) fuel rod failure, and
(C) fuel coolability.

The complete set of design criteria required in SRP Section 4.2 are summarized in Table 3.1.1-1 to Table 3.1.1-3.

Section 3.2 of this report presents a review of the Mitsubishi fuel rod and fuel assembly design criteria that address these requirements, though it is noted that for some requirements related to postulated accidents, the Safety Analysis Report (SAR) will be referenced for the detailed discussion of the requirement.

3.1.2 Plant Conditions for Fuel Design

Plant conditions for fuel assembly design are categorized according to expected frequency of occurrence and by type, as follows:

(1) normal operation
(2) anticipated operational occurrences (AOOs)
(3) postulated accidents

Normal operation typically includes the following events that are expected frequently or regularly in the course of power operation, refueling, maintenance, and maneuvering to the plant[6].

- Startup
- Shutdown(hot and cold)
- Refueling
- Hot standby
- Power operation
- Operational maneuvers
- Plant heatup and cooldown
- Load change
- Operation with permissible deviations

AOOs, as defined in Appendix A to 10 CFR Part 50, are those conditions of operation that are expected to occur one or more times during the life of the nuclear power unit. Postulated accidents are unanticipated occurrences (i.e., they are postulated but not expected to occur during the life of the nuclear power plant).

It is useful to categorize and organize analyses of AOOs and postulated accidents according to type, so that analysts can compare them on common bases, effects, and safety limits. Such comparisons can help to identify limiting events and cases for detailed examination and eliminate non-limiting cases from further consideration.

AOOs and postulated accidents can be grouped into the following seven types[6]:

(1) Increase in heat removal by the secondary system
(2) Decrease in heat removal by the secondary system
(3) Decrease in reactor cooling system (RCS) flow rate
(4) Reactivity and power distribution anomalies
(5) Increase in reactor coolant inventory
(6) Decrease in reactor coolant inventory

(7) Radioactive release from a subsystem or component

The events for AOOs and postulated accidents for the US-APWR will be categorized in Chapter 15 (Transient and accident analysis) of the SAR to specify the limiting event for fuel system integrity.

Table 3.1.1-1 Criteria for Fuel System Damage

SRP Acceptance Criteria for (A) Fuel System Damage		Plant Condition			Fuel Assembly		In-Core Control Component		Related chapter/section to be reviewed in SAR
		NO	AOO	PA	Fuel rods	Other parts	Control rods	BA	
1.A.i	Cladding Stress	x	x		x	x	x	x	Section 4.2 (Fuel system design)
	Cladding Strain	x	x		x				Section 4.2 (Fuel system design)
	Loading Limits	x	x			x			Section 4.2 (Fuel system design)
1.A.ii	Cladding Fatigue	x	x		x	x	x	x	Section 4.2 (Fuel system design)
1.A.iii	Cladding Fretting Wear	x			x	x			Section 4.2 (Fuel system design)
1.A.iv	Cladding Oxidation, Hydriding, Crud	x	x		x	x			Section 4.2 (Fuel system design) Effects of crud should be discussed in Section 4.3 and 4.4
1.A.v	Dimensional Change	x			x	x	x	x	Section 4.2 (Fuel system design)
1.A.vi	Rod Internal Pressure (no cladding liftoff, No Hydride Reorientation),	x			x		x	x	Section 4.2 (Fuel system design)
	Rod Internal Pressure (DNB propagation)		x	x	x				Section 4.2 (Fuel system design)
1.A.vii	Assembly Liftoff (Holddown Spring)	x	x	x		x			Section 4.2 (Fuel system design)
1.A.viii	Control Rod Reactivity Insertability						x		Section 4.2 (Fuel system design)

NO: Normal Operation
AOO: Anticipated Operational Occurrences
PA: Postulated Accidents
BA: Burnable Absorber

Table 3.1.1-2 Criteria for Fuel Rod Failure

SRP Acceptance Criteria for (B) Fuel Rod Failure		Plant Condition			Fuel Assembly		In Core Control Component		Related chapter/section to be reviewed in SAR
		NO	AOO	PA	Fuel rods	Other parts	Control rods	BA	
1.B.i	Hydriding (Internal)	x			x				Section 4.2 (Fuel system design)
	Hydriding (External)	x			x				Section 4.2 (Fuel system design)
1.B.ii	Cladding Collapse	x			x				Section 4.2 (Fuel system design)
1.B.iii	Overheating of cladding	x	x	x	x				Section 4.2 (Fuel system design) Section 4.4 (Thermal and Hydraulic design)
1.B.iv	Overheating of fuel pellet		x	x	x				Section 4.2 (Fuel system design) Chapter 15 (Transient and Accident Analysis)
1.B.v	Excessive Fuel Enthalpy			x	x				Chapter 15 (Transient and Accident Analysis)
1.B.vi	PCI		x		x				Section 4.2 (Fuel system design) Chapter 15 (Transient and Accident Analysis)
1.B.vii	Bursting		x	x	x				Chapter 15 (Transient and Accident Analysis)
1.B.viii	Mechanical Fracturing		x	x	x				Section 4.2 (Fuel system design)

NO: Normal Operation
AOO: Anticipated Operational Occurrences
PA: Postulated Accidents
BA: Burnable Absorber

Table 3.1.1-3 Criteria for Fuel Coolability

SRP Acceptance Criteria for (C) Fuel Coolability		Plant Condition			Fuel Assembly		In-Core Control Component		Related chapter/section to be reviewed in SAR
		NO	AOO	PA	Fuel rods	Other parts	Control rods	BA	
1.C.i	Cladding Embrittlement			x	x				Chapter 15 (Transient and Accident Analysis)
1.C.ii	Violent Expulsion of Fuel			x	x				Chapter 15 (Transient and Accident Analysis)
1.C.iii	Generalized Cladding Melting			x	x				Chapter 15 (Transient and Accident Analysis)
1.C.iv	Fuel Rod Ballooning			x	x				Chapter 15 (Transient and Accident Analysis)
1.C.v	Structural Deformation			x		x			Section 4.2 (Fuel system design)

NO: Normal Operation
AOO: Anticipated Operational Occurrences
PA: Postulated Accidents
BA: Burnable Absorber

3.2 Design Criteria and Methodology for Fuel System Damage

Fuel system damage requirements apply to normal operation and AOOs. To meet the requirements of GDC 10, as it relates to SAFDLs for normal operation, including AOOs, fuel system damage criteria should be specified for all known damage mechanisms. Fuel damage criteria should assure that fuel system dimensions remain within operational tolerances and that functional capabilities are not reduced below those assumed in the safety analysis. When applicable, the fuel damage criteria should consider high burnup effects based on irradiated material properties.

3.2.1 Cladding Stress

(1) Design Basis

Fuel system will not be damaged due to excessive stress under normal operation including AOOs.

(2) Design Criteria

The ASME Section III [7] pressure vessel criteria are applied for cladding stress. All cladding stresses except for pellet-cladding mechanical interaction (PCMI) related stress, are considered in the stress evaluation and are assessed according to ASME Section III [7].

PCMI stress is excluded in the cladding stress evaluation because it is addressed by the cladding strain criterion and the no fuel melting criterion.

(3) Design Evaluation

Cladding stresses are calculated using the FINE code and basic analytical equations. Cladding stresses take into account of the differential pressure across the cladding wall, thermal stresses, hydraulic and seismic vibration, fuel rod bowing, grid spacer contact and cladding ovality.

Cladding stress shall remain below the ASME Section III [7] criteria as summarized below:

Category	Limit	Stress due to;
Primary Membrane	Sm	Differential Pressure
Primary Membrane + Bending	1.5 Sm	Ovality, Hydraulic and seismic vibration, Fuel bowing
Primary Membrane + Bending + Local	1.5 Sm	Grid spacer contact force
Primary Membrane + Bending + Local + Secondary	3.0 Sm	Thermal stress due to temperature difference across the cladding

The allowable stress intensity, Sm, is the minimum of two third of the cladding yield stress and one third of the cladding ultimate stress, with consideration of temperature and irradiation (Appendix B).

The cladding stresses are categorized as the following table.

Loading Conditions	Stress Category	Classification	Approach
Internal-external differential pressure	Primary Membrane Stress	Pm	FINE Analysis
Hydraulic and seismic vibration	Primary Bending Stress	Pb	Vibration Analysis & Basic Equations
Grid spacer contact	Local Primary Membrane Stress	Pl	Basic Equations
Fuel bowing	Primary Bending Stress	Pb	Basic Equations
Ovality	Primary Bending Stress	Pb	Basic Equations
Thermal stress	Secondary Stress	Q	FINE Analysis

Total stress is evaluated by summing up of these stresses. The stress intensity is evaluated as the differential stress between the maximum stress and minimum stress. The stress evaluation takes into account of the effect of fuel cladding wear and oxidation. The cladding wear is on the outer surface of the cladding, and affects a small and local part of cladding. Therefore, the effect of fuel cladding wear can be defined [8].

3.2.2 Cladding Strain

(1) Design Basis

Fuel system will not be damaged due to excessive strain under normal operation including AOOs.

(2) Design Criteria

Cladding strain during normal operation shall be less than 1 % relative to the un-irradiated condition. This criterion assures that the dimensional change of the cladding due to cladding creep under normal operation remains within the ductility limits for the cladding.

During power transients associated with AOOs, the total cladding strain change, elastic plus plastic, shall remain below 1 % relative to the pre-transient condition. This criterion limits the cladding strain due to PCMI.

(3) Design Evaluation

Cladding strain under normal operation and AOOs is evaluated using the FINE code.

For normal operation, the FINE code evaluates cladding strain taking into account of cladding creepdown and subsequent outward deformation due to pellet swelling. Cladding strain during normal operation arisen from PCMI is dominant. Pellet densification, swelling, thermal expansion as well as cladding creep will become important factors. Power variation during normal operation is generally very moderate, and zirconium based alloy can cause creep deformation easily. Therefore, there is little possibility that zirconium based alloy may experience an unstable condition and then deform well beyond one percent [9],[10]. Although the integrity of cladding is preserved until the cladding strain during normal operation reaches several percent, here, strain increment of 1 % relative to the un-irradiated is conservatively applied as the criterion.

For power transients associated with AOOs, the change in the cladding strain from normal operation to the maximum power of AOOs is evaluated as the total tensile strain change (elastic and inelastic). This strain is induced mainly by pellet expansion due to thermal expansion and fission gas bubble swelling. Both the PCMI and the gas bubble swelling are due to a local power increase. To analyze this, the local power increase during AOOs is added to the power under normal operation in the FINE Code.

3.2.3 Stress and Loading Limit for Other than Cladding

3.2.3.1 Loads Applied by Core Restraint System

(1) Design Basis

To supply expected thermal power and to maintain coolable geometry of the core and safe shutdown of the reactor, significant deformation in the fuel assembly will not occur under anticipated loads during normal operation and AOOs.

(2) Design Criteria

- Under the loads imposed by a RCC scram during normal operation, the stresses in the top nozzle and the RCC guide thimbles except dashpot region are less than the acceptance limit based on ASME Section III[7].
- Stresses in the bottom nozzle and the dashpot region of RCC guide thimbles during normal operation and reactor scram are less than the acceptance limit based on ASME Section III[7]. Considerable loads are defined by adding the load during normal operation to the impact force of the RCC on the top nozzle and the reaction force when the RCC is decelerated in the dashpot region.
- Fatigue durability factors of the top and bottom nozzles and the control guide thimbles are less than 1.0 considering cyclic loading during normal operation and AOOs.
- The grid spacer spring shall not fail throughout the fuel life due to fatigue which results from hydraulic vibration of the fuel rod.

(3) Design Evaluation

Against loads in normal operation and AOOs, which includes loads by core restraint system, stresses on the above components are evaluated and identified within acceptance limits.
In the evaluation, the following loads are considered under normal operation and AOOs.

- Loads under normal operation: Holddown spring force, hydraulic lift force, buoyancy force, self-weight and reaction force from lower core plate
- Loads in AOOs: Reaction force by deceleration of the RCC in the dashpot and impact force of the RCC are added to the loads in normal operation.

The RCC scram is chosen among AOOs, since the loads at RCC scram have more influence on the fuel assembly in terms of mechanical characteristics.
Impact force on the top nozzle by dropping RCCA is obtained from dropping velocity which is solved in momentum equation, while retainer spring with the rod control cluster is being compressed after the rod control cluster touches the plate of the top nozzle. Reaction force resulting from a decelerated RCCA is calculated by internal pressure increase on the control rod guide thimbles which are obtained by drop-time analysis of the RCCA.

The stresses in the top and bottom nozzles and the control rod guide thimbles are evaluated by FEM analyses.

Allowable stress intensity is decided from un-irradiated material properties for conservative evaluation, instead of using those of irradiated materials with irradiation hardening.

In compliance with ASME Section III[7], the primary general membrane stress and bending stress strength (P_m+P_b) of the top and bottom nozzles are evaluated from the analysis result and compared with the allowable stress intensity (1.5 Sm) to confirm that no plastic deformation will occur.
For the stress evaluation of the control rod guide thimbles, FEM analysis is used to obtain load sharing ratio in between fuel rod bundles and the control rod guide thimbles.

The load at RCC scram is chosen as the cyclic load in fatigue characteristic evaluation for the top and bottom nozzles and the control rod guide thimbles. Fatigue durability factor means a ratio of cumulative numbers of RCC scram during the fuel life to acceptable cyclic numbers of loading at expected stress level. The Langer-O'Donnel's fatigue design curve is used for the control rod guide thimble made of Zircaloy-4 and a corresponding curve in ASME Section III[7] is used for the top and bottom nozzles made by austenitic stainless steel, respectively.

3.2.3.2 Load Applied in Fuel Handling and Shipping

(1) Design Basis

To obtain expected performance in the reactor, the fuel assembly will not experience excessive deformation during shipping and handling, including uncertainties.

(2) Design Criteria

- Under axial loading during shipping and handling, stresses of the top and bottom nozzles and the control rod guide thimbles shall be less than allowable stress intensity on ASME Section III[7].
- Under axial loading during shipping and handling, forces occurring in connection points between the top nozzle, the grid spacers and the control rod guide thimbles shall be less than the acceptance limit.
- Under lateral loading during shipping and handling, inelastic deformation of the grid spacer spring shall not be increased.
- The grid spacer spring shall not be damaged due to vibration during shipping.

(3) Design Evaluation

Occurred stress of the top and bottom nozzles are evaluated to by FEM stress analyses which are carried out to the load anticipated during fuel handling and shipping. The stresses are identified to be within the allowable stress intensity.

By structural analysis with an analytical model which simulates mechanical characteristic of the fuel assembly in the axial direction, occurred load during fuel handling and shipping are provided in linkages of the control rod guide thimbles to which the top nozzle and the grid spacers, respectively. It is identified that the analytically obtained loads are lower than limiting elastic loads which are given by the tensile tests of the linkages.

As for the control rod guide thimble, maximum stress is obtained just beneath the top nozzle because the part burdens the entire axial load without sharing with the fuel rods. The provided stress is evaluated by comparing with the allowable stress intensity.

It is certified whether plastic deformation of the grid spacer spring is not progressed to lateral load during handling and shipping.

3.2.4 Cladding Fatigue

(1) Design Basis

Fuel system will not be damaged due to excessive fatigue under normal operation including AOOs.

(2) Design Criteria

The cumulative number of strain fatigue cycles shall be less than the design fatigue lifetime, which includes a safety factor of 2 on stress amplitude or a safety factor of 20 on the number of cycles, whichever is larger. The fatigue design curve [11] as shown in Figure 3.2.4-1 is applied to this criterion.

(3) Design Evaluation

Cladding fatigue is evaluated under reactor startup/shutdown operation, AOOs and other power changing operation if necessary. The FINE code is used in order to obtain the cladding stress for each operational condition. The cumulative fatigue damage is assessed by summing the fatigue life usage associated with each duty cycle as determined by the number of anticipated load cycles divided by the number of cycles to failure at that load condition as determined by the fatigue design curve with consideration of the required safety factors. This estimated cumulative fatigue usage shall remain below 1.0.

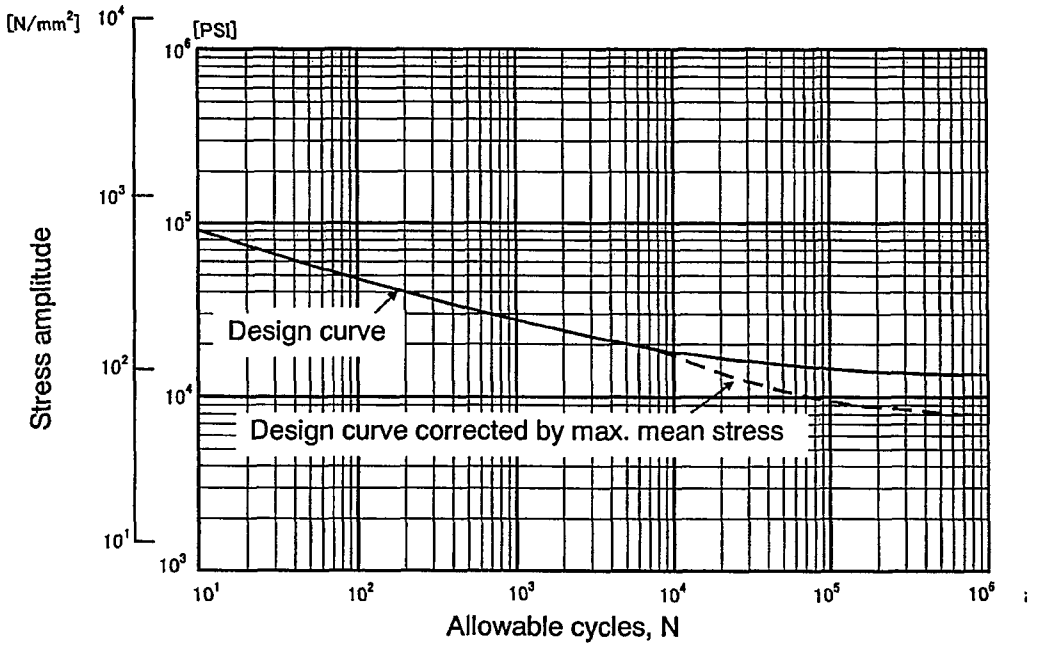

Figure 3.2.4-1 Fatigue Design Curve

3.2.5 Fretting Wear

(1) Design Basis

To supply expected thermal power and to prevent leakage from the fuel rod, the fuel rod will not be damaged by fuel cladding fretting wear due to hydraulic vibration during normal operation.

(2) Design Criteria

The maximum fretting wear depth on the cladding surface shall be less than [ ] % of the initial wall thickness.

(3) Design Evaluation

The fretting wear of the fuel rod cladding is evaluated by long-tem hydraulic-flow tests and analytical evaluations.

The fuel rod vibration characteristics and measured wear depth are obtained from hydraulic flow tests and used as reference data for the analytical evaluation, where the wear depth is extrapolated to predict the maximum wear depth at the end of life in the reactor.

The analytical evaluation for predicting fretting wear in the fuel rod cladding is based on test results and developed in a semi empirical manner. The procedure consists of three steps: evaluation of the fuel rod vibration, amplitude evaluation of the fuel rod vibration due to hydraulic flow, and the wear depth evaluation for the cladding at point supported by the grid spacer.

The characteristics for each evaluation steps are described below.

- The step for modal analysis of the fuel rod vibration
  This step provides vibration characteristics of the fuel rod such as natural frequencies and mode shapes, using a FEM analysis that simulates one fuel rod considering its stiffness, mass distribution and axial support conditions. The analysis considers characteristics such as the variation of the vibration due to relaxation of the grid spacer spring force, using an algorithm that is based on the results of fuel rod vibration tests performed with the fuel rod restraint condition as a parameter.

- The step for amplitude calculation of the fuel rod vibration due to hydraulic flow
  Using the fuel rod vibration characteristics provided by the modal analysis described above and an experimentally defined damping factor, the amplitude of the fuel rod vibration due to the axial coolant flow is calculated. For this calculation, a semi-empirical equation developed by J. R. Reavis[12] has been adopted. The equation gives the vibration amplitude of the fuel rod at the center between adjacent grid spacers. The amplitude is used to calculate the vibration amplitude at the dimple location in the grid spacer by considering the vibration mode shapes. In addition, the force resulting from the vibration is compared with the slippage limiting force of the gird spacer spring to determine if fuel rod slippage occurs and, if so, the slippage distance at the dimple is analyzed.

- The step for wear depth calculation of the cladding
  The wear volume is estimated using Archard's equation[13]

$$V = \alpha \times F \times L$$

where:
V = Wear Volume
α = Specific Wear Ratio Determined by Contacted Materials and Conditions
F = Contacted Force at Dimple in the Grid Spacer
L = Slippage Distance

F is the restraint force on the fuel rod at the dimple, which is calculated from inputs such as initial grid spacer spring force and irradiation history. L is the slippage distance analyzed in the amplitude evaluation. α is the specific wear ratio experimentally provided by the materials for the fuel rod cladding and the grid spacer. The ratio considers the existence of an oxide layer and the variation of fretting states such as sliding and impacting when a gap is opening between the fuel rod cladding and the dimple. Growth of the oxide layer on the cladding outer surface is calculated by a built-in corrosion model.

The wear depth is converted from the calculated wear volume considering geometric forms of the dimple and the worn surface of the cladding,

The above process is repeated to simulate the whole irradiation period, leading to the prediction of the end of life wear depth.

3.2.6 Cladding Oxidation and Hydriding (and Crud Buildup)

(1) Design Basis

Fuel system will not be damaged due to excessive cladding corrosion under normal operation and AOOs.

(2) Design Criteria

During normal operation and AOOs, the cladding surface temperature shall remain below the temperature at which an acceleration of corrosion could occur, as verified by the out of pile Zircaloy-4 cladding corrosion tests. To prevent the acceleration of cladding corrosion, the calculated the cladding metal-oxide interface temperature shall be less than [ ] [ ]. These are the conservative design limits because they are based on Zircaloy-4 cladding corrosion tests, and the temperature required for accelerated corrosion of ZIRLO™ cladding is higher than that of Zircaloy-4.

The cladding hydrogen content shall remain below the value required to prevent degradation of cladding mechanical properties. Based on mechanical test data for irradiated and un-irradiated cladding material, the hydrogen content limit is established as [ ] ppm.

The test data to support these design limits are presented in Appendix B.

(3) Design Evaluation

The cladding metal-oxide interface temperature during irradiation is evaluated by the FINE code under normal operation and AOOs. It increases together with the power increase during AOOs, but oxidation does not increase during this period because AOO events are short.

Cladding hydrogen content at the end of irradiation is also evaluated by FINE code under normal operation. Since oxidation does not increase during AOOs due to short time as described above, hydrogen absorption will not increase during AOOs.

The effect of crud buildup on DNB analysis is discussed in Section 4.4 of SAR.

3.2.7 Dimensional Change

3.2.7.1 Fuel Assembly Growth

(1) Design Basis

To maintain a coolable geometry in the core and assure safe shutdown of the reactor, the fuel assembly will not be excessively distorted nor damaged by compressive loads due to interference with the upper and lower core plates during irradiation.

(2) Design Criteria

Clearance between the top nozzle and the upper core plate shall be maintained throughout the fuel assembly irradiation.

(3) Design Evaluation

The fuel assembly growth is evaluated at cold condition because the thermal expansion between the core plates is more than that of the fuel assembly at hot condition.
Fuel assembly growth as a function of burnup is defined on the basis of measured assembly length change data.

Considering the fuel assembly maximum growth at the end of life predicted by the function and the minimum distance between the core plates, overall length of the fuel assembly is determined so as to maintain clearance between the top nozzle and the upper core plate during the fuel life.

3.2.7.2 Fuel Rod Axial Growth

(1) Design Basis

To supply expected thermal power and maintain fuel rod integrity during irradiation, the fuel rods should not cause excessive bowing nor be damaged by excessive compressive loading due to interference between the fuel rod and the top and bottom nozzles during irradiation that results from the difference in axial growth between the fuel rods and the fuel assembly.

(2) Design Criteria

Clearance between the fuel rods and the top and bottom nozzles shall be maintained during whole of the fuel assembly life.

(3) Design Evaluation

To preclude interference between the fuel rod and the nozzles, the fuel rods and fuel assembly are designed with an initial clearance between the fuel rod ends and the top and bottom nozzles.

The sum of each clearance between the top and bottom nozzles and both fuel rod ends is called total gap. The variation with burnup, which is subtracted fuel rod growth from the fuel assembly growth, is used as design curve for the total gap evaluation. The design curve is

determined by existing data from the visual inspection of the irradiated fuel assemblies.

This initial total gap is designed to be sufficient to accommodate the maximum anticipated fuel rod growth in combination with the minimum fuel assembly growth, and with appropriate consideration of fabrication tolerances.

3.2.7.3 Rod Bowing

(1) Design Basis

To avoid fuel rod damage due to obstruction of coolant flow, excessive fuel rod bowing should not occur.

(2) Design Criteria

Departure from Nucleate Boiling (DNB) shall not occur at a 95 % probability at a 95 % confidence level basis with consideration of the DNB penalty due to rod bowing during normal operation and AOOs.

(3) Design Evaluation

Fuel rod bow is a phenomenon observed in irradiated fuel assemblies and leads to spacing closure in between adjacent two fuel rods. While the mechanism is not yet fully understood, it seems to be related to bowing of the fuel rods as fabricated, restraint force by grid spacers, irradiation growth of both fuel rods and control rod guide thimbles and so on.

A significant fuel rod bow may have somewhat influences on thermal-hydraulic characteristic such as departure from nucleate boiling ratio (DNBR).

Fuel rod bundle between adjacent grid spacers is called span. In outer view inspection of the fuel assembly, all of the peripheral rod to rod spacing on four faces is measured and mean value and standard deviation are calculated in each span. 0.3 percentile spacing closure rate is calculated from the mean value and the standard deviation of the span which has the biggest standard deviation in all of the spans.

Based on the 0.3 percentile fuel rod to rod spacing closure rate accumulated by irradiated fuel assemblies as a function of burnup, fuel rod to rod spacing closure at EOL is predicted. The obtained spacing closure provides the estimate of DNB penalty increase.

The distance between the grid spacers, or span length, and the grip spring restraint force on the fuel rods are designed to suppress the rod bowing and the consequent DNB penalty to the acceptable level.

3.2.7.4 Dimensional Stability of Grid Spacers

(1) Design Basis

To maintain sufficient restraint on the fuel rods during irradiation and loading and unloading performance of the fuel assemblies, the grid spacer will maintain dimensional stability during irradiation.

(2) Design Criteria

The grid spacers shall maintain fuel rod to rod spacing during irradiation. The grid spacers also contribute to locating the fuel assemblies in their correct core position. In addition, the dimensional change of the grid spacers shall not cause excessive interference with neighboring structures such as other fuel assemblies and core baffles.

(3) Design Evaluation

Especially with regard to the grid spacer made of Zircaloy-4 which shows irradiation growth, increase of its outer size at the end of life is evaluated according to the measured outer size in irradiated fuel assemblies.

3.2.8 Rod Internal Pressure

(1) Design Basis

Fuel system will not be damaged due to excessive rod internal pressure under normal operation.

(2) Design Criteria

The fuel rod internal pressure must be below the lowest internal pressure limit among the following three internal pressure limits.

- No cladding liftoff during normal operation
- No reorientation of the hydrides in the radial direction in the cladding
- A description of any additional failures resulting from departure of nuclear boiling (DNB) caused by fuel rod overpressure during transients and postulated accidents

(3) Design Evaluation

(a) Liftoff Pressure

Rod internal pressure shall remain below the cladding liftoff pressure, where the liftoff pressure is defined as that pressure at which the pellet-cladding gap increases due to outward cladding creep. Cladding liftoff must be avoided to eliminate the possibility of thermal feedback, where the gap opening leads to increased pellet temperatures which further accelerate the fission gas release and thus further increase the internal pressure. The FINE code is used both to calculate the rod internal pressure and to calculate the pressure at which cladding liftoff can occur.

The FINE Code evaluates the fuel rod internal pressure experienced during the life by taking into consideration of the power history in the reactor.

The internal pressure evaluation above must take into consideration of the uncertainties of the manufacturing and the FINE code. These uncertainties are considered statistically and the total uncertainty is evaluated by Square Root of the Sum of the Squares (SRSS) method at a 95 % probability at a 95 % confidence level.

The liftoff internal pressure limit is evaluated by the FINE Code.

(b) Hydride Reorientation Pressure

The hydrogen absorbed in connection with oxidation is precipitated as hydride if hydrogen content exceeds the hydrogen solubility limit, causing reduction in the ductility of cladding. For this purpose, the hydrogen absorption is evaluated and confirmed to be below the limit. In the fuel cladding, these hydrides have characteristics to be oriented in the circumferential direction under circumferential stress, but be reoriented in the radial direction under the high circumferential stress. If hydrides are oriented in the radial direction, the cracks may occur along the hydrides. Therefore, it is necessary to prevent reorientation of hydrides from the viewpoint of the integrity of fuel cladding.

The tensile stress in the circumferential direction of cladding due to the fuel rod internal

pressure occurs when the internal pressure is higher than the external pressure. Appendix B shows an example where the circumferential stress of fuel cladding is evaluated with the system pressure. In this manner, the internal pressure shall be below the limit to avoid hydride reorientation.

(c) DNB Propagation

If DNB occurs on a fuel rod which has higher internal pressure than system pressure, it may increase the probability of fuel rod expanding due to cladding temperature increasing and difference between internal and external pressure. Since the fuel rod expanding impairs the coolability of adjacent rods, there is a probability that adjacent rods will be in DNB condition subsequently.

For departure from nucleate boiling ratio (DNBR), there shall be at a 95 % probability at a 95 % confidence level that the hot rod in the core does not experience DNB or boiling transition condition during normal operation or AOOs. The probability that excessive DNB propagation may occur will be low.

To evaluate above, the probability that a high pressure rod occurs and the probability that rods will be in DNB condition shall be considered. This evaluation will lead to the result that the probability of DNB propagation occurrence is quite low.

The power of high pressure fuel rods will be decreasing because these rods shall be in high burnup region. Therefore, high pressure rods will have some margin below the DNB power. And above assessment will be conservative.

The detailed evaluation for the postulated accidents is discussed in Section 3.4.4.

3.2.9 Assembly Liftoff

(1) Design Basis

To keep the fuel stack in the proper position and to prevent fuel assembly damage due to impact following liftoff, fuel assembly liftoff will not occur due to hydraulic forces during normal operation and AOOs, except for pump-over-speed.

If fuel assembly liftoff does occur during pump-over-speed, the functionality of the fuel assembly holddown spring will not be degraded.

(2) Design Criteria

- Normal operation and AOOs except pump-over-speed:
  At cold condition for reactor startup in the beginning of life, which is the most critical period for the liftoff evaluation of the fuel assembly, the holddown spring force of the top nozzle shall be larger than the residual force which is calculated by "hydraulic lift force + buoyant force – fuel assembly weight".
- At the pump-over-speed:
  Inelastic deformation of the holddown spring shall not occur during lifting of the fuel assembly due to the hydraulic force at the pump-over-speed.

(3) Design Evaluation

The overall length of the fuel assembly is increased by irradiation, so the force of the hold down spring increases as it is irradiated. Consequently, the function of the holddown spring should be evaluated in the un-irradiated state where the spring force is the smallest.
A mechanical force balance calculation, considering the fuel assembly weight, the holddown force, the hydraulic lift force and the buoyant force, is used to evaluate that the fuel assembly does not experience liftoff at cold startup condition in the beginning of life.

The hydraulic test of the fuel assembly is carried out for evaluation of the design margin.
As long as the deflection of the holddown spring due to the liftoff at the pump-over-speed is not beyond the maximum deflection at the cold startup condition, extra plastic deformation does not take place in the holddown spring. This is also verified by the same mechanical balance calculation as that in normal operation and AOOs.

3.3 Design Criteria and Methodology for Fuel Rod Failure

Fuel rod failure applies to normal operation, AOOs, and postulated accidents. Fuel rod failure is defined as the loss of fuel rod hermeticity. The fuel rod is designed with sufficient margin to design limits so that fuel failure is not expected during normal operation and AOOs. Some fuel rod failures are permitted during postulated accidents, but the consequences of these failures must be accounted for in the dose analysis for each postulated accident.

To meet the requirements of (1) GDC 10 as it relates to SAFDLs for normal operation, including AOOs and (2) 10 CFR Part 100 as it relates to fission product releases for postulated accidents, fuel rod failure criteria must be specified for all known fuel rod failure mechanisms.

Fuel rod failures can be caused by overheating, PCI, hydriding, cladding collapse, bursting, mechanical fracturing, and fretting. When applicable, the fuel rod failure criteria should consider high burnup effects based on irradiated material properties data.

The fuel failure criteria to be applied to the Mitsubishi fuel design are defined below.

3.3.1 Hydriding

(1) Design Basis

The fuel rod will not fail due to excessive hydriding.

(2) Design Criteria

Primary hydriding is prevented by maintaining the level of moisture and other hydrogenous impurities very low during the UO_2 pellet manufacturing. The moisture content shall remain below the limit of 1.3 ppm (hydrogen from all sources for fuel pellets)[14].

External hydriding is addressed by limiting the cladding hydrogen content during irradiation to less than [ ] ppm as previously described in Section 3.2.6.

(3) Design Evaluation

Appropriate process controls are in place to maintain moisture content during the pellet manufacturing at values less than the above criteria.

This problem has been resolved by strengthening the Quality Controls for moisture content in the pellet manufacturing, and by the use of higher density pellets. Current pellet nominal density for Mitsubishi fuel is 95 % TD and 97 % TD, as compared with fuel pellet densities of about 93 % TD and below that were in use at the time hydriding failure occurred. As a result, the moisture content is kept sufficiently low compared with its limit of 1.3 ppm (hydrogen from all sources for fuel pellets).

External hydriding is evaluated in Section 3.2.6.

3.3.2 Cladding Collapse

(1) Design Basis

Fuel rod failure will not occur due to cladding collapse.

(2) Design Criteria

The number of fuel rods which causes cladding collapse shall be less than 1 rod during fuel life.

(3) Design Evaluation

The Mitsubishi fuel design uses high density fuel pellets, which are stable with respect to fuel densification. In addition, the fuel rods are initially pressurized with helium. The combination of stable fuel and pre-pressurized fuel rods has been quite effective in eliminating the formation of axial gaps in the fuel column due to densification. After the adoption of 95 % TD pellet and initial pressurization with helium in the fuel design more than 30 years ago, Mitsubishi has had no incidents of cladding collapse. For the US-APWR fuel rod design, Mitsubishi is intending to use fuel pellets with a higher initial density of 97 % TD. This pellet design is even more stable with respect to fuel densification due to the reduced initial porosity, and will therefore have greater margin to cladding collapse than that already demonstrated with 95 % TD initial fuel density.

On the basis of the extensive operating experience of Mitsubishi fuel in Japan, it is concluded that cladding collapse does not occur for fuel rods with initial fuel pellet density of 95 % TD or greater and with initial fuel rod pressurization with helium. Maintaining current pellet fabrication process controls with initial pellet density of 95 % TD and greater and with current initial helium pressurization levels is therefore sufficient to prevent cladding collapse from occurring. However, Mitsubishi does maintain the capability to perform cladding collapse calculations should it become necessary to do so.

3.3.3 Overheating of Cladding

(1) Design Basis

Fuel rod failure will not occur under normal operation and AOOs due to cladding overheating. Fuel rod failure under postulated accidents will be accounted for in the dose calculations for those events.

(2) Design Criteria

Overheating of the cladding is precluded by maintaining thermal design margins (DNBR criteria) for normal operation and AOOs. Under postulated accidents, the rods which exceed the DNBR criteria are assumed to fail for the purpose of the radiological dose calculation.

(3) Design Evaluation

The DNBR design basis and evaluation methods are discussed in the topical report "Thermal Design Methodology"[15].

The fraction of rods in the core which exceeds the DNBR criteria under postulated accidents is assumed to fail and is accounted for in the radiological dose calculations for those postulated accidents.

3.3.4 Overheating of Fuel Pellets (Melting)

(1) Design Basis

Fuel rod failure will not occur due to overheating of fuel pellets under normal operation and AOOs. Fuel rod failure under postulated accidents will be accounted for in the dose calculation.

(2) Design Criteria

To prevent fuel from overheating under normal operation and AOOs, the calculated fuel centerline temperature shall not exceed the melting temperature of the fuel. The melting temperature for un-irradiated UO_2 pellet is defined as 5072 deg.F (2800 deg.C), decreasing with burnup by 58 deg.F(32 deg.C) per 10 GWd/t (see Appendix B).

Under postulated accidents, the rods that experience centerline melting are assumed to fail for the purpose of the radiological dose calculation.

(3) Design Evaluation

Peak centerline temperature is calculated by the FINE code. In this calculation, appropriate uncertainties of the manufacturing and the FINE code are considered. The calculated centerline temperature is compared with melting temperature to evaluate the potential for fuel melting during postulated accidents. Under postulated accidents, the total number of fuel rods that are predicted to exceed the centerline melting temperature, with consideration of uncertainties, are accounted for in the radiological dose calculations.

Best estimate models in the FINE code are used for fuel temperature analysis, however, conservative model based on RG-1.126[16] is used for fuel densification in consideration of manufacturing data. The following is the design procedure for local linear power limit (See Figure 3.3.4-1).

(a) Fuel centerline temperature analysis (Best estimate calculation)
Fuel centerline temperature as a function of local linear power is calculated at various burnup by the FINE code (See Figure 3.3.4-2).

(b) Fuel centerline temperature uncertainties
Fuel centerline temperature uncertainties of the manufacturing and the FINE code are evaluated at a 95 % probability at a 95% confidence level.

(c) Design limit for fuel temperature analysis
Design limit for fuel temperature analysis is provided by subtracting uncertainties of the manufacturing and the FINE code from melting temperature.

(d) Linear Power corresponding to design limit
Linear power which corresponds to design limit is calculated at various burnup based on the correlation between fuel centerline temperature and linear power (See Figure 3.3.4-3).

(e) Local linear power limit
Local linear power limit as a function of burnup is set adequately below the linear power

which corresponds to the design limit for fuel centerline temperature (See solid line in Figure 3.3.4-4).

The local linear power is verified to meet its design limit for each reload core.

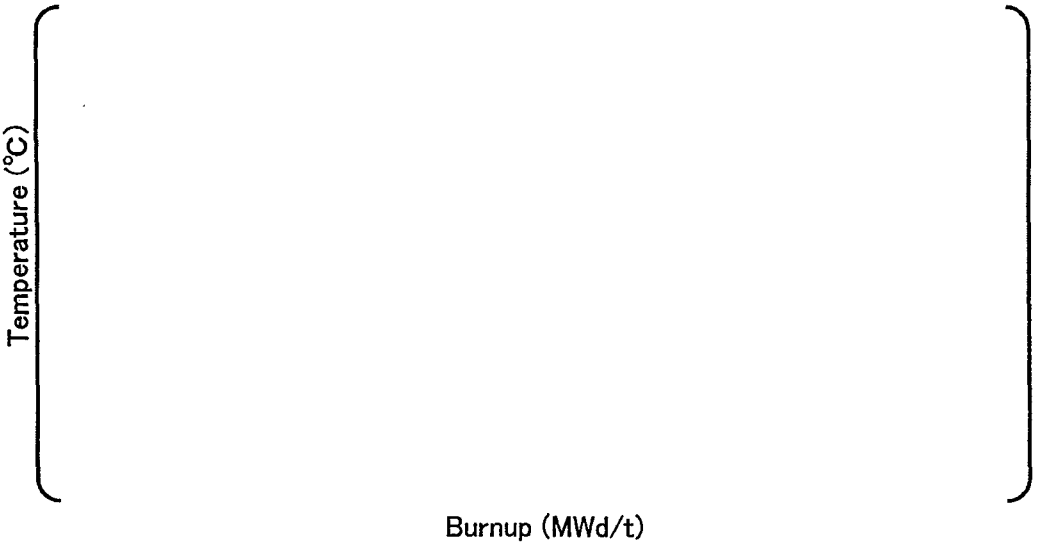

Figure 3.3.4-1 Fuel Temperature Design Limit versus Burnup

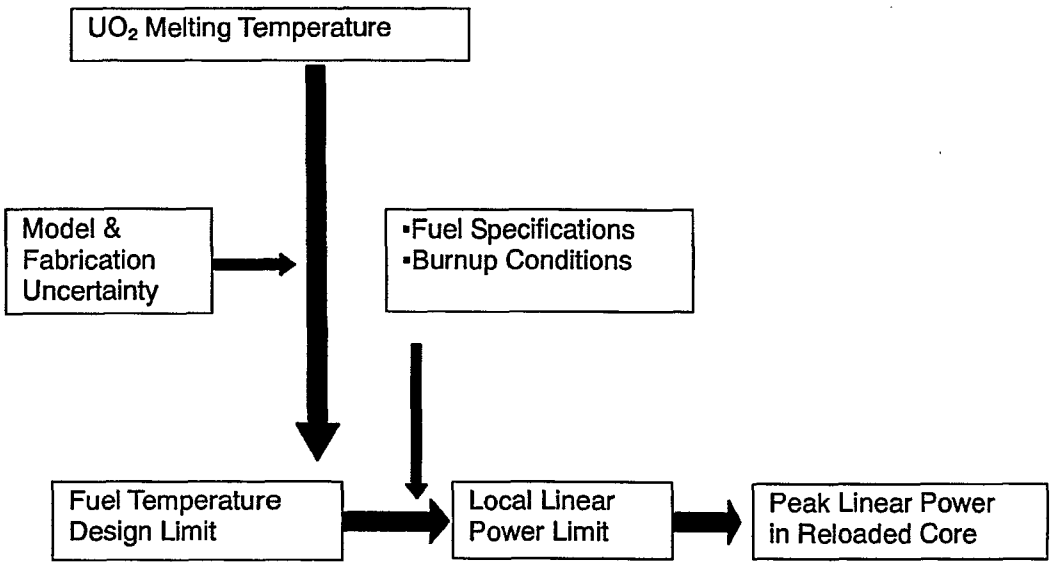

Figure 3.3.4-2 Design Procedure for Local Linear Power Limit

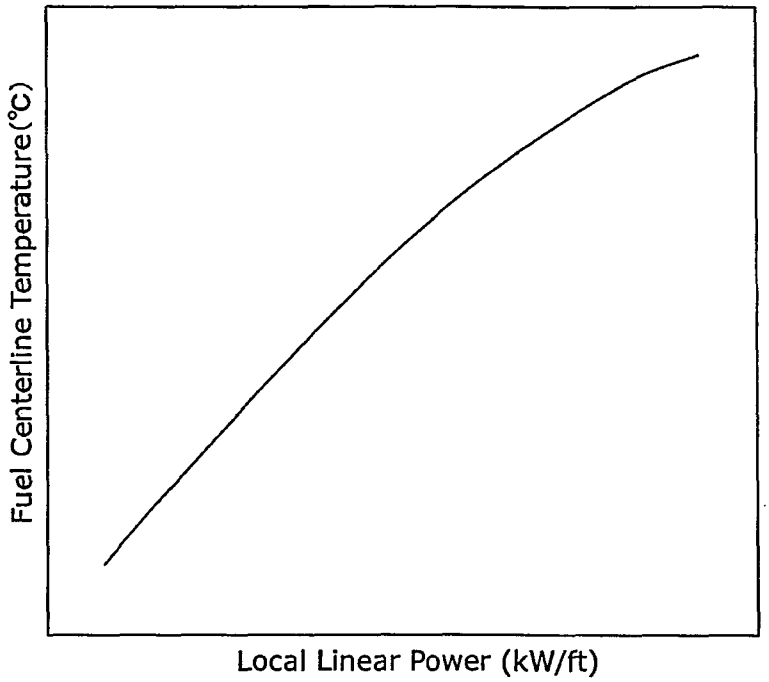

Figure 3.3.4-3 Fuel Centerline Temperature versus Local Linear Power (Conceptual Diagram)

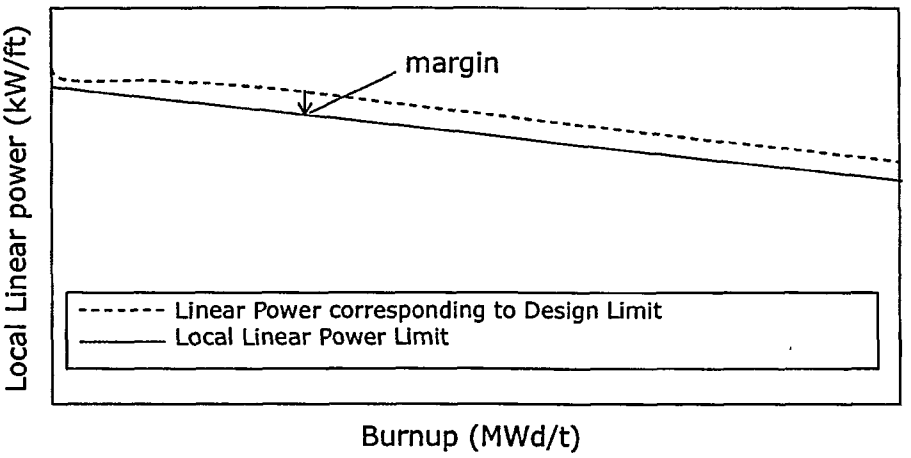

Figure 3.3.4-4 Local Linear Power Limit versus Burnup (Conceptual Diagram)

3.3.5 Excessive Fuel Enthalpy

(1) Design Basis

Fuel rod failure under postulated accidents will be accounted for in the dose calculation.

(2) Design Criteria

The total number of fuel rods that must be considered in the radiological assessment is equal to the sum of all of the fuel rods failing each of the criteria below.

1. High cladding temperature failure
   - Zero power condition
     - If rod internal pressure is at or below system pressure, the failure criterion is a peak radial average fuel enthalpy greater than 170 cal/g.
     - If rod internal pressure exceeds system pressure, the failure criterion is a peak radial average fuel enthalpy greater than 150 cal/g.
   - Intermediate and full power conditions
     - Fuel cladding failure is assumed to occur if the local heat flux exceeds thermal design limits (DNBR).
2. PCMI failure

   The PCMI failure criteria adopted by Mitsubishi for evaluation of RIA events is that specified in Figure B-1 (PWR) in the NRC standard review plan, Revision 3, which is presented herein as Figure 3.3.5-1. This criterion specifies that a change in radial average fuel enthalpy greater than the corrosion-dependent limit depicted in Figure 3.3.5-1 will be assumed to cause fuel rod failure for the purpose of dose calculations.

(3) Design Evaluation

The detailed evaluation of this criterion is discussed in Chapter 15 (Transient and Accident Analysis) of the SAR.

FIGURE B-1: PWR PCMI Fuel Cladding Failure Criteria

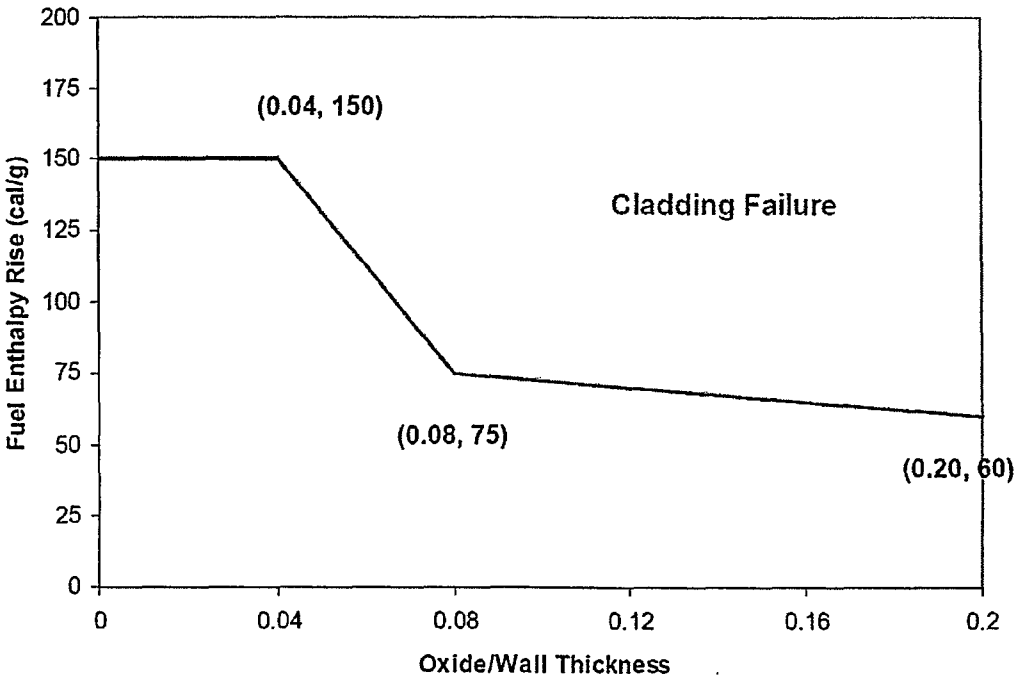

Figure 3.3.5-1 PWR PCMI Fuel Cladding Failure Criteria [1]

3.3.6 Pellet / Cladding Interaction (PCI)

(1) Design Basis

Fuel failure will not occur due to pellet cladding interaction (PCI) during normal operation and AOOs. Fuel rod failure under postulated accidents will be accounted for in the dose calculation.

(2) Design Criteria

Mitsubishi does not apply a PCI specific design criterion. Instead, PCI is addressed by two existing criteria: (1) cladding strain during AOOs must remain below 1%, and (2) fuel centerline melting does not occur.

The cladding strain criterion is described in Section 3.2.2. The fuel centerline melting criterion is described in Section 3.3.4.

(3) Design Evaluation

The methodology for the cladding strain design evaluation is described in Section 3.2.2 and that for fuel centerline melting is described in Section 3.3.4.

3.3.7 Bursting

(1) Design Basis

Fuel rod failures are permitted during postulated accidents, but they will be accounted for in the dose analysis.

(2) Design Criteria

Rod failure as predicted to occur by the ECCS evaluation shall be accounted for in the dose analysis.

(3) Design Evaluation

A calculation of the swelling and rupture of the ZIRLO™ cladding, based on the temperature distribution in the cladding and the pressure differences between the inside and outside of the cladding, is performed for the ECCS evaluation in order to meet the requirements of 10CFR 50.46.

The details of this evaluation are discussed in Chapter 15 (Transient and Accident Analysis) of the SAR.

3.3.8 Fuel Rod Mechanical Fracturing

(1) Design Basis

To supply the expected thermal power and maintain fuel rod integrity, the fuel rod will not fail due to loads resulting from hydraulic flow and movement of the core plates under AOOs and postulated accidents.

(2) Design Criteria

Combined cladding stresses resulting from response to earthquake and postulated accidents shall be less than 90% of cladding yield stress at operating temperature.

(3) Design Evaluation

For the seismic response to accelerations of the upper and lower core plates, time-dependent horizontal displacement of the fuel assembly is analyzed by a group vibration analysis modeling of the fuel assemblies array. To consider interactions among adjacent fuel assemblies and core barrels, the group vibration analysis is needed for the horizontal direction. The calculated maximum displacement is input to the fuel assembly structural model which simulates mechanical performance, and component stresses, including the fuel rod cladding stresses, are analyzed by a FEM analysis.

Horizontal response and stresses including the cladding are analyzed for the postulated accident, as well as the seismic response.

The resulting stresses to the horizontal response during the earthquake and postulated accidents are combined by the SRSS method.

In the vertical direction, load on the fuel assembly obtained by core internal response analysis is directly used as input for stress analyses of seismic and postulated accident responses because it is not as important to consider such interaction as that in the horizontal direction.

The loads are provided to respective stress analyses for seismic and postulated accident response in the vertical direction.
The resultant stresses of the cladding during both events are combined by the SRSS method.

In addition, the cladding stresses which are individually provided for the horizontal and vertical directions are combined by the SRSS method. The combined stress shall be less than 90 % of the cladding yield stress at operating temperature.

The evaluation procedure for calculation of the cladding stress under combined earthquake and postulated accident loading is explained in Appendix D.

3.4 Design Criteria and Methodology for Fuel Coolability

Coolability, or coolable geometry, implies that the fuel assembly retains its rod-bundle geometry with adequate coolant channels to permit removal of residual heat. Reduction of coolability can result from cladding embrittlement, violent expulsion of fuel, generalized cladding melting, gross structural deformation, and extreme coplanar fuel rod ballooning.

The fuel coolability criteria described below are applied to the analysis of postulated accidents, and the details of the evaluations and analyses performed to assess these criteria are presented in Chapter 15 (Transient and Accident Analysis) of the SAR.

3.4.1 Cladding Embrittlement

(1) Design Basis

Coolability of the core will be maintained under postulated accidents.

(2) Design Criteria

For Zircaloy-4 or ZIRLO™ cladding, the design criteria for cladding embrittlement are

- The peak cladding temperature shall remain below 2200 deg.F.
- The peak cladding oxidation shall remain below 17 percent ECR.

(3) Design Evaluation

The detailed evaluation of the design criteria for cladding embrittlement is discussed in Chapter 15 (Transient and Accident Analysis) of the SAR.

3.4.2 Violent Expulsion of Fuel

(1) Design Basis

Coolability will be maintained under postulated accidents.

(2) Design Criteria

- Peak radial average fuel enthalpy must remain below 230 cal/g.
- Peak fuel temperature must remain below incipient fuel melting condition.
- Mechanical energy generated as a result of (1) non-molten fuel-to-coolant interaction and (2) fuel rod burst must be addressed with respect to reactor pressure boundary, reactor internals, and fuel assembly structural integrity.
- No loss of coolable geometry due to (1) fuel pellet and cladding fragmentation and dispersal and (2) fuel rod ballooning.

(3) Design Evaluation

The detailed evaluation is discussed in Chapter 15 (Transient and Accident Analysis) of the SAR.

3.4.3 Generalized Cladding Melting

Generalized (i.e., non-local) melting of the cladding could result in the loss of rod-bundle fuel geometry. For Zircaloy-4 or ZIRLO™ cladding, the criteria for "cladding embrittlement" (Section 3.4.1 above) are more limiting than this generalized cladding melting criteria, so that no specific criterion for generalized cladding melting is required.

3.4.4 Fuel Rod Ballooning

(1) Design Basis

Coolability will be maintained under postulated accidents with consideration of cladding ballooning and flow blockage.

(2) Design Criteria

- LOCA
  To meet the requirements of 10CFR50.46, the analysis of the core flow distribution shall account for burst strain and flow blockage caused by ballooning (swelling) of the cladding.

- non-LOCA
  Non-LOCA accidents that result in cladding ballooning shall examine the possibility of DNB propagation resulting from ballooning.

(3) Design Evaluation

In Chapter 15 (Transient and Accident Analysis) of the SAR, burst strain and flow blockage of ZIRLO™ are properly taken into account in LOCA evaluation.
The possibility of DNB propagation is examined in non-LOCA evaluation.

3.4.5 Structural Deformation

(1) Design Basis

Core coolability and safe shutdown of the reactor will be maintained with consideration of the combination of earthquake and postulated accident loads.

(2) Design Criteria

Under combined earthquake and postulated accident loads,

- Deformation of the grid spacer shall not prevent the control rods from being inserted into the fuel assembly.
- The stress in the control rod guide thimbles and the top and bottom nozzles shall be less than the allowable stress intensity based on ASME Section III[7].
- The control rod guide thimble shall not experience buckling due to axial loads caused by earthquake and postulated accidents.

(3) Design Evaluation

For seismic accelerations of the upper and lower core plates in the horizontal direction, the time-dependent horizontal displacement of the fuel assembly is analyzed by a group vibration analysis modeling of the fuel assemblies array. The calculated maximum displacement is input to the fuel assembly model simulating mechanical performance and component stresses, including the control rod guide thimble stresses, are analyzed by a FEM analysis.

Stresses to the horizontal response due to a postulated accident are calculated in the same way.

The resulting seismic and postulated accident's stresses on the components such as the control rod guide thimbles are combined by the SRSS method.

As described in the Section 3.3.8, load on the fuel assembly obtained by core internal response analysis is directly used as input for stress analyses of seismic and postulated accident responses in the vertical direction. The loads are provided to respective stress analyses for seismic and postulated accident response in the vertical direction. The resultant stresses of the both events are combined by the SRSS method.

The combined stress of the control rod guide thimble under combined earthquake and postulated accident loads is determined by the SRSS method, and is determined to be less than the allowable stress intensity for the control rod guide thimble.

The buckling load of the control rod guide thimble is evaluated for the combined axial load due to earthquake and postulated accident.

For the grid spacer, each grid deformation at a seismic condition and postulated accident is individually analyzed by the horizontal response analysis. Both grid spacer deformations are combined by the SRSS method and the resulting deformation is compared with a limiting value which is experimentally defined to assure control rod insertion.

For the top and bottom nozzles, individual loads obtained by seismic and postulated accident

analyses, respectively, are combined by the SRSS method. Stress analysis of each nozzle is carried out with the combined load. The resulting stresses of the nozzles are determined to be within the allowable stress intensity based on ASME Section III[7].

The evaluation procedure for combined earthquake and postulated accident loads described above is further explained in Appendix D.

3.5 References

(1) U.S. Nuclear Regulatory Commission, Standard Review Plan (NUREG-0800) Section 4.2, March 2007
(2) 10 Code of Federal Regulation 50 Appendix A
(3) 10 Code of Federal Regulation 50.46
(4) 10 Code of Federal Regulation 100
(5) U.S. Nuclear Regulatory Commission, Regulatory Guide 1.70. Section 4.2
(6) ANSI/ANS57.5-1981, ANSI/ANS-51.1 1983
(7) American Society of Mechanical Engineers Boiler and Pressure Vessel Code Section III
(8) S.L.Davidson and D.L.Nuhfer, "VANTAGE+ Fuel Assembly Reference Core Report", WCAP-12610, June 1990
(9) B.Watkins and D.S.Wood, "The Significance of Irradiation-Induced Creep on Reactor Performance of a Zircaloy-2 Pressure Tube Applications – Related Phenomena for Zirconium and its Alloys", ASTM STP 458, American Society for Testing and Materials, PP.226-240, 1969
(10) D.S.Wood and B.Watkins, "A Creep Limit Approach to the Design of Zircaloy-2 Reactor Pressure Tubes at 275 C", Journal of Nuclear Materials 41 327-340, May 1971
(11) W.J.O'Donnel and B.F.Langer, "Fatigue Design Basis for Zircaloy Components", Nuclear Science and Engineering 20 pp.1-12, 1964
(12) J. R. Reavis, "Vibration Correlation for Maximum Fuel-Element Displacement in Parallel Turbulent Flow", Nuclear Science and Engineering: 38, 63-69, 1969
(13) J. F. Archard, "Contact and Rubbing of Flat Surfaces", Journal of Applied Physics 24, p981, (1953)
(14) American Standards and Testing Methods (ASTM) C776-06, Standard Specification for Sintered Uranium Dioxide Pellets
(15) Y.Makino, et al., "Thermal Design Methodology", MUAP-07009-P, May 2007
(16) U.S. Nuclear Regulatory Commission, Regulatory Guide 1.126

4.0 FUEL ROD DESIGN COMPUTATIONS (FINE CODE)

Mitsubishi developed the FINE (Fuel rod INtegrity Evaluation) fuel rod design code in the 1980's for application to the evaluation of high burnup fuel (up to 48 GWd/t fuel assembly average burnup). The FINE code was approved by the Japanese authorities and has been used for fuel rod integrity evaluations. This high burnup (48GWd/t) fuel has been loaded in all the PWR power plants in Japan. Mitsubishi fuel has had excellent irradiation experience, with very few fuel failures. Further improvements have been made to apply the code to higher burnups (55GWd/t fuel assembly average burnup) in Japan. The models used in the MHI improved FINE code have been developed from data obtained from post irradiation examinations and other tests, and it has been approved by the Japanese authorities as the high burnup FINE code. High burnup fuel, designed for the 55 GWd/t burnup limit using the high burnup FINE code, is currently in operation in some Japanese PWR power plants. (described in Appendix A)
The detailed features of the high burnup FINE code are described in this chapter. All references to FINE in this chapter are references to the high burnup FINE code.

4.1 Applicability of the FINE Code

The FINE code predicts the expected fuel rod behavior under nuclear reactor operation, such as fission gas production and its release, pellet and cladding temperatures, thermal expansion of the pellets and the cladding, pellet densification and swelling, cladding creep, growth, and elastic deformation, pellet-cladding mechanical interaction, etc in order to evaluate the fuel temperatures, internal pressure, cladding stress, cladding strain, etc.
The FINE code is applicable to fuel with the following design features:

(a) pellet

Type: UO_2, Gd_2O_3 doped fuel
Shape: Solid (normal) or annular pellets, with dish and/or chamfer, which is accounted for in the rod free volume calculation

(b) cladding

Type: Cold-worked stress-relieved Zircaloy-4 or Corrosion resistant Zirconium based alloy (ZIRLO™)

(c) rod

Non-pressurized or pressurized with Helium, Air, Nitrogen, Argon or fission gas.

The range of applicability of the FINE code is determined from the verification data range. Figure 4.1-1 shows the verification data range for internal pressure. The applicable range of FINE is summarized as follows:

(d) applicable burnup
up to 65 GWd/t rod average,

(e) linear heat rate under normal operation
up to 37 kW/m (11kW/ft) rod average (derived from BR3 High Burnup Data)

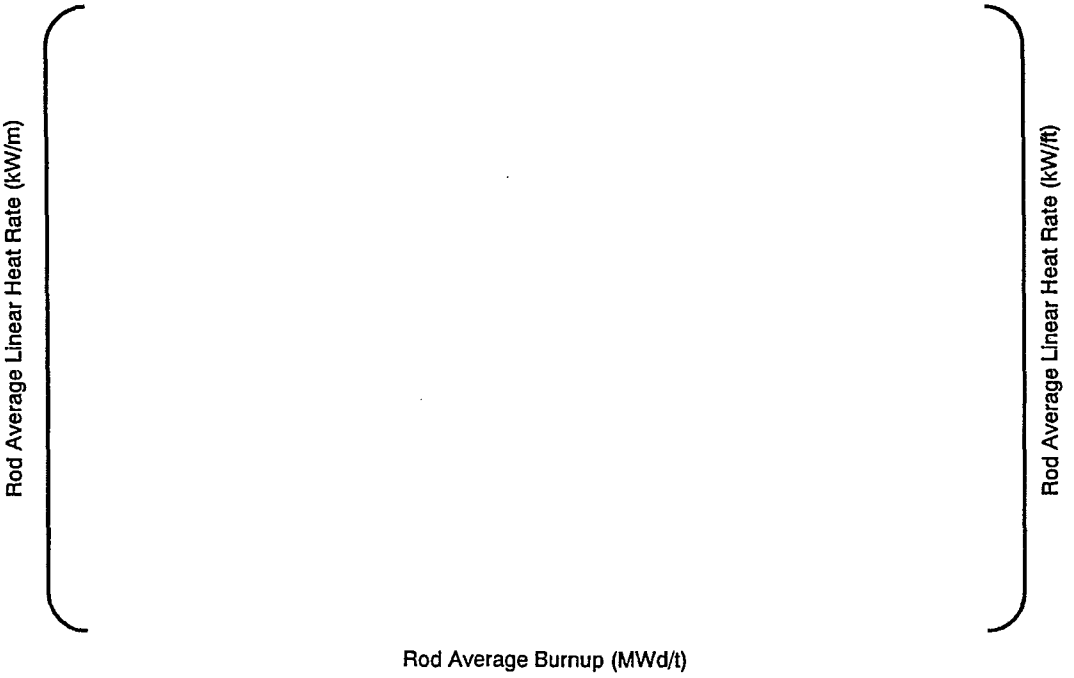

Figure 4.1-1 Burnup and Linear Heat Rate Range of the FINE Code Rod Internal Pressure Verification Data

4.1.1 Axial and Radial Calculation Elements

The FINE code uses a 2-dimensional axisymmetric model of the fuel rod. In the FINE code the fuel pellet is divided into 10 equal area radial elements. The axial calculation element is the same for both the pellet and the cladding. Annular pellets are modeled with the input of the central hole diameter.
In the radial direction the FINE code calculates the dimensional changes of the cladding and pellet, and the mechanical interaction between the pellet and cladding. FINE performs the temperature calculation in the radial direction with no axial variation within each axial element, taking into consideration the axial dimensional changes of the pellet and cladding.

4.1.2 Time Step

All time dependent parameters are input to the FINE code for each time step, such as power history, coolant temperature, etc. Constant values for each of these time dependent input parameters are used throughout each time step, as shown in Figure 4.1.2-1.

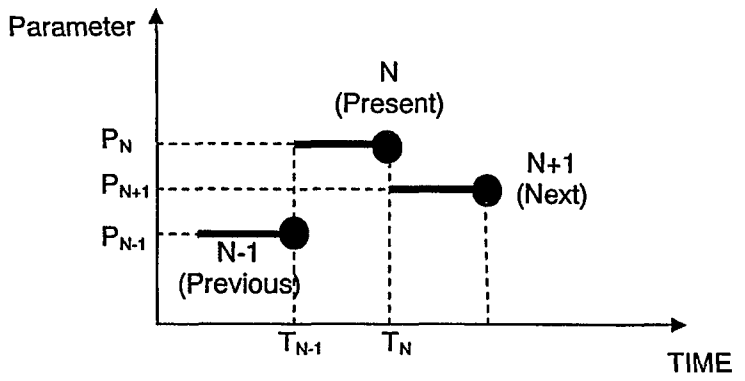

Figure 4.1.2-1 Schematic of Time Step and Input Parameter Usage

4.1.3 Calculation Flow

Figure 4.1.3-1 shows the calculation flow chart for the FINE code. The output from the FINE code, such as the pellet and cladding temperatures, the rod pressure, the pellet and cladding stresses and strains, is used in the fuel integrity evaluation. In addition, the FINE code has the capability to evaluate any fuel rod in the core. The code input is generally applicable to any fuel rod and includes fuel rod specification, power history, reactor system parameters, etc. Sample input and output are summarized in Appendix C.
In each time step the FINE code begins with the calculation of the coolant and cladding temperatures, using a single channel coolant flow model. The gap conductance is then calculated based on an assumed rod pressure from the previous time step. The pellet temperature, dimensions and gas release from the pellet are then calculated. These calculations continue iteratively until pressure converges.
These calculations are done for each axial calculation element. After the calculations are completed for all the axial elements, the FINE code calculates the total rod gas release, the

cladding stresses, and the rod internal gas pressure. This result for the rod pressure is compared with the initially assumed pressure and checked to determine if it meets the convergence criterion. If the convergence criterion is not met, this procedure is iterated. If the convergence criterion is met, the FINE code calculation moves onto the next time step.

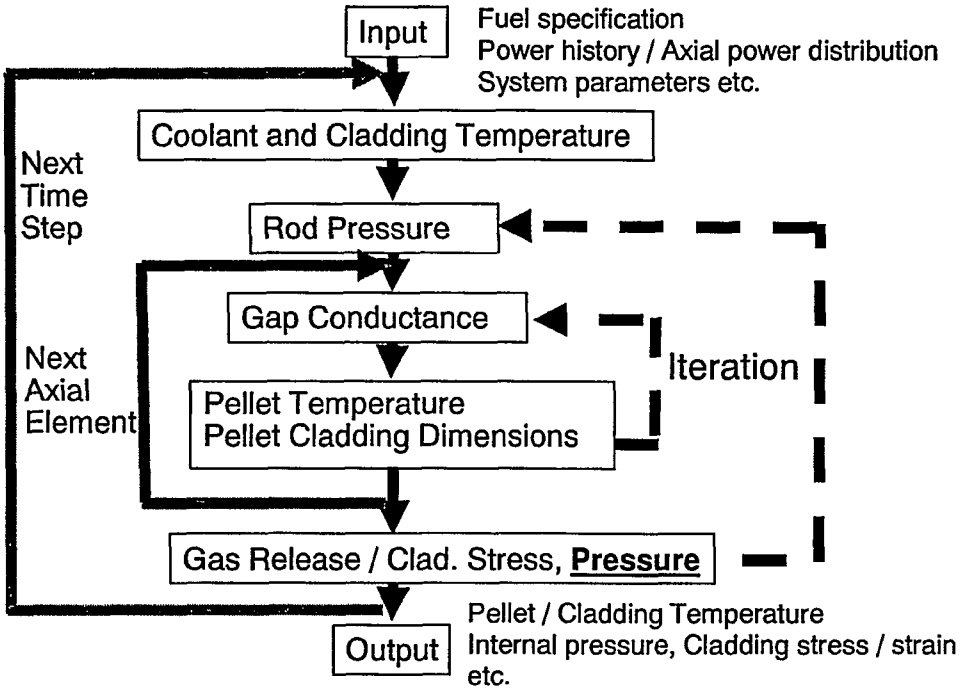

Figure 4.1.3-1 FINE Code Calculation Flow

4.2 Analysis Models

In this sub-section, analysis models used in the FINE code are described.

4.2.1 Thermal Models

Thermal models in the FINE code are described as follows.

4.2.1.1 Coolant Temperature and Cladding Temperature

(a) Coolant Temperature
A single channel coolant flow model is used in the FINE code. All the heat generated in the fuel rod is transferred to the coolant in the channel. Therefore, the coolant temperature is calculated as follows:

$$T_{bulk}(z) = T_{in} + \int_0^z \frac{4q''(z')}{C_p G D_e} dz' \qquad \text{(eq. 4.2.1.1-1)}$$

where

$T_{bulk}(z)$: coolant bulk temperature at axial position z (deg.F)
$q''(z)$: heat flux at axial position z (BTU/hr/ft^2)
C_p : coolant specific heat (BTU/lbm/deg.F)
G : mass flow rate in a channel (lbm/hr/ft^2)
D_e : hydraulic equivalent diameter (ft)
T_{in} : inlet coolant temperature (deg.F)

If $T_{bulk}(z)$ exceeds the saturation temperature, T_{sat}, then:

$$T_{bulk}(z) = T_{sat} \qquad \text{(eq. 4.2.1.1-2)}$$

The saturation temperature is calculated as a function of pressure. The relation between saturation temperature and pressure is shown in Figure 4.2.1.1-1, and compared with that given in the ASME steam tables[1].

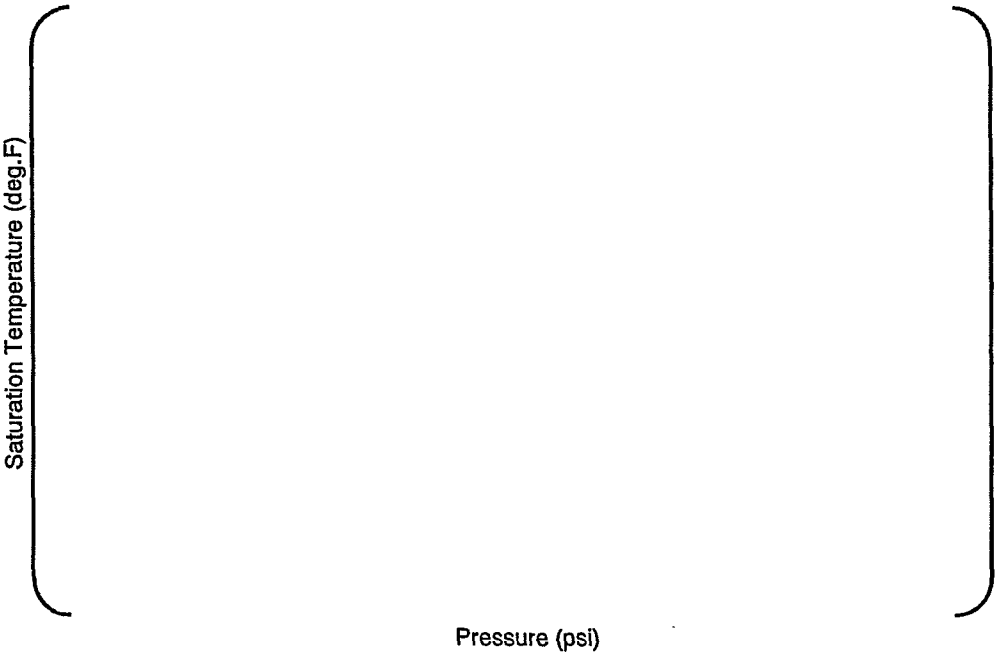

Figure 4.2.1.1-1 Saturation Temperature

(b) Cladding Surface Temperature

The cladding surface temperature ($T_{sur}(z)$) is calculated as the minimum of the following equations:

$$T_{sur}(z) = T_{bulk}(z) + \Delta T_{film}(z) + \Delta T_{crud}(z) \quad (deg.F) \qquad \text{(eq. 4.2.1.1-3)}$$

$$T_{sur}(z) = T_{sat} + \Delta T_{L.B.}(z) \quad \text{(under nucleate boiling) (deg.F)} \qquad \text{(eq. 4.2.1.1-4)}$$

- $\Delta T_{film}(z)$ is given by

$$\Delta T_{film}(z) = q''(z)/h_{film} \quad (deg.F) \qquad \text{(eq. 4.2.1.1-5)}$$

where the Dittus-Boelter correlation[2] is used

$$h_{film} = \frac{0.023 \cdot k}{D_e}(Re)^{0.8}(Pr)^{0.4} \qquad \text{(eq. 4.2.1.1-6)}$$

Where

h_{film}	: heat transfer coefficient (BTU/hr/ft^2/deg.F)
k	: thermal conductivity of fluid (BTU/hr/ft/deg.F)
D_e	: hydraulic equivalent diameter (ft)
Re	: Reynolds number
Pr	: Prandtl number

- $\Delta T_{crud}(z)$ is calculated as follows.

$$\Delta T_{crud}(z) = q''(z)\,\delta_{crud}/K_{crud} \quad (deg.F) \qquad \text{(eq. 4.2.1.1-7)}$$

$$\delta_{crud} = \left(\qquad \right) \qquad \text{(eq. 4.2.1.1-8)}$$

where

K_{crud} : crud thermal conductivity in convection ( ) BTU/hr/ft/deg.F)

τ : operating time (hr)
ACRUD1 : Crud deposition rate under forced convection. (mils/year)
ACRUD2 : Maximum crud thickness under forced convection. (mils)

- $\Delta T_{L.B.}(z)$ is calculated as follows:
Under nucleate boiling, $\Delta T_{L.B.}(z)$ is calculated using the maximum obtained from either the Thom film heat conductance or the Tong film heat conductance,

$$\Delta T_{L.B.}(z) = \max(\Delta T_{L.B.}(THOM), \Delta T_{L.B.}(TONG)) \quad \text{(eq. 4.2.1.1-9)}$$

The Thom model[3] is given by

$$\Delta T_{L.B.}(THOM) = \frac{0.072\sqrt{q''(z)}}{\exp[P/1260]} \quad \text{(deg.F)} \quad \text{(eq. 4.2.1.1-10)}$$

where P is the system pressure (psi)
and the Tong model is given by

$$\Delta T_{L.B.}(TONG) = \frac{q''(z)\delta'_{crud}}{K'_{crud}} \quad \text{(deg.F)} \quad \text{(eq. 4.2.1.1-11)}$$

where,
δ'_{crud} = crud thickness (ft),
K'_{crud} = crud thermal conductivity in nucleate boiling ([ ] BTU/hr/ft/deg.F)

- Cladding Metal Surface Temperature $T_{clad}(z)$
The above equations give the cladding surface temperature. Taking into account the temperature change across the Zirconium oxide layer, the cladding metal surface temperature is given by

$$T_{clad}(z) = T_{sur}(z) + \Delta T_{ZrO2}(z) \quad \text{(deg.F)} \quad \text{(eq. 4.2.1.1-12)}$$

where
$T_{sur}(z)$: cladding surface temperature (deg.F)
$\Delta T_{ZrO2}(z)$: temperature drop across the Zirconium oxide (deg.F)

The temperature drop across the Zirconium oxide is calculated as

$$\Delta T_{ZrO_2}(z) = q''(z)\frac{\delta_{ZrO_2}(z)}{K_{ZrO_2}} \quad \text{(eq. 4.2.1.1-13)}$$

where,
$\delta_{ZrO2}(z)$: ZrO_2 thickness (ft)
K_{ZrO2} : ZrO_2 thermal conductivity ([ ] BTU/hr/ft/deg.F ([ ]W/m/K))
The value used for K_{ZrO2} is based on the report[4]. The data in this report show, there is little or no temperature dependence. Therefore, the constant value of[ ] BTU/hr/ft/deg.F ([ ] W/m/K), the mean value of the in-reactor material data, is used. The corrosion model with this thermal conductivity has been verified with an extensive cladding corrosion data base.

(c) Cladding Temperature
The temperature drop through the cladding is given by eq.4.2.1.1-14.

$$\Delta T_{clad}(Z) = \frac{q''(z)R_0 \ln(R_0/R_i)}{K_{clad}} \quad \text{(deg.F)} \quad \text{(eq. 4.2.1.1-14)}$$

$$TCI = TCO + \Delta T_{clad}(z) \quad \text{(deg.F)}$$

In the FINE code, the cladding thermal conductivity, K_{clad}, is a linear function of temperature

$$K_{clad} = A + BT \qquad \text{(eq. 4.2.1.1-15)}$$

therefore, the cladding inner temperature, TCI, is given by :

$$TCI = \frac{1}{B}\left(\sqrt{(A + B \cdot TCO)^2 + 2 \cdot B \cdot q''(z) \cdot R_0 \cdot \ln(\frac{R_0}{R_i})} - A\right) \qquad \text{(eq. 4.2.1.1-16)}$$

where

K_{clad} : thermal conductivity of cladding (BTU/hr/ft/deg.F)
for T[ ]
for T[ ] see Appendix B
TCI : cladding inner diameter temperature (deg.F)
q"(z) : heat flux at axial position z (BTU/hr/ft^2)
R_o : cladding outer radius (ft)
R_i : cladding inner radius (ft)
TCO : cladding outside temperature (deg.F)

4.2.1.2 Gas Mixture Thermal Conductivity

The thermal conductivity of the gas mixture in the fuel-cladding gap is given by the Brokaw[5] model, as follows:

$$K_{mix} = \sum_{i=1}^{n} \frac{k_i}{1 + \sum_{j=1, j\neq 1}^{n} \psi_{ij} \cdot \frac{x_j}{x_i}} \qquad \text{(eq. 4.2.1.2-1)}$$

where

$$\psi_{ij} = \phi_{ij} \cdot \left[1 + 2.41 \frac{(M_i - M_j)(M_i - 0.142 M_j)}{(M_i + M_j)^2}\right] \qquad \text{(eq. 4.2.1.2-2)}$$

$$\phi_{ij} = \frac{\left[1 + \left(\frac{k_i}{k_j}\right)^{1/2} \cdot \left(\frac{M_i}{M_j}\right)^{1/4}\right]^2}{2\sqrt{2} \cdot \left(1 + \frac{M_i}{M_j}\right)^{1/2}} \qquad \text{(eq. 4.2.1.2-3)}$$

i,j : index for the gas species in the gap gas mixture
M_i: molecular mass of the i^{th} component of the gas mixture
x_i : mole fraction of the i^{th} component of the gas mixture
k_i : thermal conductivity of the i^{th} component of the gas mixture

The thermal conductivities of Xenon, Krypton, Nitrogen, Hydrogen, Argon and Helium are calculated as follows:

Xenon
Krypton
Air
Nitrogen
Hydrogen [ ]

Argon [ ]

Helium

The thermal conductivity of the fission gas is one of the key factors in the thermal calculation. The Xenon and Krypton composition of fission gas used in the FINE code is expressed by the next equation derived from the irradiation data base.

[ ] (eq. 4.2.1.2-4)

where

Bu : burnup (MWd/t)

The Xr/Kr of 5.67 at the beginning of the life assumes 15% of Krypton and 85% of Xenon.

- Thermal conductivity of Helium gas

The bulk gas thermal conductivity models given above are based on a continuum assumption, which is not appropriate if the mean free path of the gas molecules are more than 0.01 of assumed dimensional gap in the system of interest. In this case, the heat flux from the solid to the gas depends on the accommodation coefficient, defined as the ratio of the effective exchange energy to the maximum acceptable exchange energy between the solid surface and the gas[3]. For heavy molecules, such as Argon and Xenon, the accommodation coefficient is very close to 1 and this effect is negligible. In the case of light molecules, such as Helium, however, the effect is significant. An effective Helium thermal conductivity, K_{eff}, is used in FINE to account for this effect:

$$K_{eff} = K_{He}/f \quad \text{(eq. 4.2.1.2-5)}$$

$$f = 1 + \left[1.6787 \times 10^{-5}\left(\frac{2-A}{A}\right)\cdot\overline{K_{He}}\cdot\sqrt{T}\right]\Big/\left[P_f \cdot \delta\right] \quad \text{(eq. 4.2.1.2-6)}$$

where

A = [ ]

The factor f is derived from the thermal conductivity theorem of Dean[6] as follows:

$$f_a = 1 + \left(\frac{\alpha_1 + \alpha_2 - \alpha_1\cdot\alpha_2}{\alpha_1\cdot\alpha_2}\right)\left(\frac{4}{C_P + Cv}\right)\left(\frac{K_{He}}{\mu}\right)\left(\frac{\lambda}{\delta}\right) \quad \text{(eq. 4.2.1.2-7)}$$

α_1, α_2 : accommodation coefficient of fuel pellet and cladding
C_P : specific heat at constant pressure
C_v : specific heat at constant volume
K_{He} : bulk thermal conductivity of Helium gas
μ : gas viscosity (lbm/ft/hr)
λ : mean free path of gas molecules (ft)
δ : radial gap (ft)

Applying the relation [ ] and the relationship derived from kinetic theory of gases to eq. 4.2.1.2-7 gives eq. 4.2.1.2-6 when the following are also used:

T : deg. R

P_f : psia

δ : [ ]

Gap : diameteral gap (in)

EXO : surface roughness multiplier

4.2.1.3 Gap Conductance

The pellet surface temperature is given by

$$Ts = TCl + \Delta T_{gap} \quad \text{(eq. 4.2.1.3-1)}$$

with

$$\Delta T_{gap} = q''(z)/h_{gap} \quad \text{(eq. 4.2.1.3-2)}$$

Two expressions are used for the gap conductance, h_{gap}, depending on whether pellet-cladding contact occurs.

(a) No Pellet-Cladding Contact

The gap conductance without pellet-cladding contact is given by

[ ] (eq. 4.2.1.3-3)

(eq. 4.2.1.3-4)

(eq. 4.2.1.3-5)

where,

Kmix : gas mixture thermal conductivity (BTU/hr/ft/deg.F)
Gap : diameteral gap (in)
EXO : surface roughness multiplier
The nominal roughness of 14.4×10^{-6} (ft) is the value given by Dean[6]

(b) Pellet-Cladding Contact

Dean[6] measured the contact resistance between UO_2 and Zircaloy-2 surfaces as a function of surface roughness and contact pressure. Dean[6] has fit these data with eq. 4.2.1.3-6, with α of 0.6.

$$hcon = \alpha \cdot Pct + \frac{Kmix}{14.4 \times 10^{-6} \cdot EXO} \quad \text{(eq. 4.2.1.3-6)}$$

In the FINE code, hcon is given by:

[ ] (eq. 4.2.1.3-7)

[ ] (eq.4.2.1.3-8)

where,

hcon : gap conductance with pellet-cladding contact (BTU/hr/ft/deg.F)
Pct : pellet-cladding contact pressure (psi)

4.2.1.4 Pellet Temperature

Temperatures within the pellet are calculated based on the following fundamental equation for heat transfer.

$$\frac{1}{r}\cdot\frac{d}{dr}(rk(T)\frac{dT}{dr})+q'''(r)=0 \qquad \text{(eq. 4.2.1.4-1)}$$

where

r : radial distance from the center of the pellet (ft)
T : pellet temperature at radius (deg. F)
k(T) : pellet thermal conductivity at temperature T (BTU/hr/ft/deg.F)
q'''(r) : heat generation density at radius r (BTU/hr/ft^3)

The FINE calculation of the pellet temperatures accounts for the radial variation of the pellet thermal conductivity and the heat generation within the pellet. The thermal conductivity model for pellet is given in Section 4.2.1.5.

$$\int_{Ts}^{Tc}K(T)dT=\frac{q'\cdot F}{4\pi} \qquad \text{(eq. 4.2.1.4-2)}$$

where,

Tc : pellet centerline temperature (deg.F)
Ts : pellet surface temperature (deg.F)
K(T) : thermal conductivity of pellet (BTU/hr/ft/deg.F) at temperature T (deg.F)
q' : heat generation rate per unit length (BTU/hr/ft)
F : power depression factor

The power depression factors used in FINE are based on nuclear calculation results obtained from the PHOENIX-P nuclear calculation code[7]. FINE uses these nuclear calculation results in a tabular format, with the relative radial powers given as a function of enrichment and burnup for the 10 radial rings used by the FINE pellet model.

The temperature calculation for an annular pellet is given by

$$\int_{Ts}^{Tc}K(T)dT=\frac{q'\cdot F}{4\pi}\left(1-\frac{2\ln(A_o/A_i)}{(A_o/A_i)^2-1}\right) \qquad \text{(eq. 4.2.1.4-3)}$$

where,

A_o : pellet outer diameter (ft)
A_i : pellet center hole diameter (ft)

4.2.1.5 Pellet Thermal Conductivity

The thermal conductivity model for 95%TD UO_2 fuel is given by eq. 4.2.1.5-1.

$$k_{95} = \frac{1}{11.8 + 0.0238 \cdot T} + 8.775 \times 10^{-13} \cdot T^3 \qquad \text{(eq. 4.2.1.5-1)}$$

$$\int_0^{2800} k_{95}(T)dT = 93W/cm$$

This equation has been derived from extensive measured UO_2 thermal conductivity data. The comparison of this model with a widely used model of MATPRO is made in Appendix B. The integral thermal conductivity from 32 deg.F (0 deg.C) to the UO_2 melting point (assumed to be 5072 deg.F (2800 deg.C)) is 2.8kW/ft (93W/cm). Furthermore, the thermal conductivity up to 2372 deg.F (1300 deg.C) is in good agreement with the IAEA[8] recommendation.

Eq. 4.2.1.5-1 gives the thermal conductivity for 95%TD UO_2. For other densities the thermal conductivity is given by eq. 4.2.1.5-2, proposed by Bakker[9] based on a finite element model.

$$\frac{k}{k_{100}} = (1-P)^{1.7} \qquad \text{(eq. 4.2.1.5-2)}$$

where

k : thermal conductivity at the porosity ratio of P, with % TD = 100 - P/100
k_{100} : thermal conductivity at theoretical density (no porosity)

UO_2 thermal conductivity degradation with burnup has been identified in a number of published papers. Wiesenack[10]has proposed a quantitative model for this degradation effect, based on fuel centerline temperature measurements in the Halden Boiling Water Reactor. Wiesenack models the burnup effect on the pellet thermal conductivity as the accumulation of fission products in the UO_2 matrix, such that the fission products in the fuel lattice interfere with thermal conduction due to phonon-phonon collisions. The FINE code uses eq. 4.2.1.5-3 to account for this effect:

[ ] (eq. 4.2.1.5-3)

where,

k_{95} : thermal conductivity of 95%TD pellet (W/cm/deg.C)
T : pellet temperature (deg.C)
Gd : Gadolinium content (Gd mol%)
Bu : burnup (MWd/kgUO_2)

The effect of the conductivity degradation with burnup is given in the denominator of the first term of the right-hand side, which is the phonon conduction contribution to the thermal conductivity. Wiesenack proposes β of 0.35 K/(W/cm)/(MWd/kgUO_2) for this effect. The FINE code uses the same effect as a modification of the unirradiated UO_2 thermal conductivity given by eq. 4.2.1.5-1.
Wiesenack has also proposed a recovery effect, due to the temperature increases. For conservatism, the FINE code does not use this recovery effect.

The burnup degradation effect of FINE code is illustrated in Figure 4.2.1.5-1. Phonon conduction is dominant at the lower temperatures and the degradation effect is obvious.

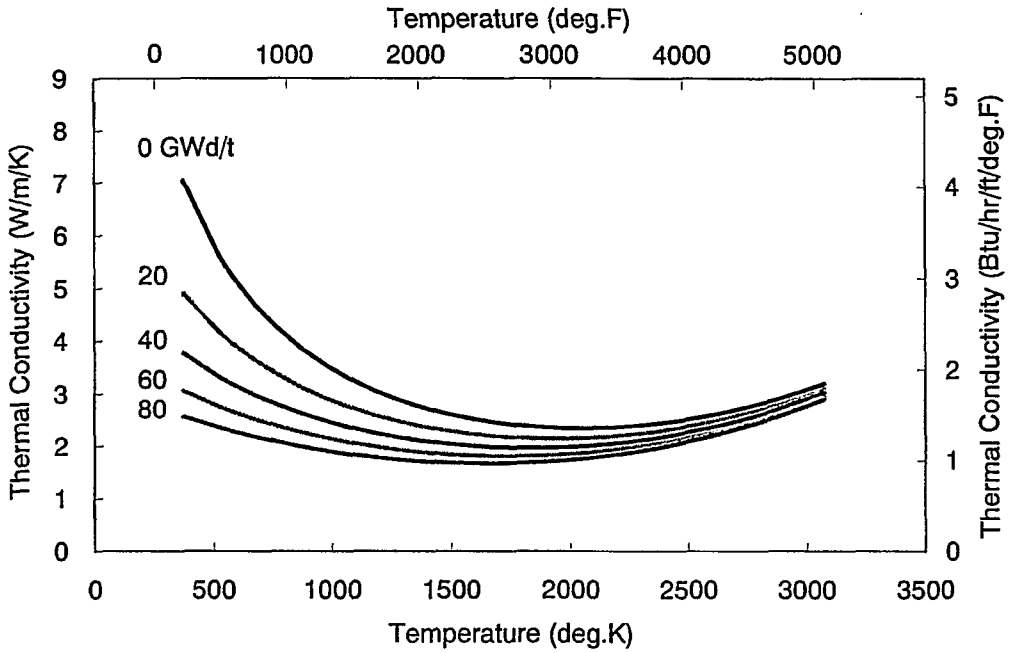

Figure 4.2.1.5-1 Thermal Conductivity Degradation Effect of the FINE Model (95%TD UO_2 fuel)

Eq. 4.2.1.5-3 also includes the effect of Gadolinia doping on the pellet thermal conductivity. In this equation Gadolinia is treated as an impurity which degrades the phonon conduction contribution to the thermal conductivity. The coefficients for the Gadolinia effect have been derived from out-of-pile measurements[11]. The comparison between the FINE model and the measurements is shown in Figure 4.2.1.5-2. The FINE model gives a good fit to the 6 wt% Gadolinia data, and underpredicts the 10 wt% Gadolinia data, and it is expected that the FINE code temperature predictions will be conservative for Gadolinia concentrations above 6 wt%.

The burnup degradation effect for Gadolinia doped fuel is compared with that for UO_2 fuel in Figure 4.2.1.5-3[12]. This figure shows that the burnup degradation effect is essentially the same in Gadolinia doped fuel and undoped UO_2. The UO_2 value of β of 0.35 is therefore used for Gadolinia fuel in the FINE code.

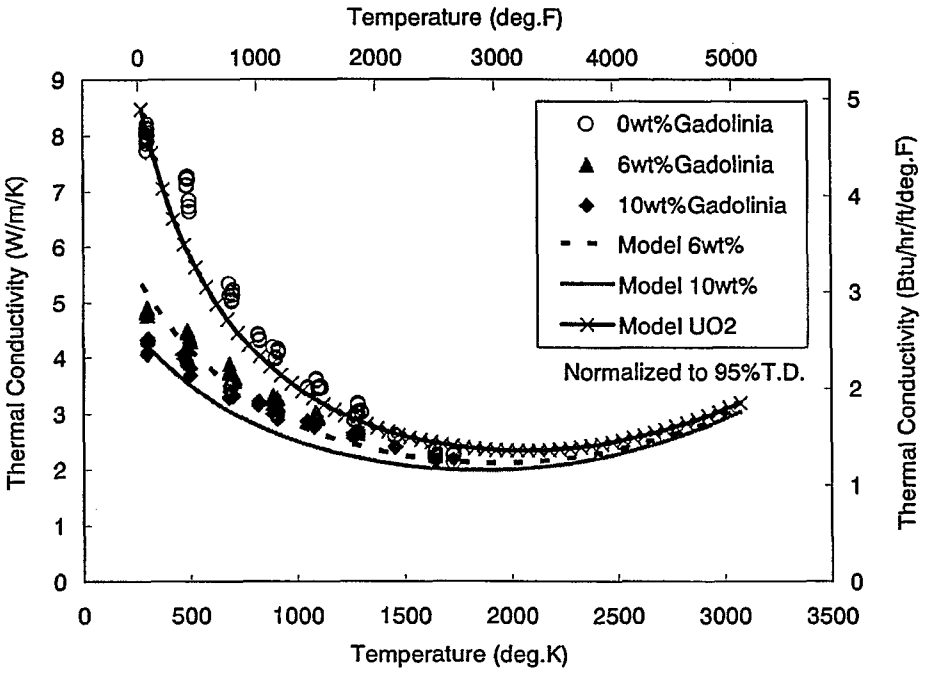

Figure 4.2.1.5-2 Thermal Conductivity of Gadolinia Doped Pellet (Unirradiated Material) [11]

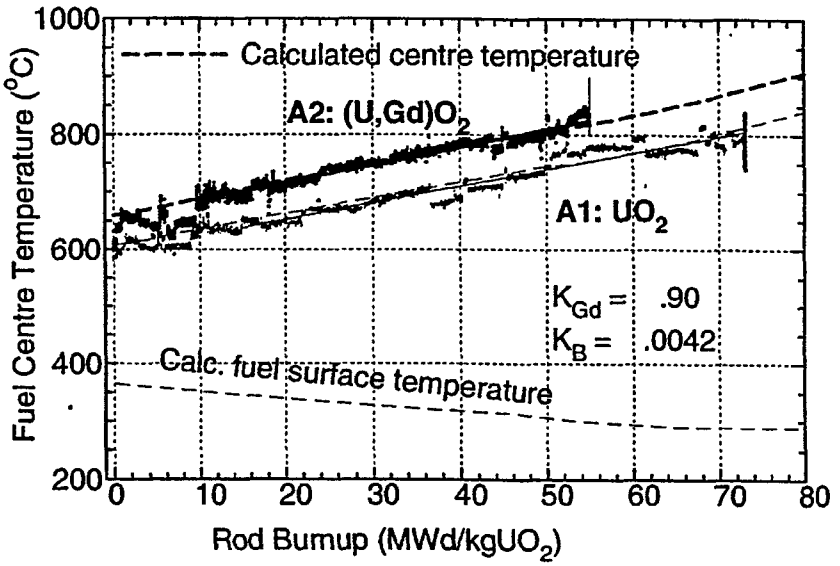

Figure 4.2.1.5-3 Comparison of Thermal Conductivity Degradation Effect between Gadolinia Doped Fuel and UO_2 Pellet[12]

4.2.1.6 RIM Formation

A region of high porosity and small (sub-micron) grain size, referred to as the RIM region, has been observed at the periphery of high burnup fuel[13].
A typical porosity distribution as a function of pellet radius is examined in the reference[14]. In this reference, the porosity at the pellet periphery region is very high, up to 14-15%. Since, as described above, the pellet thermal conductivity is a function of porosity, the higher porosity (lower density) in the RIM region reduces the thermal conductivity. The RIM region is therefore a thermal barrier and it is treated as such in the FINE code.
The FINE code models the threshold for the formation of the RIM microstructure, the RIM width and the porosity in the RIM region. Fission gas release from RIM region is described in the subsection describing the FINE calculation of fission gas release, 4.2.2.1. (c) below.

(a) RIM formation threshold
A systematic investigation for the threshold for formation of the RIM region microstructure has been performed in the High Burnup Rim Project (HBRP). The HBRP focused on irradiation temperature and burnup as the primary variables affecting the threshold, and the disk pellets used in the HBRP were designed to give a flat radial distribution of temperature and burnup. The HBRP results are summarized in Figure 4.2.1.6-1[15].
The results for the RIM formation threshold are summarized as follows[15]:

- the burnup threshold is between 55 and 82 MWd/kgU.
- the temperature threshold (maximum temperature for RIM region formation) is 2012 ±180 deg.F (1100 ±100 deg.C), at least up to 100MWd/kgU

The FINE code threshold conditions for RIM region formation are therefore:

- pellet surface burnup $\geq$ ( )
- pellet surface temperature $\leq$ ( )

The local pellet burnup is highest at the pellet periphery and therefore the RIM region threshold burnup is determined from the pellet surface burnup.

As stated above, the pellet is divided into 10 equal area rings in the FINE model for the pellet. The pellet surface burnup, BU_{rim}, is calculated from the burnup of the 10^{th} ring (the outermost circumferential ring).

$$\left(\right) \qquad \text{(eq. 4.2.1.6-1)}$$

where,

BU_{rim} : pellet surface burnup (GWd/t)
$BU_{at\ 10th\ RING}$: ring average burnup of the 10^{th} RING

On the other hand, pellet surface temperature is defined as the RING surface temperature and the temperature is compared with the above temperature threshold.

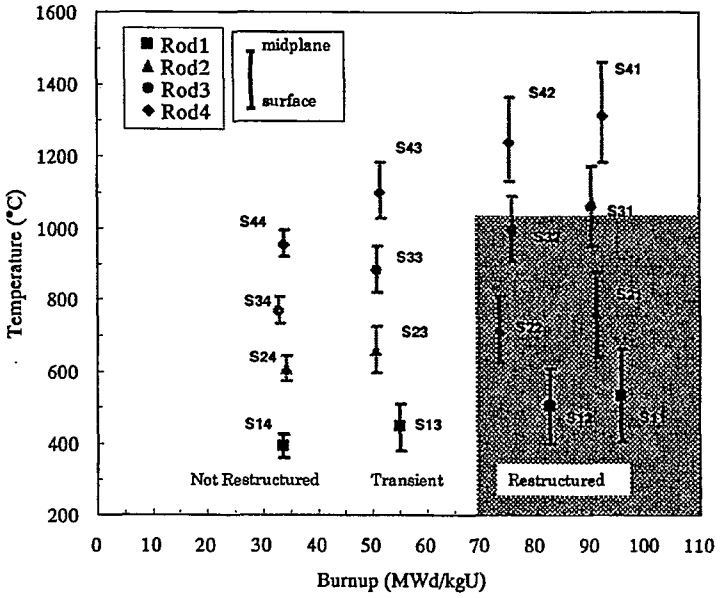

Figure 4.2.1.6-1 Temperature and Burnup of HBRP Disc Specimens. Maximum (Center) and Minimum (Surface) Temperatures of the Discs are Shown by the Vertical Bars

(b) RIM width

Barner[13] has proposed the following equation for the RIM width:

$$W^2 = -21014 + 391.4(BU)\,;\ \text{BU>53.7 MWd/kgM (GWd/t)}$$

This equation is based on the data, which shows the optical and EPMA measurement results. This model is used in the FINE code, with the threshold burnup changed from 53.7 GWd/t to [ ] to be consistent with the above burnup threshold.

[ ] (eq. 4.2.1.6-2)

where,

BU_{rim} : pellet surface burnup (GWd/t)

W : Rim width (μm)

The RIM width model is demonstrated in Figure 4.2.1.6-2.

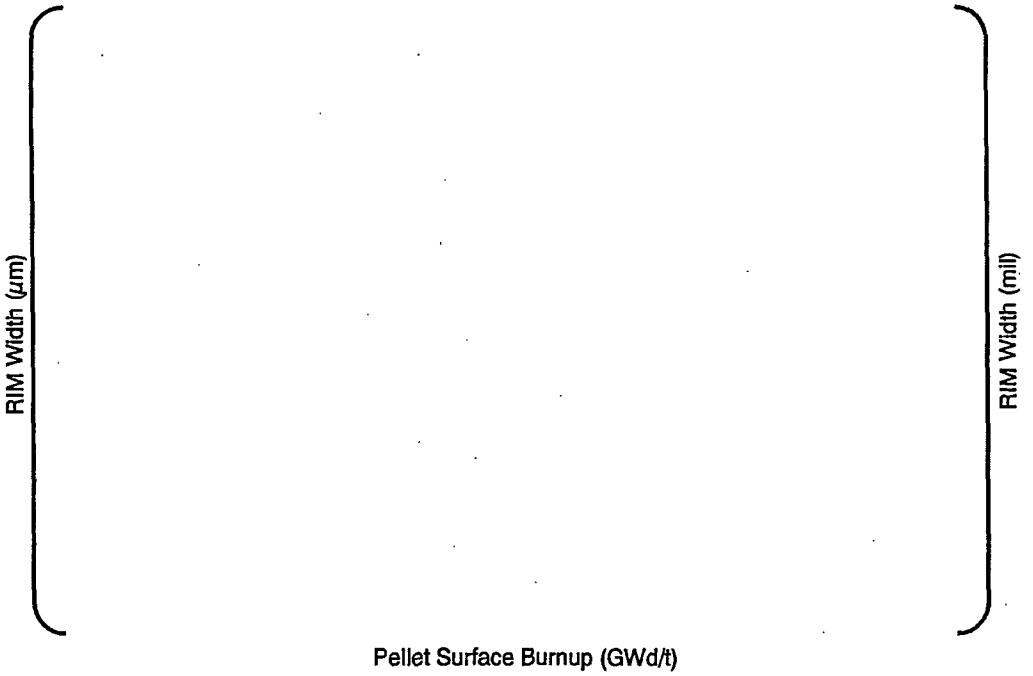

Figure 4.2.1.6-2 Demonstration of the RIM Width model

(c) RIM porosity

As described above, the porosity in the RIM region can be reached to 14-15% at most [14]. According to the data[14], It seems that the maximum local porosity is a constant, with no dependence on the local burnup.

Eq. 4.2.1.6-3 is used to calculate the RIM porosity in the FINE code. The maximum porosity is [ ], consistent with the reference[12], and the RIM porosity calculated from Eq. 4.2.1.6-3 is consistent with the RIM region threshold burnup of [ ]. The total porosity is the sum of the RIM porosity and residual fabrication porosity.

[ ] (eq. 4.2.1.6-3)

where

P_{rim} : porosity in RIM region (%)

BU_{rim} : pellet surface burnup (GWd/t)

This porosity model is shown in Figure 4.2.1.6-3. The FINE code assumes a constant porosity in the RIM region whose width is demonstrated in Figure 4.2.1.6-2, whereas the actual porosity distribution across the RIM region is lower inside and higher at peripheral region up to 14-15% of porosity[14]. Thermal calculation of RIM region is discussed later.

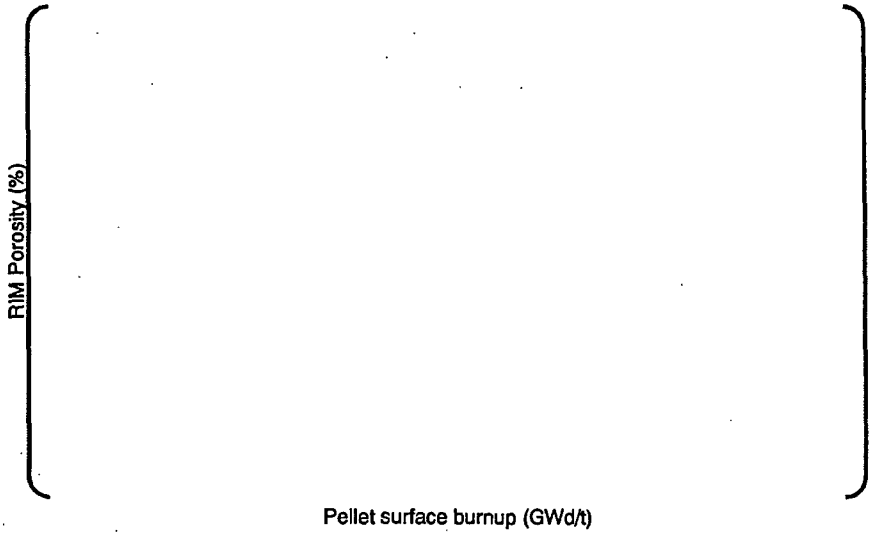

Figure 4.2.1.6-3 RIM Porosity Model

(d) Thermal calculation

The RIM region is formed when the pellet surface burnup exceeds [ ] in the FINE code. The RIM width and porosity are given by the models described in the previous subsections. The effects of the RIM region on the thermal calculation are due to the lower thermal conductivity in the RIM region, due to its increased porosity.

The FINE code uses a 10 ring pellet model. When the RIM region is contained entirely within the 10th, outermost ring, the effective thermal conductivity of this ring is calculated as follows: There are two layers in the outer ring when the RIM forms: the RIM region and a non- RIM region as illustrated in Figure 4.2.1.6-4. The effective thermal conductivity is calculated based on a one dimensional thermal conduction equation, assuming constant temperatures in the RIM and non-RIM regions. The effective porosity is calculated from an area-weighed average of the RIM and non-RIM regions.

Non-RIM region $$q'' = -k_1 \frac{T_1 - T_0}{t_1}, \quad T_0 - T_1 = q'' \frac{t_1}{k_1},$$ (eq. 4.2.1.6-4)

RIM region $$q'' = -k_2 \frac{T_2 - T_1}{t_2}, \quad T_1 - T_2 = q'' \frac{t_2}{k_2},$$ (eq. 4.2.1.6-5)

Outer ring $$q'' = -k_{eff} \frac{T_2 - T_0}{t_1 + t_2}, \quad T_0 - T_2 = q'' \frac{t_1 + t_2}{k_{eff}},$$ (eq. 4.2.1.6-6)

where,

- q" : heat flux (BTU/hr/ft^2)
- k_1 : thermal conductivity in the non-RIM region (BTU/hr/ft/deg.F)
- k_2 : thermal conductivity in the RIM region (BTU/hr/ft/deg.F)
- k_{eff} : effective thermal conductivity of the outer ring (BTU/hr/ft/deg.F)
- T_0 : ring inner temperature (deg.F)
- T_1 : temperature at the boundary between RIM and non-RIM region (deg.F)
- t_1 : thickness of non-RIM region (ft)
- t_2 : thickness of RIM region (ft)

The sum of eq. 4.2.1.6-4 and 4.2.1.6-5 gives

$$T_0 - T_2 = q''(\frac{t_1}{k_1} + \frac{t_2}{k_2}) \qquad \text{(eq. 4.2.1.6-7)}$$

The comparison of eq. 4.2.1.6-6 and 4.2.1.6-7 gives

$$k_{eff} = \frac{k_1 k_2 (t_1 + t_2)}{(t_1 k_2 + t_2 k_1)} \qquad \text{(eq. 4.2.1.6-8)}$$

In terms of the porosity correction, the thermal conductivity in the non-RIM and RIM regions can be written as:

$$k_1 = k_{95} f(p) \qquad \text{(eq. 4.2.1.6-9)}$$

$$k_2 = k_{95} f(p + p_{rim}) \qquad \text{(eq. 4.2.1.6-10)}$$

and the effective thermal conductivity of the outer ring is then given by

$$k_{eff} = k_{95} \frac{f(p) \cdot f(p + p_{rim}) \cdot (t_1 + t_2)}{(t_1 \cdot f(p + p_{rim}) + t_2 \cdot f(p))} \qquad \text{(eq. 4.2.1.6-11)}$$

$$k_{eff} = k_{95} \cdot f(p) \cdot \frac{k_{95} \cdot f(p + p_{rim}) \cdot (t_1 + t_2)}{(t_1 \cdot k_{95} \cdot f(p + p_{rim}) + t_2 \cdot k_{95} \cdot f(p))}$$

$$k_{eff} = \frac{(t_1 + t_2) \cdot k_{rim} \cdot k_{non-rim}}{(t_1 \cdot k_{rim} + t_2 \cdot k_{non-rim})} \qquad \text{(eq. 4.2.1.6-12)}$$

Where,

k_{rim} : thermal conductivity at RIM (= $f(p + p_{rim}) \cdot k_{95}$)

$k_{non-rim}$: thermal conductivity at non RIM (= $f(p) \cdot k_{95}$)

The effective porosity is an area weighed average of the porosities in the non-RIM and RIM regions:

$$p_{eff} = \frac{p \cdot \pi \cdot \left\{(r_0 + t_1)^2 - r_0^2\right\} + (p + p_{rim}) \cdot \pi \cdot \left\{(r_0 + t_1 + t_2)^2 - (r_0 + t_1)^2\right\}}{\pi \cdot \left\{(r_0 + t_1 + t_2)^2 - r_0^2\right\}} \qquad \text{(eq.4.2.1.6-13)}$$

$$p_{eff} = p + \frac{\left\{(r_0 + t_1 + t_2)^2 - (r_0 + t_1)^2\right\}}{\left\{(r_0 + t_1 + t_2)^2 - r_0^2\right\}} \cdot P_{rim} \qquad \text{(eq.4.2.1.6-14)}$$

where,

p_{eff} : effective porosity of the outer ring (%)

r_0 : inner radius of the non-RIM region (ft)

The RIM width is defined by eq. 4.2.1.6-2 and RIM porosity is defined by eq. 4.2.1.6-3. In the FINE code, the RIM porosity is assumed as uniform over its width. The actual porosity, however, is higher at peripheral and lower inside. Therefore, the uniform RIM porosity derived from eq. 4.2.1.6-3 over the width from eq. 4.2.1.6-2 is conservative.

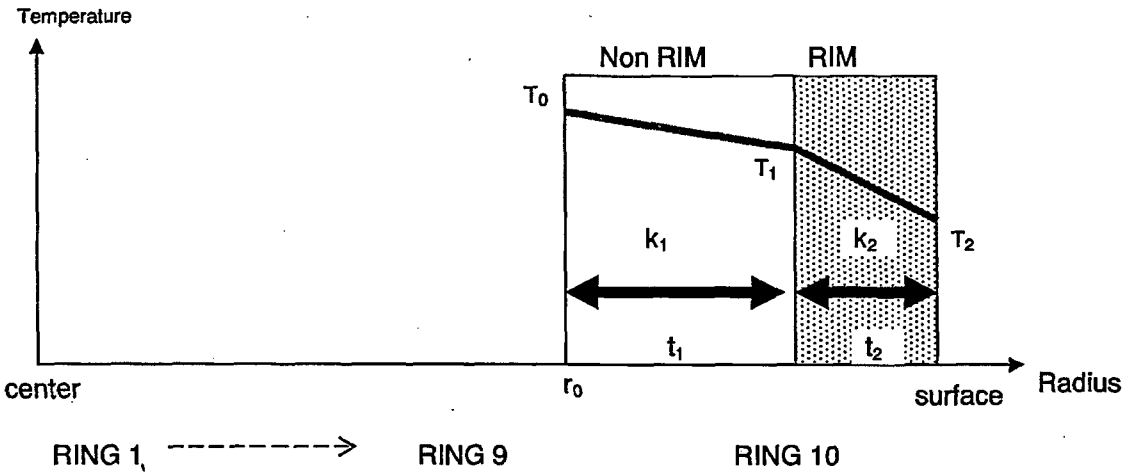

Figure 4.2.1.6-4 Schematic Illustration of Ring Geometry Used in the RIM Thermal Calculation

When the RIM width is greater than the thickness of the 10th, outermost ring, the porosity of the 10th ring is constant, the sum of the RIM porosity and the residual fabricated porosity, and the thermal calculation for the 9th ring follows the methods given above, with the RIM width within the 9th ring set equal to the RIM width W, as given by eq. 4.2.1.6-2, minus the thickness of the 10th ring.

4.2.2 Gas Release Models

The FINE code models the release of the fission gases Xenon and Krypton, and the release of Helium generated by fission. The FINE code also models the absorption of Helium in the as-fabricated gas composition.

4.2.2.1 Fission Gas Release

Three fission gas release mechanisms are modeled in the FINE code: release due to diffusion processes, which is dominant at high fuel temperatures, and recoil & knockout, which is dominant at low fuel temperatures, and fission gas release from the RIM region, which is a contributor to the total fission gas release at high burnups.

(a) Diffusion Release

The FINE model for fission gas release due to diffusion is based on the model proposed by Speight[16]. Fission gas is generated within the grains and accumulates within the grains. The gas diffuses to the grain boundary, driven by the gas concentration gradient. On the other hand, irradiation causes solution of the gas at the grain boundary back into the grain. Diffusion from the grain to the grain boundary and solution from the grain boundary back into the grain are assumed to be in balance until the concentration of gas on the grain boundary reaches a maximum value. Diffusion release to the rod void volume occurs when the fission gas concentration within the grain exceeds this maximum grain boundary concentration. This model gives the following expression for the diffusion fission gas release ΔRD in a time interval dt:

$$\Delta RD = KD\,(C - C^*)dt \qquad (C \geq C^*)$$
$$= 0 \qquad (C < C^*) \qquad \text{(eq. 4.2.2.1-1)}$$

where,

- ΔRD : fission gas release (mol/cm^3)
- KD : fission gas release rate per unit time (/hr)
- C : accumulated fission gas in the grain accounting for production, solution and release (mol/cm^3)
- C* : Retainable fission gas in the grain boundary (mol/cm^3)

In the FINE code the fission gas release is calculated for time steps with a significant duration. The fission gas release, ΔRD_i, from time, t_{i-1}, to time t_i, ($=t_{i-1} + \Delta t_i$), is calculated by the following equation.

$$\Delta RD_i = \beta_i \cdot \Delta t_i - (C_i^* + \frac{\beta_i}{KD_i} - C_{i-1})\{1 - \exp(-KD_i \cdot \Delta t_i)\} \qquad \text{(eq. 4.2.2.1-2)}$$

where,

- ΔRD_i : fission gas release during Δt_i (mol/cm^3)
- β_i : fission gas production rate during Δt_i (mol/cm^3/hr)
- C_{i-1} : accumulated fission gas concentration in grain at t_{i-1} (mol/cm^3)
- C_i^* : Retainable fission gas in the grain boundary at t_i (mol/cm^3)
- KD_i : fission gas release rate per unit time at t_i (/hr)

$$\left[\qquad \right] \qquad \text{(eq.4.2.2.1-3)}$$

[ ] (eq.4.2.2.1-4)

T : pellet ring temperature (deg.R)
Bu : pellet ring burnup (MWd/t)

Vitanza[17], Hargreaves[18] and Nerman[19] have proposed models similar to the above. The fission gas release threshold temperature obtained with this model is compared with the Vitanza model in sub-section 4.2.3.3, on gas bubble swelling.

(b) Recoil & Knockout

Fission gas release due to the recoil and knockout mechanism is dominant at low fuel temperatures. At the high burnup, fission gas release from the RIM region is an additional low temperature release mechanism.

The FINE recoil and knockout model is described as follows and the part of the model equation is consistent with that used in the ANS-5.4[20] fission gas release model with the contribution of (S/V) x Bu:

$$\Delta RK^i = AFRK \cdot b_1 \cdot \left(\frac{S}{V}\right) \cdot Bu \cdot \left(\sum_{j=1}^{i} \beta_j \Delta t_j\right) \qquad \text{(eq. 4.2.2.1-5)}$$

where S/V is the surface-to-volume ratio, given by the next equation. This S/V equation expresses the effect that S/V increases with the number of cracks in the pellet and that the number of cracks increases with burnup and the temperature difference across the pellet.

[ ] (eq. 4.2.2.1-6)

and

[ ]

ΔRK^i : Accumulated fission gas release due to recoil & knockout during i^{th} time step (mol)
Bu : burnup (MWd/t)
β_i : fission gas production rate during the j^{th} time step (mol/cm^3/hr)
Δt_j : duration of the j^{th} time step (hr)
ΔTsc : temperature difference between pellet center and surface (deg. R)
The maximum difference is taken for ΔTsc. $\Delta Tsc = \max(\Delta Tsc_1, \Delta Tsc_2, , , \Delta Tsc_i)$

(c) RIM region Fission Gas Release

Barner[13] has proposed a fission gas release model from the RIM region, based on the data shown in Figure 4.2.2.1-1.

$$Fr = 0.00625 \times (BU - 62.2) \quad \text{BU>62.2GWd/t} \qquad \text{(eq. 4.2.2.1-7)}$$

This equation based on EPMA measurements of the Xe depletion. It is known that EPMA can only measure the gas in the porosity close to the surface and does not detect the gas in the closed porosity at some depth from the surface. Therefore, EPMA results for the Xe depletion give an overestimate of the amount of depletion, i.e., an overestimate of the fission gas release from the RIM region. Barner has stated that eq. 4.2.2.1-3 is an upper bound for the fission gas release from the RIM region and that the lower bound is no fission gas release from the RIM region.

The FINE code model for the fission gas release modifies eq. 4.2.2.1-7 by including an additional multiplicative coefficient, AFRIM, and is given by eq. 4.2.2.1-4.

$$Fr = AFRIM \times 0.00625 \times (BU - 62.2) \quad \text{BU>62.2GWd/t} \qquad \text{(eq. 4.2.2.1-8)}$$

AFRIM=[ ]

The AFRIM value of [ ] and the AFRK value of [ ] have been obtained in order to express the lower fission gas release without diffusion release. One of the examples, prediction for a ZION rod, is demonstrated in Figure 4.2.2.1-1.

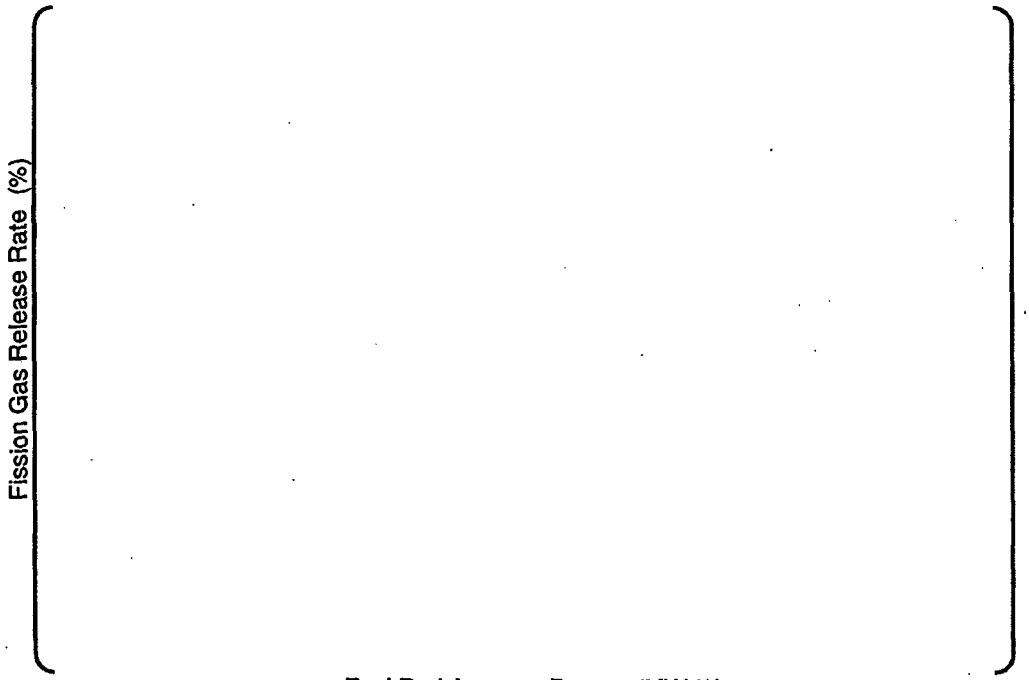

Figure 4.2.2.1-1 Recoil and Knockout and RIM Region Fission Gas Release for Low Temperature Fuel

(d) FGR calculation

The FINE code calculates the total fission gas release by adding the fission gas release fractions of the three models described above:

$$F_i = \frac{\sum_{j=1}^{i} (\Delta RD^j + \Delta RK^j)}{\sum_{j=1}^{i} \beta_j \Delta t_j} + Fr_i \qquad \text{(eq. 4.2.2.1-9)}$$

If the fuel temperature exceeds [ ], the FINE code assumes that all of the fission gas is released, i.e., 100% fission gas release:

$F_i = 1 \quad (T > [\ ])$ (eq. 4.2.2.1-10)

where,

ΔRD^i : fission gas release due to diffusion during time increment Δt_i

ΔRK^i : fission gas release due to Recoil and Knockout during time increment Δt_i

Fr_i : RIM region fission gas release fraction

Δt_i : time increment (hr)

β_i : fission gas production rate; [ ] is assumed. The Xe/Kr ratio is given by eq. 4.2.1.2-4. The FINE code only calculates Xe and Kr as fission gases which have significant influence on thermal calculation.

The FINE code calculates the fission gas release for each pellet ring in each axial segment.

4.2.2.2 Helium Model

Helium is one of the most important gases in the fuel rod void volume. Mitsubishi fuel is initially pressurized with Helium during fabrication. The FINE code treats Helium gas behavior with three models: Helium generation, Helium release from the pellets and Helium absorption in the pellets.

Helium generation and release models can be confirmed by ZORITA non pressurized rods, which don't include helium gas inside at their fabrication. Therefore, the helium amount in the free volume is the result of the generation and release.

The contribution of Helium absorption can be derived by subtracting the Helium release from total helium in the free volume. Mitsubishi expresses the helium absorption model as a function of fabricated pellet density and initial helium pressure.

Regarding high burnup usage, the Helium models are adjusted to give the slightly conservative Helium gas at the high burnup. As the result of that, the Helium generation and release models overestimate the ZORITA non pressurized rods. However, the Helium models provide the good estimation to the rods with the specification of interest.

(a) Helium generation

For high burnup usage, the FINE Helium generation model is developed based on the results of an ORIGEN calculation for 3.5 wt% BWR UO_2 [21].

[ ] (mol/g UO_2) (eq. 4.2.2.2-1)

where

BU : Burnup (GWd/t)

This model is demonstrated in Figure 4.2.2.2-1.

(b) Helium release

The release fraction for the Helium generated by fission is given by:

[ ] (eq. 4.2.2.2-2)

Where,

BU : burnup (GWd/t)

(c) Helium absorption

The FINE Helium absorption model is given in terms of Helium solubility for the Helium in the rod at fabrication. The Helium solubility is given by:

[ ] (eq. 4.2.2.2-3)

where

S_0 : Helium solubility (mol/gUO_2)

ρ_0 : Initial pellet density (%TD)

P_0 : Initial Helium Pressure (psi)

This model, combined with the Helium generation and release models given above, has been verified by comparison of the predicted results with an extensive post-irradiation examination database for the Helium at end-of-life. Verification is described in Section 4.3.

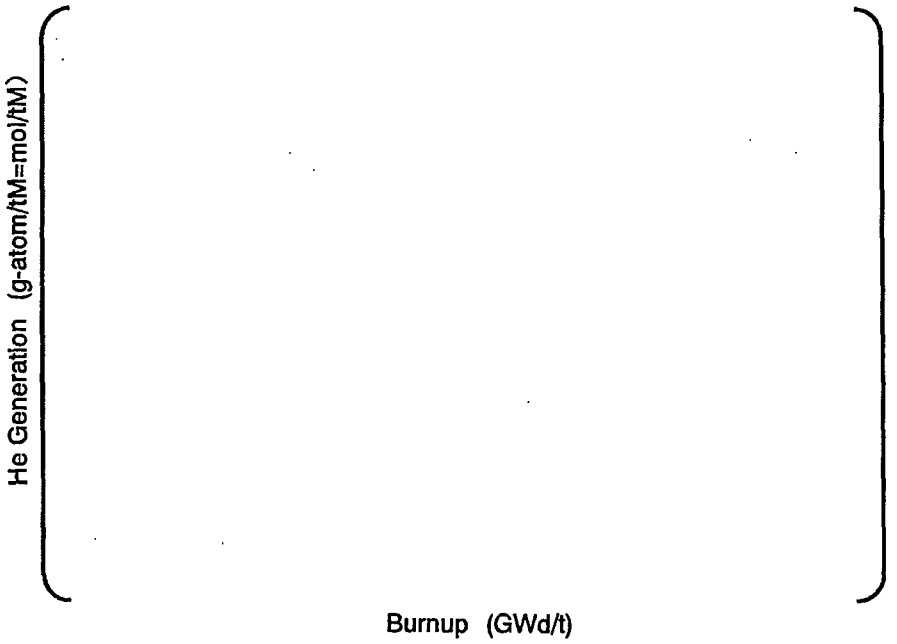

Figure 4.2.2.2-1 Helium Generation Model

4.2.3 Pellet Dimension Change Models

Densification, solid swelling and gas bubble swelling contribute to the pellet dimensional changes, as well as the pellet thermal expansion.

4.2.3.1 Densification

Densification is the process where the fabricated porosity decreases due to thermal and irradiation induced effects[22]. The FINE densification model is a function of the initial density and burnup:

[ ] (eq. 4.2.3.1-1)

where

ρ_0 : Initial pellet density (%TD)
C : constant ([ ]) (fission/cc)
F : number of fissions (fission/cc)
1 Mwd/t = [ ] (fission/cc)
Ef : Energy/fission ([ ])
N : densification rate, [ ]
Ts : densification parameter

4.2.3.2 Solid Swelling

The fission product deposition in the fuel matrix increases with increasing burnup .The accumulation of the solid fission products in the fuel matrix, proportional to the number of fissions, increases the fuel volume. The FINE solid swelling modeled is given by:

$$\left.\frac{\Delta V}{V_0}\right|_{solidswelling} = -\left.\frac{\Delta \rho}{\rho}\right|_{solidswelling} = A \cdot F \qquad \text{(eq. 4.2.3.1-2)}$$

where

A : solid swelling rate, ( ) (1/(fission/cc))
F : number of fissions (fission/cc), given by eq. 4.2.3.1-1

This FINE solid swelling rate is similar to the MATPRO Version 11 model [23], 0.25 %ΔV/V per 10^{26} fissions/m^3, corresponding to about 0.6 %ΔV/V per 10 GWd/t when the initial density of the pellet is 95%TD.

The pellet dimensional change due to both densification and solid swelling is given by eq. 4.2.3.1-3.

( ) (eq. 4.2.3.1-3)

4.2.3.3 Gas Bubble Swelling

As described in sub-section 4.2.2.1, gas bubbles are formed at high fuel temperatures when the fission gas diffuses from the grain interior to the grain boundaries.
Figure 4.2.3.3-1 gives the schematic view of gas bubble swelling model. Gas bubbles are formed when the fuel temperature exceeds the temperature denoted as "TEMPR", where the diffusion out of the grain is greater than resolution from the grain boundaries. Maximum fission gas bubble swelling occurs when fuel temperature reaches the temperature denoted by "T16". Fission gas is released from the bubbles when the fuel temperature exceeds "T16" because the amount of the fission gas in the grain boundary exceeds the retainable fission gas amount (C* in eq. 4.2.2.1-1). At higher temperatures the fission gas is released from the grain boundaries and the accumulated fission gas on the grain boundaries decreases. When the temperature reaches [ ] (denoted as "T20"), the porosity level is reduced to the as-fabricated porosity, i.e., there are no gas bubbles for temperatures above [ ]. As described in sub-section 4.2.2.1, it is assumed that all the fission gas is released for temperatures above [ ]

[ ] (eq. 4.2.3.1-4)

[ ] (eq. 4.2.3.1-5)

[ ] (eq. 4.2.3.1-6)

where

[ ]

Eq. 4.2.3.1-4 has been derived from eqs. 4.2.2.1-1 and 4.2.2.1-3 with the assumption of isothermal irradiation at a constant fission gas production rate. The constants a1, a2 and ab in eq. 4.2.3.1-5 are the same as those used in eq. 4.2.2.1-3 for the diffusion fission gas release model.

Figure 4.2.3.3-2 illustrates the behavior of this gas bubble swelling model as a function of burnup. The curve denoted by T16 is the fission gas release threshold for the FINE diffusion fission gas release model. Figure 4.2.3.3-3 compares the FINE diffusion model fission gas release threshold with the one defined by Vitanza[17]. There is a slight difference between the two fission gas release thresholds for burnups above 10000 MWd/t. One explanation for this difference is that the Vitanza fission gas release threshold is based on Halden reactor data as a function of the rod average burnup, and the FINE model is given in terms of the pellet local

radial burnup. Considering this difference in the definition of the burnup used in each of these models, there is excellent agreement between these two fission gas release threshold curves.

Figure 4.2.3.3-1 Schematic Representation of the Gas Bubble Swelling Model

Figure 4.2.3.3-2 Schematic Representation of the Gas Bubble Swelling Model as a Function of Burnup

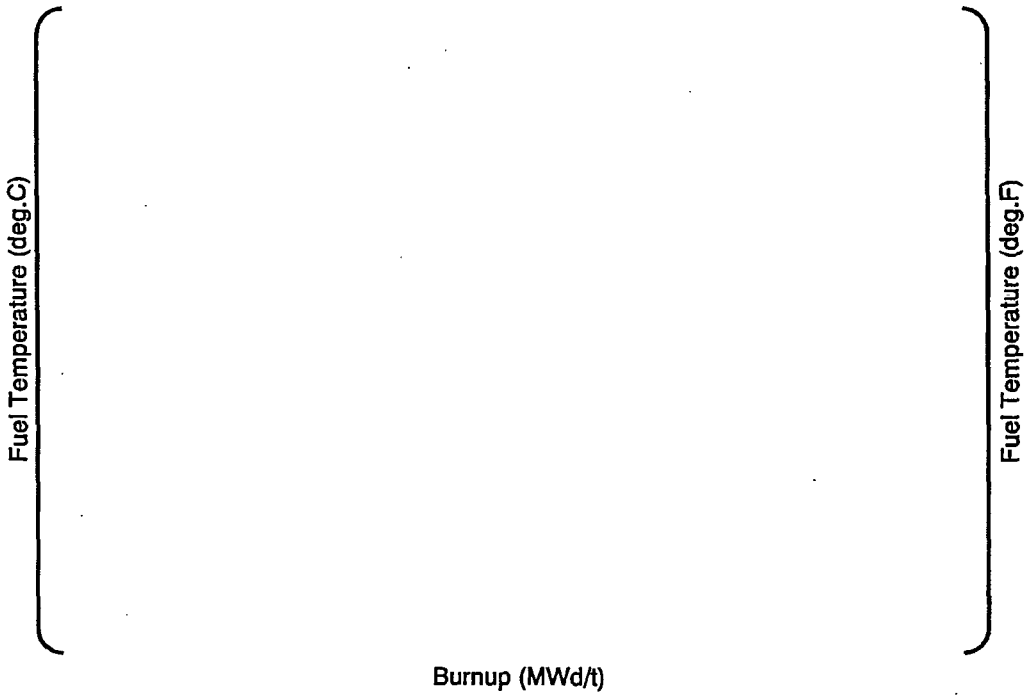

Figure 4.2.3.3-3 Comparison of Fission Gas Release Thresholds

4.2.4 Cladding Models

The FINE code contains models for both Zircaloy-4 and ZIRLO™ cladding. ZIRLO™ is the cladding used for high burnup fuel, with rod average burnup up to 62 GWd/t,

4.2.4.1 Cladding Corrosion Model

The FINE code cladding corrosion model was originally developed for Zircaloy-4 cladding. Improvement factors are defined to modify this model for ZIRLO™ cladding.

(a) Zircaloy-4 model
The Zircaloy-4 corrosion model is given by separate models for the pre-transition and post-transition behavior.
1) Pre-Transition region (W(t)<WT)

( ) (eq. 4.2.4.1-1)

where
WT : weight gain of the oxide layer at transition point of ( ) (mg/dm^2)
A : corrosion rate adjustment factor
{ }for Zircaloy-4
{ } for improved Zircaloy-4 (low Tin Zircaloy-4)
{ } for ZIRLO™
a : { } $((mg/dm^2)^3/day)$,
T : =metal-oxide interface temperature (K)
α : { }(K)
2a) Post-Transition region (WT = W(t) < WB)

( ) (eq. 4.2.4.1-2)

where
WB : second transition point,
{ }for Zircaloy-4,
{ } for improved Zircaloy-4, ZIRLO™ (mg/dm^2)
b : { } $((mg/dm^2)^3/day)$,
β : { } [K]
2b) WB = W(t)

( ) (eq. 4.2.4.1-3)

where
c :{ }
A crud thickness of { } is assumed for these models.
Cladding wall thinning due to corrosion is accounted for by reducing the cladding wall thickness by OT/(O/M), where
O/M = 1.6 is the oxide-to-metal thickness ratio
OT : oxide thickness (mils)

(b) ZIRLO™ model

The FINE corrosion model for ZIRLO™ cladding is obtained by using the adjustment factors given in the above description of the Zircaloy-4 corrosion model.

4.2.4.2 Hydrogen Absorption Model

Hydrogen is generated during the cladding oxidation process, and a fraction of this hydrogen is absorbed in the cladding. The FINE code uses a hydrogen absorption model proportional to the oxide thickness, given by eq. 4.2.4.2-2:

$$Zr + 2H_2O \rightarrow ZrO_2 + 2H_2 \qquad \text{(eq. 4.2.4.2-1)}$$

$$\left(\qquad \right) \qquad \text{(eq. 4.2.4.2-2)}$$

where

H : hydrogen content (ppm)

K_H : hydrogen pickup rate

$\left\{ \quad \right\}$ for Zircaloy-4,

$\left\{ \quad \right\}$ for Low Tin Zircaloy-4 and ZIRLO™

δ_{ZrO2} : oxide thickness (mil)

t_0 : initial cladding metal thickness (in)

H_0 : initial hydrogen content as fabricated (default = $\left(\quad \right)$)

The hydrogen pickup rates have been determined from post-irradiation examination data. The measured cladding hydrogen content as a function of the measured oxide thickness is shown in Figure 4.2.4.2-1. The hydrogen pickup rates given above have derived from these data.

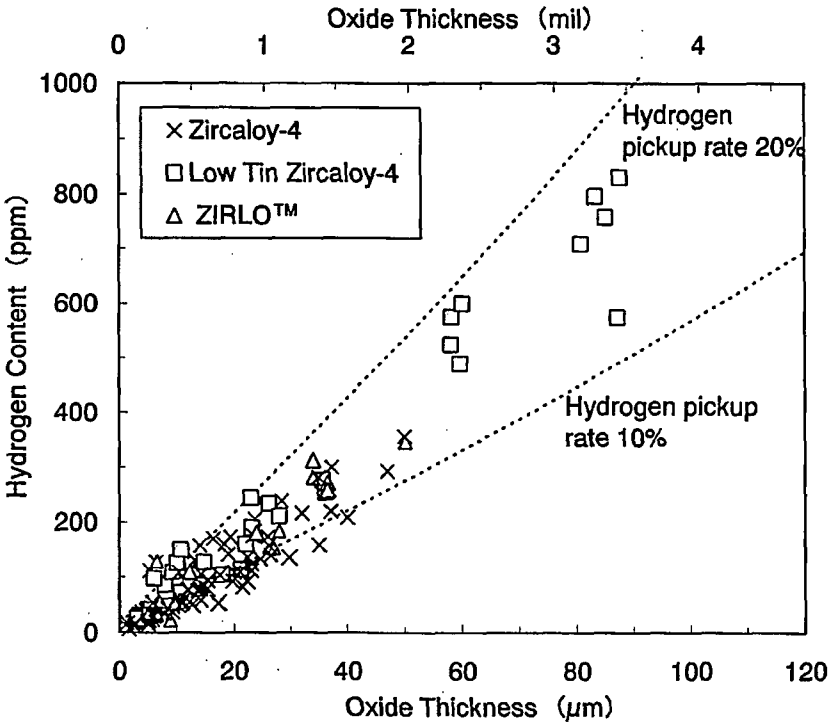

Figure 4.2.4.2-1 Hydrogen Pickup Rate

4.2.4.3 Rod Growth Model

Mitsubishi has obtained an extensive database for fuel rod growth for both Zircaloy-4 and ZIRLO™. Figure 4.2.4.3-1 shows the fuel rod growth data as a function of the fast neutron fluence. The database includes a variety of commercial reactor operating conditions and so many points especially for Zircaloy-4. Therefore, most of the Zircaloy-4 data are represented by the following Zircaloy-4 model.
The FINE code model for fuel rod growth given as a power law in the fast fluence ϕ_t :

$$\frac{\Delta L}{L} = A \cdot \phi_t^B \qquad \text{(eq. 4.2.4.3-1)}$$

where

$\frac{\Delta L}{L}$: rod growth (%)
ϕ_t : fast fluence (> 1MeV) (n/cm^2)
A : constant
B : constant

The constants A and B have been obtained by fitting to the databases identified with the following equations:

(a) Zircaloy-4

[ ] (eq. 4.2.4.3-2)

Where

ϕ_t : fast fluence (> 1MeV) (n/cm^2)

DATABASE :( )

(b) ZIRLO™
As shown in Figure 4.2.4.3-1, the growth of ZIRLO™ is almost half that of Zircaloy-4. The ZIRLO™ growth model has been obtained by fitting to ZIRLO™ database. The uncertainty of the ZIRLO™ model is assumed to be the same as that of Zircaloy-4, because the Zircaloy-4 growth database is more extensive than the ZIRLO™ database and covers a wider variety of reactor conditions. This is described in more detail in the discussion of the rod growth model verification in Section 4.3.

[ ] (eq. 4.2.4.3-3)

Where

ϕ_t : fast fluence (> 1MeV) (n/cm^2)

DATABASE:( )

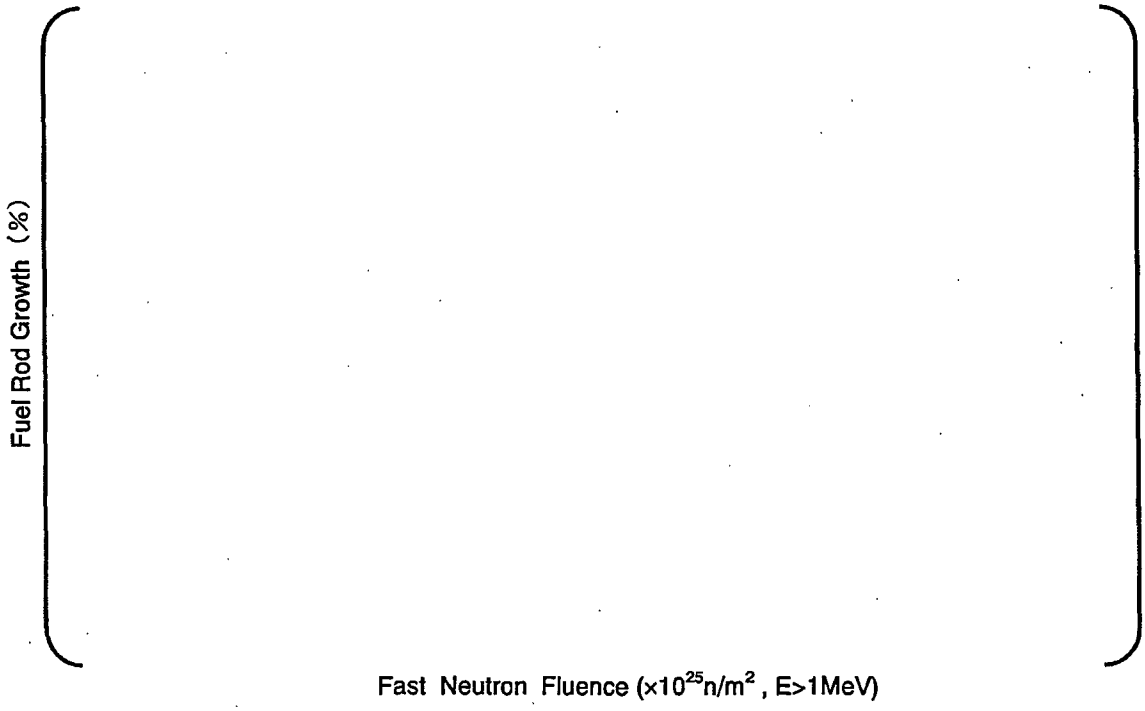

Figure 4.2.4.3-1 Fuel Rod Growth Data

4.2.4.4 Creep Model

The creep model is given by the sum of separate creep models for the thermal creep, the irradiation creep, and the diameteral change due to growth:

$$\dot{\varepsilon}_{creep} = \dot{\varepsilon}_{thermal} + \dot{\varepsilon}_{irradiation} + \dot{\varepsilon}_{growth} \quad \text{(eq. 4.2.4.4-1)}$$

where

$\dot{\varepsilon}_{creep}$: total creep strain rate (/hr)
$\dot{\varepsilon}_{thermal}$: thermal creep strain rate (/hr)
$\dot{\varepsilon}_{irradiation}$: irradiation creep strain rate (/hr)
$\dot{\varepsilon}_{growth}$: fuel rod growth contribution to circumferential strains (/hr)

The thermal creep model is based on Norton's law [24] and the strain hardening rule:

Norton's law

$$\dot{\varepsilon} = A \cdot \sigma^{B} \quad \text{(eq. 4.2.4.4-2)}$$

Strain hardening rule

$$\dot{\varepsilon} = a \cdot \varepsilon^{b} \quad \text{(eq. 4.2.4.4-3)}$$

where,

$\dot{\varepsilon}$: creep strain rate (/hr)
A,B : coefficients
a, b : coefficients

The primary temperature dependence of the thermal creep rate is given by Arrhenius temperature dependence:

$$\dot{\varepsilon} = \alpha \cdot \exp(-\beta \cdot T) \quad \text{(eq. 4.2.4.4-4)}$$

where,

$\dot{\varepsilon}$: creep strain rate (/hr)
α,β : coefficients

The final form of the FINE code thermal creep model is:

$$\dot{\varepsilon}_{thermal} = A \cdot \exp(a + b \cdot T) \cdot \sigma^{c+d \cdot T} \cdot \varepsilon^{e+f \cdot T} \quad \text{(eq. 4.2.4.4-5)}$$

Irradiation creep is given by the following equation[25]:

$$\dot{\varepsilon}_{irradiation} = A \cdot Cd \cdot \sigma^{n} \cdot \phi^{p} \cdot \exp(-Q/T) \quad \text{(eq. 4.2.4.4-6)}$$

where

A : material constant
Cd : anisotropy factor
σ : effective stress
ϕ : flux
T : temperature

The FINE code mechanical analysis uses only the irradiation creep in the circumferential direction, and the model used is given by:

$$\dot{\varepsilon}_{irradiation} = A \cdot \sigma^{B} \cdot \phi^{C} \quad \text{(eq. 4.2.4.4-7)}$$

where

A, B, C : constants

Eq. 4.2.4.4-7 is the same as eq. 4.2.4.4-6, with the assumption that there is no significant temperature dependence. The constants A, B and C used in eq. 4.2.4.4-7 are obtained by fitting to irradiated fuel rod diameter change data.

(a) Zircaloy-4

The creep model for Zircaloy-4 has been determined by the following procedure:
- the thermal creep model is determined from out-of-pile creep test data
- the irradiation creep model is determined by subtracting the thermal creep contribution and rod growth effects from the in-reactor fuel rod creep data.

(1) Thermal Creep

The Zircaloy-4 thermal creep model is based on extensive out-of-pile creep tests. The test conditions (time, temperature and equivalent stress) are summarized as follows.
- Time : ~ 3000 Hrs
- Temperature : 626 ~ 788 (deg.F) (330 ~ 420 (deg.C))
- Stress : 11379 ~ 39825 (psi)

The FINE code thermal creep model is given in terms of the equivalent stress and strain, with coefficients obtained from least squares fitting:

[ ] (eq. 4.2.4.4-8)

where

$\dot{\varepsilon}_{thermal}$: thermal creep equivalent strain rate (/hr)

$\varepsilon_{thermal}$: thermal creep equivalent strain (fractional)

T : temperature (K)

σ_e : equivalent stress (kgf/mm^2)

When used in the FINE code, the equivalent stress is calculated from the volume average of the equivalent stress calculated from the thick wall solution with internal and external pressure loading:

[ ]

$$K = \frac{DCO}{DCI}$$

DCO : cladding outer diameter (mm)

DCI : cladding inner diameter (mm)

Pf : rod internal pressure (kgf/mm^2)

Pct : contact pressure between pellet and cladding (kg$_f$/mm^2)

Ps : system pressure (kgf/mm^2)

(2) Irradiation Creep

The Zircaloy-4 Irradiation creep model is given by:

$\dot{\varepsilon}_{irradiation}$ [ ] (eq. 4.2.4.4-9)

where

$\dot{\varepsilon}_{irradiation}$: irradiation creep equivalent strain rate (%/hr)

σ_e : equivalent stress (kgf/mm^2)

ϕ : fast neutron flux (n/cm^2, E > 1 MeV)

This model has been developed by fitting to creep data obtained from the following rods:

[ ]

where any data that was affected by pellet-cladding contact has been excluded.

(3) Growth effect

The FINE axial growth model has been given in sub-section 4.2.4.3 above. The fuel rod growth contribution to the circumferential strains is given by:

[ ] (eq. 4.2.4.4-10)

where

ε^{z}_{growth} : axial growth strain, as given by eq. 4.2.4.3-2

The factor of [ ] is consistent with the value derived from the following equations. Zircaloy cladding growth is expressed with f_z by the next equation[26].

$$\frac{\Delta L}{L} = A \cdot \left[\exp(\frac{240.8}{T})\right] \cdot (\phi \cdot t)^{0.5} \cdot (1 - 3f_z) \cdot (1 + 2.0 \cdot CW)$$

Where

$\Delta L/L$: irradiation growth

A : 1.407×10^{-15} $(n/m^2)^{-0.5}$

T : cladding temperature (K)

ϕ : neutron flux ($n/m^2/s$) (>1.0MeV)

t : time (s)

The growth is proportion to the $(1-3f_z)$, anisotropic factor. The relative growth contribution to the circumferential direction is derived by the next equation.

[ ] using f_θ =[ ] and f_z =[ ] (which are consistent with the fabrication experience)

(4) Creep Model

The total mid-wall hoop creep strain is given by:

[ ] (eq. 4.2.4.4-11)

with each term calculated as described above:

[ ]

This cladding creep model has been verified by comparison with in-core creep data. The description of the cladding creep model verification is given in Section 4.3.

(b) ZIRLO™

The creep model for ZIRLO™ has been determined by the following procedure:
- the thermal creep model is determined from out-of-pile creep test data
- the irradiation creep model is determined by subtracting the thermal creep contribution and rod growth effects from the in-reactor fuel rod creep data.

(1) Thermal Creep

Eq. 4.2.4.4-5 is also used for the ZIRLO™ thermal creep model. Each constant in this equation has been obtained by fitting to out-of-pile creep test data obtained under the conditions summarized as follows.
- Time : ~1080 (hours)
- Temperature : 626 ~ 788 (deg.F) (330 ~ 420 (deg.C))
- Stress : 11379 ~ 28447 (psi)

The data at conditions closest to those encountered at in-reactor fuel rod conditions, such as the data at the lower creep rates and lower temperatures, were selected for the fit for the ZIRLO™ thermal creep model. These data are indicated by the heavy outlining in the table.
The model for the ZIRLO™ thermal creep obtained from this fit is:

[ ] (eq. 4.2.4.4-12)

A comparison of this model with the creep test data at all the out-of-pile test conditions summarized in Table 4.2.4.4-3 is shown in Figure 4.2.4.4-1. Data with creep strains of [ ] or more are not shown in the figure, because these data are assumed to come from tertiary creep, a condition that will not occur under fuel rod operating conditions.
As shown in Figure 4.2.4.4-1, this model gives good agreement with the data. For the data at 788 deg. F (420 deg. C), the model tends to overpredict the creep strain. However, in general fuel rod cladding temperatures are less than 734 deg. F (390 deg. C), and these high temperature overpredictions of the creep strain are not a concern.

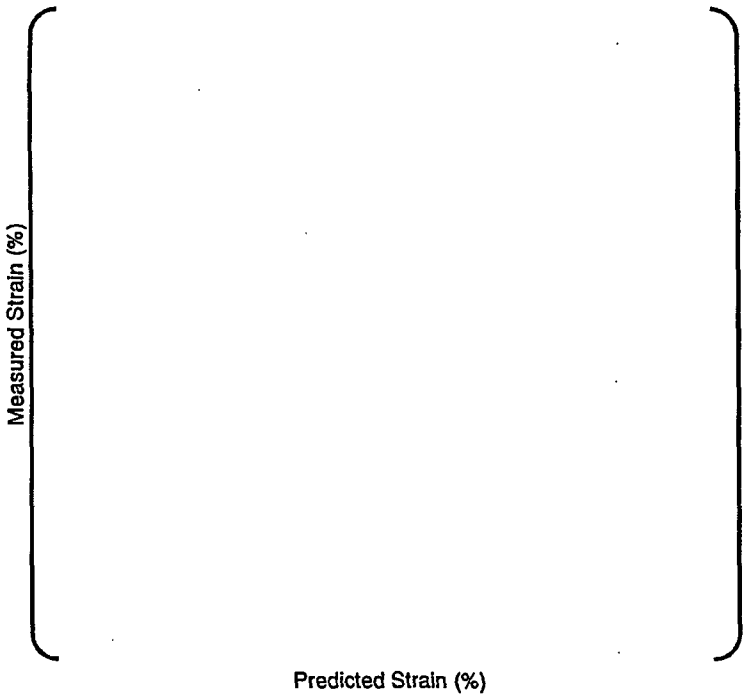

Figure 4.2.4.4-1 Comparison between Measured and Calculated Out-of-Pile ZIRLO™ Creep Strains

(2) Irradiation Creep

Fuchs et.al[27]. have shown that the in-core diameter change of Zirconium based alloys is a function of the alloy's Tin content and dissolved Niobium. Fuchs et.al. have shown that dissolved Niobium is twice effective as Tin in reducing irradiation creep, up to the maximum Niobium solubility as 0.5%. These results have been used to obtain a quantative evaluation of the differences between ZIRLO™ and Zircaloy-4 irradiation creep, as follows:

ZIRLO™ has a Niobium content of 1.0% and a Tin content of 1.0%, and the ZIRLO™ Tin + Niobium content factor, F_{ZIRLO}, is estimated to be

$$F_{ZIRLO} = 1.0 + 0.5 \times 2 = 2.0$$

for 1.0% Tin content and a maximum dissolved Niobium of 0.5%.

On the other hand, Zircaloy-4 has a Tin content of 1.5%, which gives a Zircaloy-4 Tin + Niobium content factor, $F_{Zircaloy-4}$, of 1.5. Based on this, it is expected that ZIRLO™ will have reduced irradiation creep, compared with Zircaloy-4, by a factor of 1.5/2.0 = 0.75.

Another study, Kido et.al[28], with ZIRLO™ indicates that dissolved Niobium restrained irradiation creep rate and rod growth by a factor of 1/2 to 2/3 as shown in Figure 4.2.4.4-2. Therefore, irradiation creep of ZIRLO™ is expected about a factor of 1/2 to 3/4 from Zircaloy-4. The FINE model for ZIRLO™ is therefore given by the Zircaloy-4 irradiation creep model with a reduction factor:

[ ] (eq. 4.2.4.4-13)

where

A : reduction factor for ZIRLO™

The value for the reduction factor A has been obtained from fitting this model to in-core creep data.

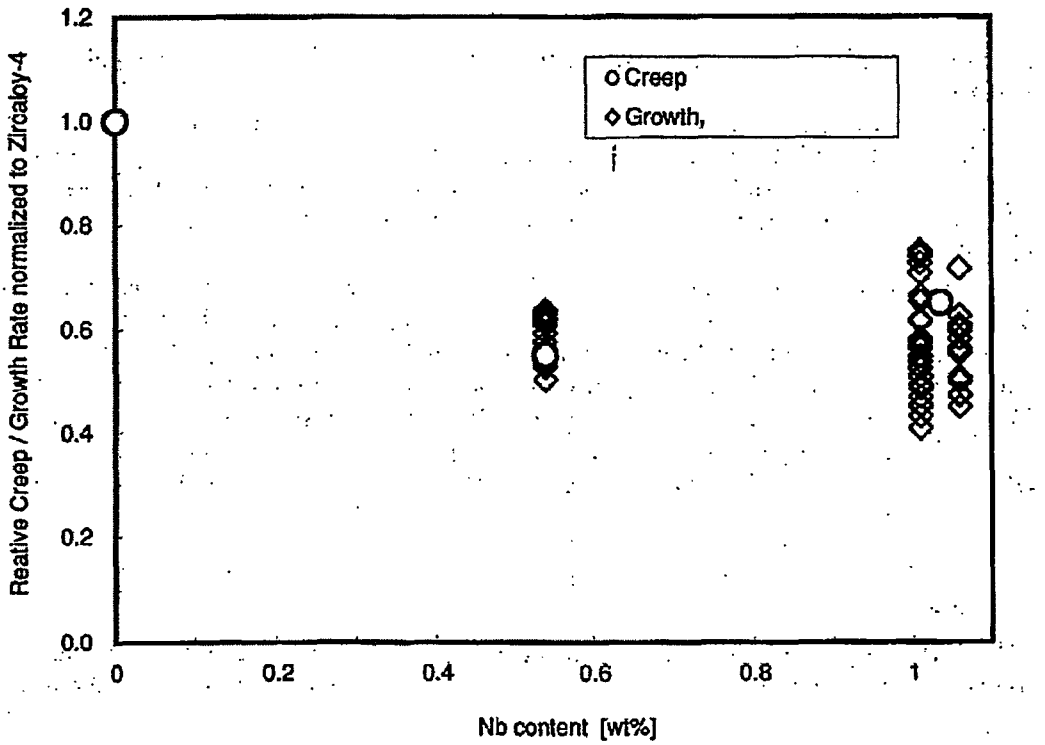

Figure 4.2.4.4-2 The Effect of Niobium Content on Irradiation-Induced Dimensional Changes[28]

(3) Growth effect

As described above for Zircaloy-4, the circumferential strain due to axial growth is given by eq. 4.2.4.4-14.

$$\varepsilon^{\theta}_{growth} = A \cdot \varepsilon^{Z}_{growth} \qquad \text{(eq. 4.2.4.4-14)}$$

where

ε^{Z}_{growth} : axial growth strain

A : constant

The constant A in this equation can be determined from Adamson's equation and the ZIRLO™ fabrication characteristics. Mitsubishi's experience with ZIRLO™ gives the value of f_r of more than [ ]. With this value of f_r, f_θ is around[ ], assuming f_z of[ ] . These values give a value for A close to zero:

[ ] with f_r of[ ], f_θ of[ ] and f_z of [ ]

The FINE code model for the growth contribution to the ZIRLO™ circumferential strain uses A [ ]

(4) Creep Model

The creep model for ZIRLO™ has been obtained by calibrating the FINE code to fuel rod profilometry data from the database summarized in Table 4.2.4.4-1. The axial profile of the rod outer diameter data has been examined so that only data with no pellet-cladding interaction, such that the fuel rod diameter decrease is solely due to cladding creep strains, are used. Both one cycle and two cycle data have been used. The rod diameter data have been averaged over each grid-to-grid span length.

As described above, the effect of rod growth is[ ]in the FINE ZIRLO™ model. Therefore, the coefficients for both thermal and irradiation creep, $f_{thermal}$ and $f_{irradiation}$, are determined from the rod profilometry data.

The thermal creep model given by eq. 4.2.4.4-12 overpredicts the diameter change even when it is assumed that there is no irradiation creep. Therefore, the in-reactor contribution of the ZIRLO™ thermal creep is less than that estimated from the out-of-pile tests. The reason of this is not clear. The equation used to calculate the total creep strain is

[ ] (eq. 4.2.4.4-15)

[ ] (eq. 4.2.4.4-16)

[ ] (eq. 4.2.4.4-17)

Where

$f_{thermal}$: coefficient for thermal creep component

$f_{irradiation}$: coefficient for irradiation creep component

Figure 4.2.4.4-3 and Figure 4.2.4.4-4 illustrate the axial profile of the diameter decrease. The coefficients $f_{thermal}$ and $f_{irradiation}$ have been determined by matching the diameter decrease axial profile. It has been found that $f_{thermal}$ is[ ] which has been confirmed from the diameter decrease data at the bottom or top of the fuel rod, where the fluence is lower than in the middle of the fuel rod. Figure 4.2.4.4-5 gives the comparison between measured and predicted diameter change data from the top or bottom spans, confirming[ ]

The FINE code ZIRLO™ cladding creep model in FINE code is summarized by the following equations:

[ ] (eq. 4.2.4.4-18)

where

ϕ_t : fast neutron fluence [> 1 MeV] (nvt) / 10^{20}

[ ] (eq. 4.2.4.4-19)

Where,

ϕ : fast neutron flux (n/cm^2, E > 1 MeV)

Table 4.2.4.4-1 ZIRLO™ Creep Model Database

Reactor	Initial Helium Pressure	No.of Cycles	Number of rod	Burnup range
[ ]				

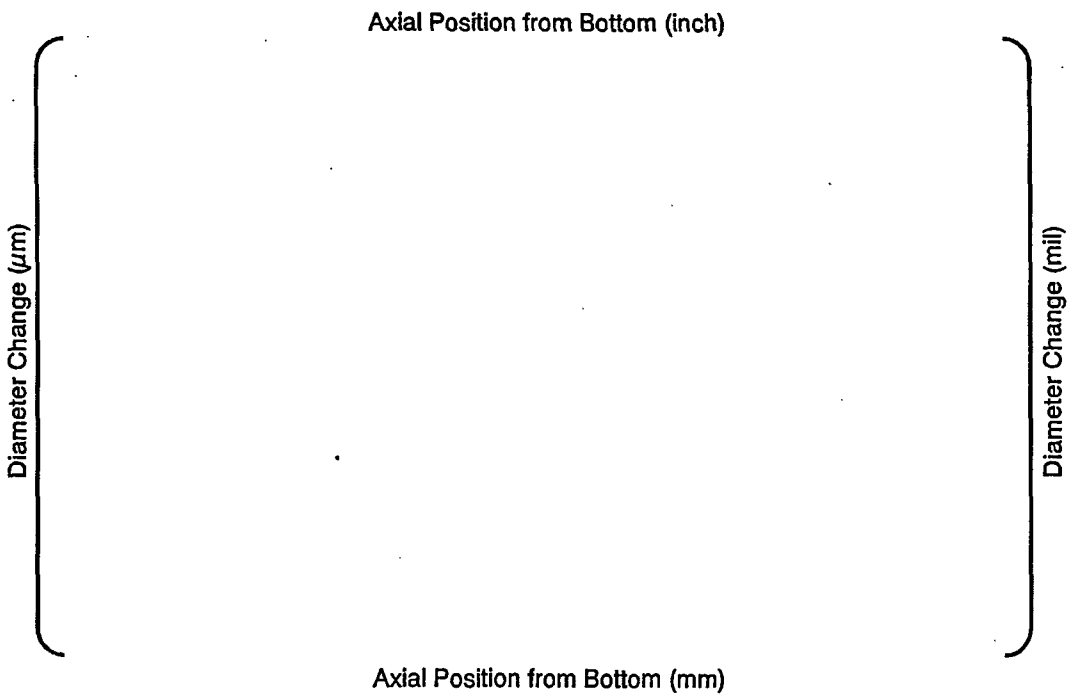

Figure 4.2.4.4-3 Axial Profile Comparison for WZtR162

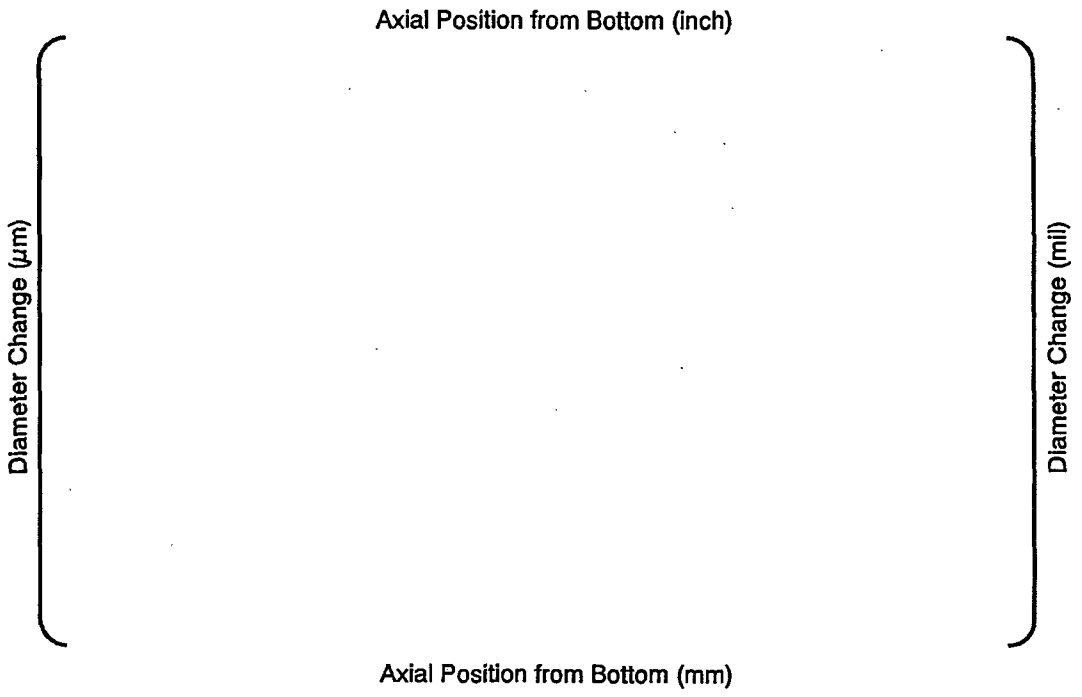

Figure 4.2.4.4-4 Axial Profile Comparison for WZR0058

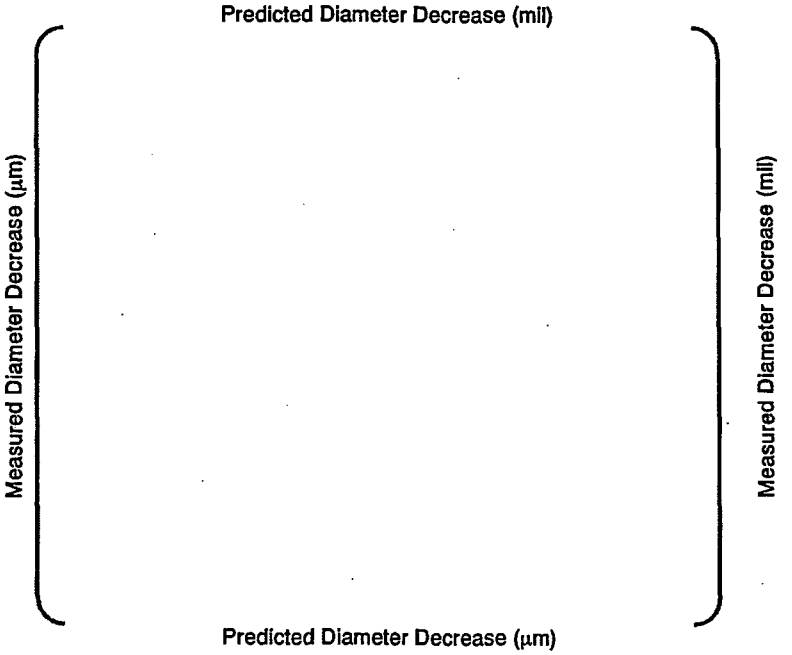

Figure 4.2.4.4-5 Comparison of Diameter Decrease at the Lower Fluence Positions

4.2.4.5 Cladding Fuel Side Oxidation Model

Oxygen is released from the pellet after the fission of UO_2. Zirconium reacts chemically with the Oxygen, forming a ZrO_2 layer on the cladding inner diameter. A significant ZrO_2 layer is observed after irradiation to moderate burnups. Figure 4.2.4.5-1 summarizes the development of ZrO_2 thickness with burnup[29]. Figure 4.2.4.5-1 (b) gives the overview of the fuel side oxide formation as a function of pellet burnup.There is no significant ZrO_2 formation at the cladding inner diameter until the burnup exceeds 25 GWd/t. At higher burnups more than 40GWd/t, the oxide formation almost reaches to 100%. At the same time, Figure 4.2.4.5-1 (a) shows the constant fuel side oxide thickness at more than 40GWd/t. It can be said that fuel side oxide thickness seems to reach its maximum value of approximately[ ]at a certain burnup more than 40GWd/t.

The FINE code uses the following model for the cladding fuel side corrosion:

[ ] (eq.4.2.4.5-1)

Where,

δ_{ZrO2} : fuel side ZrO_2 thickness (μm)

Bup : local burnup (GWd/t)

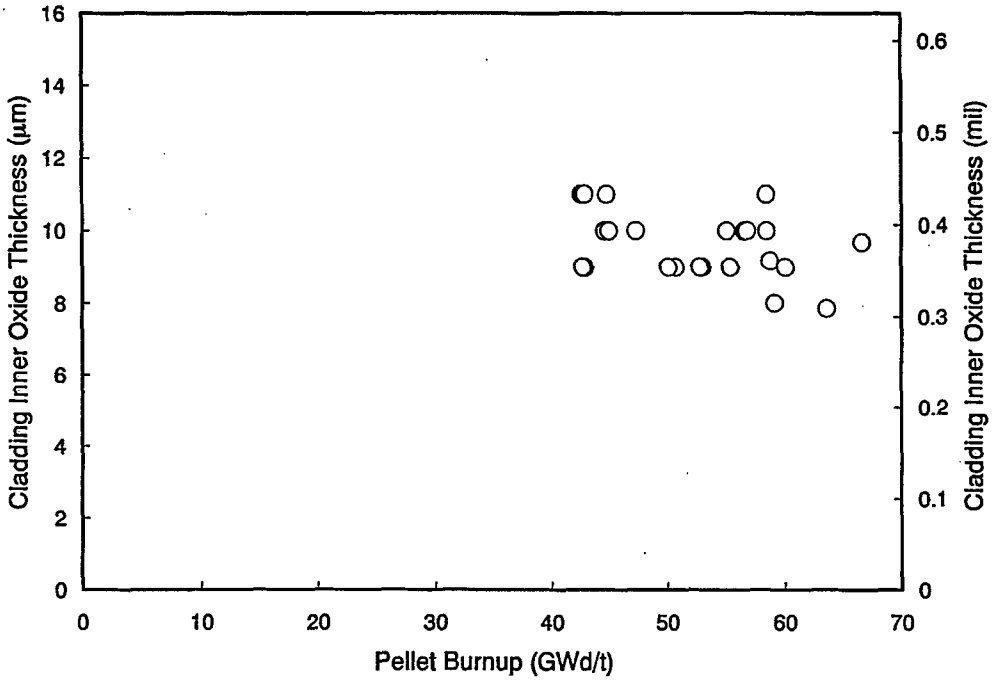

(a) fuel side oxide thickness versus pellet burnup

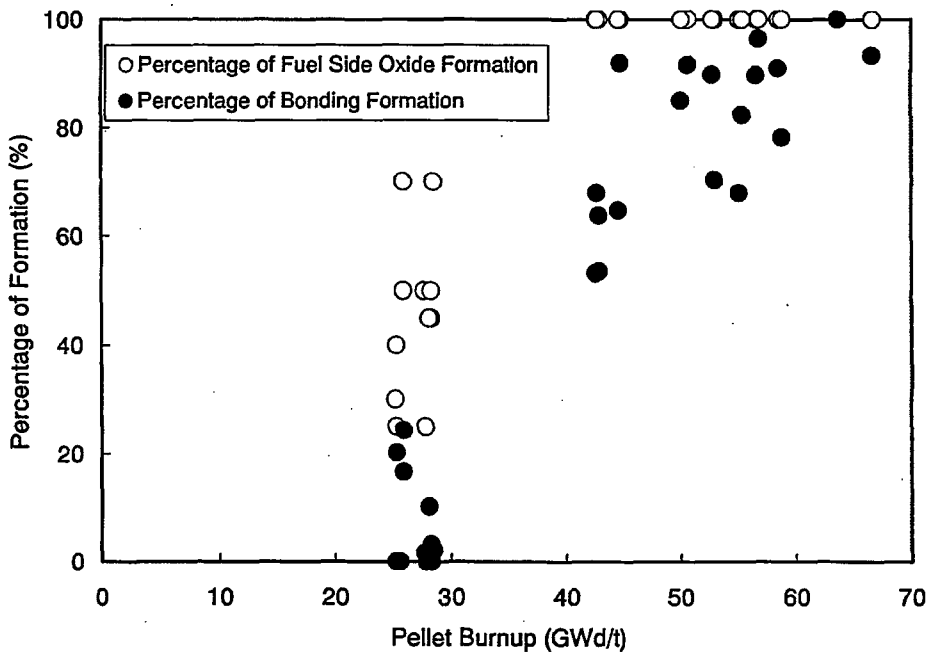

(b) percentage of fuel side oxide formation versus pellet burnup

Figure 4.2.4.5-1 Fuel Side Oxidation Development with Burnup[29]

4.2.5 Mechanical Analysis

The FINE mechanical calculation models are summarized in this section.

(a) Stress-strain relationship of the cladding

The FINE code uses the following stress-strain relationship. The( ) stress-strain relationship is applied in the FINE code. The elastic limit is defined as( ) of yield stress as shown in Figure 4.2.5-1.

The stress-strain relationship is expressed by the following equations.

$$\sigma = E \cdot \varepsilon \qquad \sigma < EL \qquad \text{(eq.4.2.5-1)}$$

$$\left[\quad\right] \qquad \sigma \geq EL \qquad \text{(eq.4.2.5-2)}$$

Where,

σ : stress
ε : strain
YS : yield stress
EL : elastic limit =( )x YS
ε_1 : strain at EL
ε_2 : strain at YS
E : Young Modulus (ref. Appendix B)

Once stress exceeds the elastic limit, plastic strain is remained.

Figure 4.2.5-1 Stress-Strain Relationship in the FINE Code

(b) Stress calculation

Cladding stresses are calculated based on the thick-walled cylinder equation stress solution.

$$\sigma_r = \frac{1 - K^2/R^2}{K^2 - 1} P' - \frac{K^2 - K^2/R^2}{K^2 - 1} Po \qquad \text{(eq. 4.2.5-3)}$$

$$\sigma_\theta = \frac{1 + K^2/R^2}{K^2 - 1} P' - \frac{K^2 + K^2/R^2}{K^2 - 1} Po \qquad \text{(eq. 4.2.5-4)}$$

$$\sigma_z = \frac{1}{K^2 - 1} P' - \frac{K^2}{K^2 - 1} Po \qquad \text{(eq. 4.2.5-5)}$$

where

σ_r	: radial stress
σ_θ	: circumferential stress
σ_Z	: axial stress
P'	: sum of rod internal pressure (Pi) and pellet-cladding contact pressure (Pct)
Po	: system pressure (rod outside pressure)
K	: r_o / r_i
R	: r / r_i
r_i	: cladding inner radius
r_o	: cladding outer radius
r	: radius

The pellet-cladding contact pressure is calculated using the pellet-clad elastic interference model:

$$P_{ct} = \frac{\frac{\delta}{r_i}}{\frac{K^2 + 1}{K^2 - 1} \times \frac{1}{E_1} + \frac{1}{E_2} + \frac{\nu_1}{E_1} + \frac{\nu_2}{E_2}} \qquad \text{(eq. 4.2.5-6)}$$

where

E_1	: pellet Young's modulus
E_2	: cladding Young's modulus
ν_1	: pellet Poisson's ratio
ν_2	: cladding Poisson's ratio
δ	: pellet-clad interference in contact

(c) Thermal stresses

The stresses due to the temperature gradient across the cladding wall are calculated using the following equations:

$$T(r) = \frac{T_o ln(r/r_i) + T_i ln(r_o/r)}{ln(K)} \qquad \text{(eq.4.2.5-7)}$$

$$\sigma_r = \frac{aE_1}{2(1-\nu_1)} \left\{ \frac{(K^2 T_O - T_i) - (T_O - T_i)(r_o/r)^2}{(K^2 - 1)} - T(r) \right\} \qquad \text{(eq. 4.2.5-8)}$$

$$\sigma_\theta = \frac{aE_1}{2(1-\nu_1)}\left\{\frac{(K^2T_O - T_i) + (T_O - T_i)(r_o/r)^2}{(K^2-1)} - \frac{(T_O - T_i)}{\ln K} - T(r)\right\} \quad \text{(eq. 4.2.5-9)}$$

$$\sigma_z = \frac{aE_1}{1-\nu_1}\left\{\frac{(K^2T_O - T_i)}{(K^2-1)} - \frac{(T_O - T_i)}{2\ln K} - T(r)\right\} \quad \text{(eq .4.2.5-10)}$$

where

α	: thermal expansion coefficient for cladding
T_o	: cladding outer surface temperature
T_i	: cladding inner surface temperature
E_1	: cladding Young's modulus
ν_1	: cladding Poisson's ratio
K	: r_o / r_i
r_o	: cladding outer radius
r_i	: cladding inner radius

4.2.6 Rod Internal Pressure Calculation

(a) Pressure calculation

$$P = \frac{nR}{\sum_i \frac{V_i}{T_i}} \qquad \text{(eq. 4.2.6-1)}$$

where

P : rod internal pressure
n : total gas in the rod void volume
V_i : volume of void volume component i
T_i : temperature of void volume component i
i : void volume component index
R : gas constant

(b) Void volume and temperature calculation

The void volume components and temperatures used in the rod internal pressure calculation are summarized in Table 4.2.6-1.

Table 4.2.6-1 Void Temperature and Void Volume Calculation Summary

Type of Void	Void Temperature	Void Volume Calculation	Remarks
Dish Chamfer	Average of pellet average temperature in axial segments i and i+1 Average of pellet surface temperature in axial segments i and i+1	Thermal expansion, densification and swelling are calculated for each fuel ring and accounted for in the dish and chamfer void volume calculations	Dish void volume is assumed to be 0 for an annular pellet
Radial cracks	Pellet average temperature		
Pellet-Cladding Gap	Gap average temperature	The void volume is calculated from the pellet outer diameter and the cladding inner diameter. Pellet thermal expansion, densification and swelling are accounted for in the pellet outer diameter calculation. The cladding elastic and plastic deformation, including creep deformation, are accounted for in calculating the cladding inner diameter.	For 95%TD pellets, the open porosity is assumed to be ( )
Open porosity	Pellet average temperature	( )	Fabrication experience
Surface roughness and chip volume	Pellet surface temperature	( ) When there is a pellet chamfer, the chamfer volume is subtracted from the chip volume	
Lower plenum Upper plenum	Coolant inlet temperature ( ) Tcoolant : coolant outlet temp. f(z) : ratio of local power at the top of the fuel stack to the rod average power q' : rod average power (kw/ft)	The plenum void volume calculations include the effects of pellet and cladding thermal expansion, cladding growth and pellet densification and swelling, and the thermal expansion of the plenum holddown spring	

4.2.7. Others

The FINE code uses pellet radial power distributions obtained from the PHOENIX-P[7] nuclear calculation code. The power distribution of the PHOENIX-P is validated by the MCNP[30] calculation result. The FINE code uses the radial power distribution data in the form of tables of relative power as a function of enrichment, burnup, and pellet ring. The table for an enrichment of 4.8 wt% U^{235} is shown in Table 4.2.7-1 as an example. The radial power distribution data covers the U^{235} enrichment range from ( ). The FINE code interpolates these tables for power calculation.
The FINE code uses the UO_2 radial power distributions for Gadolinia doped fuel as well. For the verification of the FINE code shown in section 4.3, the UO_2 radial power distributions are used both for UO_2 and Gadolinia doped fuel under light water reactor condition.

Table 4.2.7-1 Sample Radial Power Distribution Table (4.8wt% Enrichment)

( )

4.3 Verification

In this section, FINE code calculation is verified with measured data. The models for fuel temperature, fission gas release, pellet density change, helium gas mol, corrosion, hydrogen pickup, growth and creep models are verified with the extensive database. The verification results provide an uncertainty for each model used in the FINE code. The uncertainties are applied to the fuel integrity analysis. On the other hand, the predicted result of void volume and rod internal pressure is compared with the measured data in order to demonstrate the integral view of the models. For the transient calculation, fuel rod diameter measurement before and after ramp tests is good indicator to verify the integral performance of the FINE code as well.

4.3.1 Fuel Centerline Temperature

To verify the thermal model of FINE code, calculated fuel centerline temperature is compared with measured data. All the data of centerline temperature were obtained in HALDEN Heavy Water Boiling Water Reactor (HBWR).
Data base is summarized as follows. The detailed specification is shown in Table 4.3.1-1.

FA (RIG) No.	No. of rods	Maximum Burnup (MWd/t)	Pellet type	Instrumentation*
[ ]				

*TC : Thermocouple, ET : Extension Thermometer

Table 4.3.1-1 Summary of Rod Specification for Fuel Temperature

ID	Rig.No	Rod No.	235-U Enrichment [wt%]	Gadolinia Content [wt%]	Density [%T.D.]	Pellet Diameter [in]	Pellet Centerhole Diameter [in]	Cladding Outer Diameter [in]	Diametral Clearance [in]	Stack Length [ft]	Loop Condition

4.3.1.1 UO_2 fuel

A rod-by-rod summary of the UO_2 fuel centerline temperature results is given in Table 4.3.1.1-1. The statistical results (average and standard deviation for the Measured - Predicted (M - P) differences) are given for each rod.

Figure 4.3.1.1-1 shows the variation of the M - P results as a function of burnup. This figure shows that the FINE code predictions do not have any significant bias as a function of burnup.

Figure 4.3.1.1-2 shows the variation of the M-P results as a function of linear power. There is no bias in the scatter as a function of linear power, though the scatter increases for linear powers above 30 kW/m (9.1kW/ft).

Figure 4.3.1.1-3 shows the variation of the M - P results as a function of diametral gap. The data points in the Figure with a negative value of the "gap" are plotted versus the pellet-cladding interference used in the elastic interference model to calculate the contact pressure. The FINE code results for an open gap do not show a systematic bias. However, the code does underestimate the temperature for the small gap IFA-11 & -21 rods, especially in the closed gap condition.

The results in these Figures show that the FINE code gives a good prediction of the measured fuel centerline temperatures for UO_2 fuel. From the results shown in Table 4.3.1.1-1, the uncertainties at a 95% probability at a 95% confidence level in the FINE code fuel centerline predictions are:

Number of data	[ ]
M-P average	[ ]
M-P σ	[ ]
Uncertainty	
Upper bound	[ ]

Mitsubishi puts some margin on this upper bound and sets the uncertainty of [ ] ( ).

[ ]

Figure 4.3.1.1-4 shows the result of "power to melt test". The fuel rod was ramped quickly up to the high power to allow the melting at center part of fuel. The curve in the Figure is the FINE code prediction of the fuel centerline temperature as a function of axial elevation. The bold portion of this curve shows the extent of the fuel centerline melting observed in the test, as determined from the post-test measurements. The extent of the region where the FINE code predicted melting is shown by the dashed vertical lines. This Figure shows that the FINE code gives conservative predictions of the fuel temperatures at conditions close to the UO_2 melt temperature.

On the other hand, the pellet-cladding gap of the power to melt rod is closed in the FINE calculation. This result shows that the FINE code gives conservative prediction under the negative gap condition. Therefore, the underestimation seen in IFA-11 and -21 rods is not systematic.

Futhermore, it should be mentioned that the FINE code does not take into account the eccentricity model of pellet and relocation model even though the actual fuel pellet does not always stay at the center of the cladding and the pellet relocates. The above comparison includes the effect of the actual fuel pellet behavior in the measurement. Therefore, the FINE code covers the effect of the eccentricity implicitly and is verified by the measurement.

Table 4.3.1.1-1 Summary of Fuel Temperature Comparison

ID	Rod No.	Burnup [MWd/t]	Number of data	(M-P) average [deg.F]	(M-P) standard deviation [deg.F]
[ ]					

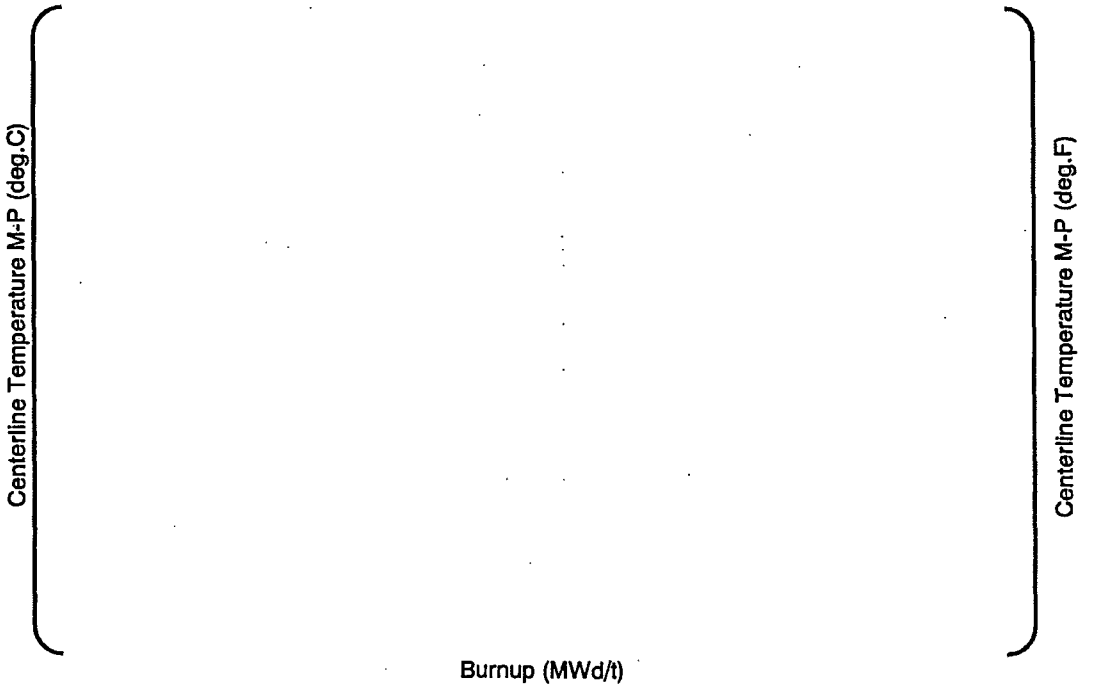

Figure 4.3.1.1-1 (M-P) versus Burnup of Fuel Centerline Temperature

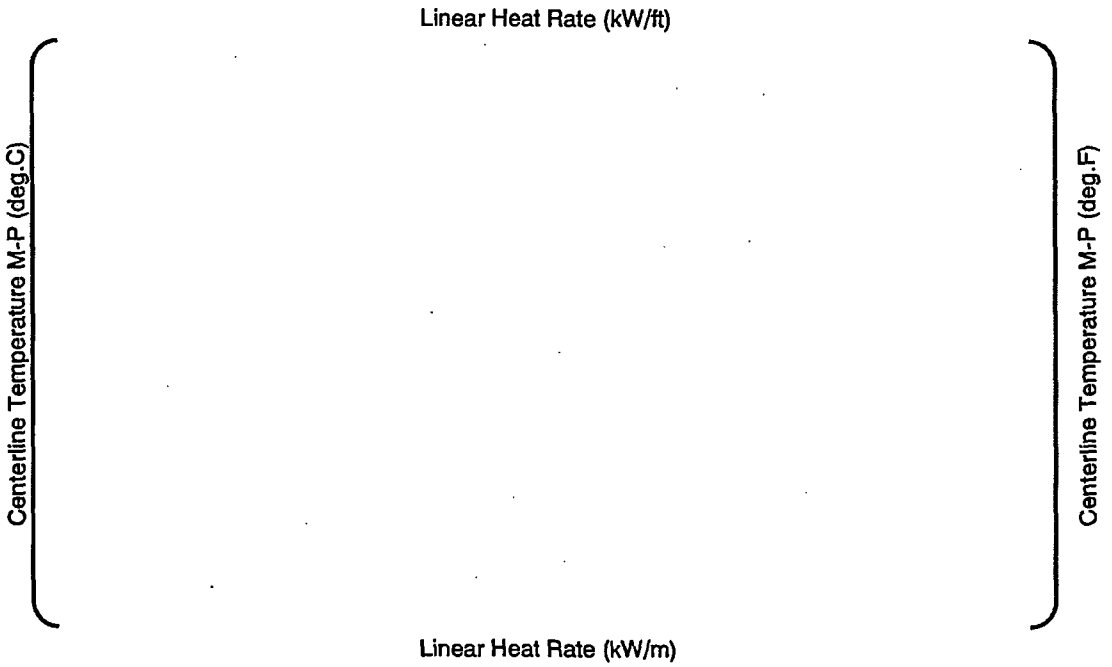

Figure 4.3.1.1-2 (M-P) versus Rod Power of Fuel Centerline Temperature

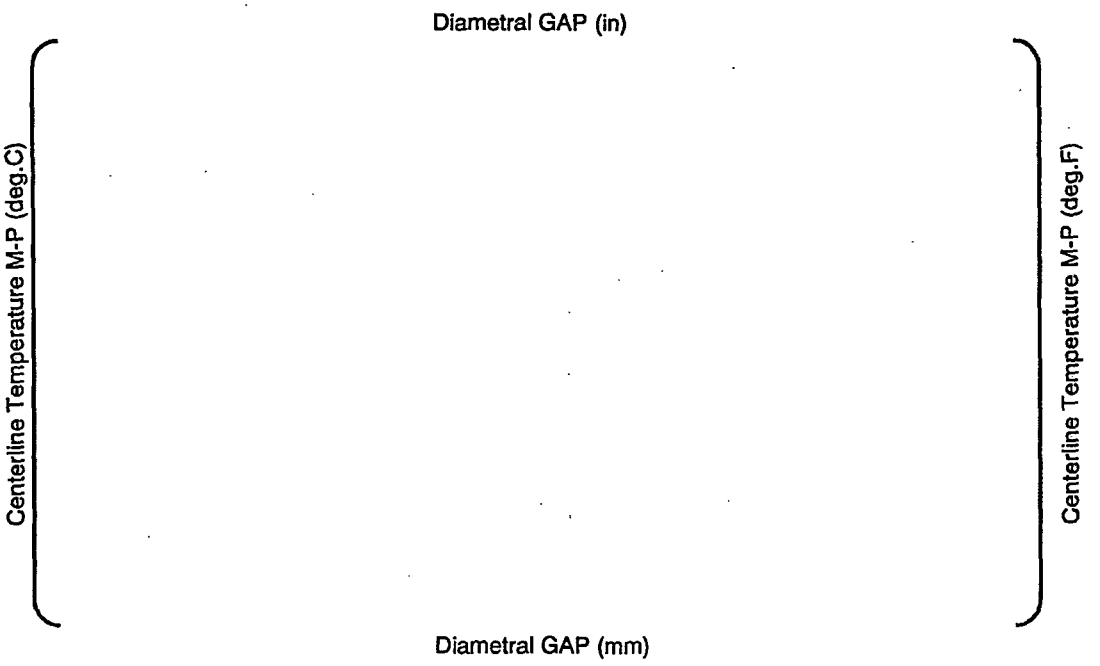

Figure 4.3.1.1-3 (M-P) versus Diametrial Gap of Fuel Centerline Temperature

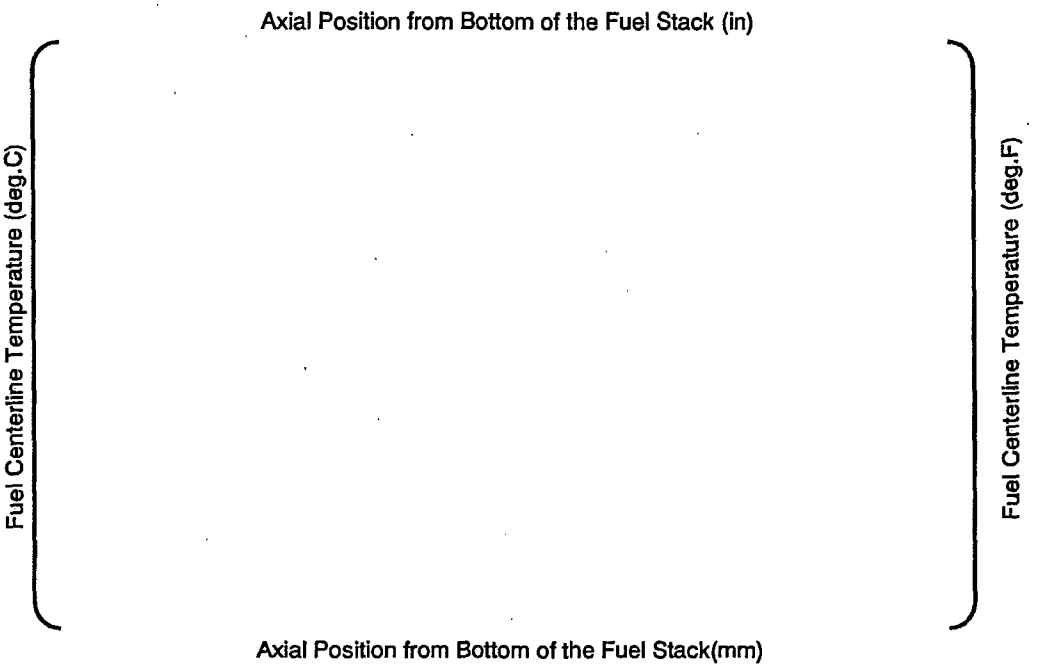

Figure 4.3.1.1-4 Power to Melt Test Result (UO_2)

4.3.1.2 Gadolinia Doped Fuel

The FINE code predictions fuel centerline temperatures of the IFA-539 6 wt% Gadolinia doped pellet and IFA-561 10 wt% Gadolinia doped pellet. The temperatures have been calculated using radial power depression factors that accounted for the strong neutron absorption of Gadolinium. The power depression factors used in the IFA-539 and IFA-561 fuel centerline temperature calculations are shown in Figure 4.3.1.2-1 and Figure 4.3.1.2-2, respectively as a function of burnup. As shown in Figure 4.3.1.2-1, the depression factor of IFA-539 decreases at the beginning of the irradiation and subsequently it increases. At the certain burnup where the Gadolinia is burned out, it becomes higher than that of UO_2 expected under Halden condition in this case.

In order to give the larger uncertainty (minimizing the prediction to give maximum M - P), the prediction for IFA-539 and IFA-561 is given by the minimum of the calculated temperature with the Gadolinia depression factor and that with UO_2 depression function.

On the other hand, the IFA-515 8 wt% Gadolinia doped pellets were specially prepared with ^{161}Gd, which is a weak neutron absorber, and the FINE predictions of the IFA-515 fuel centerline temperatures have been calculated using UO_2 radial power depression factors.

A rod-by-rod summary of the Gadolinium doped fuel centerline temperature results is given in Table 4.3.1.2-1. The statistical results (average and standard deviation for the Measured - Predicted (M - P) differences) are given for each rod.

Figure 4.3.1.2-3 shows that there is no bias in the FINE code predictions for 8 wt% and 10 wt% Gadolinium, as a function of power, though there is a conservative bias to increasing overprediction of the 6 wt% Gadolinium data with increasing power. Figure 4.3.1.2-4 shows that there is no bias in the FINE code predictions as a function of burnup.

The results in these Figures show that the FINE code gives a good prediction of the measured fuel centerline temperatures for Gadolinium doped fuel. From the results shown in Table 4.3.1.1-1, the uncertainties at a 95% probability at a 95% confidence level in the FINE code fuel centerline predictions are

Number of data	: ( )
M-P average	:
M-P σ	:
Uncertainty	
Upper bound	:
Lower bound	:

Mitsubishi sets the same uncertainty as UO_2 fuel of ( ).

Figure 4.3.1.2-5 shows the result of a comparison of the FINE code predictions to the data obtained in a power to melt test conducted with the 10 wt% Gadolinium doped fuel. The curve in the Figure is the FINE code prediction of the fuel centerline temperature as a function of axial elevation. The bold portion of this curve shows the extent of the fuel centerline melting observed in the test, as determined from the post-test measurements. The extent of the region where the FINE code predicted melting is shown by the dashed vertical lines. This Figure

shows that the FINE code gives fairly well predictions of the fuel temperatures at conditions close to the Gadolinium doped fuel melt temperature.

Table 4.3.1.2-1 Comparison for Each Data Base

Rod I.D.	Gadolinia content (wt%)	Number of Data	(M-P) average (deg.F)	(M-P) standard deviation (deg.F)
[redacted]				

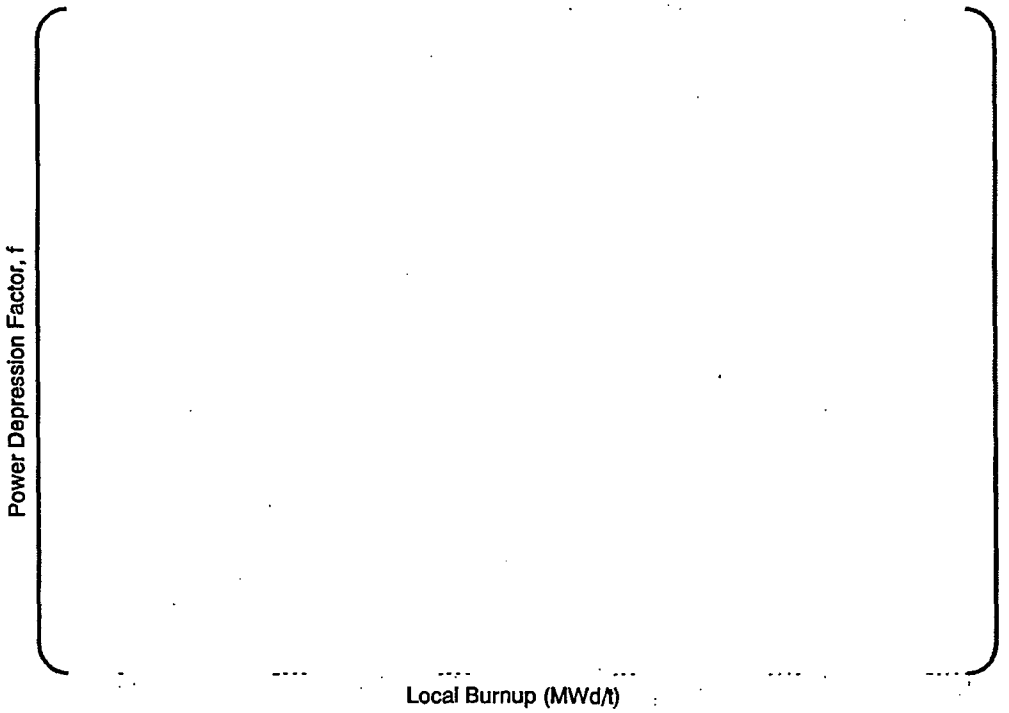

Figure 4.3.1.2-1 Depression Factor Development with Burnup of 6wt% Gd

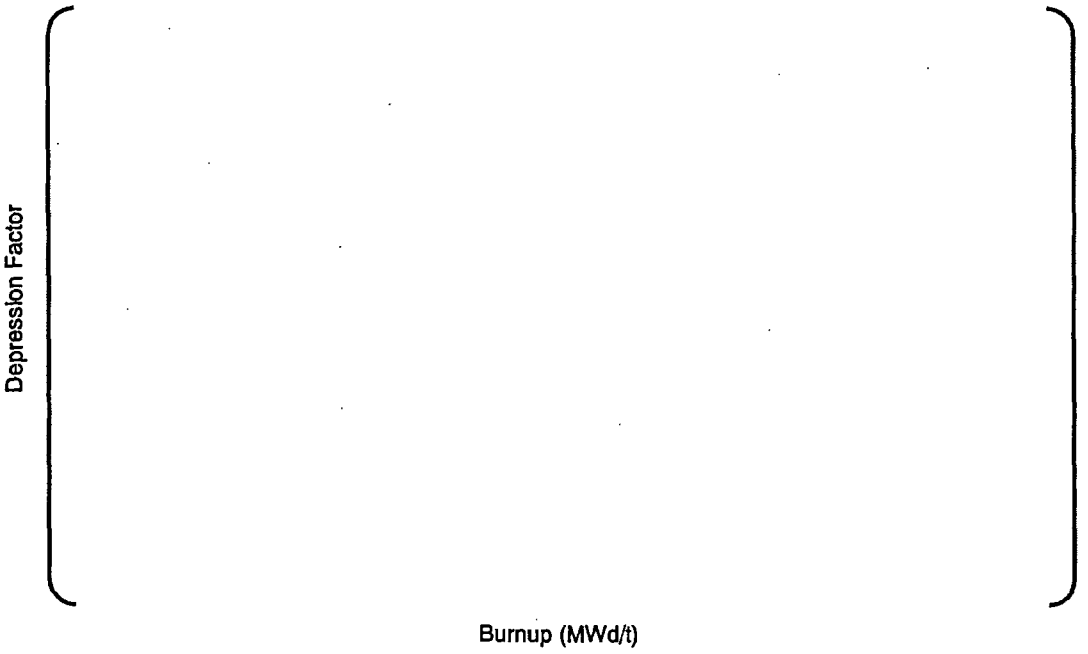

Figure 4.3.1.2-2 Depression Factor Development with Burnup of 10wt% Gd

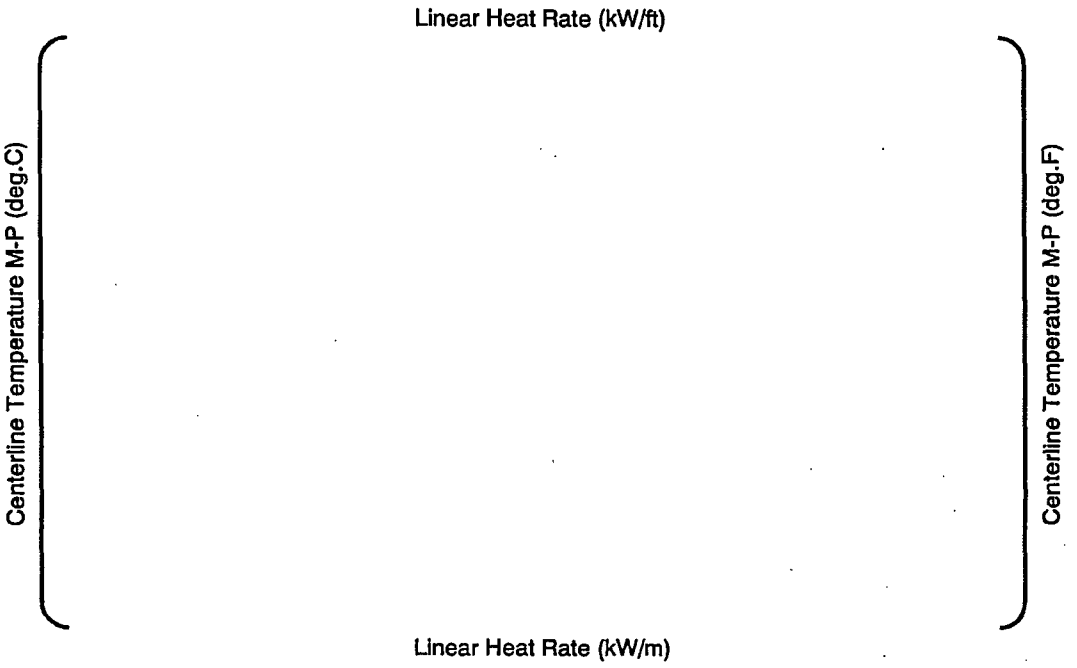

Figure 4.3.1.2-3 M-P versus Rod Power

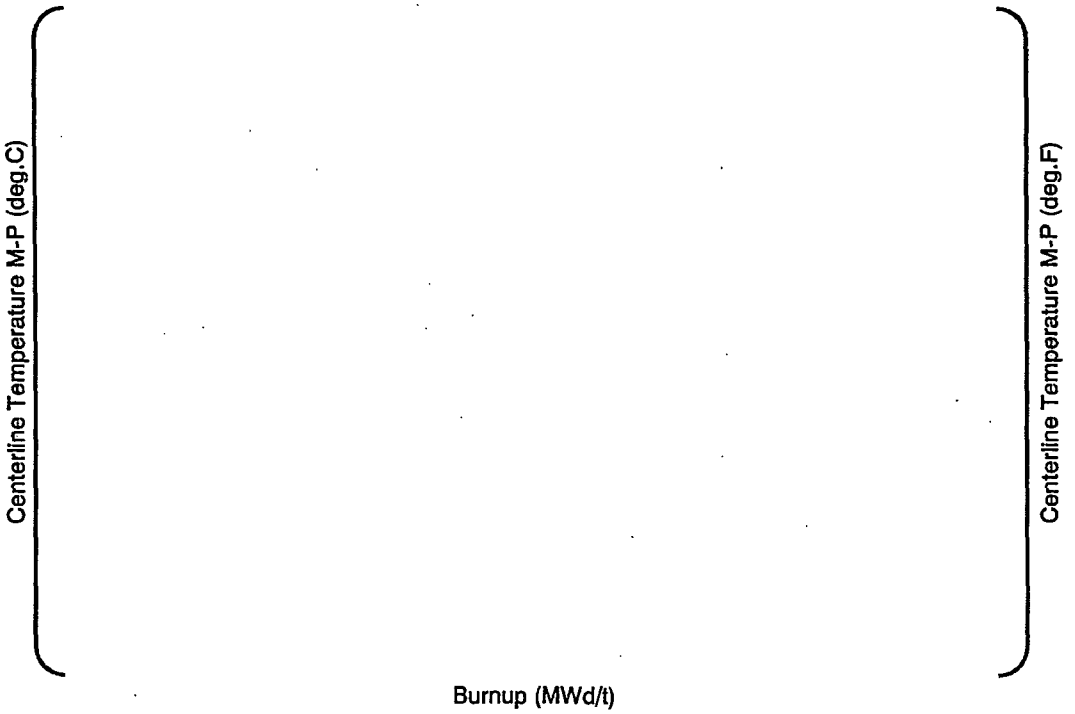

Figure 4.3.1.2-4 M-P versus Burnup

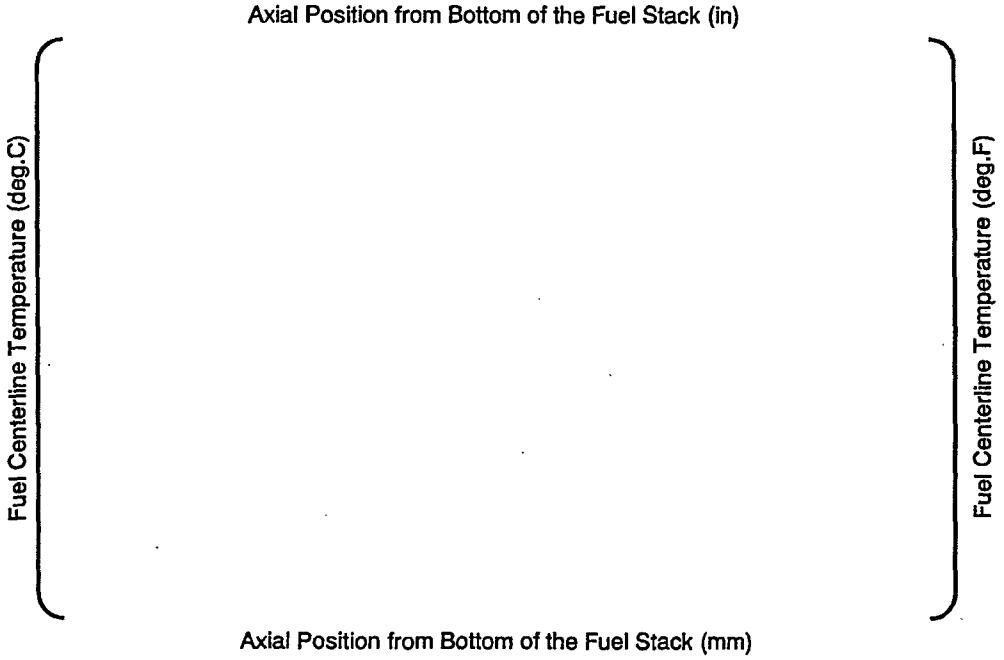

Figure 4.3.1.2-5 Power to Melt Test Result with 10wt% Gd

4.3.2 Fission Gas Release

The FINE code fission gas release (FGR) models have been validated with an extensive database of fission gas release measurements. This database is summarized in Table 4.3.2-1.

Figure 4.3.2-1 shows the plot of the fission gas release M/P ratios as a function of rod average burnup. The low burnup data that are underpredicted by the FINE code are either fuel with pellet densities less than 94% TD, or have a measured fission gas release less than 1%. This Figure confirms that there is no significant bias in the FINE fission gas release predictions as a function of the rod burnup.

Figure 4.3.2-2 plots the Measured-to-Predicted (M/P) ratios as a function of the measured fission gas release. The scatter is relatively large for the fuel with a measured FGR less than 1%. However, the FINE code overpredicts most of these low FGR data. The FINE code also tends to overpredict the FGR data for measured FGRs between 1 and 10%, and gives a best estimate prediction for the rods with a steady state FGR greater than 10%. In addition, the FINE code fission gas release models overpredict all of the overpower ramp test FGR data.

The upper bound uncertainty of the fission gas release model has been determined by the following data selection out of the data in Table 4.3.2-1. The rationale for the selection of these data is:

( )

The FINE code overpredicts the fission gas release of Gadolinia doped fuel as well.

The uncertainties at a 95% probability at a 95% confidence level in the FINE code are:

Number of data	( )
M/P average	
M/P standard deviation	
Uncertainty	
Upper bound	

Mitsubishi has used somewhat conservative uncertainty of ( )(for upper bound) in advance of the above final setting. Therefore, uncertainty of FGR is set as ( ).
- FGR at transient condition (Ramp data)

As noted above, the FINE code fission gas release model uniformly overpredicts the overpower ramp test FGR data. Additional confirmation of this conclusion is shown in Figures 4.3.2-3, 4.3.2-4, 4.3.2-5 and 4.3.2-6, which show the ramp test M/P ratios as a function of burnup, ramp terminal power level (Pmax), measured FGR and ramp hold time, respectively. None of these Figures show any systematic trends as a function of these parameters, and

therefore the FINE code fission gas release model is expected to uniformly give a conservative overprediction of the FGR in fuel integrity analyses of anticipated operational occurrences (AOOs).

Table 4.3.2-1 (1/7) Database for FGR

ID	Pellet Type	Gadolinia Content [wt%]	Ramp	Rod Average Burnup [GWd/t]	Measured FGR [%]	Predicted FGR [%]	M/P

Table 4.3.2-1 (2/7) Database for FGR

ID	Pellet Type	Gadolinia Content [wt%]	Ramp	Rod Average Burnup [GWd/t]	Measured FGR [%]	Predicted FGR [%]	M/P

Table 4.3.2-1 (3/7) Database for FGR

ID	Pellet Type	Gadolinia Content [wt%]	Ramp	Rod Average Burnup [GWd/t]	Measured FGR [%]	Predicted FGR [%]	M/P

Table 4.3.2-1 (4/7) Database for FGR

ID	Pellet Type	Gadolinia Content [wt%]	Ramp	Rod Average Burnup [GWd/t]	Measured FGR [%]	Predicted FGR [%]	M/P

Table 4.3.2-1 (5/7) Database for FGR

ID	Pellet Type	Gadolinia Content [wt%]	Ramp	Rod Average Burnup [GWd/t]	Measured FGR [%]	Predicted FGR [%]	M/P

Table 4.3.2-1 (6/7) Database for FGR

ID	Pellet Type	Gadolinia Content [wt%]	Ramp	Rod Average Burnup [GWd/t]	Measured FGR [%]	Predicted FGR [%]	M/P

Table 4.3.2-1 (7/7) Database for FGR

ID	Pellet Type	Gadolinia Content [wt%]	Ramp	Rod Average Burnup [GWd/t]	Measured FGR [%]	Predicted FGR [%]	M/P

Figure 4.3.2-1 M/P versus Rod Burnup

Figure 4.3.2-2 M/P against Measured FGR

Figure 4.3.2-3 M/P versus Rod Burnup for RAMP Rods

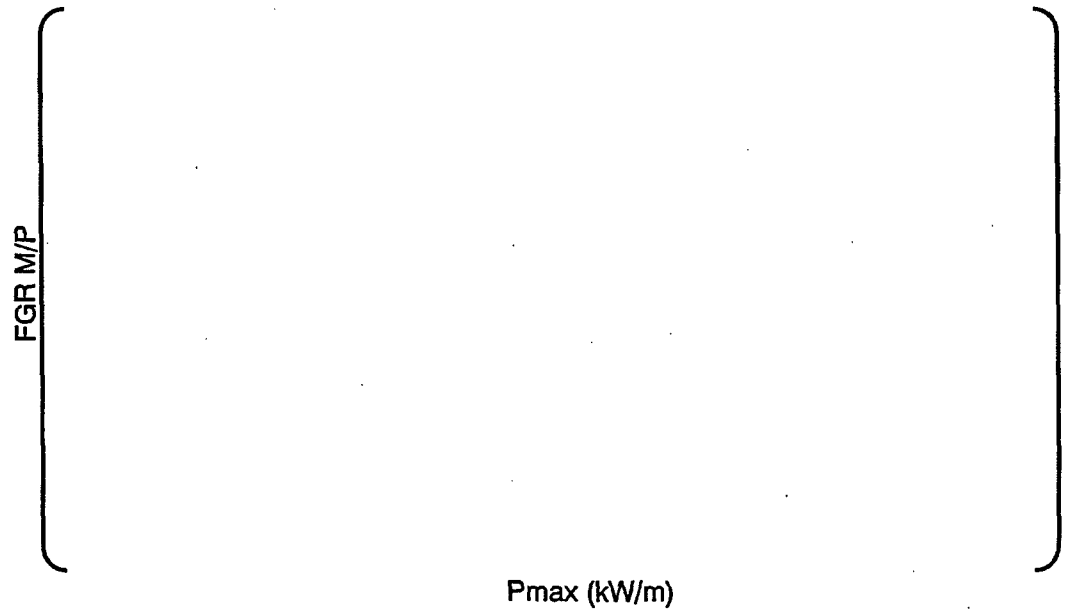

Figure 4.3.2-4 M/P versus Pmax for RAMP Rods

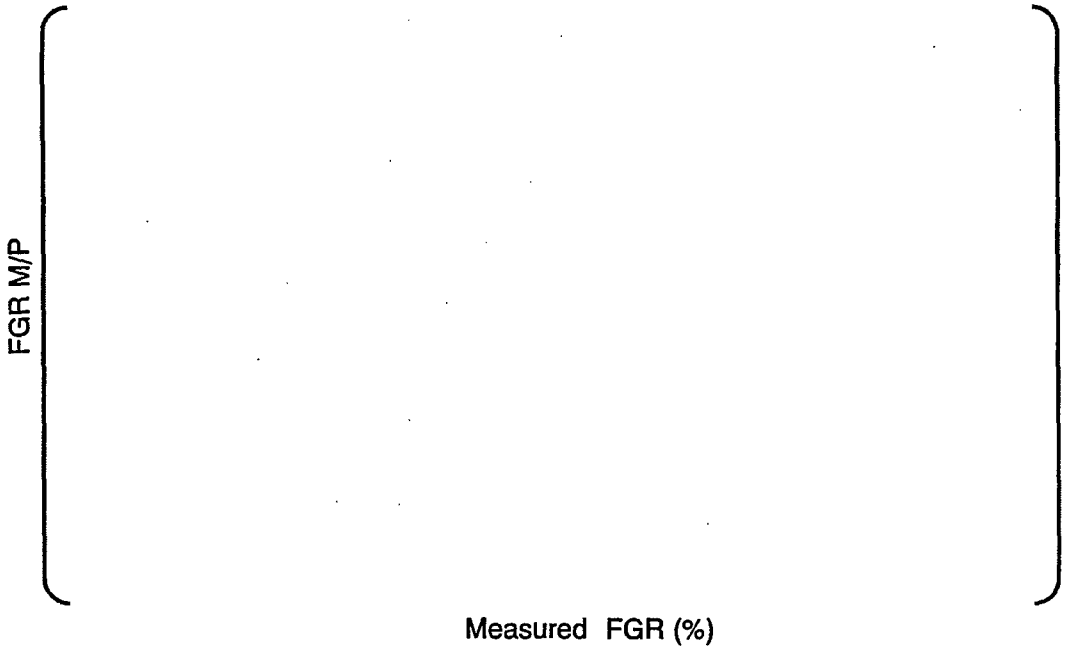

Figure 4.3.2-5 M/P versus M for RAMP Rods

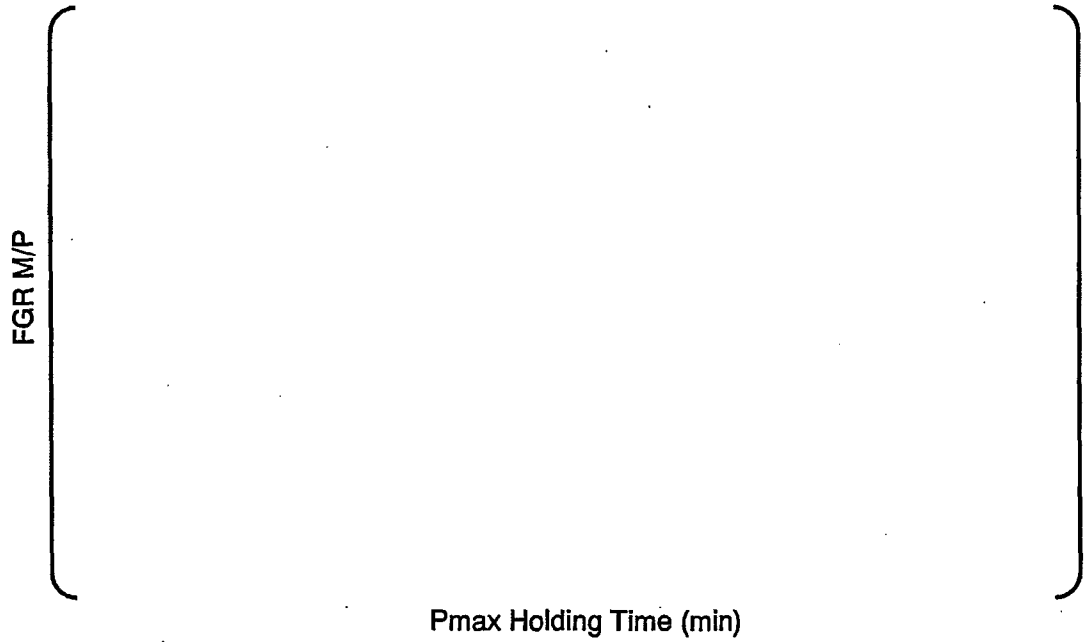

Figure 4.3.2-6 M/P versus Pmax Holding Time for RAMP Rods

4.3.3 Pellet Density Change

Pellet density is calculated regarding pellet densification, swelling and gas bubble swelling as described before. The calculated density is compared with the measured data in Table 4.3.3-1. In order to confirm parameter dependency of the prediction, M-P is plotted against burnup, and density change in Figure 4.3.3-1, and Figure 4.3.3-2 respectively. No clear tendency is found in these figures. FINE code model properly calculates the pellet density.
The pellet density change is calculated using the pellet densification, solid fission product swelling, gas bubble swelling and RIM porosity models described in Section 4.2. The database used for validation of the FINE code pellet density change models is summarized in Table 4.3.3-1.

Figures 4.3.3-1 and 4.3.3-2 are plots of the pellet density change M - P versus burnup and the measured pellet density change, respectively. Both plots show that there is no systematic bias in the FINE code pellet density change predictions.

All the data in Table 4.3.3-1, and for all the data in Table 4.3.3-1 that meets the current MHI pellet fabrication specifications are summarized.
For all the data :

Number of data	:	[ ]
M-P average	:	[ ]
M-P standard deviation	:	[ ]

For the data that meets the current MHI pellet fabrication specification, selected by the following criteria:

[ ]

Number of data	:	[ ]
M-P average	:	[ ]
M-P standard deviation	:	[ ]

Table 4.3.3-1 (1/4) Database for Pellet Density Change

ID	Pellet Type	Measured Initial Density [%T.D.]	Gadolinia Content [wt%]	Rod Average Burnup [GWd/t]	Local Burnup [GWd/t]	Measured Volume Change [%]	Predicted Volume Change [%]	M−P [%]

Table 4.3.3-1 (2/4) Database for Pellet Density Change

ID	Pellet Type	Measured Initial Density [%T.D.]	Gadolinia Content [wt%]	Rod Average Burnup [GWd/t]	Local Burnup [GWd/t]	Measured Volume Change [%]	Predicted Volume Change [%]	M−P [%]
[redacted]								

Table 4.3.3-1 (3/4) Database for Pellet Density Change

ID	Pellet Type	Measured Initial Density [%T.D.]	Gadolinia Content [wt%]	Rod Average Burnup [GWd/t]	Local Burnup [GWd/t]	Measured Volume Change [%]	Predicted Volume Change [%]	M−P [%]

Table 4.3.3-1 (4/4) Database for Pellet Density Change

ID	Pellet Type	Measured Initial Density [%T.D.]	Gadolinia Content [wt%]	Rod Average Burnup [GWd/t]	Local Burnup [GWd/t]	Measured Volume Change [%]	Predicted Volume Change [%]	M−P [%]

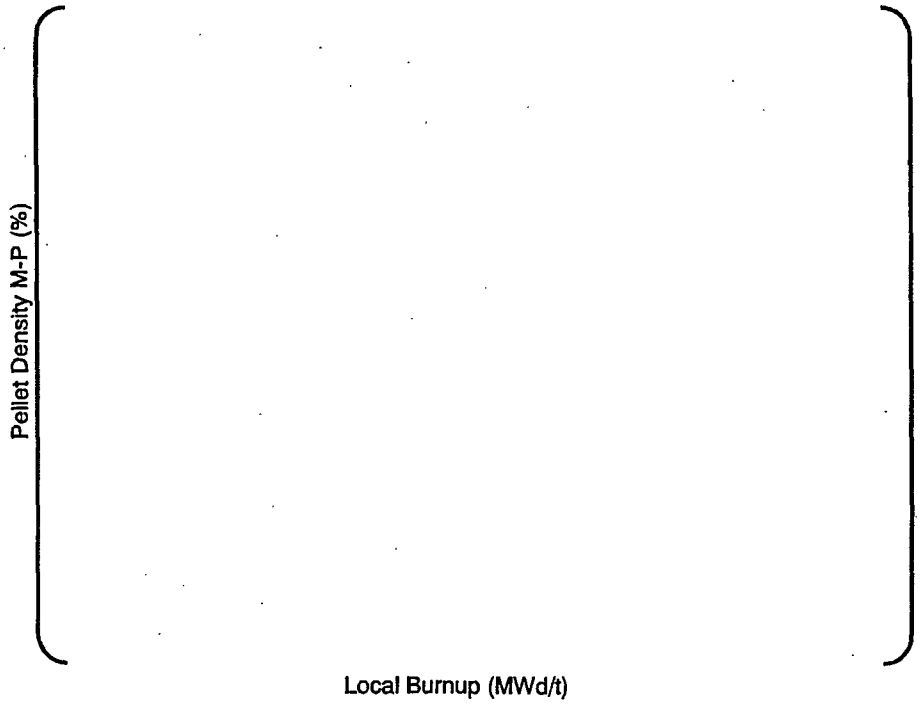

Figure 4.3.3-1 M-P versus Burnup of Pellet Density Change

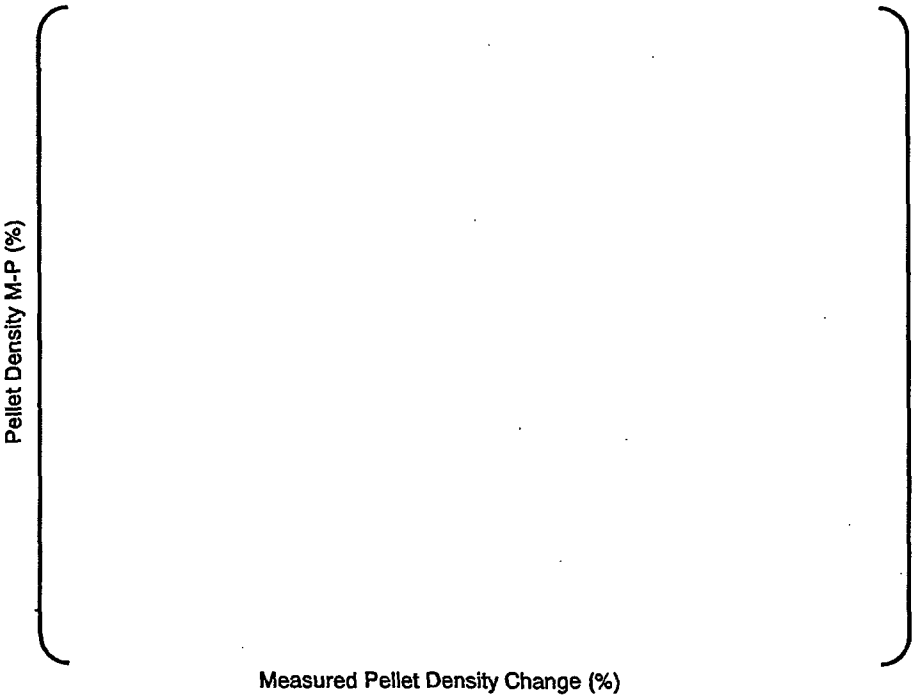

Figure 4.3.3-2 M-P versus Measured Pellet Density Change

4.3.4 Helium

The Helium in the rod void volume is calculated using the Helium generation, release and absorption models described in Section 4.2. The database used for validation of the FINE Helium models is summarized in Table 4.3.4-1. The measured Helium data are the results obtained in post-irradiation examinations for the total Helium in the rod void volume at end-of-life (EOL).

Figure 4.3.4-1 and 4.3.4-2 are plots of the EOL Helium M/P ratios versus burnup and the initial rod Helium pressure, respectively. The FINE code well demonstrates the measured data. As noted in Section 4.2., a slight overprediction is seen at EOL.

The uncertainty at a 95% probability at a 95% confidence leves is derived with( ) { }data in Table 4.3.4-1 which covers the pellet density more than { }and the initial helium pressure from( )

Number of data	( )
M/P average	( )
M/P standard deviation	( )
Uncertainty	
Upper Bound	( )

Uncertainty for Helium model is set as { }for upper bound with a small margin.

Table 4.3.4-1(1/5) Helium Mol Database

ID	Pellet Type	Gadolinia Content [wt%]	Initial Helium Pressure [psi]	Ramp	Rod Average Burnup [GWd/t]	Measured He-mol [mol]	Predicted He-mol [mol]	M/P

Table 4.3.4-1(2/5) Helium Mol Database

ID	Pellet Type	Gadolinia Content [wt%]	Initial Helium Pressure [psi]	Ramp	Rod Average Burnup [GWd/t]	Measured He-mol [mol]	Predicted He-mol [mol]	M/P

Table 4.3.4-1(3/5) Helium Mol Database

ID	Pellet Type	Gadolinia Content [wt%]	Initial Helium Pressure [psi]	Ramp	Rod Average Burnup [GWd/t]	Measured He-mol [mol]	Predicted He-mol [mol]	M/P

Table 4.3.4-1(4/5) Helium Mol Database

ID	Pellet Type	Gadolinia Content [wt%]	Initial Helium Pressure [psi]	Ramp	Rod Average Burnup [GWd/t]	Measured He-mol [mol]	Predicted He-mol [mol]	M/P

Table 4.3.4-1(5/5) Helium Mol Database

ID	Pellet Type	Gadolinia Content [wt%]	Initial Helium Pressure [psi]	Ramp	Rod Average Burnup [GWd/t]	Measured He-mol [mol]	Predicted He-mol [mol]	M/P

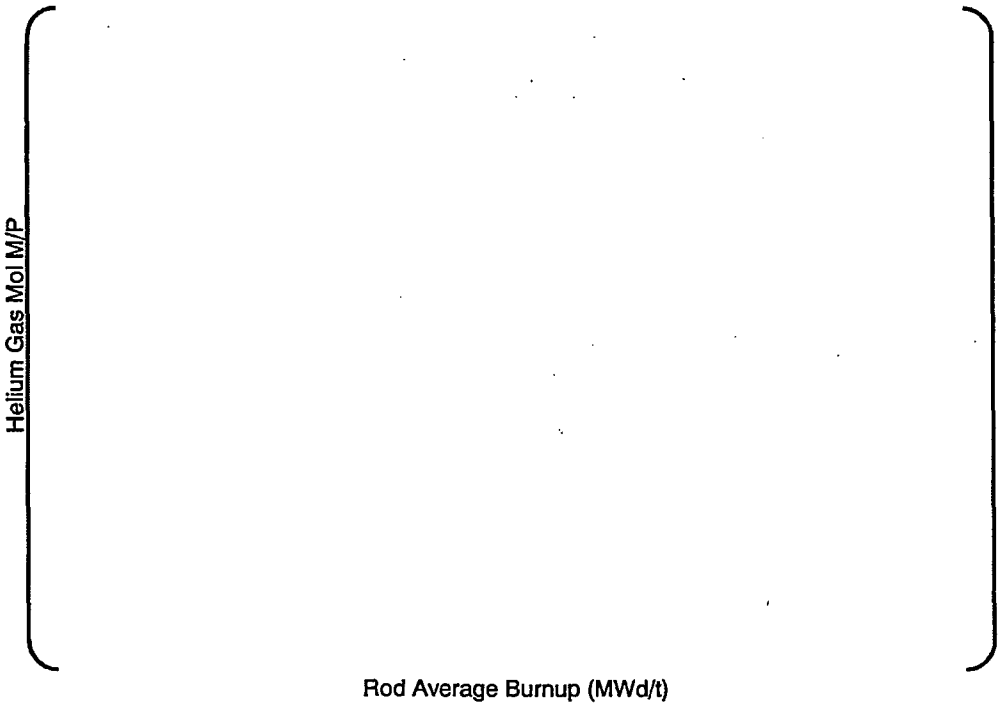

Figure 4.3.4-1 M/P of Helium Mol versus Burnup

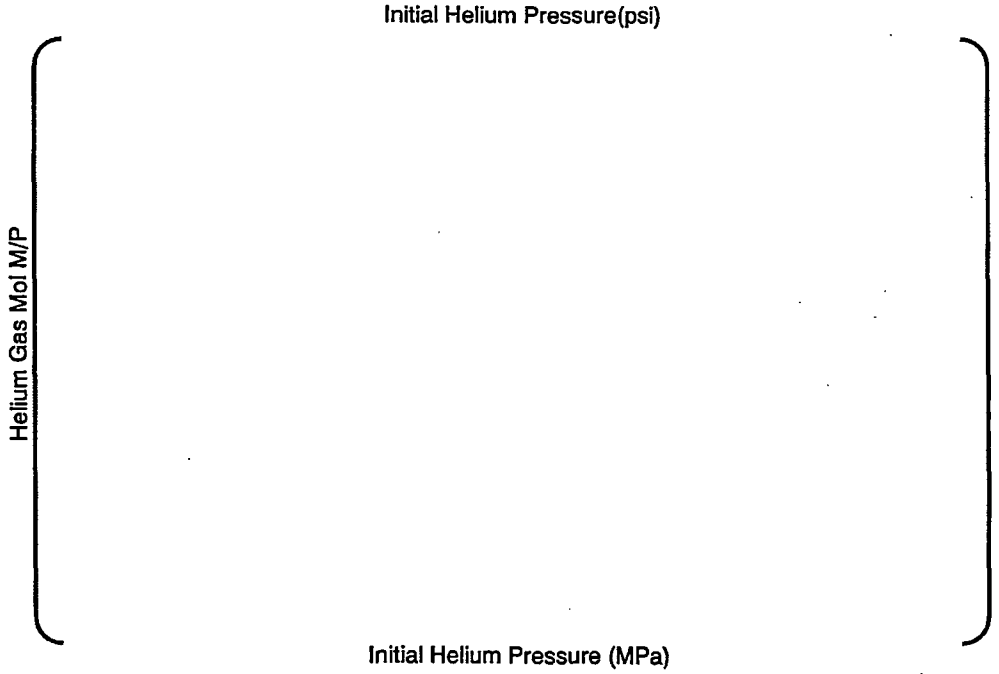

Figure 4.3.4-2 M/P of Helium Mol versus Initial Helium Pressure

4.3.5 Corrosion

The cladding corrosion models have been validated by comparison with an extensive database of cladding corrosion measurements for ZIRLO™, Zircaloy-4 and low tin Zircaloy-4 cladding. The database is summarized in Table 4.3.5-1. All the ZIRLO™ data have been obtained by ECT measurements, which have been well qualified by comparison with metallographic measurements of the oxide layer thickness.

Much of these data were obtained in on-site measurement campaigns in the spent fuel pits of the Nuclear Power Plants. Some of the measurement campaigns measured the oxide thickness for only one circumferential orientation of the rod, while others measured the oxide thickness for several circumferential orientations. The peak oxide thickness data given in Table 4.3.5-1 are the axial peak oxide thickness from the ECT measurements if the oxide thickness was measured at only one circumferential orientation, or the peak of the axial and circumferential measurements if the data were obtained for more than one circumferential orientation.

Figures 4.3.5-1 and 4.3.5-2 are plots of the oxide thickness M - P versus rod average burnup and the oxide thickness, respectively. Both plots show that there is no systematic bias in the FINE code oxide thickness predictions. The FINE code results agree well with the measured data for ZIRLO™ and low Tin Zircaloy-4, and tend to overpredict the Zircaloy-4 peak oxide thickness data.

As described in Section 4.2.4, the ZIRLO™ and low Tin Zircaloy-4 corrosion models are based on the Zircaloy-4 model, with modification of the WB (second transition point), A (corrosion rate adjustment factor) and Fp factors, where Fp is the circumferential peak-to-average ratio. The values of these constants for the different cladding materials are:

Zircaloy-4	[ ]
Low Tin Zircaloy-4	[ ]
ZIRLO™	[ ]

The model uncertainties have been determined using the ZIRLO™ data with measured oxide thicknesses[ ] The results for the uncertainties at a 95% probability at a 95% confidence level are:

The uncertainty is calculated with the data[ ] of the oxide thickness .

Number of data	[ ]
M-P average	[ ]
M-P standard deviation	[ ]
Uncertainty	
Upper Bound	[ ]

The uncertainty of ZIRLO™ corrosion model is conservatively set as [ ], which is the same value for Zircaloy-4 model.

Table 4.3.5-1(1/2) Summary of Corrosion Database

ID	Rod Average Burnup [GWd/t]	Measured Peak Oxide Thickness [mil]	Predicted Peak Oxide Thickness [mil]	(M-P) Peak Oxide Thickness [mil]

Table 4.3.5-1(2/2) Summary of Corrosion Database

ID	Rod Average Burnup [GWd/t]	Measured Peak Oxide Thickness [mil]	Predicted Peak Oxide Thickness [mil]	(M-P) Peak Oxide Thickness [mil]

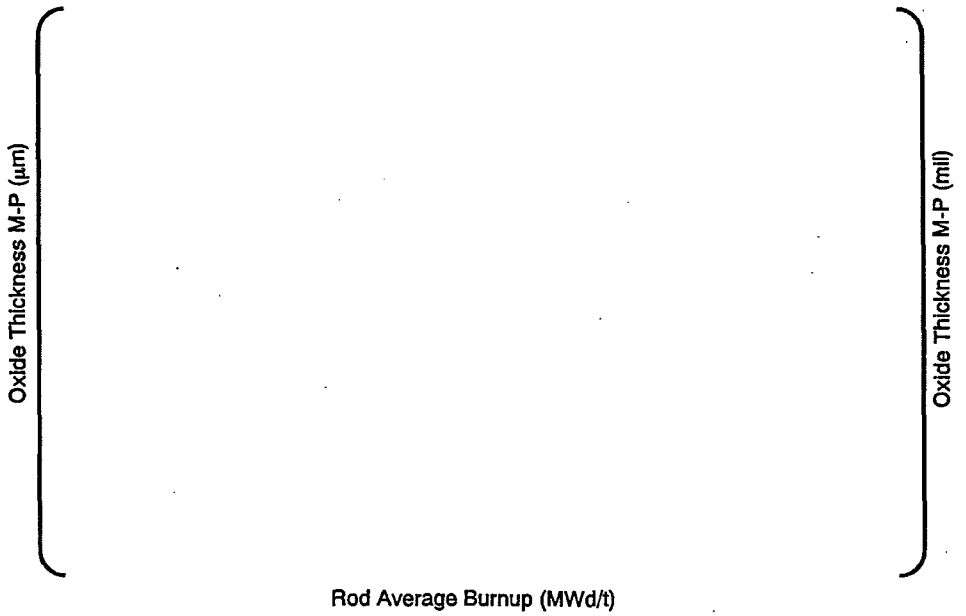

Figure 4.3.5-1 M-P versus Rod Average Burnup (Oxide Thickness)

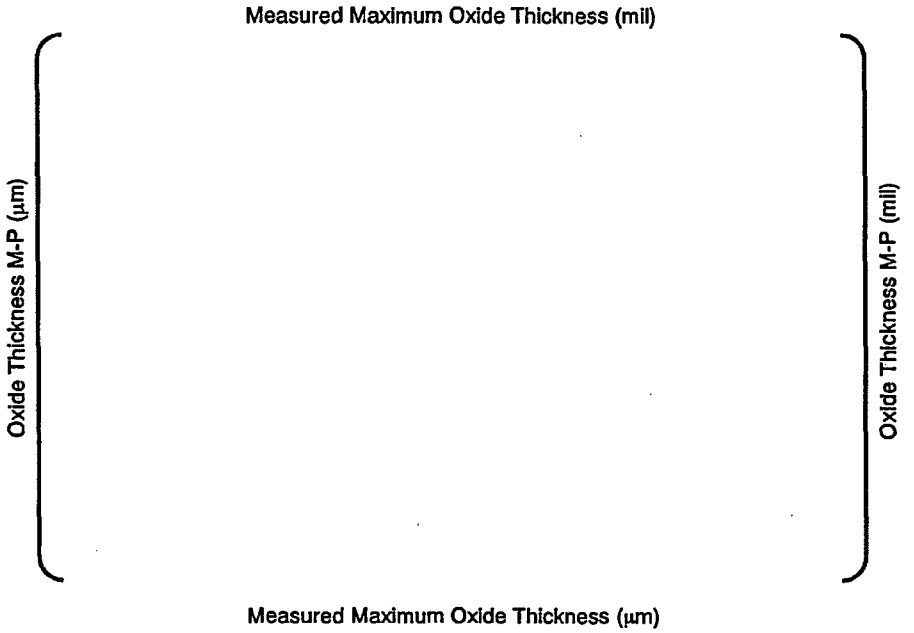

Figure 4.3.5-2 M-P versus Maximum(Peak) Oxide Thickness

4.3.6 Hydrogen

The cladding hydrogen pickup model has been validated using the data in Table 4.3.6-1. Figure 4.3.6-1 and Figure 4.3.6-2 show the hydrogen pickup M - P results as a function of rod burnup and the measured hydrogen content, respectively. At lower burnup and/or lower hydrogen content, prediction seems to give the underestimation of the hydrogen content. But the measurement tends to scatter with the low hydrogen content. No clear tendency is found in both figures. Figure 4.2.4.2-1 (mentioned in 4.2) gives the larger scatter at the lower hydrogen content and unstable hydrogen pickup rate. From a point of designing, higher hydrogen content is of interest.

As described in 4.2, the hydrogen pickup is calculated based on the corrosion model and hydrogen pickup rate derived from the measured data. The corrosion model is originally developed for Zircaloy-4 and the accommodation factors are applied for low Tin Zircaloy-4 and ZIRLO™. The hydrogen model prediction in Figure 4.3.6-1 and 4.3.6-2 gives that the hydrogen model predicts well the data over the entire range of the data, from 0 to 800 ppm hydrogen content.

Uncertainty is calculated with the data more than ( ) of hydrogen content which is approximately corresponding to hydrogen solubility limit at around operation temperature.

Number of data	:	( )
M-P average	:	
M-P standard deviation	:	
Uncertainty		
Upper Bound	:	

Uncertainty of hydrogen content is conservative set as ( ) which is the same value applied to Zircaloy-4.

Table 4.3.6-1 Summary of Hydrogen Content Database

ID	Rod Average Burnup [GWd/t]	Measured Oxide Thickness [mil]	Predicted Hydrogen Content [ppm]	Measured Hydrogen Content [ppm]	M-P [ppm]

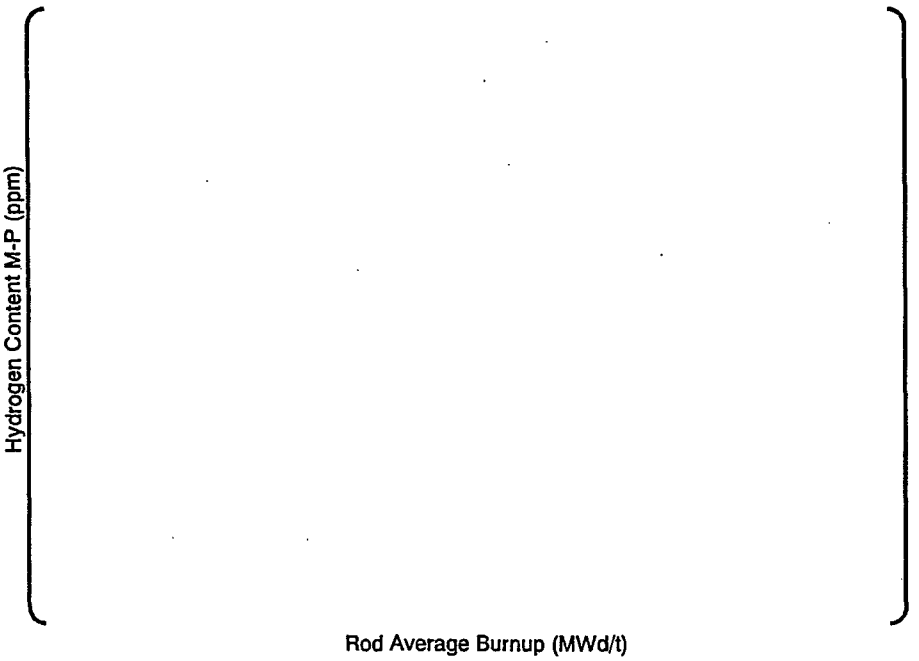

Figure 4.3.6-1 (M-P) versus Rod Average Burnup (Hydrogen Content)

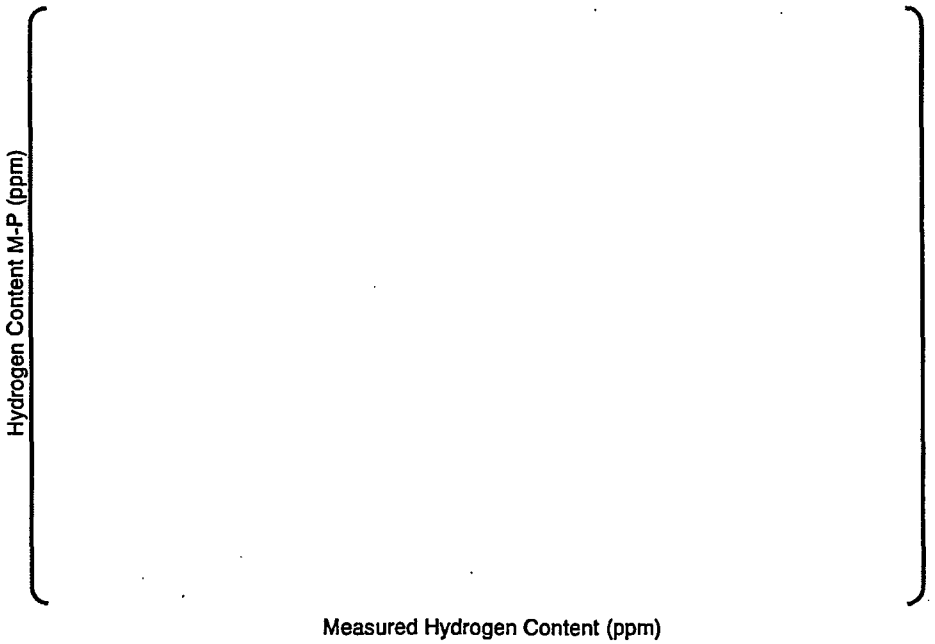

Figure 4.3.6-2 (M-P) versus Measured Hydrogen Content

4.3.7 Rod Growth

The database used for verifiation of the FINE rod growth model for ZIRLO™ cladding is given in Table 4.3.7-1. Figure 4.3.7-1 and Figure 4.3.7-2 show the rod growth M/P values as a function of fast fluence and the measured rod growth, respectively. The scatter in the M/P results is largest at low fluences and low measured rod growth, where the need to measure comparatively small length changes leads to larger variability in the measurement results. The scatter is smaller for the larger measured growth values, which are the data most relevant to fuel rod integrity evaluations. In this sense, ZIRLO™ model provides proper prediction.

To eliminate excessive conservatism due to the difficulty of making the rod growth measurements at low fluences, the FINE rod growth model uncertainties have been determined using the data for fast fluences greater than( ) n/cm^2:

Uncertainty is calculated at a 95% probability at a 95% confidence level.

Number of data	: ( )
M/P average	: ( )
M/P standard deviation	: ( )
Uncertainty	
Upper Bound	: ( )
Lower Bound	: ( )

Uncertainty of growth model is conservatively set to( ) for upper bound and( )for lower bound, which is the same value applied to Zircaloy-4.

Table 4.3.7-1(1/13) Summary of Rod Growth Database

ID	Rod Average Burnup [GWd/t]	Fast Neutron Fluence [>1MeV,n/cm^2]	Measured Rod Growth ΔL/L [%]	Predicted Rod Growth ΔL/L [%]	M/P

Table 4.3.7-1(2/13) Summary of Rod Growth Database

ID	Rod Average Burnup [GWd/t]	Fast Neutron Fluence [>1MeV,n/cm^2]	Measured Rod Growth ΔL/L [%]	Predicted Rod Growth ΔL/L [%]	M/P

Table 4.3.7-1(3/13) Summary of Rod Growth Database

ID	Rod Average Burnup [GWd/t]	Fast Neutron Fluence [>1MeV,n/cm^2]	Measured Rod Growth ΔL/L [%]	Predicted Rod Growth ΔL/L [%]	M/P

Table 4.3.7-1(4/13) Summary of Rod Growth Database

ID	Rod Average Burnup [GWd/t]	Fast Neutron Fluence [>1MeV,n/cm^2]	Measured Rod Growth ΔL/L [%]	Predicted Rod Growth ΔL/L [%]	M/P

Table 4.3.7-1(5/13) Summary of Rod Growth Database

ID	Rod Average Burnup [GWd/t]	Fast Neutron Fluence [>1MeV,n/cm^2]	Measured Rod Growth ΔL/L [%]	Predicted Rod Growth ΔL/L [%]	M/P

Table 4.3.7-1(6/13) Summary of Rod Growth Database

ID	Rod Average Burnup [GWd/t]	Fast Neutron Fluence [>1MeV,n/cm^2]	Measured Rod Growth ΔL/L [%]	Predicted Rod Growth ΔL/L [%]	M/P

Table 4.3.7-1(7/13) Summary of Rod Growth Database

ID	Rod Average Burnup [GWd/t]	Fast Neutron Fluence [>1MeV,n/cm^2]	Measured Rod Growth ΔL/L [%]	Predicted Rod Growth ΔL/L [%]	M/P

Table 4.3.7-1(8/13) Summary of Rod Growth Database

ID	Rod Average Burnup [GWd/t]	Fast Neutron Fluence [>1MeV,n/cm^2]	Measured Rod Growth ΔL/L [%]	Predicted Rod Growth ΔL/L [%]	M/P

Table 4.3.7-1(9/13) Summary of Rod Growth Database

ID	Rod Average Burnup [GWd/t]	Fast Neutron Fluence [>1MeV,n/cm^2]	Measured Rod Growth ΔL/L [%]	Predicted Rod Growth ΔL/L [%]	M/P

Table 4.3.7-1(10/13) Summary of Rod Growth Database

ID	Rod Average Burnup [GWd/t]	Fast Neutron Fluence [>1MeV,n/cm^2]	Measured Rod Growth ΔL/L [%]	Predicted Rod Growth ΔL/L [%]	M/P

Table 4.3.7-1(11/13) Summary of Rod Growth Database

ID	Rod Average Burnup [GWd/t]	Fast Neutron Fluence [>1MeV,n/cm^2]	Measured Rod Growth ΔL/L [%]	Predicted Rod Growth ΔL/L [%]	M/P

Table 4.3.7-1(12/13) Summary of Rod Growth Database

ID	Rod Average Burnup [GWd/t]	Fast Neutron Fluence [>1MeV,n/cm^2]	Measured Rod Growth ΔL/L [%]	Predicted Rod Growth ΔL/L [%]	M/P

Table 4.3.7-1(13/13) Summary of Rod Growth Database

ID	Rod Average Burnup [GWd/t]	Fast Neutron Fluence [>1MeV,n/cm^2]	Measured Rod Growth ΔL/L [%]	Predicted Rod Growth ΔL/L [%]	M/P
[ ]					

Figure 4.3.7-1 M/P versus Fluence (Rod Growth)

Figure 4.3.7-2 M/P versus Measured Rod Growth

4.3.8 Creep

The FINE creep model for ZIRLO™ cladding has been validated with rod profilometry data obtained from the database summarized in Table 4.2.4.4-1. Only data prior to pellet-cladding contact has been used in the model validation, since the rod profilometry after pellet-cladding contact is principally determined by the pellet diameter changes rather than by the cladding creep model.. Comparison of measured and calculated creep is made against rod axial position in Figure 4.3.8-1. There is no clear dependency against axial position. This indicates that the thermal and irradiation creep valance is proper.
Uncertainty of the creep model is calculated without segmented rods (short rods) and bottom and top span (schewed profile) at a 95% probability at a 95% confidence level. The data with pellet-cladding contact are excluded.

Number of data	: [ ]
M/P average	: [ ]
M/P standard deviation	: [ ]
Uncertainty	
Upper Bound	: [ ]
Lower Bound	: [ ]

The uncertainty width of creep model is set as [ ] with small conservatism. Therefore, uncertainty of creep model is [ ] for lower bound and [ ] for upper bound.
Examples of the comparison between the data and the FINE code predictions for the rod profilometry subsequent to pellet-cladding contact are shown in Figures 4.3.8-2, 4.3.8-3 and 4.3.8-4.

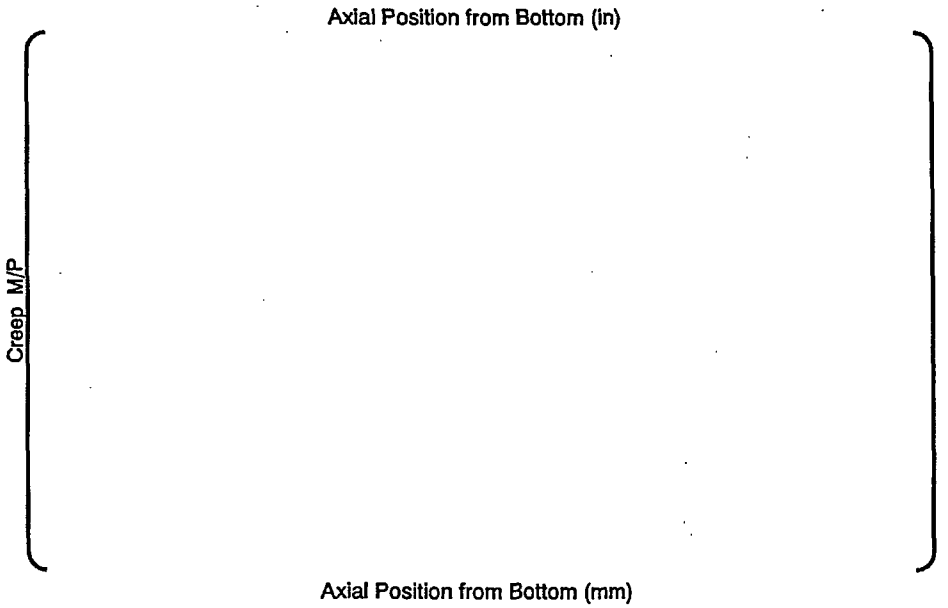

Figure 4.3.8-1 Creep M/P versus Axial Position

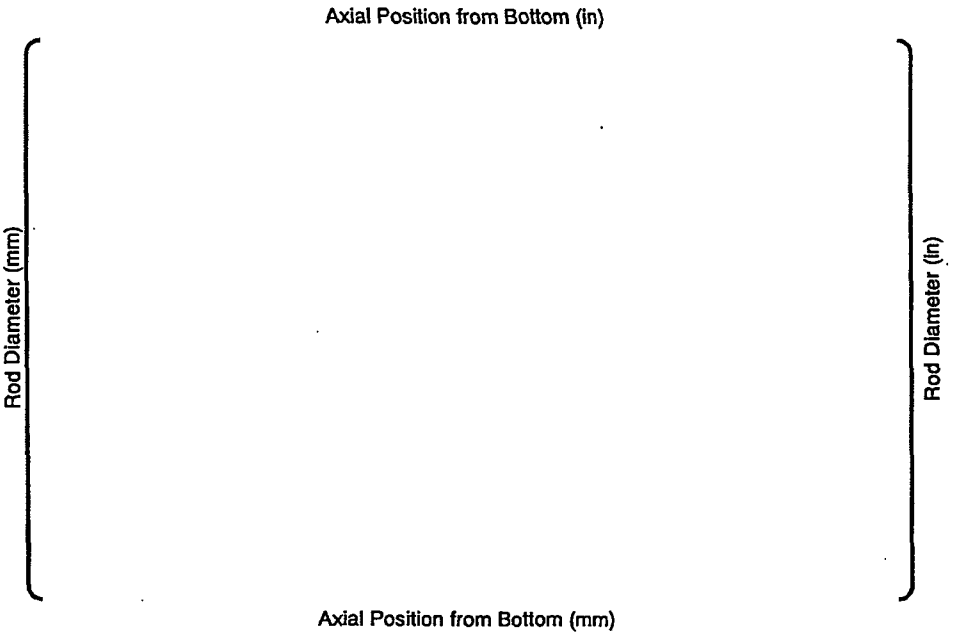

Figure 4.3.8-2 Comparison of Measured and Calculated Cladding Diameter after Pellet-Cladding Contact at Higher Burnup (Segment Rod)

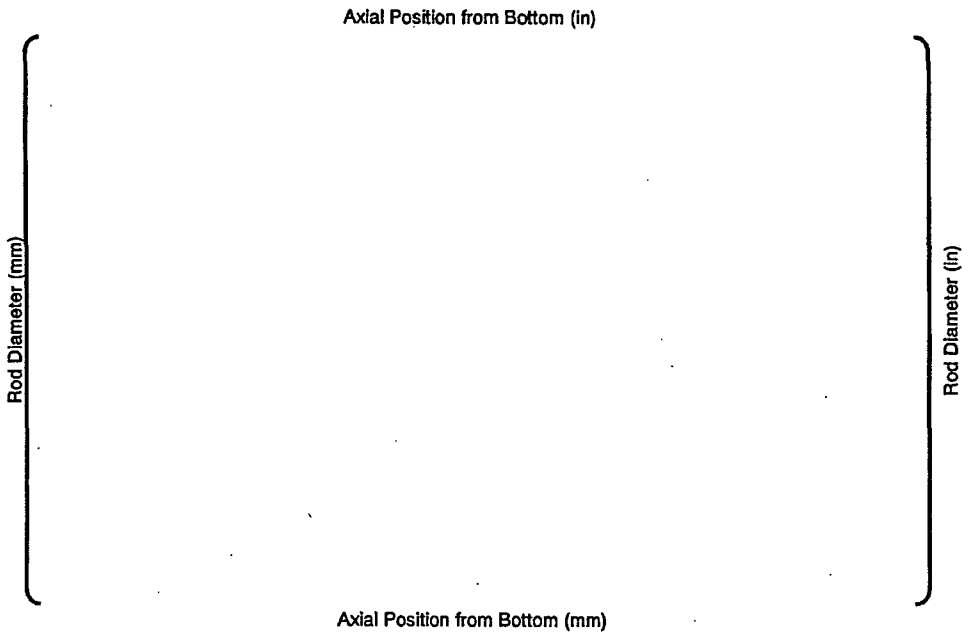

Figure 4.3.8-3 Comparison of Measured and Calculated Cladding Diameter after Pellet-Cladding Contact at Higher Burnup (UO_2 Rod)

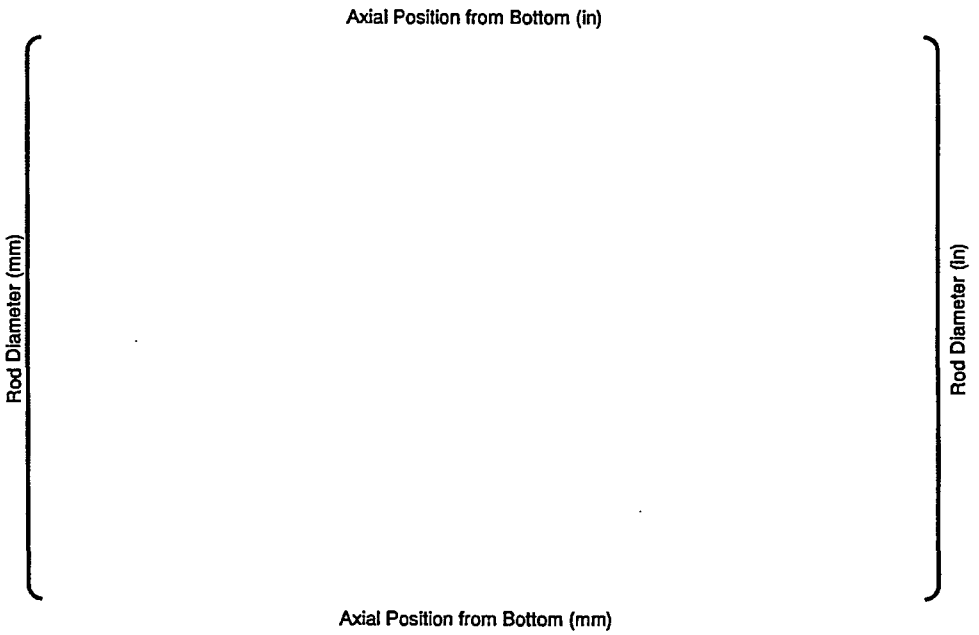

Figure 4.3.8-4 Comparison of Measured and Calculated Cladding Diameter after Pellet-Cladding Contact at Higher Burnup (10wt% Gd Rod)

4.3.9 Void Volume

Void volume provides the integral view of the models of pellet density, cladding creep and rod growth. Figure 4.3.9-1 compares the measured void volume with calculated one versus burnup. No clear dependency is observed as a function of burnup. Therefore, FINE code properly calculates void volume.

Figure 4.3.9-1 Void Volume M/P versus Burnup

4.3.10 Rod Internal Pressure

Figures 4.3.10-1, 4.3.10-2 and 4.3.10-3 show the rod internal pressure M/P ratios plotted versus rod burnup, the measured rod internal pressure and the fission gas release, respectively. These results show that the integrated FINE fuel rod performance models for fission gas release, pellet densification and swelling, cladding creep, rod growth, etc., give an excellent prediction of the fuel rod performance for a wide ranging database of prototypical PWR fuel rods, including rods with Gadolinium doped fuel and rods that have experienced an overpower test.

Figure 4.3.10-1 M/P versus Burnup

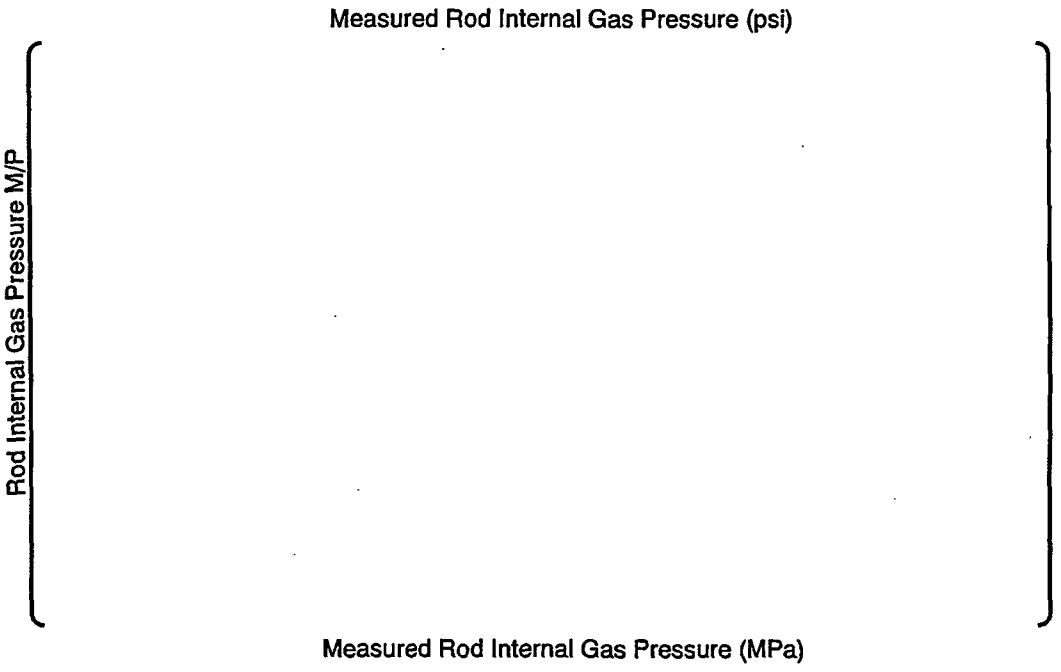

Figure 4.3.10-2 M/P versus Measured Rod Internal Pressure

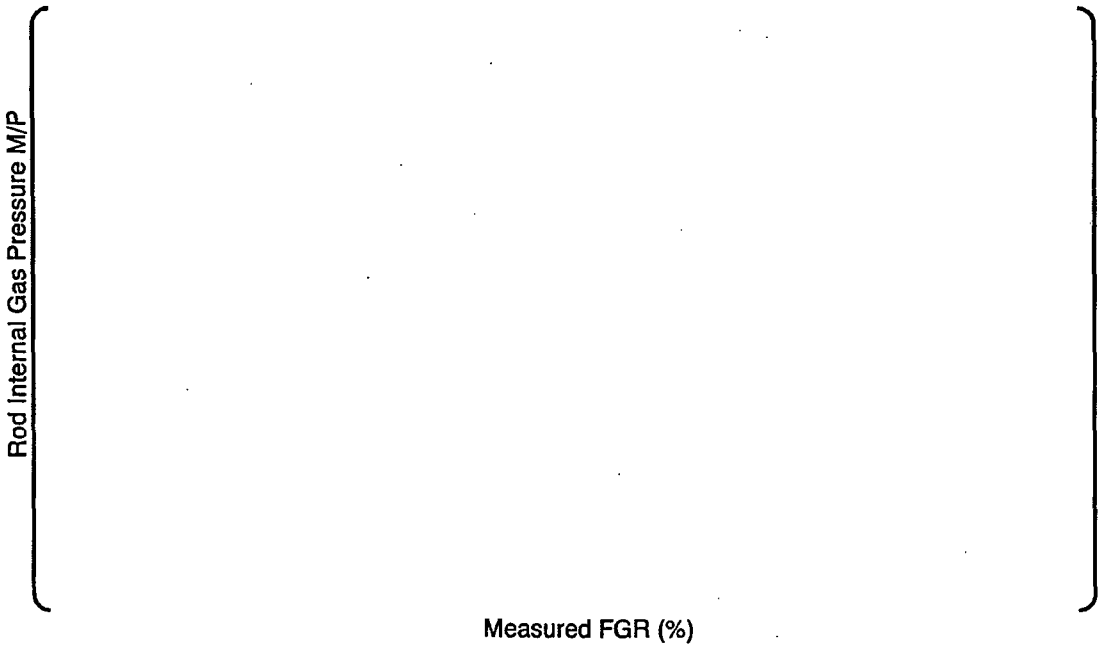

Figure 4.3.10-3 M/P versus FGR

4.3.11 Transient Calculation

FINE code is applied for the fuel integrity evaluation under Anticipated Operational Occurrences (AOOs). At the high power, cladding is deformed according to the dimension change of pellets. Thermal expansion and gas bubble swelling is driving force for this dimension change.

Pellet density change is direct measurement to confirm the validity of gas bubble swelling model of the code. Cladding diameter change before and after ramp test is another measurement to do indirectly. However cladding diameter change is a direct indicator to show strain.

Here, FINE code calculation is compared with the diameter change measurements before and after ramp tests the representative tests.

	WZ-I24 [29]	WZ-I22 [29]
Burnup	29.5 GWd/t	30.5 GWd/t
Pre-conditioning level	8.1 kW/ft (26.5 kW/m)	8.1 kW/ft (26.7kW/m)
Ramp terminal level (RTL)	12.5 kW/ft (40.9 kW/m)	12.0 kW/ft (39.4 kW/m)
Power change	4.4 kW/ft (14.4 kW/m)	3.9 kW/ft (12.7 kW/m)
Holding time at RTL	6 hours	

Figure 4.3.11-1 and Figure 4.3.11-2 show the comparison result of rod diameter before and after ramp test. FINE code demonstrates the diameter change before and after ramp well. This indicates that pellet models such as thermal expansion and gas bubble swelling are valid.

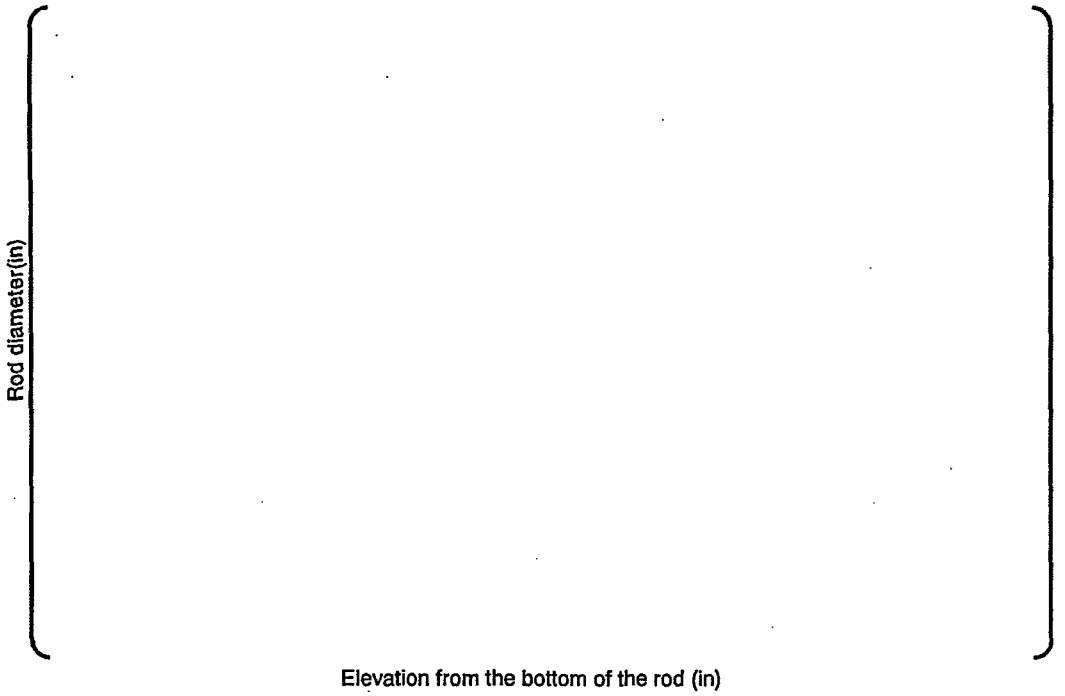

Figure 4.3.11-1 Diameter Change Comparison for Segment Fuel with ZIRLO™ (WZ-I24)

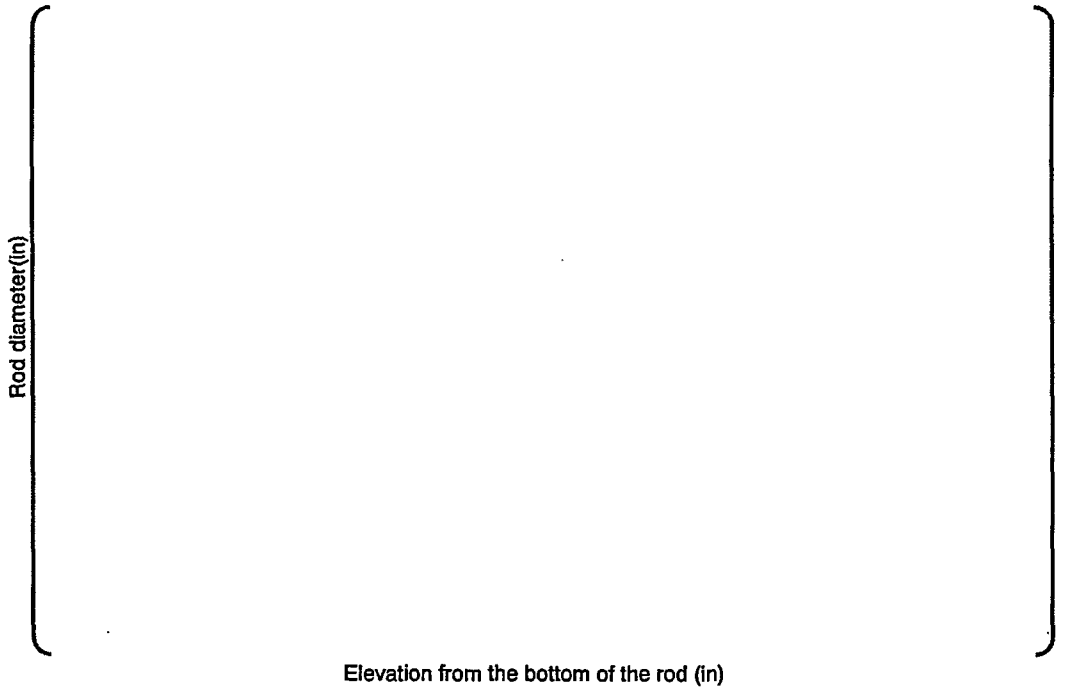

Figure 4.3.11-2 Diameter Change Comparison for Segment Fuel with ZIRLO™ (WZ-I22)

4.4 Validation of the FINE Code

PNNL provides FRAPCON-3 code and FRAPCON-3 has been used for benchmarking of vender's own calculation codes.
NUREG/CR-6534 Volume 3 PNNL-11513[43] shows the benchmark cases for code verification. Some of the results in this report are re-calculated by the further developed version of FRAPCON-3.3 code[44] . Mitsubishi made the FINE input of some benchmark cases from the document information in the reference[43]. The FINE output is compared with that of FRAPCON-3.3 code in the reference[44]. To make possible to follow the benchmark calculations of the FINE code, the inputs are listed in detailed in this section.

4.4.1 Selection of Benchmark Cases

A variety of the benchmark cases are reported in NUREG/CR-6534 Vol. 3[43]. Some of them are reported again in Vol. 4 [44] with the revised FRAPCON3 result. There is few information of the benchmark case input in Vol.4, therefore the information from Vol.3 is essential to perform the FINE calculation.
The common cases both for Vol.3 and Vol.4 are selected for the benchmarking of the FINE code. The following benchmark cases are selected among the common cases.

- Fuel Temperature
  - HUHB (IFA-562 rod 18) : The sister rod of rod 17 is already verified in Section 4.3.
  - IFA-432 Rod 3
- Fission Gas Release
  - BR3 2416, 3618, 11115, 2816, 3018 : Already shown in Section 4.3.
  - IFA-429 DH
  - Oconee-1 PWR 15309

Other rods in the common cases are not included in this benchmarking, mainly because of lack of information.

4.4.2 Benchmark Results

In this sub-section, the benchmarking results for the above selected cases are described.

4.4.2.1 IFA-562 Rod 18

Most of input for the FINE calculation is obtained from the reference[43] except for the power distribution within the pellet. The power distribution is calculated taking into account for heavy water conditions. It is the same as that used for IFA-562 rod 17. Input data are summarized in Table 4.4.2.1-1 and Figure 4.4.2.1-1.

The calculated result of the FINE code is compared with the measured data and the FRAPCON-3.3 prediction in Figure 4.4.2.1-2. The FINE code provides the conservative predictions versus the measured data and the FRAPCON result through the irradiation.

In order to see the burnup degradation effect, gap conductance is adjusted to fit the data at the beginning of the irradiation by changing the effective pellet-cladding gap. The result is shown in Figure 4.4.2.1-3. The FINE code result shows the higher temperature even though the gap conductance is adjusted ([ ] thermal calculation is assumed).

This indicates the degradation effect is somewhat larger than the measurement and the FRAPCON-3.3 result, because the fuel temperature is not so high as the corresponding temperature of onset of the significant fission gas release. This means gap conductance change due to fission gas release would not be significant. When it is roughly assumed that temperature is described by the contributions of gap conductance, rod power and thermal conductivity of the pellet, the gap conductance and rod power would not be the factor to make differences in the comparison of the measurement, FRAPCON-3.3 and FINE. Therefore, temperature change with burnup is the effect of the thermal conductivity degradation.

Table 4.4.2.1-1 Input Data Summary

Input Items	HALDEN Ultra Hi/Bu IFA-562 Rod 18	unit	Reference *1

Table 4.4.2.1-2 Axial Profile

	Axial position (relative)

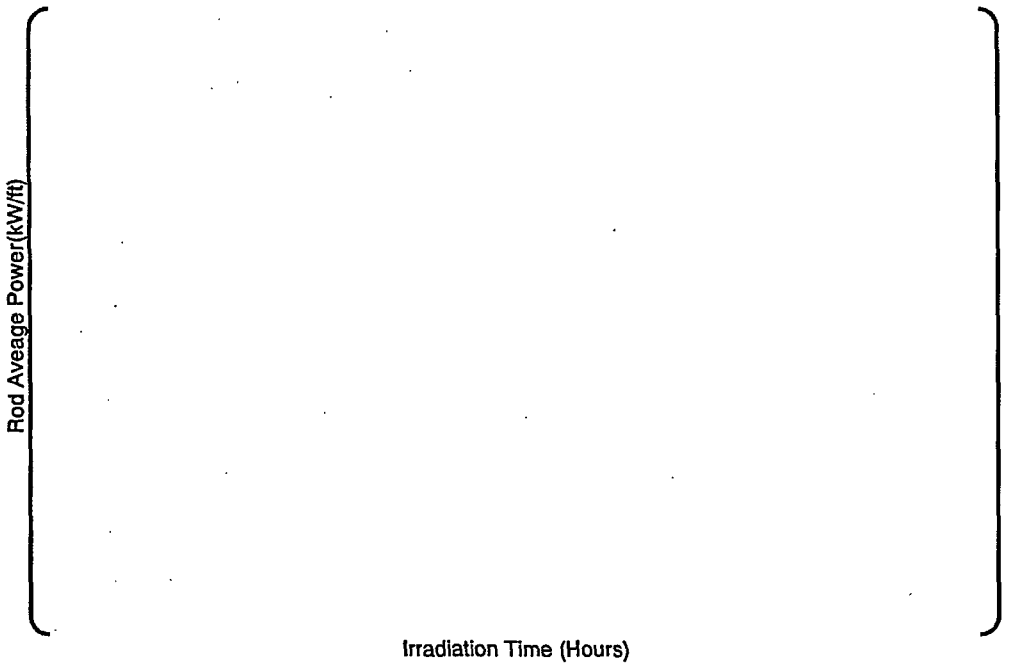

Figure 4.4.2.1-1 Power History of IFA-562 Rod 18

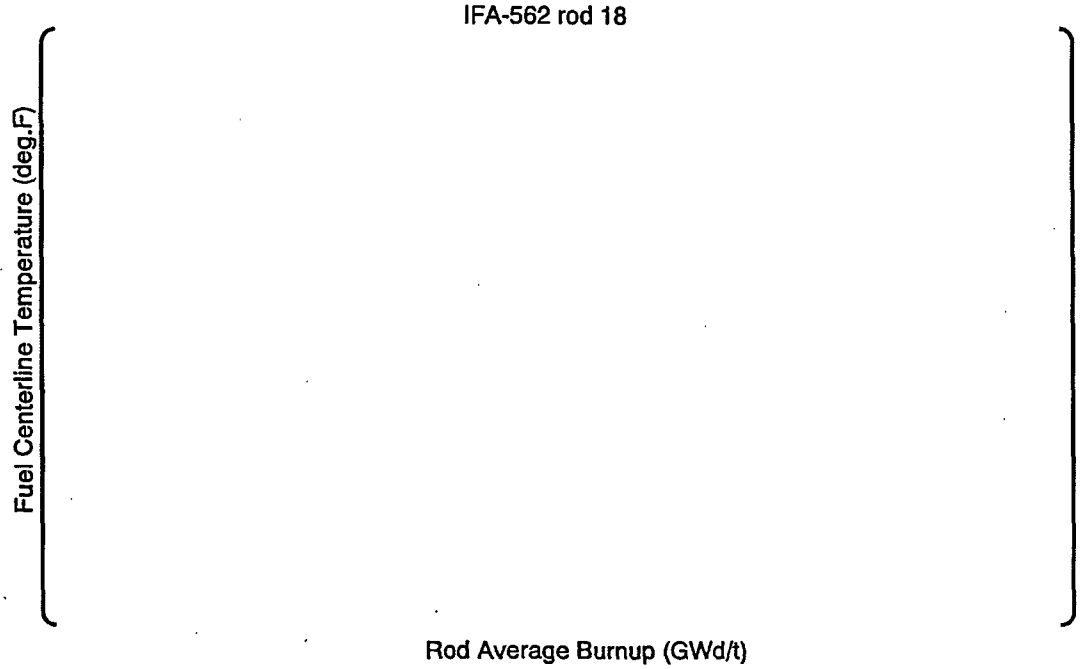

Figure 4.4.2.1-2 Benchmarking Result of IFA-562 Rod 18

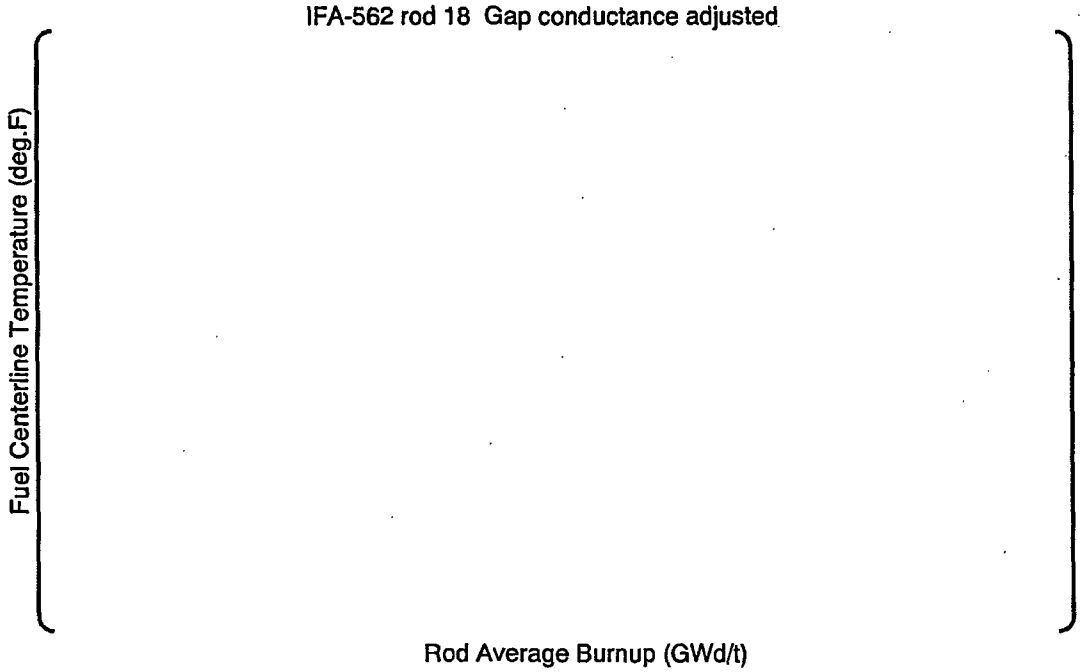

Figure 4.4.2.1-3 Benchmarking Result of IFA-562 Rod 18 (Gap Conductance Adjusted at BOL)

4.4.2.2 IFA-432

The IFA-432 experiment was performed to demonstrate the thermal effects of gap size and density. In the reference[43], this result is used to crosscheck the burnup degradation effect derived from IFA-562.
The input for FINE code is summarized in Table 4.4.2.2-1 and is obtained from the reference[24]. Rod 3 is selected for the benchmarking rod among Rod 1, 2, and 3 of IFA-432, because only Rod 3 is compared with FRAPCON-3.3 in the reference[44].

For the FINE code input, the following input are assumed.

- Flat axial power distribution
- FGR adjustment to the measurement

When the axial power distribution in the reference[43] is assumed, the power history of Rod 3 does not match well with the local power history at each thermocouple. Therefore, the input power history is assumed to be the same as that at the thermocouple position. Therefore flat axial power distribution over the rod is assumed. In addition to this, in order to adjust the gap conductance due to fission gas release, the fission gas release is adjusted to the measured data at the end of life.
Figure 4.4.2.2-2 compares the measured data, FRAPCON-3.3, and FINE result. The FINE code gives higher temperature than the measured data, especially at the high burnup. This tendency is the same as that seen in IFA-562 with the gap adjustment at the beginning of the irradiation. In this sense, the comparison of IFA-432 is a crosscheck of the burnup degradation effect derived from IFA-562.
On the other hand, the result of the FINE code is higher than that of FRAPCON-3.3 up to 15000 hours in Figure 4.4.2.2-2. After that, FRAPCON gives higher temperature than FINE. But both of the code gives the higher temperature than the measured data.

Table 4.4.2.2-1 Summary of Input for IFA-432 Rod 3

Input Items	IFA-432 No.3	unit	Reference *1

*1
NUREG/CR-6534 Vol.3 PNNL-11513 PNNL-11513 / Table A.2.1 : IFA-432 Test Rod General Design Specification
NUREG/CR-6534 Vol.3 PNNL-11513 PNNL-11513 / Table A.2.2 : IFA- 432 Test Rod Design Variation
NUREG/CR-6534 Vol.3 PNNL-11513 PNNL-11513 / Table A.2.3 : Nominal Halden Reactor Operating Conditions
NUREG/CR-6534 Vol.3 PNNL-11513 PNNL-11513 / Table A.2.5 : IFA-432,Rod1,2,and 3 Input for FRAPCON-3 and Notes on Derivation

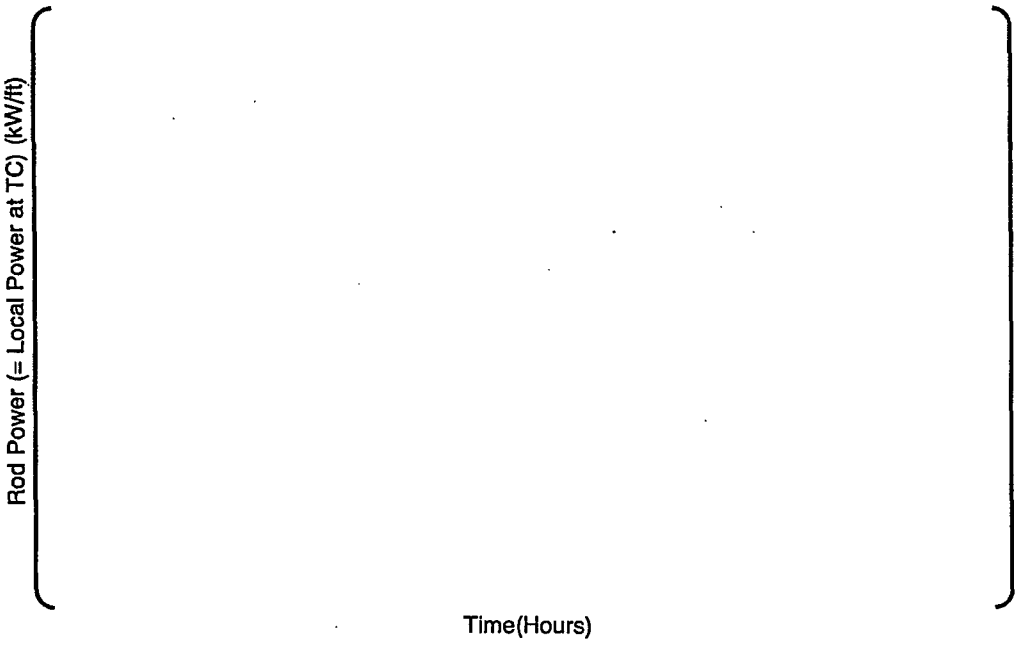

Figure 4.4.2.2-1 Power History of IFA-432 Rod 3

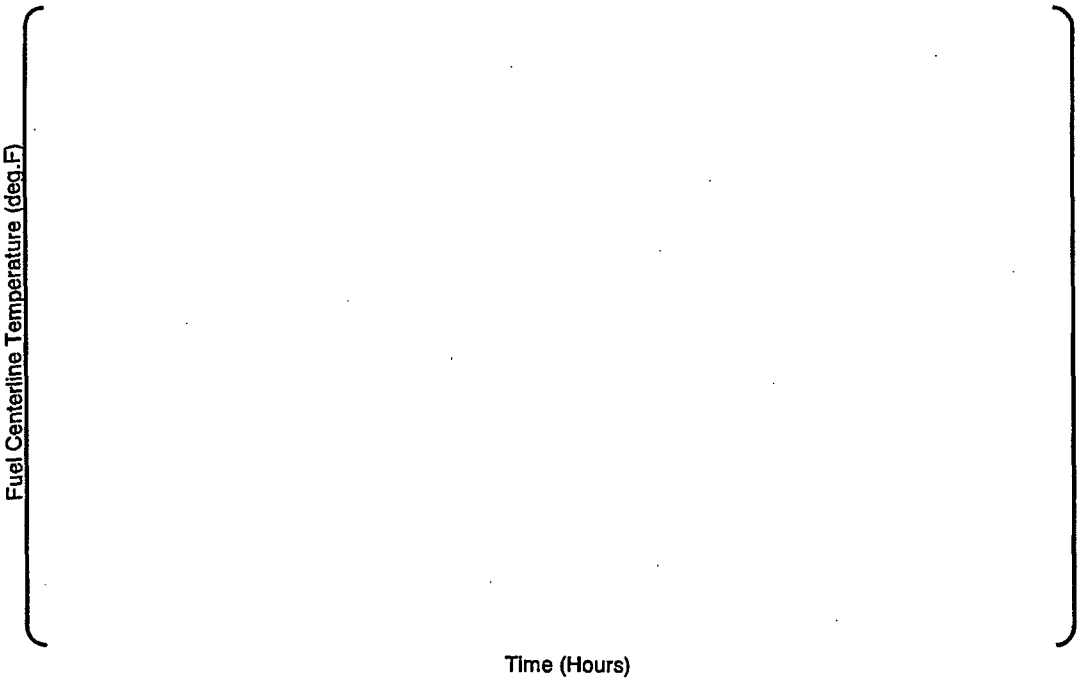

Figure 4.4.2.2-2 Benchmarking Result of IFA-432 Rod 3

4.4.2.3 BR3

The FGR prediction for the BR3 rods by the FINE code is summarized in Table 4.4.2.3-1 with the measured data and also with the FRAPCON-3.3 result[44]. The FGR prediction by the FINE code shows the good agreement with the measured data as well does the FRAPCON-3.3.

Table 4.4.2.3-1 Summary of Fission Gas Release for BR3

Reactor / FA I.D	Rod I.D	Measured Rod Average Burnup (GWd/t) [35]	Measured FGR (%) [35]	Predicted FGR (%) FRAPCON-3.3 [43]	Predicted FGR (%) FINE

4.4.2.4 IFA-429 Rod DH

IFA-429 Rod DH is selected as benchmarking, because FGR was relatively high at 24% release, the rod achieved a very high rod-average burnup level of 74GWd/t, and the relatively high LHGRs of 9 to 12 kW/ft towards the EOL[43].

In order to calculate FGR by FINE code, the input of FRAPCON-3 described in reference[24] is used. The radial power distribution across the pellet is appropriated from that for IFA-596 (see in the previous section) with 10 wt% 235-U enrichment which was prepared for Halden Boiling Water condition. The diameter of the IFA-596 is smaller than that of IFA-429 but the enrichment is the same.

The fission gas release is compared with the measured and the predicted both by FRAPCON-3.3 and FINE. The FINE code conservatively predicts fission gas release compared to the measured data. This is the same tendency as FRAPCON.
Figure 4.4.2.4-2 compares the measured data with the FINE result against burnup development. This figure shows that the FINE code predicts the onset of fission gas release fairly well.

Table 4.4.2.4-1 Summary of Input for IFA-429 Rod DH

Input Items	IFA-429 DH	unit	Reference *1

*1
NUREG/CR-6534 Vol.3 PNNL-11513 PNNL-11513 / Table A4.1 : Fuel Rod Components and Specifications for IFA-429,Rods C and DH
NUREG/CR-6534 Vol.3 PNNL-11513 PNNL-11513 / Table A4.2 : Nominal Halden Reactor Operating Conditions
NUREG/CR-6534 Vol.3 PNNL-11513 PNNL-11513 / Table A4.3 : Background Notes on IFA-429 Rod DH Input for FRAPCON-3

Table 4.4.2.4-2 Summary of Fission Gas Release for IFA-429 Rod DH

Reactor / FA I.D	Rod I.D	Measured Rod Average Burnup (GWd/t) [44]	Measured FGR (%) [44]	Predicted FGR (%) FRAPCON-3.3 [44]	Predicted FGR (%) FINE

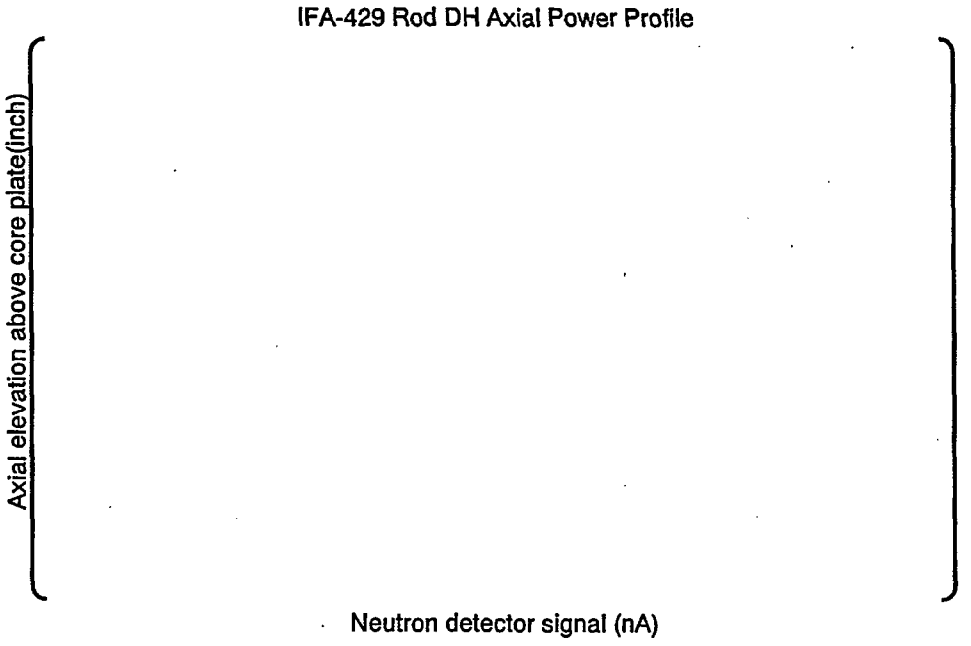

Figure 4.4.2.4-1 Axial Power Shape of IFA-429

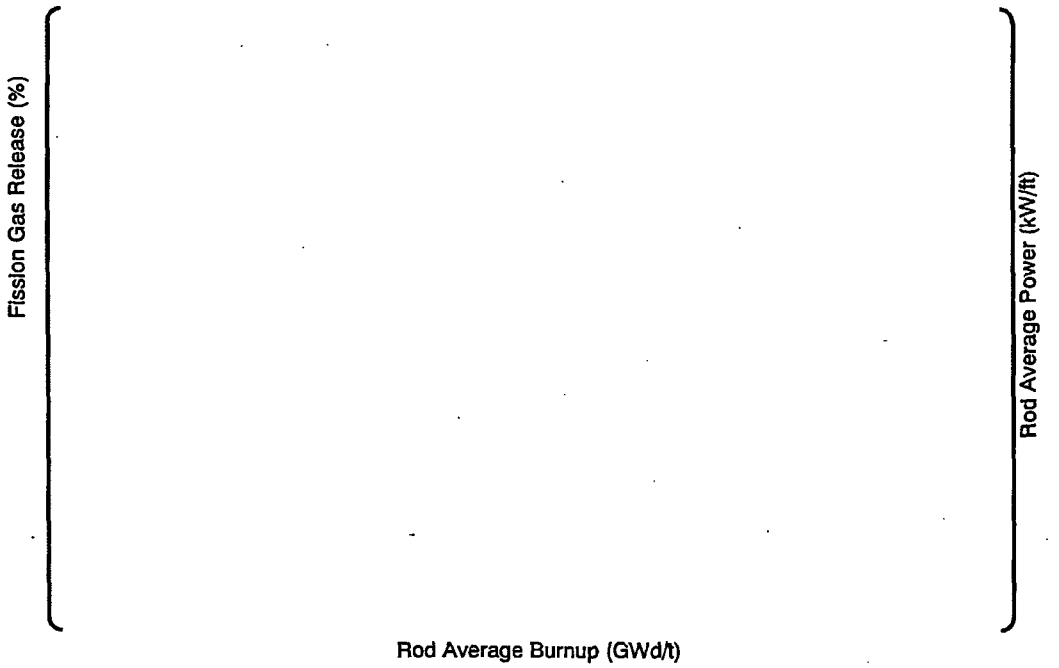

Figure 4.4.2.4-2 Fission Gas Release with Rod Average Burnup IFA-429 Rod DH.

4.4.2.5 Oconee-1 PWR 15309

Oconee-1 Rod 15309 is used as the benchmark with the commercial PWR reactor rod. The input for this rod is summarized in Table 4.4.2.5-1 and the power history is shown in Figure 4.4.2.5-1. These inputs come from the reference[43].

The fission gas release is summarized in Table 4.4.2.5-2. The FINE code gives higher fission gas release than the measured data and also than FRAPCON-3.3.

Table 4.4.2.5-1 Summary of Input for Oconee-1 Rod15309

Input Items	Oconee-1 15309	unit	Reference*1
[ ]			

*1
NUREG/CR-6534 Vol.3 PNNL-11513 PNNL-11513 / Table A11.1 : Fuel Rod Components and Specifications for Oconee 5-Cyle,Rod 1
NUREG/CR-6534 Vol.3 PNNL-11513 PNNL-11513 / Table A11.2 : Oconee Reactor Operationg Condition
NUREG/CR-6534 Vol.3 PNNL-11513 PNNL-11513 / Table A11.4 : Oconee PWR Rod 15309 Input for FRAPCON-3 and Notes on Deri

Table 4.4.2.5-2 Summary of Fission Gas Release for Oconee-1 PWR 15309

Reactor / FA I.D	Rod I.D	Measured Rod Average Burnup (GWd/t)	Measured FGR (%)	Predicted FGR (%) FRAPCON-3.3	Predicted FGR (%) FINE
[ ]					

Figure 4.4.2.5-1 Axial Power Shape[45]

Figure 4.4.2.5-2 Power History

4.4.3 Summary

In order to validate the FINE code, several benchmark cases are made using the FINE code and the results of the FINE code are compared with that of FRAPCON-3.3 and with the measured data.

The FRAPCON-3.3 result is obtained from the open literatures[43], [44]. The benchmarking is made for fuel temperature and fission gas release.

(a) fuel temperature
The burnup effect on thermal conductivity of the FINE code is similar to FRAPCON-3.3 code. The temperature prediction of the FINE code is similar to that of FRAPCON-3.3. The prediction of the FINE code with gap conductance adjustment at BOL for IFA-562 is consistent with that of the FRAPCON-3.3, though the FINE gives somewhat higher temperature prediction.

(b) fission gas release
Fission gas release prediction of FINE code is consistent with the FRAPCON-3.3 code.

From these benchmarks, it is concluded that the FINE code is validated by FRAPCON-3.3.

4.5 References

(1) William T. Parry et al, "ASME INTERNATIONAL STREAM TABLES FOR INDUSTRIAL USE", CRTD-Vol.58, 2000
(2) H.W.Graves Jr, "Nuclear Fuel Management", Japanese translation, 1983
(3) L.S.Tong and J.Weisman, "Thermal Analysis of Pressurized Water Reactors", American Nuclear Society, 1970
(4) Kraftwerk Union, Combustion Engineering, "Waterside Corrosion of Zircaloy Fuel Rods", EPRI NP-2789, December 1982
(5) R.S.Brokaw, "Alignment Charts for Transport Properties, Viscosity, Thermal Conductivity and Diffusion Coefficients for Nonpolar Gases and Gas Mixtures at Low Density", Report NASA TR R-81 (1961)
(6) R.A.Dean, "Thermal contact conductance between UO2 and Zircaloy 2", CVNA-127, May 1962
(7) Nguyen, T. Q. et. al., "Qualification of the PHOENIX-P/ANC Nuclear Design System for Pressurized Water Reactor Cores," WCAP-11597-A(Nonproprietary), June, 1988
(8) International Atomic Energy Agency, "Thermal Conductivity of Uranium Dioxide." Report of the Panel held in Vienna, April 1965, IAEA Technical Reports Series, No.59, Vienna, The Agency, 1966
(9) K.Bakker et al, "Determination of a Porosity Correction Factor for the Thermal Conductivity of Irradiated UO2 Fuel by means of the Finite Element Method", Journal of Nuclear Materials, 226, 1995, pp.128-143
(10) W.Wiesenack, "Assessment of UO2 Conductivity Degradation Based on In-Pile Temperature Data", ANS 1997 International Topical Meeting on LWR Fuel Performance, March 1997, Portland, Oregon
(11) K.Kosaka et al., "Thermal Properties and Irradiation Behaviour of Gd Fuel", IAEA Technical Committee Meeting on Advances in Pellet Technology for Improved Performance at High Burnup, October 1996, Tokyo
(12) T.Tverberg et al., "Study of Thermal Behaviour of UO2 and (U,Gd)O2 to High Burnup (IFA-515)", HWR-671, Enlarged HPG Meeting, March 2001, Lillehammer
(13) J.O.Barner et al., "Relationship between Microstructure and Fission Gas Release in High Burnup UO2 Fuel with Emphasis on the RIM Region", ANS/ENS International Topical Meeting on LWR Fuel Performance, April 1991, Avignon, France
(14) J.Spino et al., "Microstructure and Fracture Toughness Characterization of Irradiated PWR Fuels In the Burnup Range 40-67GWD/TM", IAEA Technical Committee Meeting on Advances in Pellet Technology for Improved Performance at High Burnup, October-November 1996, Tokyo, Japan
(15) M.Kinoshita, "Ultra High Burnup Characteristics of UO2 Fuel", KNS/AESJ Joint Seminar, October 2002, Yong Pyung, Korea
(16) M.V.Speight, " A Calculation on the Migration of Fission Gas in Material Exhibiting Precipitation and Re-solution of Gas Atoms Under Irradiation.", Nuclear Science and Engineeringm, 37 180-185, 1969
(17) C.Vitanza et al., "Fission Gas Release From UO2 Pellet Fuel At High Burn-up", ANS Light Water Reactor Fuel Performance, Portland, Oregon, May 1979
(18) R. Hargreaves and D.A.Collins, "A Quantitative Model for Fission Gas Release and Swelling in Irradiated Uranium Dioxide", J.Br.Nucl Energy Soc. 1976 Oct., No4, 311-318
(19) H.Nerman, "Application of STAV5 code for the Analysis of Fission Gas Release in Power Reactors Rods", IAEA Specialists meeting on Water Reactor Fuel Element Performance Computer Modeling, Precston, UK, Mar. 1982

(20) USNRC,"Background and Drrivation of ANS5.4 Standard Fission Product Release Model", NUREG/CR-2507, July 1981
(21) Nuclear Power Engineering Corporation, "Fiscal Year 1994 Report on Proving Test on Reliability of Fuel Assembly (Mixed Oxide Fuel Irradiation Test)", March 1995
(22) Miller, J.V., (Ed.), "Improved Analytical Models Used in Westinghouse Fuel Rod Design Computations" WCAP-8720, October 1976
(23) "MATPRO - Version 11 A handbook of material properties for use in the analysis of light water reactor fuel rod behavior", NUREG/CR-0497, February 1979
(24) F.K.G.Odqvist, J.Hult, "KRIECHFESTIGKEIT METALLISCHER WERKSTOFFE", Springer-Verlag Berlin, 1962 (Japanese translation)
(25) V.Fidleris, "The irradiation creep and growth phenomena", Journal of Nuclear Materials, 159 (1988) P22-42,
(26) J.K.Hohorst, "SCDAP/RELAP5/MOD2 Code Manual, Vol.4 : MATPRO-A Library of Materials Properties for Light-Water-Reactor Accident Analysis", NUREG-CR-5273-Vol.4 (1990)
(27) H.P.FUCHS et.al, "Cladding and structural material development for the advanced Siemens PWR fuel "FOCUS", ANS-ENS International Topical Meeting on LWR Fuel Performance, Avignon-France, 1991
(28) T.Kido et al., "Quantitative Assessment of Irradiation Effect on Creep and Corrosion Properties of Zr-Base Alloys", ASTM STP 1423, p780-794, 2002
(29) Nuclear Power Engineering Corporation, "Fiscal Year 2001 Report on Tests of High Burnup Fuels 2001 (PWR High Burnup Fuel Comprehensive Evaluation)", March 2002
(30) X-5 Monte Carlo Team, "MCNP - A General N-Particle Transport Code, Version 5 - Volume I: Overview and Theory," LA-UR-03-1987, Los Alamos National Laboratory, April, 2003
(31) G.Kjaerheim et al.,"IN-PILE DETERMINATION OF UO2 THERMAL CONDUCTIVITY, DENSITY EFFECTS AND GAP CONDUCTANCE", HPR-80, December 1967
(32) W.Wiesenack et al., "Assessment of UO2 CONDUCTIVITY DEGRADATION based on in-pile temperature data", HWR-469,1996
(33) P.Blanpain et al., "GAIN" Final Report, GN89/48, 1991
(34) M. Lippens, "GAP" Final Report, GP 90/28 D, 1990
(35) M.G.Balfour et al., "BR-3 High Burnup Fuel Rod Hot Cell Program, Volume 1: Final Report", WCAP-10238, Vol.1, DOE/ET 34073-1, 1982
(36) Studsvik Energiteknik AB "The Studsvik Over-Ramp Project " Final Report, EPRI-NP-3007, 1983
(37) Studsvik Energiteknik AB " Final Report of The Super-Ramp Project " STUDSVIK-STSR-32,1984
(38) J.A.Kuszyk, "Hot Cell Examination of Surry Three- and Four-Cycle 17 × 17 Demonstration Fuel, Volume 1: Principal Results and Evaluation", WCAP-10514, Vol.1, DOE/ET 34014-14, 1984
(39) Battelle, "High Burnup Effects Program-Final Report, HBEP-61(3P27), 1990
(40) M.G.Balfour et al., Final Report "EP80-16, Hot Cell Examination of Zion Fuel Cycle 1 through 4, WCAP-10473",ESEERCO report, 1985
(41) M.G.Balfour et al., "Zorita Research and Development Program: Volume 1, Final Report", WCAP-10180, Vol. 1, 1982
(42) H.Kunishi, " Final Summary Report on Post-Irradiation Examinations of North Anna Advanced Material Demonstration Assemblies " , PPE-97-136, 1997
(43) D.D.Ranning et.al, "FRAPCON-3: Integral Assessment", NUREG/CR-6534 Volume 3 PNNL-11513

(44) D.D.Ranning et.al, "FRAPCON-3 Updates, Including Mixed-Oxide Fuel Properties", NUREG/CR-6534, Vol.4, PNNL-11513
(45) L.W.Newman, "THE HOT CELL EXAMINATION OF OCONEE 1 FUEL RODS AFTER FIVE CYCLES OF IRRADIATION", DOE/ET/34212-50, BAW-1874, October 1986 UC-78

5.0 CONCLUSION

This topical report describes the Mitsubishi design criteria and methodology and demonstrates that the fuel rods and fuel assembly design criteria that are to applied to the US-APWR complies with Title 10 of Code of Federal Regulations Part 50 (10CFR50), Regulatory Guide 1.70, and Standard Review Plan (NUREG-0800). The report further demonstrates that Mitsubishi developed FINE code is verified by significant irradiation data and also be validated by comparing predictions made by the FINE code with results of FRAPCON-3 for benchmark cases for code verification that is provided by PNNL.

Appendix A

MITSUBISHI FUEL EXPERIENCE

May 2007

Table of Contents

List of Tables

List of Figures

A.1.0 INTRODUCTION

At least 3.6 million Zirconium based alloy (Zircaloy-4, MDA[*1] and ZIRLO™[*2]) cladding fuel rods fabricated by Mitsubishi, beginning in the late 1960's, have been irradiated through to discharge or are under irradiation in commercial reactors in Japan as of the end of March 2007. During this time, Mitsubishi PWR fuel has being undergoing continuous improvement, with reliability being the primary focus, but also in support of extended fuel burnup, improved uranium resource efficiency, reduced spent fuel generation and reduction in fuel cycle cost.

This appendix provides a summary of the Mitsubishi fuel operation experience. Section A.2 addresses the evolution of the Mitsubishi fuel design in response to industry wide issues and the commitment to zero defect fuel design. Section A.3 describes Mitsubishi's development programs to establish a database of fuel rod performance, including participation in joint industry fuel performance programs. Section A.4 summarizes Mitsubishi commercial fuel irradiation experience. Section A.5 provides an overall summary and conclusion.

[*1] MDA is Mitsubishi Developed Alloy which consists of 0.5%Nb, 0.8%Sn, 0.2%Fe, 0.1%Cr and about 98% Zr.
[*2] ZIRLO™ is a registered trademark of the Westinghouse Electric Corporation.

A.2.0 DESIGN CHANGES HISTORY IN MITSUBISHI FUEL

Mitsubishi PWR fuel has being undergoing continuous improvement, with reliability being the primary focus, but also in support of extended fuel burnup, improved uranium resource efficiency, reduced spent fuel generation and reduction in fuel cycle cost.

In Japanese PWRs, high burnup fuel program has progressed step by step. High burnup step 1 fuel whose licensed assembly average burnup was 48 GWd/t has been utilized since 1990.

The higher burnup step 2 fuel where the licensed assembly average burnup was 55 GWd/t was introduced to Ohi unit 4 in 2004. Although the high burnup step 1 fuel was the same as the previous fuel design except for decreasing helium pre-pressurization level for 48 GWd/t fuel,
The high burnup step 2 fuel was adopted higher density pellet of 97 %TD, higher gadolinia content of 10 wt% doped pellet and improved fuel cladding (ZIRLO and MDA), in addition to optimized fuel rod length and helium pre-pressurization level.

PWR fuel utilities and vendors have experienced significant performance issues such as primary hydriding, cladding creep collapse, fuel bowing, debris fretting, grid fretting and incomplete rod insertion (IRI).

The US-APWR fuel introduces the latest design such as ZIRLO cladding, higher density pellet of 97 %TD, gadolinia doped fuel with 10 wt% gadolinia content, the anti-debris bottom nozzle with built-in filter, the high performance grid spacer and the improved control rod guide thimble tube and thimble screw design as a countermeasure against IRI ,described below.

This section describes the evolution of PWR fuel design in response to industry wide fuel performance issues. Specifically, the countermeasures introduced in the design and fabrication of Mitsubishi fuel to address these issues are presented.

A.2.1 Primary Hydriding Failure

In the early 1970's, fuel failures due to primary hydriding of Zircaloy cladding were observed at the Ginna reactor in the U.S., the Beznau reactor in Switzerland, and in some other reactors. This primary hydriding was found to be due to insufficient moisture controls during the fabrication of fuel pellets at that time.

This problem has been resolved by strengthening the Quality Controls for moisture content in the UO_2 pellet manufacturing, and by the use of higher density UO_2 pellets. Current pellet nominal density for Mitsubishi fuel is 95 %TD for 48 GWd/t fuel and 97 %TD for 55 GWd/t fuel, as compared with fuel pellet densities of about 93 %TD and below that were in use at that time. As a result, the moisture content is kept sufficiently low compared with its limit of 1.3 ppm (hydrogen from all sources for fuel pellets) specified in "Standard Specification for Sintered Uranium Dioxide Pellets" to American Standards and Testing Methods (ASTM) C776-06.

A.2.2 Fuel Pellet Densification and Cladding Creep Collapse

Fuel cladding collapse failures were observed worldwide as early as the 1960's in fuel assemblies operated in PWR plants such as the Ginna and the Beznau reactors. The fuel rods

that experienced cladding collapse contained lower density fuel pellets and were either unpressurized or lower-pressurized rods. Fuel column lengths were shortened by densification shrinkage of the lower density fuel pellets, which were less stable, during the irradiation. Fuel column shrinkage and pellet hang up on the inner surface (i.e. pellet-clad gap closure) created empty sections (axial gaps) in the fuel column. Under the external coolant pressure load, the cladding tubes developed increased ovality of with irradiation time due to creep strain until they reached a point of instability where the external pressure caused the complete collapse, or flattening, of the cladding into the axial gaps.

The industry wide investigation of this issue concluded that excessive fuel pellet densification shrinkage could be avoided by the use of higher density fuel pellets, resulting in a target fuel density of about 95 %TD or more. In addition, pre-pressurization of the fuel rods with helium reduced the compressive loading on the cladding. Implementation of these changes has effectively eliminated cladding collapse failures in current generation fuel.

The adoption of a higher nominal pellet density of 97 %TD that is less densification for US-APWR fuel, will be even more effective in eliminating the potential for cladding creep collapse.

A.2.3 Fuel Rod Bowing

In 1973, fuel rod bowing with PWR fuel was discovered at Mihama Unit 2, and similar discoveries followed. Fuel rod bowing involves the following mechanisms:

(1) Binding force bowing: When the grid spacer spring forces on the fuel rods prevent slippage, the compressive force applied to the fuel rod in the axial direction caused by the difference in irradiation growth of the fuel rod and the control rod guide thimble produces a bending moment in the fuel rod, and subsequent fuel rod creep results in plastic rod bowing.

(2) PCMI bowing: If there is a large increase in fuel rod power after partial pellet-cladding adhesion has occurred, thermal expansion of the pellets creates an axial tensile force in the cladding, which produces bending moment acting on the cladding, and cladding creep results in plastic bowing.

To restrict this phenomenon, it is necessary to decrease the bending moment that acts on the fuel rods during operation and decrease specification deviations in manufacture. Therefore, bowing was reduced in Mitsubishi fuel by optimizing the restraint force of the grid spacer spring and dimples by improving the shape of the grid spacer springs. Increasing the number of grid spacers in the fuel assembly design, thereby reducing the span lengths between the grid spacers, also reduced the bending moment and subsequent rod bowing. In addition, improvements in fuel cladding manufacturing controls and design tolerances for cladding wall eccentricity were implemented in the manufacturing phase.

As a result of these design and manufacturing improvements, excessive fuel rod bowing has been eliminated in Mitsubishi fuel operation.

A.2.4 Debris Fretting[1],[2]

Improved fuel inspection techniques showed that debris made of foreign material contaminating the primary coolant is a potential cause of fuel rod leakage. Depending on the shape and composition of the debris, the debris can be captured in the bottom of the lowest

grid spacer of the fuel assembly. Reactor coolant flow produces vibration of the debris material which can lead to fretting damage in adjacent fuel rods.

In the initial response to prevent debris fretting, the design was changed to lower the position of the bottom grid spacer in the fuel assembly and to lengthen the bottom end plug in the fuel rod, so that debris which is captured in the bottom grid spacer is in contact with the solid bottom end plug in the fuel rod and not in direct contact with the cladding. In addition, the flow holes of the bottom nozzle were made smaller and their number increased to achieve the equivalent pressure drop, thus using the "Debris Filter Bottom Nozzle (DFBN)" to prevent entry of the debris into the fuel assembly.

The problem of fuel rod damage caused by debris was effectively resolved by applying these foreign material countermeasures to actual fuel.

In order to ensure the elimination of debris fretting as a potential failure mechanism in the 17x17 type high burnup fuel assembly design (55 GWd/t fuel assembly average burnup), a debris filter (DF) is installed on the top of the Low Pressure drop Bottom Nozzle (LPBN). The DF and the lower end plug of the fuel rod form a narrow flow area. Figure A.2.4-1 shows the DF and LPBN. The dimple of the DF is located at the bottom end plug, so debris will be trapped by the DF at the solid bottom end plug, and fretting wear is restricted to the bottom end plug, thereby preventing fuel leakage. Moreover, a skirt is installed in the LPBN which effectively prevents debris from passing through or between the bottom nozzles to the gap between fuel assemblies.

In a 14x14 type and a 15x15 type high burnup (55 GWd/t fuel assembly), from the point of decreasing rod internal pressure, longer end plug is impracticable. An anti-debris bottom nozzle with built-in filter is applied, which consists of a groove on the surface of the DFBN and long and thin Inconel straps called "blade". The blades are embedded in the groove and welded to the bottom nozzle at multiple points. Figure A.2.4-2 shows the schematic view of the anti-debris bottom nozzle with built-in filter. This type of debris filter can trap smaller debris than the former debris filter bottom nozzle without longer end plug. Moreover, a skirt is installed in the bottom nozzle in order to improve the debris trap performance further and make it equivalent to that of a 17x17 type.

This type of debris filter will be applied to the 17x17 type fuel assembly design and also US-APWR fuel design.

A.2.5 Grid Fretting [1],[2]

Fretting wear called grid fretting which is occurred in between the grid spacer and the fuel rod is caused by vibration of the fuel assembly, grid spacer strap, and/or the fuel rod. A low grid spacer spring force could cause a sliding displacement between fuel rod and the grid spacer spring/dimple due to fuel rod vibration and thus induce fretting wear. There had been reports of grid fretting in PWR fuel in countries other than Japan, and the occurrence of this phenomenon was documented in Japan in the late 1980s.

The occurrence of grid fretting in Japan was a special type of grid spacer to rod fretting in that it occurred in a fuel assembly loaded at the periphery of the core and facing a baffle plate. The interaction of the coolant flow in the gap between the baffle plate and the fuel assembly, with grid spacer structure, created pressure fluctuations, which induced the vibration of the grid spacer.

One of the countermeasures used in Japan is improvement of the grid spacer structure that suppresses the fluctuation in pressure between the baffle plates and the fuel assembly structure, such that even the worst-case vibration is easily attenuated. No problems have occurred since the countermeasures were implemented.

Additionally, Mitsubishi has developed an improved grid spacer design called the "I type grid spacer" which improves the performance of the fuel rod support system. Figure A.2.5-1 shows the outline of the I type grid spacer. A feature of this spring design is good stability of the spring force even after an excessive displacement due to fuel rod vibration or after the decreased spring deflection due to the creep-down of the outer diameter of the fuel rod cladding.

These countermeasures improve the resistance against grid fretting, and there has been no evidence of fuel leakage due to grid fretting during approximately 16 years of experience with over 3,500 assemblies using the Mitsubishi I type grid spacer design.

A high performance grid spacer called Z3 type has been developed keeping the characteristics of the I type grid spacer design for use in uprated operation, long cycle operation, and higher burnup fuel assemblies. The principal features of the high performance grid spacer are as follows.

- Improved DNB performance and reduced pressure-drop due to design improvements for the mixing vane.
- Improved seismic performance due to design improvements of the grid spacer strap. The improved design reduces stress at the spring due to improvement of the spring shape.

Figure A.2.8-1 shows the high performance grid spacer. The results of the hydraulic testing, the DNB testing and the impact testing showed good performance.

A.2.6 Incomplete Rod Insertion (IRI) [3]

In 1996, Incomplete Rod Insertion (IRI) events occurred in the U.S and in Europe. In this phenomenon, the Rod Cluster Control Assemblies (RCCAs) become stuck at the dashpot region of control rod guide thimble and failed to insert completely. Mitsubishi fuel has never experienced an IRI event, and drag force analysis results show no potential risk.

However, with burnup increasing from 48 GWd/t to 55 GWd/t, the RCCA drag force is expected to increase because of increasing control rod guide thimble distortion. At the dashpot region, where the gap between RCC rodlet and the control rod guide thimble is small, the drag force is sensitive to control rod guide thimble distortion. Increasing the gap between the RCC rodlet and the control rod guide thimble is effective in preventing this fundamental cause of an IRI event.

Therefore, as a preventive countermeasure, the inner diameter of the lower span of the control rod guide thimble was enlarged. Figure A.2.6-1 shows the outline of the improved control rod guide thimble. Test results of drag force measurements with locally bowing control rod guide thimble confirmed that the improved control rod guide thimble design reduces the RCCA drag force caused by control rod guide thimble distortion to less than 5 % as compared with the conventional design.

This improvement is considered to be very effective in reducing the potential for IRI. However, the lower span of the control rod guide thimble also has an important dashpot function giving the RCCA a soft landing on the top nozzle when a scram occurs. In order to maintain this dashpot function with the enlarged diameter of the control rod guide thimble, a new type of thimble screw with a small diameter flow hole was introduced. This screw produces a large pressure drop for the downward flow that is generated by the insertion of the RCCA in a scram event. The large pressure drop maintains the dashpot functionality for reducing the speed of the RCC rodlet motion and thereby cushioning the contact with the top nozzle.

After the introduction of the improved control rod guide thimble and thimble screw design, an RCC scram test was performed. In the scram test, the RCC insertion speed and acceleration were measured. It was shown that the RCC performance of the improved design was the same as that of the conventional fuel.

A.2.7 In-Reactor Performance

Mitsubishi fuel operation experience in Japan has been excellent, and it confirms the effectiveness of the design modifications that have been made to the fuel assembly and fuel rod design over time. The rate of fuel failure for Mitsubishi fuel, as shown in Figure A.2.7-1, has significantly decreased since 1992, because of the reliable quality control in manufacturing fuel, in addition to the countermeasures against debris fretting and grid fretting.

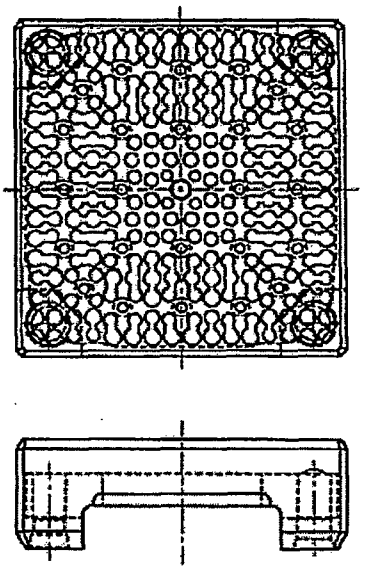

Low pressure bottom nozzle

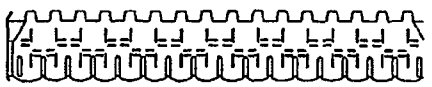

Side view

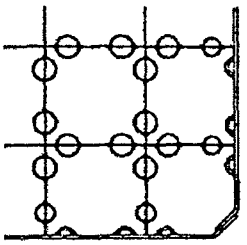

Top view

Debris filter

Figure A.2.4-1 Schematic View of Debris Filter and Low Pressure Bottom Nozzle

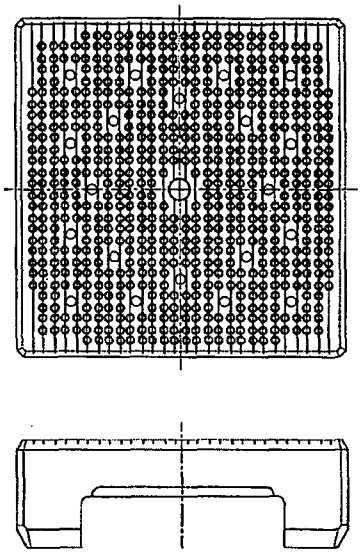

Figure A.2.4-2 Schematic View of the Anti-Debris Bottom Nozzle with Built-In Filter

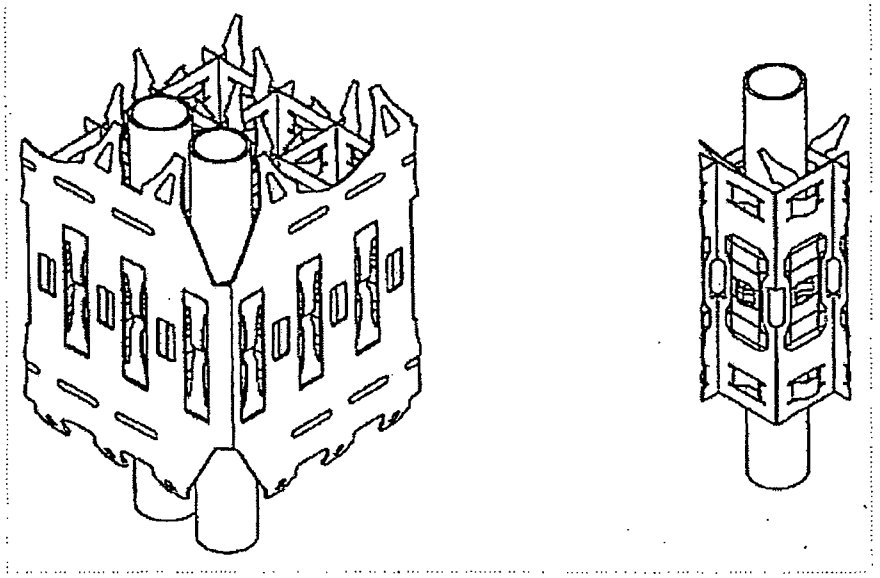

Figure A.2.5-1 Schematic View of I-type Grid Spacer

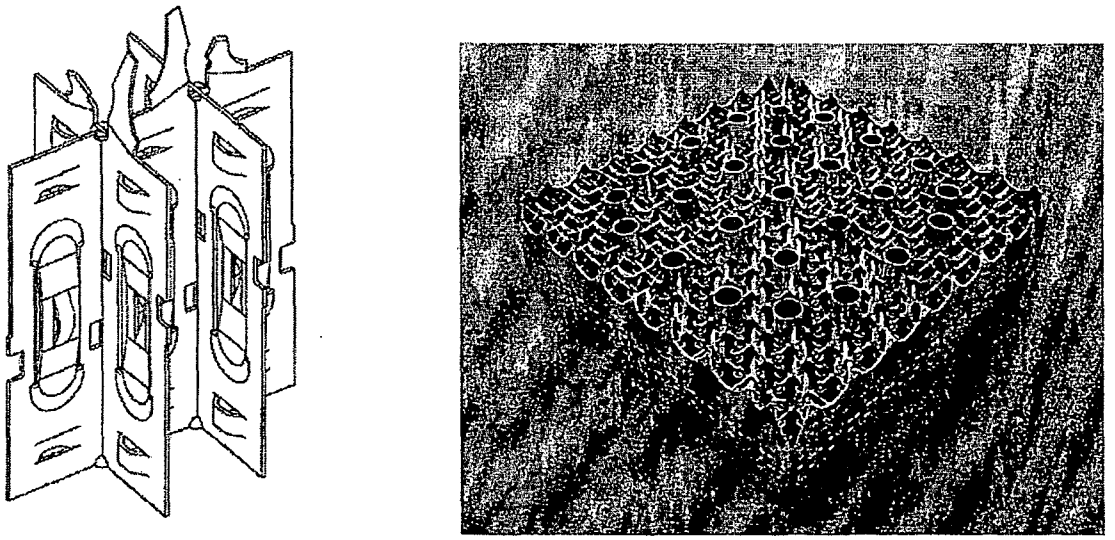

Figure A.2.5-2 Schematic View of High Performance Grid Spacer

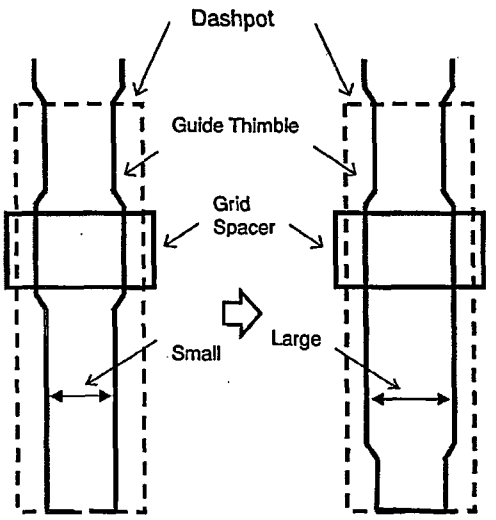

Figure A.2.6-1 Schematic View of Dashpot in the Control Rod Guide Thimble

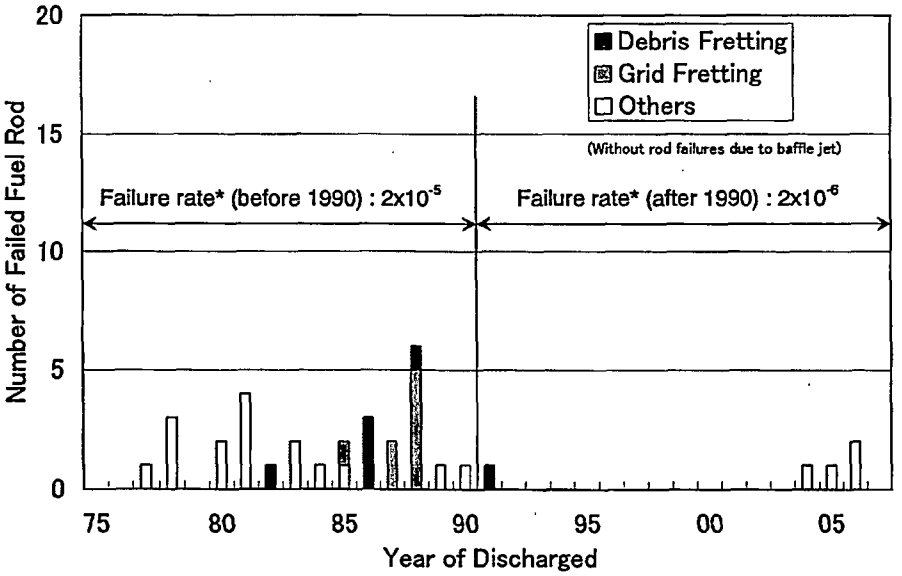

***Failure Rate : Number of failed rods / Total number of fabricated rods**

Figure A.2.7-1 Mitsubishi Fuel Performance History

A.3.0 MITSUBISHI POST IRRADIATION EXAMINATION PROGRAMS

Mitsubishi has been committed to the development of an extensive database of PWR fuel and cladding performance data since the early 1970's. This database is important for verification of good fuel performance and also for improving the basic understanding of fuel and cladding performance issues for the purpose of improved fuel modeling and design. Section A.3.1 provides an overview of the industry fuel irradiation programs conducted in support of high burnup fuel design which has been included in the Mitsubishi database. Section A.3.2 summarizes some of the Mitsubishi development programs which have been conducted in support of the Japanese nuclear industry. The data from all of these programs provide a foundation for the design of the US-APWR fuel assembly.

A.3.1 Industry Test Irradiation Programs

PWR fuel irradiation experience in both test reactor and commercial reactor operation has been accumulating in Japan, the United States and around the world[4],[5]. Many of these data collection programs have been intended to support the implementation of increased fuel discharge burnup. The use of high burnup fuel is desired to achieve lower fuel cycle cost, longer operating cycles and to reduce the number of discharged fuel assemblies. These programs have contributed to the improved understanding of PWR fuel performance and are summarized here for completeness.

Table A.3.1-1 summarizes the results of Westinghouse experimental fuel rod irradiation programs. Westinghouse achieved a maximum burnup of about 51 GWd/t (peak pellet) at the Saxton reactor in May of 1972, about 63 GWd/t [6] (peak pellet) was achieved at the Zorita reactor in September 1973, and 69.7 GWd/t[7] (peak pellet) was achieved at the BR3 reactor in September 1980. Tables A.3.1-2 and A.3.1-3, which summarize the peak linear heat rates for these test rod irradiations as a function of rod average burnup, demonstrate that these fuel rod discharge burnups were achieved at rod power levels at or exceeding the maximum power levels expected in typical commercial reactor irradiations.

In addition to these higher power test rod irradiation testing programs, vendor high burnup commercial fuel demonstration irradiation programs(e.g, Hot cell examination of fuel rods in ZION[8],[9],Surry[10], summarized in Table A.3.1-4, confirmed the absence of technical problems associated with extended burnup irradiation[11] and further contributed to the understanding of PWR fuel performance.

Mitsubishi has also been involved in the following joint industry fuel irradiation testing programs: OverRamp Project (R2), SuperRamp Project (R2), TRIBULATION Program, High Burnup Effects Program (HBEP) (BR2) [12], NFIR (Halden, R2), GAIN Project (BR2) [13], GAP[14] Project , and the high burnup RIM project[15]. These programs have provided detailed fuel performance data related to transient fuel behavior, including fission gas release and pellet clad mechanical interaction (PCMI), high burnup fission gas release and corrosion behavior, gadolinia doped fuel rod performance and the high burnup rim formation.

Based on the results of the above test rod and commercial reactor irradiation programs, discharge burnup limits have been successfully increased with continuing good fuel performance. The current maximum fuel rod average discharge burnup limit in the United States is 62 GWd/t (equivalent to fuel assembly maximum burnup of 56 GWd/t), the assembly

average burnup limit in Japan is 55 GWd/t, and in France the fuel assembly average burnup limit is 52 GWd/t.

A.3.2 Mitsubishi Test Reactor and Commercial Fuel Irradiation Test Programs

Mitsubishi has also been actively involved in efforts to develop improved PWR fuel design and manufacturing technology, beginning in 1964 through the Mitsubishi – Saxton project. Mitsubishi also participated in the Halden Project in a joint research effort with the Japan Atomic Energy Agency. The focus of these early efforts was to establish fuel manufacturing capability and to develop a database of PWR fuel irradiation experience. Later, additional programs were conducted to support the introduction of gadolinia doped fuel up to 6 wt% and later 10 wt% as an integral fuel burnable absorber, to support higher burnup fuel design with increased initial fuel density, and to develop improved corrosion resistance cladding. These programs are summarized below.

A.3.2.1 Test Reactor Fuel Irradiation Test Programs

a. Fuel Centerline Temperature Measurement In Halden Reactor

On-line measurements of centerline temperature for both UO_2 fuel and gadolinia doped fuel with a maximum of 10 wt% gadolinia content have been performed in a number of test programs conducted in the Halden test reactor using highly instrumented test rods. Fuel temperature measurements for fuel with burnup up to 86 GWd/t have been accumulated and are available for use in the validation of fuel temperature predictions for both UO_2 and gadolinia doped fuel throughout the anticipated range of PWR operating conditions.

b. Power Ramp and Power Cycling Test in Studsvik R2 Reactor[16]

Power ramp and cycling tests were performed at the R2 test reactor in Studsvik to generate fuel rod performance data under the conditions of power increase during Anticipated Operational Occurrences (AOOs) and during power cycling consistent with daily load follow maneuvers. Following base irradiation at the BOCA loop, six fuel rods were subjected to power ramp testing in the R2 reactor. Following the ramp tests, detailed post irradiation examinations were performed.

Another set of six test rods were base irradiated in the BR3 reactor in Mol, Belgium, and then transported to the R2 test reactor in Studsvik, where they were power cycled during 31 days to simulate daily load following. These rods were then subjected to a power ramp test, after which detailed post irradiation examinations were performed.

These tests provide data to evaluate the potential impact of AOOs on fuel that has experienced daily load follow.

A.3.2.2 Commercial Reactor Fuel Irradiation Test Programs

a. Proof Test on the Reliability of PWR 15x15 Fuel Assemblies[17]

A proof test on the reliability of Japanese PWR 15x15 type fuel assemblies was conducted by NUPEC (Nuclear Power Engineering Corporation test center) under the sponsorship of the Ministry of International Trade and Industry (MITI) during the period from 1976 to 1987. The

objective of this test was to demonstrate the high reliability of current PWR fuels in Japan. Ten candidate fuel assemblies for the fourth region of Mihama Unit 3 were fabricated by normal manufacturing processes, but with detailed pre-characterization examination. These fuel assemblies were irradiated under normal operational conditions up to three irradiation cycles. After each irradiation cycle, on-site inspections were conducted, and one fuel assembly was selected for detailed post irradiation examinations at a hot cell. The average burnups for the three fuel assemblies selected for hot cell examinations were 8.4, 17.6 and 31.4 GWd/t, for one, two and three cycle operation, respectively. The fuel performance during irradiation was evaluated using these data, and it was confirmed that all three fuel assemblies completed irradiation in good condition. The proof test (1) demonstrated the integrity of current PWR 15X15 fuel assemblies, (2) verified the acceptability of the 15X15 fuel design and (3) provided a highly reliable data base for future evaluation of PWR fuel rods and assemblies.

b. Lead Use Assembly(LUA) of 6wt%Gadolinia Doped Fuel in Ohi Unit 2

Before the introduction of 6 wt% gadolinia doped fuel as an integral fuel burnable absorber, four Mitsubishi LUAs that include 16 gadolinia doped fuel rods per an assembly, were irradiated from 1984 to 1987, for up to two cycles with a maximum assembly burnup of about 32.5 GWd/t in Ohi Unit 2. Four gadolinia doped fuel rods with maximum rod average burnup of 23.6 GWd/t and two UO_2 fuel rods with maximum rod average burnup of 31.3 GWd/t were examined at the Nuclear Development Corporation (NDC) hot cell (1987-1989). Fuel rod puncture test, pellet density measurement, gamma scanning measurement and other tests showed the good fuel performance of 6 wt% gadolinia doped fuel.

c. High Burnup Demonstration Program

Two Mitsubishi 17 x 17 demonstration fuel assemblies that is the conventional design with Zircaloy-4 cladding and 95 %TD fuel were selected from of the forth region fuel assemblies that had been irradiated up to three cycles and irradiated during additional one cycle (Cycle 7) for a total of four cycles in the Ohi Unit 1 reactor (started in December, 1986). These assemblies were discharged in December, 1987, with the assembly average burnups of 45.7 GWd/t and 45.9 GWd/t.

These fuel assemblies were confirmed to have operated successfully with good fuel performance, based on onsite inspections at the end of the irradiation cycles. Furthermore, the post-irradiation examinations of fuel rods removed from assembly D35 conducted at NDC hot cell, confirmed the good condition of the fuel after completing the high burnup irradiation that there are no indication of threats to fuel integrity.

d. Irradiation Test for Verification of PWR 48GWd/t High Burnup Fuel [27]

The irradiation test for verification of the high burnup fuel performance was conducted by NUPEC under the sponsorship of MITI from 1989 to 1998. Two Mitsubishi 17 x 17 fuel assemblies had been irradiated from 1990 to 1993 in Takahama Unit 3. The assemblies installed both Zircaloy-4 and low Tin Zircaloy-4 cladding tube with UO_2 or 6 wt% Gadolinia doped pellet of 95 %TD. One of the assemblies was unloaded after two cycles of irradiation and the other was unloaded after three cycles of irradiation. The discharged burnup was 31.9 GWd/t and 42.8 GWd/t of assembly burnup respectively.

The detailed fabrication inspections, on-site examinations and hot cell examinations at NDC were conducted on the two Mitsubishi assemblies. The high burnup fuel performance was verified by the result of these tests.

e. Zircaloy Grid Spacer Lead Use Assembly (LUA)

Zirconium based alloy grid spacers were in use for several years in PWR reactors[18]-[22] around the world before they were considered for application in Japan, due to regulatory concerns associated with grid spacer strength during seismic events. To prepare for the implementation of Zircaloy grid spacers in Japanese PWR's, Mitsubishi conducted a demonstration irradiation program where four 17 x 17 fuel assemblies with Zircaloy grid spacers were loaded into the Tsuruga Unit 2 reactor in Cycle 10 (starting October 1998). After three successful irradiation cycles, these assemblies were discharged in June 2002. The average burnup achieved in these demonstration assemblies was about 43 GWd/t.

Additional irradiation experience with grid spacers made of Zircaloy-4 was achieved in a Lead Test Assembly (LTA) program that was conducted in the Vandellos Unit 2 reactor in Spain. Four fuel assemblies that contained segmented fuel rods and with Zircaloy grid spacers were irradiated for four cycles in Vandellos Unit 2 from 1994 to 1999, achieving an assembly burnup of about 53 GWd/t.[20] Additional details on this LTA program are presented in the next section.

f. Vandellos High Burnup Lead Test Assembly (LTA) [23],[24]

The segmented fuel rod Irradiation program consists of three major phases: Phase I: design, licensing, fabrication and characterization of the LTA fuel assemblies, Phase II: irradiation of the fuel assemblies and on-site examination, Phase III: ramp testing and hot cell Post Irradiation Examination (PIE). Phase I has been performed as a collaborative program between the Japanese utilities, with Kansai Electric Power Co., Inc. (KEPCO) representing the other Japanese PWR utilities, Mitsubishi, ENDESA, S.A. representing A.N. Vandellos Unit 2, and Empresa National Uranio, S.A. (ENUSA), with the collaboration of Westinghouse Electric Company. Phases II and III are being conducted by the Nuclear Power Engineering Corporation (NUPEC) under the sponsorship of the Japanese Ministry of International Trade and Industry (MITI).

The segmented rod program started in 1991 and completed in 2001. The purpose is to obtain performance data on advanced fuel materials at high burnup (55 GWd/t). To provide a range of fuel pellet and cladding combinations, thirty-two segmented rods were fabricated and loaded into four fuel assemblies. Each segmented rod consists of seven segments, joined by intermediate end plugs. The main design feature of the segments is cladding alloy composition (ZIRLO, MDA and Low-tin Zircaloy-4). Four fuel assemblies containing segmented rods were irradiated in Vandellos unit 2 in Spain from 1994. 48 rods with ZIRLO cladding and 16 fuel rods with MDA cladding were irradiated, achieving a maximum rod average burnup of about 57 GWd/t. Six ZIRLO cladding rods and four MDA cladding rods were selected for further irradiation and achieved maximum fuel rod average burnup of about 75 GWd/t, with maximum pellet burnup of about 80 GWd/t or more.

The fourth cycle irradiation was completed in March 1999 with the lead assembly at a burnup of 53 GWd/t assembly average. On-site examinations, including underwater TV inspection and Eddy Current Test (ECT) oxide thickness measurements, were performed after each irradiation cycle. After the second, third and fourth-cycle irradiation, some segmented rods were withdrawn from fuel assemblies and sent to Studsvik Nuclear AB (Studsvik) in Sweden

for hot cell examination and ramp testing. Hot cell examination and ramp testing were already completed on 2, 3 and 4 cycles. The results of the on-site examinations, hot cell PIE and ramp testing showed good performance in high burnup.

g. Ohi Unit 4 High Burnup Lead Use Assmebly(LUA) [25]

To support the increase in the licensed burnup limit in Japan from 48 GWd/t to 55 GWd/t, a high burnup Lead Use Assembly (LUA) program was conducted in the Ohi Unit 4 reactor. Four Mitsubishi LUAs were irradiated in Ohi Unit 4 from 1997 to 2002, to a maximum assembly average burnup of about 52 GWd/t. The LUA's in this program included 178 ZIRLO clad fuel rods and 298 MDA clad fuel rods. In addition, the integral fuel burnable absorbers in these assemblies were gadolinia doped fuel with gadolinia content of 10 wt%(24 gadolinia doped fuel rods per an ssembly), to provide for a more flexible core management. After completion of the irradiation cycles, on-site inspections were conducted to confirm good fuel integrity. Thirteen fuel rods from one of the LUAs were extracted and transported to the NDC hot cell facility. Detailed post irradiation examinations were performed to confirm the integrity of the fuel rods and to provide detailed fuel performance data to be used to validate the high burnup fuel design and to further expand the Mitsubishi fuel performance database for use in future fuel development. The results of the PIE confirmed the enhanced corrosion resistance of the advanced cladding alloys (ZIRLO, MDA) relative to that of Zircaloy-4 cladding.

Table A.3.1-1 Experimental Fuel Rod Design Specifications

Fuel rods	Fuel	Cladding			Cladding-pellet clearance (% Δd/d)	Initial internal pressure (psia)	Pellet ℓ/d	Stack length (inches)	Pellet density (%TD)
		Material	O. D. (inches)	t/d					
14 x 14, 15 x 15 fuel rods	UO_2	Zr-4	0.422	0.058	2.0	-	1.6	144	92 to 95
17 x 17 fuel rods	UO_2	Zr-4	0.374	0.060	2.0	-	1.6	144	95
Saxton mixed-oxide fuel rod	$(U, Pu)O_2$	Zr-4	0.391	0.059	2.1	15	1.1	36	94
Saxton parametric fuel rod	UO_2	Zr-4	0.391	0.059	1.6 to 2.8	15 to 500	1.8	36	89.5 to 94.5
Zorita experimental fuel rod (regions 2,3)	UO_2	Zr-4	0.422	0.059	1.8	15 500	1.6	85 to 96	94
BR3 high burn-up program	UO_2	Zr-4	0.422	0.058	2.0	200	1.6	38.4	95

Table A.3.1-2 Achieved Burnup and Linear Heat Rate for Experimental Fuel

fuel	Proof Test			High Burnup Program
	Saxton Loose Lattice	Saxton Parametric	Zorita	BR3
Burnup (GWd/t) *	51	26	63	70
Linear Heat Rate (kW/ft)	21	17	15	16

* Pellet peak

Table A.3.1-3 Saxton Fuel Rod Irradiation Experience

No. of Fuel Rods	Maximum Burnup *(GWd/t)	Maximum Linear Heat Rate (kW/ft)
2	51	17.2
49	42 to 45	18.2 to 21.2
42	40 to 44	16.3 to 18.6
60	40 to 43	14.3 to 16.2
76	39 to 42	10.6 to 14.2
20	38 to 41	<10.6

*Pellet peak at the end of Core III lifetime

Table A.3.1-4 High Burnup Irradiation Experience for Overseas PWR Fuel [11]
(Extended Burnup Irradiation of Current Design Fuel)

(As of April 1991)

Power company/ Fuel vender*/ Operating plants	Number of assemblies (Number of fuel rods)	Mean burnup (GWd/t)
Duke Power/B&W/Oconee-1	4	40.0
	1	50.6
Omaha Public Power District/ CE/Fort Calhoun	1	52.1
Baltimore Gas & Electric/ CE/Calvert Cliffs-1	2	42.8
	(8)	50.1
Arkansas Power & Light/ CE/ANO 2	1	44.8
Caroline Power & Light/ Exxon/H. B. Robinson-2	3	40.3
	1	47.7
Commonwealth Edison/ WH/Zion-1 & 2	4	54.8
Virginia Electric & Power/ WH/Surry-2	1	42.5
(None)/WH/BR-3	(5)	57.0
Virginia Electric & Power/ WH/North Anna-1	4	58.0

* Fuel manufacturers
B&W: Babcock & Wilcox
CE : Combustion Engineering
WH : Westinghouse Electric Corp.

A.4.0 MITSUBISHI COMMERCIAL PWR FUEL IRRADIATION EXPERIENCE

Over 3.6 million Mitsubishi fuel rods have been irradiated in commercial PWR's in Japan since the first region of Mitsubishi fuel was supplied to Mihama Unit 1 in 1969. The irradiation experience for Mitsubishi fuel discharged after operation in plants in Japan, from that initial region of fuel in Mihama in 1970 through March 2007, is presented in Table A.4-1. The year when Mitsubishi fuel began irradiation in each plant is identified, along with the plant power rating and the assembly lattice. The maximum assembly average burnup achieved by the Mitsubishi fuel in each plant is included in the table along with the region in which that burnup was achieved. All of the irradiation experience summarized in the table was achieved while the licensing limit for assembly average burnup in Japan was 48 GWd/t. Consistent with that limit, the maximum assembly average burnup achieved in the commercial operation summarized in the table is 47.6 GWd/t for 17X17 UO_2 fuel operating in Tsuruga Unit 2. The maximum assembly discharge burnup for 14X14 and 15X15 UO_2 fuel is 47.3 GWd/t and 46.8 GWd/t, respectively.

Mitsubishi has accumulated substantial fuel performance experience with gadolinia doped fuel as integral fuel burnable absorbers. In Table A.4-1 the maximum assembly average burnup is given for fuel assemblies with gadolinia rods in each plant. Assembly average burnups from 45 to 47 GWd/t in assemblies with 6 wt% gadolinia concentration have been achieved in all commercial reactors.

Higher burnup fuel, with design assembly average burnup limit of 55 GWd/t, was introduced to Japanese PWR's beginning in 2004 for 17x17 type and in 2005 for 14x14 type. This fuel design uses 97 %TD UO_2 fuel with improved cladding. Mitsubishi is using two advanced zirconium based alloys (ZIRLO and MDA) for high burnup fuel designs in Japan

Table A.4-2 provides a summary of the Lead Use and/or test rod irradiation experience for both ZIRLO and MDA alloys. Up to 75 GWd/t rod average burnup has been achieved for both of these alloys. On the basis of these successful test irradiations, several batch size quantities of both ZIRLO and MDA cladding have been fabricated for high burnup (55 GWd/t assembly average) operation in Japan, as summarized in.

Table A.4-3 shows the manufacturing and irradiation experience for both ZIRLO and MDA alloys. A total of 48,300 ZIRLO clad rods have been fabricated, with 22,973 of those rods under irradiation up to March 2007, although 113,128 fuel rods with MDA cladding have been fabricated, and 59,889 of those rods were under irradiation.

The ZIRLO cladding material is already in extensive use, and 11,000 or more fuel assemblies were using ZIRLO clad fuel rods by March 2003[26] in commercial reactor.

Table A.4-1 Mitsubishi PWR Fuel Irradiation Experience

(as of March 2007)

Plant	Start of operation (year)	Power output (MWe)	Fuel rod array	Current cycle	Irradiation experience of uranium fuel assembly		Irradiation experience of fuel assembly including gadolinia doped fuels***	
					Maximum Assembly Burnup*(GWd/t)	Region	Maximum Assembly burnup*(GWd/t)	Region
Mihama #1	1970	340	14 x 14	20	46.4	R14	45.6	R17
Mihama #2	1972	500	14 x 14	23	41.4	R22	44.5	R19
Mihama #3	1976	826	15 x 15	22	46.8	R19	45.0	R16
Takahama #1	1974	826	15 x 15	25	46.0	R16	44.6	R20
Takahama #2	1975	826	15 x 15	24	46.7	R16	44.9	R22
Takahama #3	1985	870	17 x 17	18	46.4	R14	46.9	R8
Takahama #4	1985	870	17 x 17	17	46.4	R16	46.7	R13
Ohi #1	1979	1,175	17 x 17	21	46.3	R17	47.2	R17
Ohi #2	1979	1,175	17 x 17	21	46.4	R20	46.4	R16
Ohi #3	1991	1,180	17 x 17	13	47.1	R6	47.3	R9
Ohi #4	1993	1,180	17 x 17	11	47.1	R8	52.1**	R6
Genkai #1	1975	559	14 x 14	25	47.2	R20	46.6	R24
Genkai #2	1981	559	14 x 14	21	47.4	R17	47.0	R20
Genkai #3	1994	1,180	17 x 17	11	47.1	R9	47.2	R4
Genkai #4	1997	1,180	17 x 17	8	47.3	R7	47.0	R4
Sendai #1	1984	890	17 x 17	18	47.5	R17	47.3	R15
Sendai #2	1985	890	17 x 17	17	47.4	R15	47.6	R11
Ikata #1	1977	566	14 x 14	24	47.3	R16	45.0	R21
Ikata #2	1982	566	14 x 14	20	47.0	R19	45.3	R17
Ikata #3	1994	890	17 x 17	10	47.3	R3	47.0	R8
Tomari #1	1989	579	14 x 14	14	47.3	R11	45.3	R8
Tomari #2	1991	579	14 x 14	13	47.0	R8	46.4	R7
Tsuruga #2	1987	1,160	17 x 17	16	47.6	R7	46.4	R8

* Irradiation experience under licensing for design limited assembly burnup of 48 GWd/t

** This is maximum assembly burnup of high burnup LUA

*** 12,16 and 16 gadolinia doped fuel rods are included in 14x14,15x15 and 17x17 fuel type, respectively.

Table A.4-2 Irradiation Experience for Improved Cladding

(Numbers in parentheses are the number of fuel rods)

Reactor \ Cladding	ZIRLO*2	MDA
BR3	About 63 GWd/t (12)	-
BR2	-	About 16 GWd/t (2)
North Anna	About 62 GWd/t (29)	About 27 GWd/t (4)
Vandellos 2 Long fuel rod	About 57 GWd/t (48) About 75 GWd/t *1 (6 of the above 48)	About 57 GWd/t (16) About 75 GWd/t*1 (4 of the above 16)
Vandellos 2 Segmented fuel rod	About 62 GWd/t (56)	About 62 GWd/t (84)
Ohi unit 4	About 56 GWd/t (178)	About 57 GWd/t (298)

*1: Pellet peak burnup: About 80 GWd/t

*2: For ZIRLO, fuel rod burnup of 65 GWd/t or more has been achieved for about 11,000 or more in PWR outside Japan .

Table A.4-3 Mitsubishi PWR Fuel Irradiation Experience (ZIRLO and MDA)

(as of March 2007)

Plant*	Number of rods manufactured		Number of rods irradiated		Current cycle
	ZIRLO	MDA	ZIRLO	MDA	
Ohi #1	–	13,728	–	3,168	1
Ohi #2	4,224	20,064	4,224	10,560	2
Ohi #3	4,224	21,120	4,224	12,672	2
Ohi #4	4,224	19,008	4,224	13,728	2
Genkai #1	1,432	5,012	1,432	4,296	2
Sendai #1	3,960	3,960	–	–	–
Sendai #2	4,488	4,488	–	–	–
Ikata #1	7,160	7,160	2,327	3,043	2
Ikata #2	6,444	6,444	1,790	6,086	2
Ikata #3	12,144	12,144	4,752	6,336	2
Total	48,300	113,128	22,973	59,889	–
Total	161,428		82,862		–

* Plants licensed for assembly design burnup of 55 GWd/t

A.5.0 CONCLUSION

Since Mitsubishi delivered their first fuel assemblies to Mihama Unit 1 in 1969, it has accumulated substantial fuel manufacturing and irradiation experience. A strong commitment to understanding fuel and cladding design and performance has resulted in the development of a large fuel performance database spanning the full range of PWR core operation, through participation in joint industry development programs and through an ongoing series of fuel examination programs in Japan. This database has been used to validate Mitsubishi fuel performance models and to provide a basis for developing improved fuel design. The reliability of Mitsubishi fuel has been continuously improved through design changes and manufacturing improvements, resulting in consistently excellent fuel performance, as demonstrated by achieving near zero fuel leakage rates.

A.6.0 REFERENCE

(1) T. Shimomura, J.Shimizu,H. Kuwahara "DESIGN IMPROVEMENTS OF MITSUBISHI FUEL ASSEMBLIES: CHALLENGES FOR NO FUEL LEAK", the 2004 International Meeting on LWR Fuel Performance Orlando, Florida, September 19-22, 2004
(2) S.Abeta,R.Fukuda,K.Kita,"DESIGN AND PERFORMANCE OF MITSUBISHI PWR FUEL FOR INCRESED RELIABILITY",ANS 1997
(3) I. NAKAJIMA1,* , H.TESHIMA1, M.YAMADA "Improvement and Innovation of Mitsubishi PWR Fuel" Proceedings of the 2005 Water Reactor Fuel Performance Kyoto, October 3-7, 2005. Paper 1037
(4) W.J. Bailey and M.S. Dunenfeld, "Fuel Performance Report for 1991," NUREG/CR-3950 Vol. 9 PNL-5210
(5) W. Slagle, "OPERATIONAL EXPERIENCE WITH WESTINGHOUSE CORE (Trough December 31, 1994)", WCAP-8183 Rev. 23 (1996)
(6) M. G. Balfour et al., "Zorita Research and Development Program Final Report", WCAP-10180,1982
(7) M. G. Balfour et al., "BR-3 High Burnup Fuel Rod Hot Cell Program Final Report", WCAP-10238,1982
(8) M.G.Balfour et al., Final Report "EP80-16, Hot Cell Examination of Zion FuelCycle 1 through 4, WCAP-10473",ESEERCO report, 1985
(9) U.P.Nayak et al., Final Report "EP80-16, Hot Cell Examination of Zion Fuel Cycle5, WCAP-10543",ESEERCO report, 1985
(10) J.A.Kuszyk, "Hot Cell Examination of Surry Three- and Four-Cycle 17x17 Demonstration Fuel, Volume 1: Principal Results and Evaluation", WCAP-10514, Vol.1, DOE/ET 34014-14, 1984
(11) P. M. Lang, "Review of Extended Burnup Research, Development, and Implementation in the U. S", IAEA 1984 Specialists' Meeting at Mol
(12) J.O.Barner et al., "High Burnup Effects Program Final Report ", HBEP-61, 1990
(13) P.Blanpain et al., "GAIN" Final Report, GN89/48, 1991
(14) M. Lippens, "GAP" Final Report, GP 90/28 D, 1990
(15) M.Kinoshita et al.,"High Burnup RIM Project (II) Irradiation and Examination to Investigate RIM-Structured Fuel", ANS 2000 International Topical Meeting on LWR Fuel Performance, April 2000, Park City, Utah
(16) T.Baba,T.Takahashi,H.Kubo Y.Fujiwara and Y.Kondo,"Power Cycling and Ramp Test in R-2and Mihama Unit 2 for MHI PWR Fuels". ResMechanica16(1985)231-240
(17) Y.Irisa et al., "Proving Test on the Reliability of PWR 15x15 Fuel Assemblies through Three Reactor Cycles in Japan", ANS Topical Meeting on LWR Fuel Performance, April 1988, Williamsburg, Virginia
(18) R.S. Kaiser et al., "Westinghouse High Burnup Experience at Farley-1 and Point Beach-2", ANS Topical Meeting, Williamsburg, Virginia (1988)
(19) J.Moon, "Farley Unit 1 EOC-7 ; 17x17 OFA Onsite Examinations Report",WCAP-11561, 1987
(20) Overview of the 17 x 17 Westinghouse Fuel Assembly WOJ-001, May, 1999
(21) L. V. Corsetti et al., "Improved BWR and PWR Fuel Design and Operating Experience at ABB" ANS Topical Meeting, Portland (1997)
(22) M. Morel et al., "UPDATED STATUS OF IN REACTOR EXPERIENCE OF FRAGEMA FUEL PRODUCTS" ANS Topical Meeting, West Palm Beach (1994)
(23) H. UCHIDA et al., "Segmented Fuel Irradiation Program Investigation on Advanced Materials" Top Fuel '99, Avignion

(24) Y. Irisa et al., "SEGMENTED FUEL ROD IRRADIATION PROGRAMME ON ADVANCED MATERIALS FOR BURNUP", ANS Topical Meeting, Park City, Utah (2000)
(25) T.Kitagawa,et al.,"Post irradiation examination of fuel rods in 55 GWd/t lead use assembly",2005 Water reactor Fuel Peformance Meeting,October 2005,Kyoto
(26) Hallstadius et al., "HIGH BURNUP PERFORMANCE OF ZIRLO, DUPLEX AND LK3 TYPE CLADDINGS" TOP FUEL 2003, Wurzburg, Germany (2003)
(27) T.Okubo et al.,"Irradiation Test for Verification of PWR 48GWd/t High Burnup Fuel", Journal of Atomic Energy Society of Japan Vol.43 No.9 pp.906-915 (2001)

Appendix B

MATERIAL PROPERTIES OF FUEL ROD

May 2007

Summary

This appendix describes the properties of the following material of fuel rod, for design evaluation for normal operation and anticipated operating occurences (AOOs). It is noted that the properties such as specific heat and emissivity for safety analysis and evaluation are excluded.

-Uranium dioxide (UO_2)
-Gd-Uranium dioxide ($(Gd,U)O_2$)
-ZIRLO™*

* ZIRLO™ is a registered trademark of the Westinghouse Electric Corporation.

Table of Contents

List of Tables

List of Figures

B.1.0 URANIUM DIOXIDE (UO_2)

B.1.1 Physical/Thermal Properties

B.1.1.1 Lattice Parameters

The lattice parameter for room temperature was measured as 5.47066 angstrom (0.547066 nm) for the $UO_{2.002}$ sample. This value agrees well with other reported values (5.4678 to 5.4712 angstrom (0.54678 to 0.54712 nm)).[1] - [6]
The measured results for lattice parameters of the peripheral areas of fuel pellets irradiated in a commercial reactor and a sample irradiated up to high-burnup at a low temperature of several hundred deg.F or less in a test reactor are reported.[7] The lattice parameter has been reported to increase roughly linearly with burnup, and saturate above 40 to 50 GWd/t.

B.1.1.2 Density

The crystal structure of un-irradiated uranium dioxide ($UO_{2.00}$) is fluorite (CaF_2) type face-centered cubic crystal structure, which has four uranium atoms and eight oxygen atoms. Therefore the theoretical density value of 684.21 lb/ft^3 (10.96 g/cm^3) is obtained from the value of the lattice parameter described above and average atomic weight of uranium and oxygen atoms.

B.1.1.3 Thermal Expansion

The thermal expansion coefficient is expressed by the following equation.[8]

$$\frac{\Delta L}{L_0} = \left\{ \qquad \right\} \cdots (1-1)$$

Where,
T: Temperature (deg.F)

The thermal expansion coefficients calculated by this equation and the recommended equation in MATPRO[9] are shown in Figure B.1.1-1. The both coefficients agree well each other. Concerning the change in the thermal expansion coefficient with burnup, the correlation between changes in stack length and fuel center temperature measured in fuel irradiation tests at the Halden reactor is shown in Figure B.1.1-2, together with the slope of the thermal expansion coefficient for un-irradiated material. The slopes of the relation between the changes in stack length and central temperature are almost constant independent of burnup, which means the change in the thermal expansion coefficient is also independent of burnup because the slope is an index of the change in the thermal expansion coefficient. Therefore, we can see that the thermal expansion coefficient of UO_2 fuel is independent of burnup.

B.1.1.4 Melting Point

Uranium dioxide has a fluorite (CaF_2) type face-centered cubic crystal structure, and the melting point of the un-irradiated material is reported to be approximately from 5,072 to 5,180 deg.F (2,800 to 2,860 deg.C).[10] - [12]
Conventionally, the melting point of UO_2 is reported to decrease with burnup as shown in Figure B.1.1-3 due to accumulation of FP.[10] - [13] In the most recent reports,[14], [15] the change in the melting point with burnup is small up to a burnup of about 45,000 MWd/t. In the fuel design, melting point decrease of 57.6 deg.F /(10,000 MWd/t) (32 deg.C /(10,000 MWd/t)) is applied in

view of the safety margin. The Christensen's data shown in the figure has large scattering and the value below 5072 deg.F (2800 deg.C) is included among them. It is considered that the cause of this large scattering is due to the measurements conducted in open system, which has relatively large uncertainties. It is confirmed that the melting point of un-irradiated UO_2 is well above 5072 deg.F (2800 deg.C) as later shown in Figure B.2.1-4.

B.1.1.5 Thermal Conductivity

The thermal conductivity of uranium dioxide pellets is considered to be mainly governed by phonon conduction on the low-temperature region and electron conduction on the high-temperature region. In addition, for phonon conduction, the equation comprises a temperature-independent term due to phonon-crystal lattice scattering and a term that is proportional to temperature due to temperature phonon-phonon scattering. Considering these phenomena, the thermal conductivity equation for UO_2 is defined based on the data reported in references [16] - [28].

Furthermore, thermal conductivity in the high-temperature region is represented by the integration quantity up to the melting point. We conclude that the value of $\int_{0℃}^{2800\,℃} k\,dt$ is 2.8 kW/ft (93 W/cm) based on the data reported in references [28] - [33].
The result of the above is that the thermal conductivity for 95 % TD is defined by the following equation (same as reference(8)).

$$k = 57.8 \times \left(\frac{1}{11.8 + 0.0238 \times (T - 32) \times \frac{5}{9}} + 8.775 \times 10^{-13} \cdot ((T - 32) \times \frac{5}{9})^3 \right) \cdots\cdots (1-4)$$

Where,

K : UO_2 thermal conductivity(BTU/(ft·hr·deg.F))
T : UO_2 temperature(deg.F)

The temperature dependence of the thermal conductivity according to this model equation is shown in Figure 4.2.1.5-1. The region from zero to 2,372 deg.F (1,300 deg.C) agrees well with the recommended values of IAEA.[34] In addition, the thermal conductivity from the design model agrees well with the one from the equation recommended by MATPRO which gives relatively small value at high temperature of melting point as shown in Figure B.1.1-4.

The latest understanding indicates that thermal conductivity decreases with burnup and the thermal conductivity is affected by a change in the microstructure of the pellet rim (the rim effect; increased porosity).[35] - [37]

Concerning the decrease in pellet thermal conductivity with burnup, a model equation based on measured values of the center temperature of fuel irradiated up to 80,000 MWd/t is recommend by the Halden Project.[36] With reference to that, the FP elements that accumulate with burnup are considered to affect the thermal conductivity by the phonon scattering effect caused by impurities. This is taken into account as the "11.8 +β·Bu" in the following equation, the pellet thermal conductivity model.

$$k_{95} = 57.8 \times \left(\frac{1}{11.8 + \beta \cdot Bu + 0.0238 \cdot (T - 32) \times \frac{5}{9})} + 8.775 \times 10^{-13} \cdot ((T - 32) \times \frac{5}{9})^3 \right)$$

..... (1 - 5)

Where,

k_{95} :Thermal conductivity of 95 % TD density pellet (BTU/(ft·hr·deg.F))

T : Uranium dioxide pellet temperature (deg.F)

Bu : Burnup (GWd/tUO_2)

β : 0.35 ((deg.C·cm/W)/(GWd/t UO_2))

Eq. (1-5) is normalized to a pellet density of 95 % TD ; for pellets of other density or pellets whose density (porosity) have changed due to densification and swelling, the thermal conductivity is corrected by the following Bakker model. [38]

$$\frac{k}{k_{100}} = (1-P)^n \quad \cdots\cdots (1-6)$$

P : Porosity, n = 1.7

k : Thermal conductivity for porosity P

k_{100}: Thermal conductivity for 100 % theoretical density (porosity 0 %)

B.1.2 Chemical Properties

B.1.2.1 Reaction between Uranium Dioxide Pellets and Zr Based Alloy

When zirconium based alloy and uranium dioxide are in contact, the excess oxygen in the uranium dioxide produced by irradiation diffuses into the zirconium based alloy and zirconium oxidation layer (ZrO_2) forms on the inside surface of the cladding. Furthermore, if the two materials are in strong contact, diffusion of uranium into the zirconium oxidation layer converts the zirconium oxidation layer into a (Zr, U) O_2 solid solution. That creates a bonding layer and causes adhesion between the pellets and the cladding.[39] That is considered to affect cladding corrosion and PCI.

Nevertheless, it has been reported that no reaction occurs even after about 500 days of close contact between uranium dioxide pellets and zirconium at 950 deg.F (510 deg.C) for un-irradiated materials.[4] In normal operation, the temperature of the surface of the pellets in contact with the cladding and with the cladding end plug does not exceed 932 deg.F (500 deg.C) for long periods of time, so the reaction is considered to be small.

Although oxidation and bonding of the inner surface of Zircaloy-4 and ZIRLO cladding fuel rods irradiated to about 60,000 MWd/t has been found in commercial reactors, the reaction layer is at most only 0.47 mil (12 μm) thickness as shown in Fig 4.2.4.5-1, and has little effect on cladding stress.

The reaction of Zircaloy-4 and ZIRLO cladding with uranium dioxide pellets originates in the diffusion of uranium atoms and zirconium atoms as described above, and thus has virtually no effect on the pellet density.

B.1.2.2 Reaction between Uranium Dioxide Pellet and the Filling Gas

In the fuel rod fabrication process, the air within the fuel rod is replaced with helium and helium is filled to the specified pressure. Helium is an inert gas and does not react with the uranium dioxide pellets. Although some air remains in the fuel rod even after the replacement with helium, the results of post-irradiation tests on fuel rods manufactured by the process described above do not show any effect on the uranium dioxide pellets due to the reaction with the air component. [40], [41]

B.1.2.3 Reaction between Uranium Dioxide Pellets and Water

When the cladding is damaged during the irradiation in the light water reactor, the primary coolant (water) could permeate into the fuel rod and the possibility of reaction with the uranium dioxide pellets is considered.

For uranium dioxide, the oxygen to uranium ratio is in the wide range from 1.75 to 2.3 - 2.4 and the crystal structure (fluorite type crystal structure) does not change. From the lattice parameter measurements, it is known that an increase in the oxygen to uranium ratio is accompanied by a slight decrease in volume.[42]

Concerning the behavior of uranium dioxide pellets in high-temperature water at approximately 644 deg.F (340 deg.C), there is a clear dependence on the amount of dissolved oxygen in the environmental water and no corrosion occurs in the low-oxygen region of about 0.01 ppm.[43] Furthermore, the increase in mass was reported to be 0.03 %, or converted to the oxygen to uranium ratio increase of about 0.005, in immersion tests in the same high-temperature water for about one year.[4] Accordingly, if the oxygen to uranium ratio changes to that degree, the pellet structure does not change and there is no increase in volume.
And the crystal structure and lattice parameters do not change in case of higher density pellets than 95 % TD. Therefore the reaction of higher density pellet with water is considered to be the same as for 95 % TD uranium dioxide pellets.

The amount of dissolved oxygen is controlled to 5 ppb or less in the primary coolant that is actually used, so it is considered that there is no reaction between the primary coolant and the uranium dioxide pellets.

While it is considered possible that radiation might promote the chemical reaction between the uranium dioxide pellets and the primary coolant by generating oxygen through decomposition of the coolant water, hydrogen is injected into the coolant to control the generation of oxygen in a pressurized light-water reactor (PWR). Therefore, there is no promotion of reaction by the irradiation.

B.1.3 Mechanical Properties

B.1.3.1 Young's Modulus (Elasticity)

Concerning the Young's modulus of stoichiometric UO_2, the model equations depending on porosity and temperature are recommended.[8]
For the porosity dependence, the following equation is used.

$$E(P) = 3.248 \times 10^7 (1-2.277P)$$

For the temperature dependence, the following equation is used.

$$E(T) = E(P) \cdot (1-0.000103x(T-32)x5/9)$$

Where,

E: Young's modulus (psi)
P: Pellet porosity (-)
T: Temperature (deg.F)

B.1.3.2 Poisson's Ratio

The Poisson's ratio is defined from the Young's modulus and the shear modulus by the following equation.

$$\mu = \frac{E}{2G} - 1$$

The Poisson's ratio is expressed as follows, using the equations described above.[8]

$$\mu = (0.361-1.439\ P)/(1-1.660\ P)$$

P: Pellet porosity (-)

B.1.4 Consideration of Pellet Densification and Cladding Collapse

To prevent creep collapse, the allowable gap of pellet to pellet in the axial direction must be below[ ] [44]. In addition, if the pellet-pellet gap is[ ]or less, the power peaking due to the axial gap is increased by [ ] or less [44].

Therefore, if the axial gap is small enough, the power peaking factor S(z) can be set as with 1.0.

The results of post Irradiation Examination for Mitsubishi fuel with pellet density of 95 %TD irradiated in TAKAHAMA Unit-3 [45] indicate that significant axial gaps are not observed. Achieved burnup of these fuel rods are shown in Table B.1.1-1. The result of the gamma scanning measurements do not show any significant axial gaps as shown in Figure B.1.1-5 and Figure B.1.1-6. Additionally, to investigate the detail of the axial gap, the X-ray permeation tests were carried out, and summarized in Table B.1.1-2. The results show that the maximum gap is 0.024 inch (0.6 mm; 2Cy Rod) and 0.063 inch (1.6 mm; 3Cy Rod).

In-core measurement by Movable Detector (M/D) [46] for 7376 fuel assemblies detected 107 small signals which might include noises as shown in Table B.1.1-3. Figure B.1.1-7 shows that the axial distribution of the blips. It is not easy to determine the axial gap size from the M/D signals, but in-core measurement indicates that the axial gap is quite small and that the Mitsubishi Fuels with pellet density of 95%TD are quite stable against the axial large gaps.

Therefore, Mitsubishi fuel has less probability to occur larger than axial gap of[ ] [ ] which influence on the power peaking or axial gap of [ ] at which the creep collapse occur.

As higher density pellet has less densification, the occurrence of creep collapse or power peaking increase due to the axial gaps is negligible for Mitsubishi fuel with pellet density of 97 %TD,.

B.1.5 References

(1) S. Fukushima et al., "The effect of gadolinium content on the thermal conductivity of near-stoichiometric (U,Gd)O_2 solid solutions", Journal of Nuclear Materials, 105 (1982) 201

(2) R.J. Beals et al., "Solid solutions in the system Uranium-Rare-Earth oxides: I, UO_2-$GdO_{1.5}$", Journal of the American Ceramic Society, 48 (1965) 271

(3) K. Suzuki et al., "Activated sintering of Uraniu dioxide fuel, (III) Measurement of lattice constant by X-ray ", Journal of the Atomic Energy Society of Japan, 5 (7) 1963, p. 587

(4) J. Belle (Ed.), "Uranium Dioxide, Properties and Nuclear Applications" USAEC (1961), Chapter 5 W.H.Duckworth (Ed), "Physical Properties of Uranium Dioxide", P173

(5) T. Ohmichi, et al., "On the relation between lattice parameter and O/M ratio for uranium dioxide-trivalent rare earth oxide solid solution ", Journal of Nuclear Materials, 102 (1981) 40

(6) T. Wada, et al., "Behaviour of UO_2-Gd_2O_3 fuel", Proc. Intern. Conf. on Nuclear Fuel Performance, London, 1973, p. 63.1

(7) K. Une, et al., "Microstructural change and its influence on fission gas release in high burnup UO_2 fuel ", Journal of Nuclear Materials, 188 (1992) 65-72

(8) P.J.Kuchirca, "Properties of Fuel and Core component Materials", WCAP-9179,revision 1,WCAP-9224(Non proprietary)

(9) MATPRO-Version11(Rev.2), "A Handbook of Materials Properties for Use in the Analysis of Light Water Reactor Fuel Rod Behavior", NUREG/CR-0497, Tree-1280, Rev.2, 1981

(10) J.A. Christensen et al., "Melting Point of Irradiated Uranium Dioxide", WCAP-6065 UC-25, Metals, Ceramics and Materials, 1965

(11) J.L. Bates, "Melting Point of Irradiated Uranium Dioxide", Journal of Nuclear Materials, 36, 1970, pp. 234-236

(12) R.E. Latta et al., "Determination of Solidus-Liquidus Temperatures in the UO_{2+x} System (-0.50<X<0.20)", Journal of Nuclear Materials, 35, 1970, pp. 195-210

(13) J.A. Christensen, "Irradiation Effects on Uranium Dioxide Melting", HW-69234 UC-25, Metals, Ceramics and Materials, 1962

(14) S. Yamanouchi et al., "Melting Temperature of Irradiated UO_2 and UO_2-2wt%Gd_2O_3 Fuel Pellets up to Burnup of about 30GWd/tU", Journal of Nuclear Science Technology, 25, 6, 1988, pp. 528-533

(15) Harada et al., "Development of Equipment for Measuring the Melting Point of High-burnup Fuel Pellets," JAERI-Tech 2000-031, 2000

(16) V.C. Howard and T.F. Gulvin, "Thermal Conductivity Determinations on Uranium Dioxide by a Radial Flow Method", UKAEA IG Report 51 (RD/C) (1961)

(17) R.W. Dayton, C.R. Tipton, Jr., "Progress Relating to Civilian Applications during June 1960", July 1 1960, BMI - 1448 (rev.)

(18) J.L. Daniel, J. Matolich, Jr., and H.W. Deem, "Thermal Conductivity of UO_2", HW-69945, September (1962)

(19) A.D. Feith, "Thermal Conductivity of UO_2 by a Radial Heat Flow Method", TM63-9-5 (1963)

(20) J. Vogt, L. Grandell and U. Runfors, "Determination of the Thermal Conductivity of Nonirradiated Uranium Dioxide", AB Atomenergi Report RMB-527, 1964. (Quoted by IAEA Technical Reports Series No. 59 on Thermal Conductivity of Uranium Dioxide.)

(21) T. Nishijima, T. Kawada and A. Ishihata, "Thermal Conductivity of Sintered $U0_2$ and Al_20_3 at High Temperatures", J. Amer. Ceram. Soc., Vol. 48, No. 131-34 (1965)

(22) J.B. Ainscough and M.J. Wheeler, "The Thermal Diffusivity and Thermal Conductivity of Sintered Uranium Dioxide", The Seventh Conference on Thermal Conductivity, p. 467, National Bureau of Standards, Washington (1968)

(23) T.G. Godfrey, W. Fulkerson, T.G. Kollie, J.P. Moore and D.L. McElroy, "Thermal Conductivity of Uranium Dioxide and Armco Iron by an Improved Radial Heat Flow Technique", ORNL - 3556, June (1964)

(24) J.P. Stora, B. de Bernardy de Sigoyer, R. Delmas, P. Deschamps, C. Ringot and B. Lavaud, "Thermal Conductivity of Sintered Uranium Oxide under In-Pile Conditions" EURAEC-1095 (1964)

(25) A.J. Bush, "Apparatus for Measuring Thermal Conductivity to 2500 deg.C," Westinghouse R&D Report 64-1P6-401-R3, February (1965)

(26) R.R. Asamoto, F.L. Anselin and A.E. Conti, "The Effect of Density on the Thermal Conductivity of Uranium Dioxide", GEAP-5493, April (1968)

(27) O.L. Kruger, "Heat Transfer Properties of Uranium and Plutonium Dioxide", Paper 11-N-68F presented at the Fall Meeting of Nuclear Division of the American Ceramic Society, September 1968, Pittsburgh

(28) J.A Gyllander, "In-Pile Determination of the Thermal Conductivity of $U0_2$ in the Range 500-2500 Degrees Centigrade", AE-411, January (1971)

(29) M.F. Lyons et al., "UO_2 Powder and Pellet Thermal Conductivity During Irradiation", GEAP-51 00-1. March (1966)

(30) D.H Coplin et al., "The Thermal Conductivity of UO_2 by Direct In-reactor Measurement", GEAP - 5100-6, May (1968)

(31) R.N. Duncan, "Rabbit Capsule Irradiation of UO_2" June (1962)

(32) A.S. Bain "The Heat Rating Required to Produce Central Melting in Various UO2 Fuels", ASTM Symposium on Radiation Effects in Refractory Fuel Compounds, Atlantic City, June 1961, pp. 30-46, American Society for Testing and Materials, Philadelphia (1962), (ASTM STP 306)

(33) J. P. Stora. "In-Reactor Measurement of the Integrated Thermal Conductivity of UO_2 Effect of Porosity", Trans. Amer. Nucl. Soc. 13, 137 (1970)

(34) International Atomic Energy Agency, "Thermal Conductivity of Uranium Dioxide", Report of the Panel held in Vienna, April 1965, IAEA Technical Report Series, No.59 Vienna(1966)

(35) T. Tverberg et al., "Study of Thermal Behavior of UO_2 and (U, Gd) O_2 to High Burnup (IFA - 515)", HWR-671, Enlarged HPG Meeting, March 2001, Lillehammer

(36) W. Wiesenack, "Assessment of UO_2 Conductivity Degradation Based on In - Pile

Temperature Data", ANS 1997 International Topical Meeting on LWR Fuel Performance, March 1997, Portland, Oregon

(37) Kitajima et al., "Irradiation Research on the High-burnup Fuel Rim Effect (HBRP) (3)-Measurement of thermal diffusivity in high-burnup fuel and a thermal conductivity evaluation equation-", Atomic Energy Society of Japan, 2002 Annual Spring Conference, March 2002, Kobe University

(38) K. Bakker et al., "Determination of a Porosity Correction Factor for the Thermal Conductivity of Irradiated UO_2 Fuel by means of the Finite Element Method", Journal of Nuclear Materials, 226, 1995, pp. 128-143

(39) Nuclear Safety Research Association "Behavior of Light-water Reactor Fuel," Practical Text Series No. 3, Jul. 1998

(40) S. Doi et al., "High Burnup Experience of PWR Fuel in Japan", ANS/ENS International Topical Meeting on LWR Fuel Performance, April 1991, Avignon, France

(41) Y. Mishima et al., "Reliability testing of fuel assemblies for pressurized water reactors," Journal of the Atomic Energy Society of Japan 31 (1989) 1129

(42) M. Hasegawa and Y. Mishima, "Nuclear Reactor Materials Handbook," Nikkan Kogyo Shinbun

(43) Atomic Energy Society of Japan, 1995 Spring Conference Proceedings, L45, "Corrosion behavior of un-irradiated pellets in high-temperature pressurized water," (March 28-30, 1995, University of Tokyo)

(44) S.L.Davidson, R.L.Oelrech, P.J.Kersting, "Assessment of Clad Flattening and Densification Power Spike Factor Elimination in Westinghouse Nuclear Fuel", WCAP-13589-A, March 1995

(45) Nuclear Power Engineering Corporation, 1997 Report on Verification Testing for Improved Light-water Reactor Technology (concerning high-burnup fuel, etc.), March 1998, in Japanese

(46) Mitsubishi Heavy Industries, LTD., "Assessment of Power Spike due to Pellet Densification", MHI-NES-1002, Revised1, April, 1992

Table B.1.1-1 Achieved Burnup in Takahama-3 Program

2CY Irradiation Fuels

Type	Rod ID	Burnup (GWd/t)
S	F13	34.8
	J07	32.2
	L13	34.4
M	E12	34.7
	F11	34.1
	I11	34.0
	J08	32.5
	K08	32.3
	M12	34.2
Es	G11	23.4
Em	K07	22.7
	K11	23.2

3CY Irradiation Fuels

Type	Rod ID	Burnup (GWd/t)
S	F13	46.0
M	E12	46.2
Es	G11	33.2
Em	K07	32.7

S : UO_2 Pellet / Standard Zr-4 Cladding
M : UO_2 Pellet / Low Sn Zr-4 Cladding
Es: Gd Pellet / Standard Zr-4 Cladding
Em: Gd Pellet / Low Sn Zr-4 Cladding

Table B.1.1-2 Pellet-Pellet Gap from Takahama-3 Program by X Ray Photographs Measurements

2CY Irradiation Fuels

Type	Rod ID	Pellet-Pellet Gap	
		Number of Gaps	Maximum Gap Size
S	F13	0	-
	J07	0	-
	L13	0	-
M	E12	0	-
	F11	5	0.024inch (0.6mm)
	I11	0	-
	J08	0	-
	K08	0	-
	M12	0	-
Es	G11	0	-
Em	K07	0	-
	K11	0	-

3CY Irradiation Fuels

Type	Rod ID	Pellet-Pellet Gap	
		Number of Gaps	Maximum Gap Size
S	F13	7	0.028inch (0.7mm)
M	E12	4	0.024inch (0.6mm)
Es	G11	20	0.039inch (1.0mm)
Em	K07	18	0.063inch (1.6mm)

S : UO_2 Pellet / Standard Zr-4 Cladding
M : UO_2 Pellet / Low Sn Zr-4 Cladding
Es: Gd Pellet / Standard Zr-4 Cladding
Em: Gd Pellet / Low Sn Zr-4 Cladding

Table B.1.1-3 In-Core Measurement by M/D

Plant/cycle	Date of measurements	M/D traces read	No. of blips
KON-2/Cy11	H5.4.6	58	3
	H5.5.10	58	2
	H5.6.7	58	3
	H5.7.6	58	2
KON-2/Cy12	H6.6.24	58	1
	H6.8.4	58	3
	H6.10.6	58	4
	H6.12.6	58	1
	H7.2.3	58	1
KTN-2/Cy14	H5.3.6	50	12
	H5.4.14	50	9
	H5.7.13	50	12
	H5.8.9	50	6
	H5.11.15	50	14
	H5.12.9	50	10
KTN-2/Cy15	H7.1.27	50	16
	H7.8.16	50	8
Total	**17**	**922**	**107**

Each M/D signal detected the gap occurrence in 8 of the surrounding rods

The blip size, in percent, is defined as follows;

$$\text{Blip size} = \frac{\text{Measured} - \text{Nominal}}{\text{Nominal}} \times 100$$

Measured is the flux level as recorded on the trace
Nominal is the flux level with no gap present.

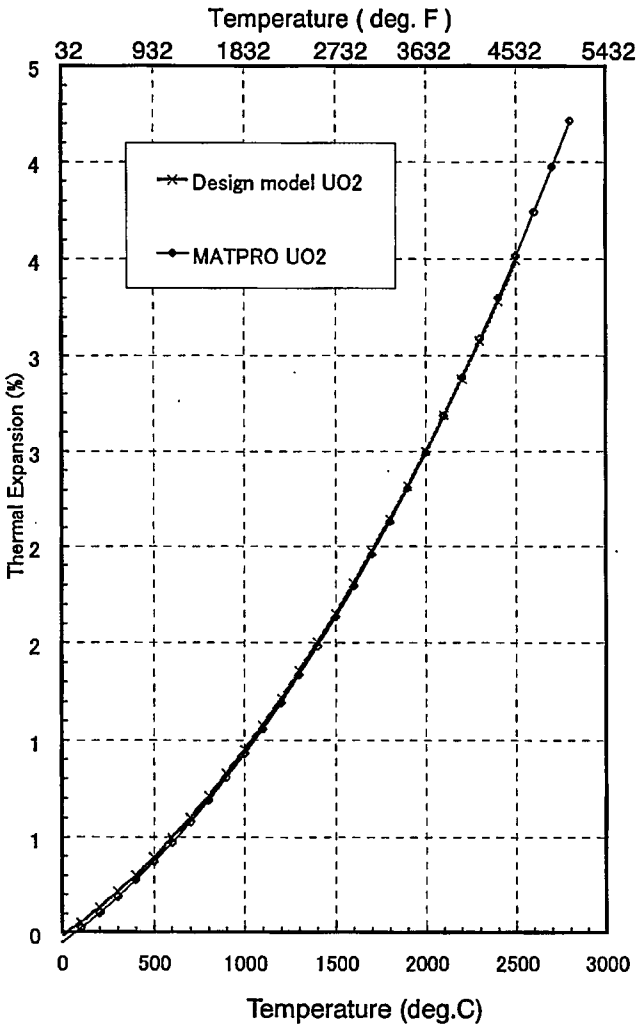

Figure B.1.1-1 Thermal Expansion of Uranium Dioxide Pellets

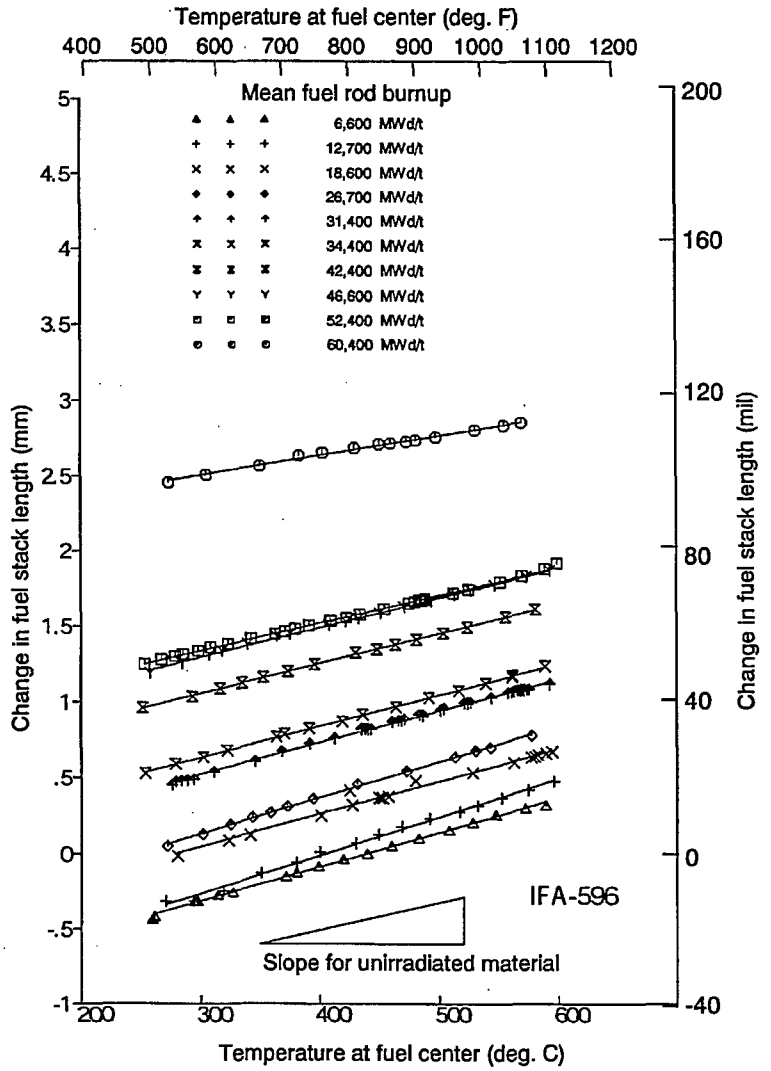

Figure B.1.1-2 Correlation of the Change in UO_2 Pellet Fuel Stack Length and Fuel Center Temperature (From Results of Fuel Irradiation Tests at the Halden Reactor)

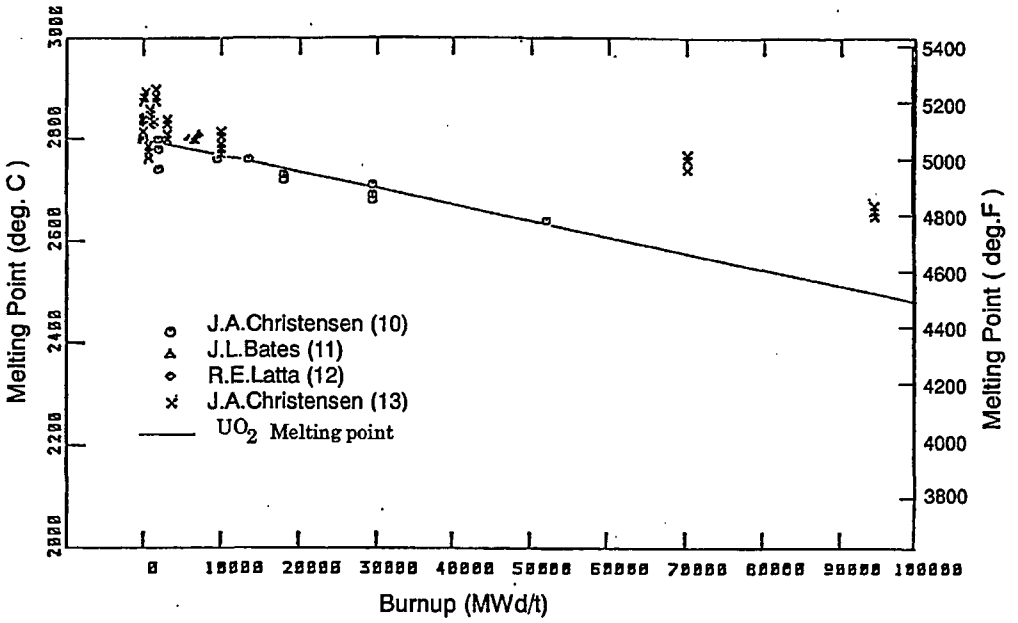

Figure B.1.1-3 The UO_2 Pellet Melting Point with Burnup[10] - [13]

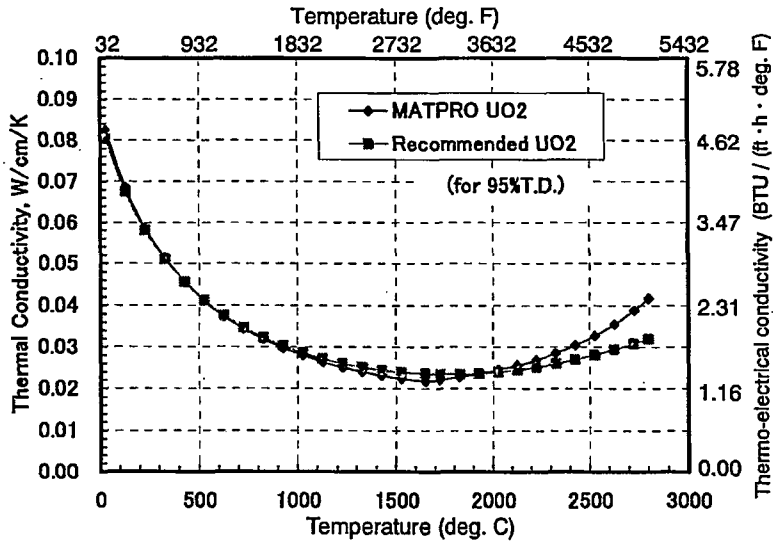

Figure B.1.1-4 Comparison with the Reported Thermal Conductivity of Uranium Dioxide

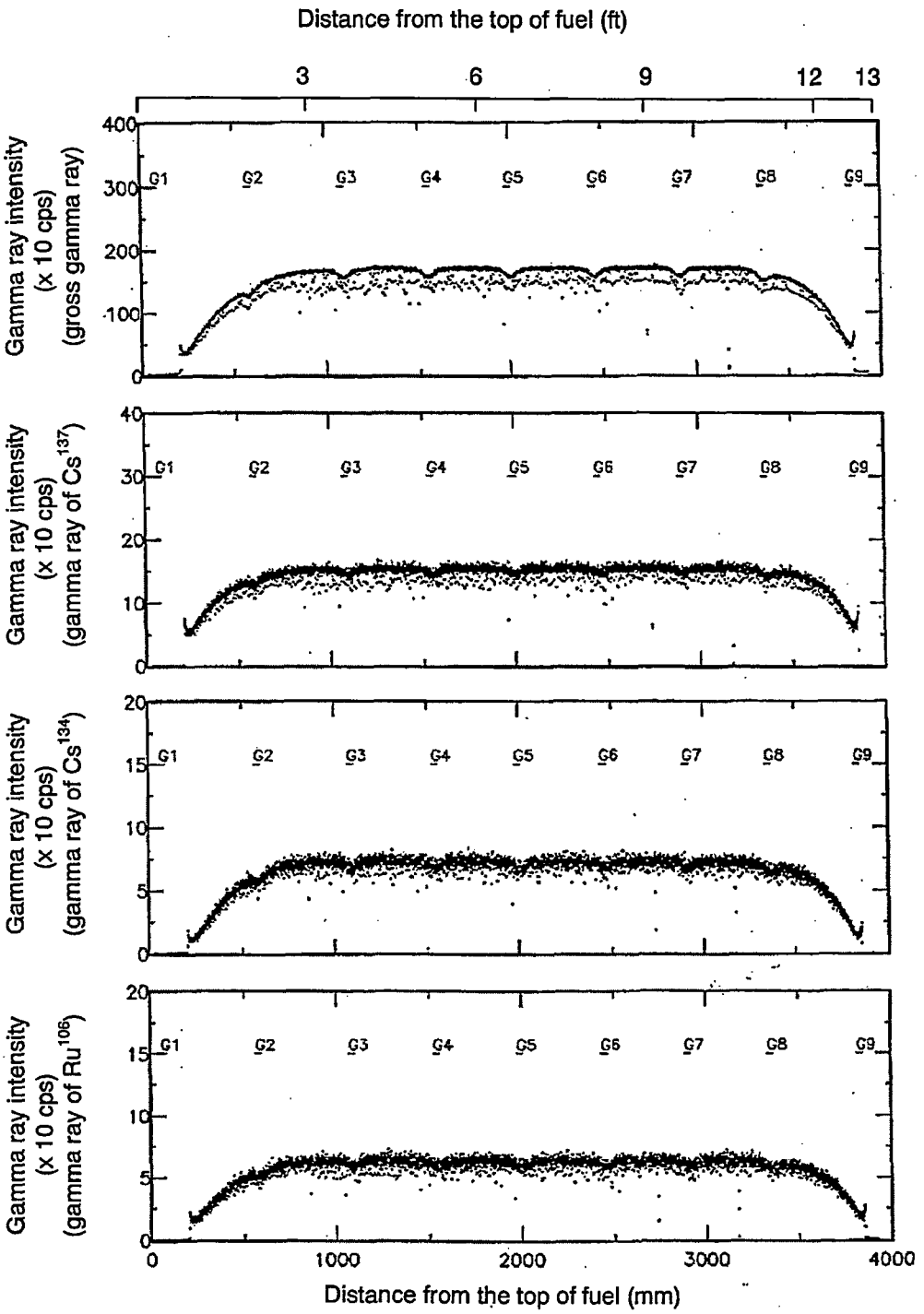

Figure B.1.1-5 Result of Gamma Scanning Measurements for K07 Rod

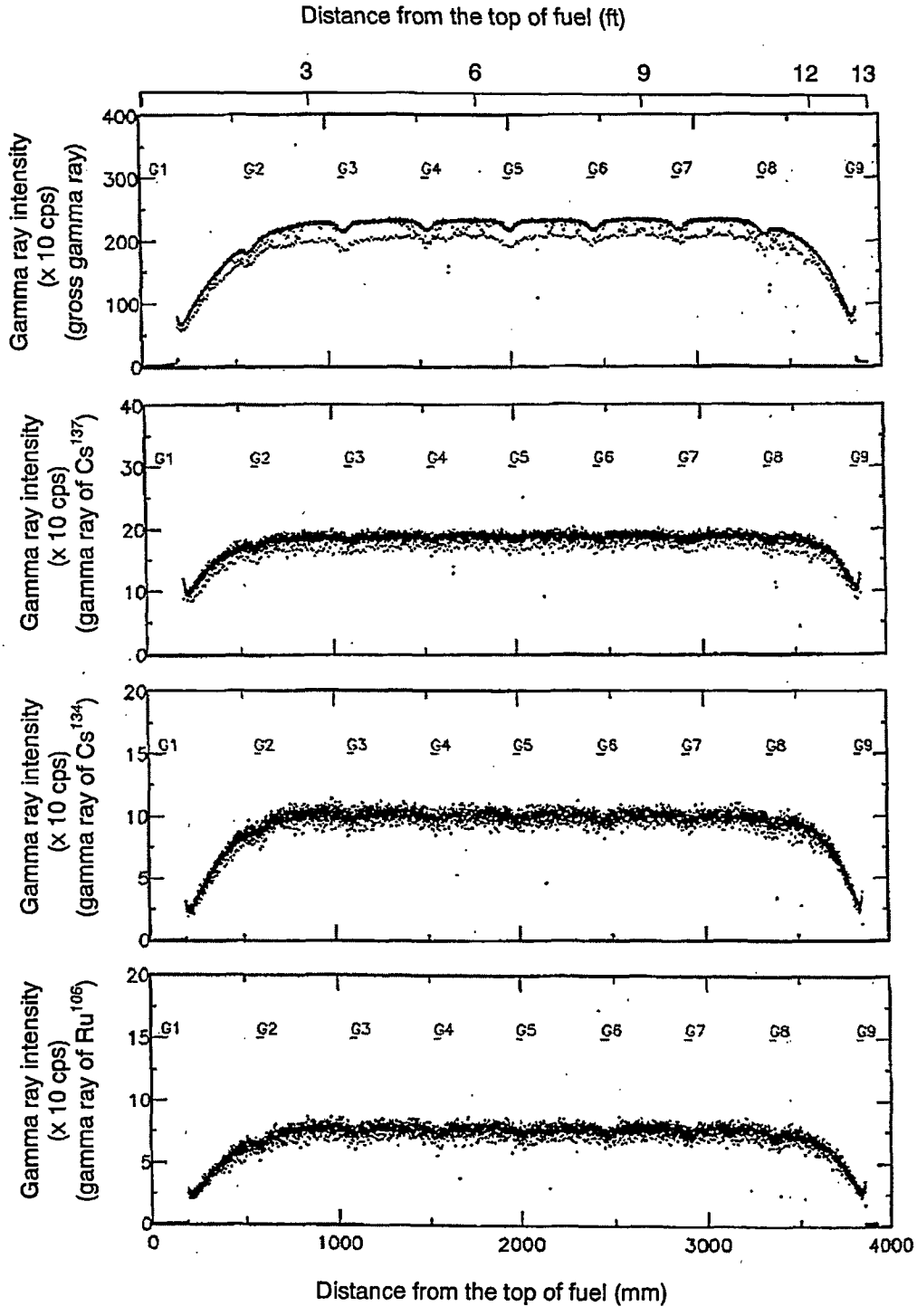

Figure B.1.1-6 Result of Gamma Scanning Measurements for E12 Rod

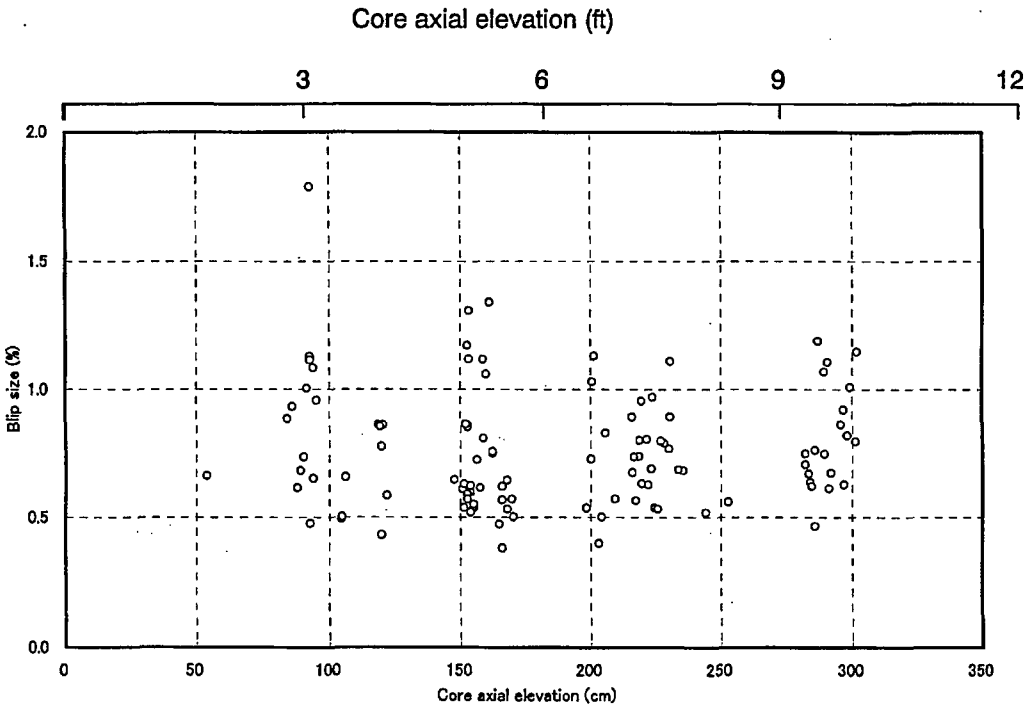

Figure B.1.1-7 The Axial Distribution of the Blips

B.2.0 GD-URANIUM DIOXIDE ($(U, Gd)O_2$)

B.2.1 Physical/Thermal Properties

B.2.1.1 Lattice Parameters

At room temperature, the lattice parameters were measured over the range of gadolinia content from 0 to 10 wt%, and the following empirical formula was obtained. Those measured values are compared with values from other sources[1-4] in Figure B.2.1-1.

$$a = [\quad] \qquad \text{(2-1)}$$

Where,
a: Lattice parameter (angstrom)
C: Gadolinia content (wt%)

B.2.1.2 Density

The crystal structure of Gadolinium doped uranium oxide is same as Uranium dioxide, which is face-centered cubic CaF_2 structure. In this structure, a part of 4 Uranium atoms in the unit lattice is replaced with Gadolinium atoms. The theoretical density of this structure is calculated from the lattice parameter value calculated by the experimental equation (2-1) and the atomic mass value at the given Gadolina contents.

There is a linear correlation between the gadolinia content and the theoretical density computed on the basis of the empirical formula described above. The results approximated for the maximum 10 wt% range show that the theoretical density decreases with respect to the gadolinia content (wt%) at the rate of [ ]. From these results and the lattice parameters of undoped UO_2 pellets, the following equation is obtained for the theoretical density of un-irradiated gadolinia-doped uranium dioxide as a function of the gadolinia content.

$$\rho_{TD} = [\quad] \qquad \text{(2-2)}$$

ρ_{TD}: Theoretical density (lb/ft^3)
C : Gadolinia content (wt%)

B.2.1.3 Thermal Expansion

Concerning the thermal expansion coefficient of gadolinia doped pellets, the results of measurements with gadolinia content as a parameter [4],[5] are shown in Figure B.2.1-2. According to this figure, the difference of the thermal expansion coefficient with respect to Gadolinium content is negligible up to about 10 wt% within the range of the data scatter. Consequently the thermal expansion of Gadolinia doped uranium dioxide comparable with that Uranium dioxide and the equation (1-1) is applicable for the Gadolinia doped Uranium oxide.

B.2.1.4 Melting Point

Gadolinia (Gd_2O_3) differs from uranium dioxide in having a body-centered cubic crystal structure at room temperature, but when mixed with uranium dioxide and sintered in a reducing atmosphere, it forms a solid solution in which uranium (U) atoms and gadolinium (Gd) atoms are exchanged. This solid solution has the same CaF_2-type FCC structure as uranium dioxide,

and a thermally stable phase up to the melting point is formed. It is reported that the melting point of un-irradiated gadolinia-doped uranium dioxide decreases to below the melting point of uranium dioxide as the gadolinia content increases by Beals et al.,[6] Wada et al.,[4] Grossman et al.,[7] and Mizuno et al.[8]

Of that data, the data of Beals et al. and Grossman et al. are indicated to have different measurement conditions from others. Based on the fact that the solidus and liquidus lines show the systematically reasonable decrease with the Gadolinia content and the melting point result of non-doped UO_2 indicate reasonable agreement with the previously reported values in the results of Mizuno et al. shown in Figure B.2.1-3, it is recommended that the melting point at the maximum gadolinia content of 10 wt% should be 4,892 deg.F (2,700 deg.C).

In addition, concerning the decrease in melting point due to burning, in the gadolinia content region up to 2 wt%, exchange-type solid solution in which U atoms and Gd atoms are exchanged gadolinia-doped uranium dioxide uranium dioxide exhibits the same behavior,[9] Furthermore, in the gadolinia content region above 2 wt% , even if the gadolinium is subjected to neutron irradiation, the only effect is conversion to other gadolinium isotopes. Because there is no conversion to other elements, the crystal structure does not change, and the burnup dependence of the melting point of gadolinia-doped uranium dioxide exhibits the same tendency as for uranium dioxide,[10]-[13] as shown in Figure B.2.1-4.

Accordingly, in the fuel temperature evaluation, the change in melting point with burnup is a decrease of 57.6 deg.F (32 deg.C) per 10,000 MWd/t, the same as for uranium dioxide.

B.2.1.5 Thermal Conductivity

The thermal conductivity of UO_2 is reduced by the solid solution of impurities. The results of measurements by the laser flash method show a tendency for the thermal conductivity to decrease as the gadolinia content increases (Figure B.2.1-5). Compared to the data of Fukushima et al.[14] (shown in the same figure), the measurements of Kosaka et al.[15],[16], and Hirai et al. [17] show a smaller proportion of decrease.

Furthermore, fuel center temperature measurement results [18] for 8 wt% gadolinia-doped pellets irradiated in the Halden reactor shown in Figure 4.2.1.5-5 and described later, the center temperature increase with burnup of UO_2 pellets irradiated under the same conditions showed the same temperature increase rate. In other words, the rate of decrease in thermal conductivity is the same.

The effect of gadolinia doping on thermal conductivity is considered due to the scattering effect of lattice vibration caused by impurities, and is taken into account as a function of the gadolinium content in the phonon-lattice scattering term of the model equation for UO_2 pellet thermal conductivity. The value of α here is determined on the basis of the above measured values of thermal conductivity.

$$k_{95} = 57.8 \times \frac{1}{11.8 + \alpha \cdot w + \beta \cdot Bu + 0.0238 \cdot (T - 32) \times \frac{5}{9}} + 8.775 \times 10^{-13} \cdot ((T - 32) \times \frac{5}{9})^3$$

Where,

k_{95} : Thermal conductivity (BTU/(ft·hr· deg.F)) of density 95 % TD pellets

T : Uranium dioxide pellets temperature (deg.F)

w : Gadolinium content (Gd mol%)
Bu : Burnup (GWd/tUO_2)
β : $0.35((\ deg.C \cdot cm/W)/(GWd/tUO_2))$
α : [ ] (deg.C·cm/W/Gd mol%)

Comparison of the temperature dependence of thermal conductivity obtained from this model equation to measured values (Figure 4.2.1.5-4) shows that the model makes appropriate predictions.

B.2.2 Chemical Properties

B.2.2.1 Reaction of Gadolinia-Doped Uranium Dioxide Pellets and Zirconium-Based Alloy Cladding

Gadolinia-doped uranium dioxide, as described in section B.2.1.5, forms an exchange-type solid solution and is stable. It has been reported that up to a gadolinia content of 10 wt%, gadolinia-doped uranium dioxide and Sn-Fe-Cr zirconium alloy (Zircaloy-4), the compatibility is the same as or higher than for uranium dioxide.[19] Accordingly, there is no large difference in the reaction of gadolinia-doped uranium dioxide pellets and Zircaloy-4 or ZIRLO cladding and the reaction of uranium dioxide pellets with those same materials. Furthermore, as described above, gadolinia-doped uranium dioxide pellets are stable in co-existence with the cladding end plug.

In the same way as for uranium dioxide, the compatibility in not affected by an increase in the pellet density.

B.2.2.2 Reaction of Gadolinia-Doped Uranium Dioxide Pellets and the Filling Gas

The helium filling gas is inert and does not react with gadolinia-doped uranium dioxide as described in chapter 1.2.2.

B.2.2.3 Reaction of Gadolinia-Doped Uranium Dioxide Pellets and Water

When used in the reactor, the cladding may develop penetrating defects or incur damage that may allow the primary coolant to permeate into the interior of the fuel rod. Nevertheless, it has been confirmed that gadolinia-doped uranium dioxide pellets do not undergo a change in mass even when immersed in water at about 572 deg.F (300 deg.C) for over 100 hours.[20] Even considering the reaction between gadolinia (Gd_2O_3) and water, the standard free energy of gadolinia is smaller than that of uranium dioxide as shown in Figure B.2.2-1. Therefore, gadolinia is more stable as a compound than is uranium dioxide, and there is no reaction of the uranium dioxide with high-temperature water.

As explained in the section on uranium dioxide, even an increase in pellet density has no effect on the reactivity with water.

B.2.3 Mechanical Properties

B.2.3.1 Young's Modulus (Elasticity)

The Young's modulus of UO_2 pellets is considered to be little affected by additives.[21] The recommended equation for UO_2 pellets is considered applicable for gadolinia-doped pellets as well.

B.2.3.2 Poisson's Ratio

In the same way as for the Young's modulus, the recommended equation for UO_2 pellets is considered applicable for gadolinia-doped pellets as well.

B.2.4 References

(1) S. Fukushima et al., "The effect of gadolinium content on the thermal conductivity of near-stoichiometric (U,Gd)O_2 solid solutions", Journal of Nuclear Materials, 105 (1982) 201

(2) R.J. Beals et al., "Solid solutions in the system Uranium-Rare-Earth oxides: I, UO_2-$GdO_{1.5}$", Journal of the American Ceramic Society, 48 (1965) 271

(3) R. Manzel., et al., " Manufacturing and irradiation experience with UO_2/Gd_2O_3 fuel", Ceramic Bulletine, 59 (6), 1981, 601

(4) T. Wada, et al., "Behaviour of UO_2-Gd_2O_3 fuel", Proc. Intern. Conf. on Nuclear Fuel Performance, London, 1973, p. 63.1

(5) Irisa et al., "Outside-reactor Property Tests on High-concentration Gadolinia-doped Fuel (1) -Coefficient of thermal expansion measurements-," Atomic Energy Society of Japan, 1990 Fall Plenary Session, Oct. 1990, University of Tokyo

(6) R.J. Beals, J.H. Handwerk and B.J. Wrona, "Behavior of Urania-Rare-Earth Oxides at High Temperatures", Journal of the American Ceramic Society, Vol. 52 No. 11 578-581 (1969)

(7) L.N. Grossman, D.R. Packard and H.W. Hill, "(U, Gd) $O_{2.00}$ Phase Equilibrium at High Temperatures", Paper 205, presented to C.N.R.S. colloquium, 1972

(8) Mizuno, et al., "Outside-reactor Property Tests on High-concentration Gadolinia-doped Fuel (3) –Melting Point Measurement-," Atomic Energy Society of Japan, "1990 Fall Plenary Session," Oct. 1990, University of Tokyo

(9) N. Oi et al., "BWR Fuel Performance and Recent Trend of R&D in Japan", ANS 1988 (Williamsburg)

(10) J. A. Christensen et al., "Melting Point of Irradiated Uranium Dioxide", WCAP-6065 UC-25, Metals, Ceramics and Materials, 1965

(11) J. L. Bates, "Melting Point of Irradiated Uranium Dioxide", Journal of Nuclear Materials, 36, 1970, pp. 234-236

(12) R. E. Latta et al., "Determination of Solidus-Liquidus Temperatures in the UO_{2+X} System (-0.50<X<0.20)", Journal of Nuclear Materials, 35, 1970, pp.195-210

(13) J. A. Christensen, "Irradiation Effects on Uranium Dioxide Melting", HW-69234 UC-25, Metals, Ceramics and Materials, 1962

(14) S. Fukushima et al., "The Effect of Gadolinium Content on the Thermal Conductivity of Near-Stoichimetric (U, Gd)O_2 Solid Solution", Journal of Nuclear Materials, 105, 1982, pp. 201-210

(15) K.Kosaka et al., "Thermal Properties and Irradiation Behavior of Gd Fuel", IAEA Technical Committee Meeting on Advances in Pellet Technology for Improved Performance at High Burnup, October 1996. Tokyo

(16) Kosaka et al., "Outside-reactor Property Tests on High-concentration Gadolinia-doped Fuel (2) -Thermal conductivity measurements-," Atomic Energy Society of Japan, 1990 Fall Plenary Session, Oct. 1990, University of Tokyo

(17) M. Hirai et al., "Thermal Diffusivities and Thermal Conductivities of UO_2-Gd_2O_3", Journal

of Nuclear Science Technology, 28, 11, 1991, pp.995-1000

(18) T. Tverberg et al., "Study of Thermal Behavior of UO_2 and (U, Gd)O_2 to High Burnup (IFA-515)", HWR-671, Enlarged HPG Meeting, March 2001, Lillehammer

(19) Matsuoka et al., "Research on gadolinia-doped UO_2 fuel and Zircaloy-4 Compatibility," Atomic Energy Society of Japan, 1990 Fall Plenary Session, Oct. 2-5, 1990, Tokyo University

(20) R.M. Adams and A. Glassner, "Reactor Development Program Progress Report", ANL-6705, April 15, 1963

(21) M.Hirai et al., "Young's modules of Gd_2O_3-UO_2, Nb_2O_5-UO_2 and TiO_2-UO_2 pellets", Fall Meeting of Japan Atomic Energy Society, Oct. 1991, F58, p20

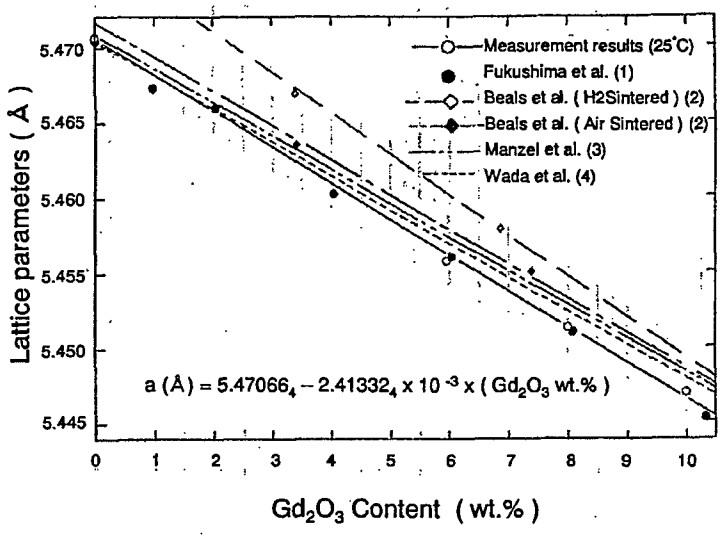

Figure B.2.1-1 Changes in the Lattice Parameter of Unranium Dioxide Pellets by Gadolinia Doping

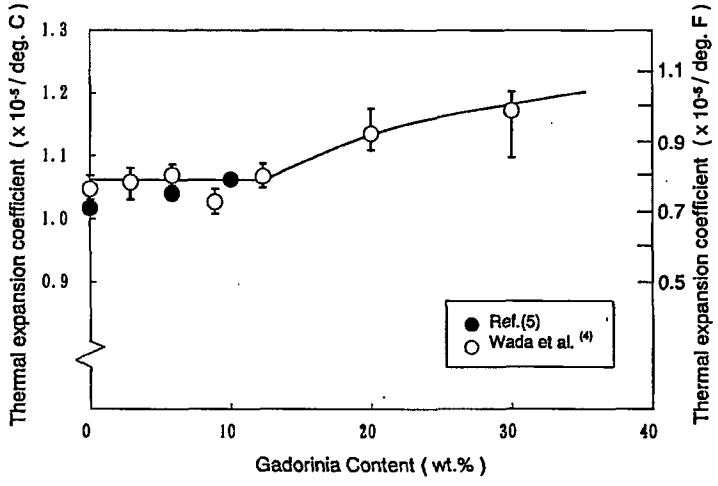

Figure B.2.1-2 Thermal Expansion Coefficient of Gadolinia-Doped Pellets[4],[5]

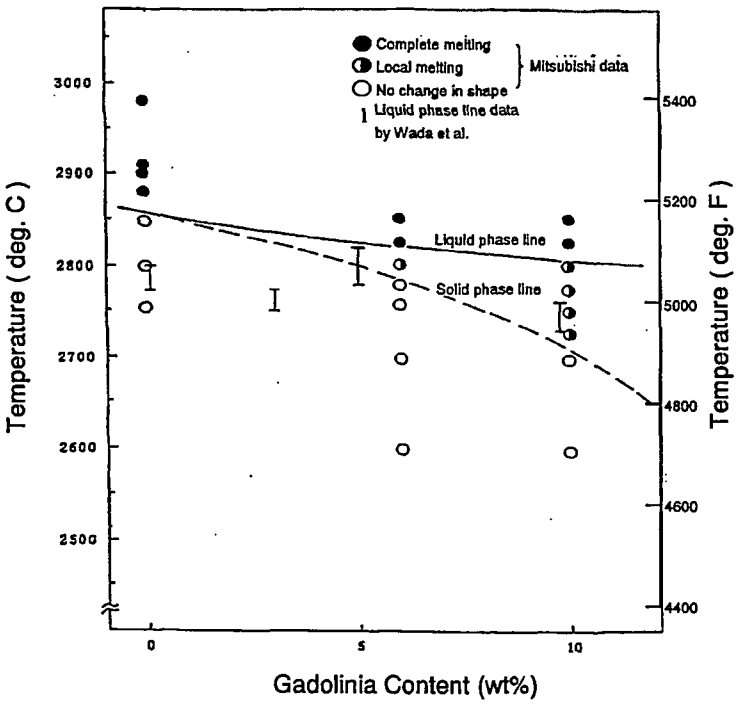

Figure B.2.1-3 Melting Point of Gadolinia-Doped Pellets[6],[8]

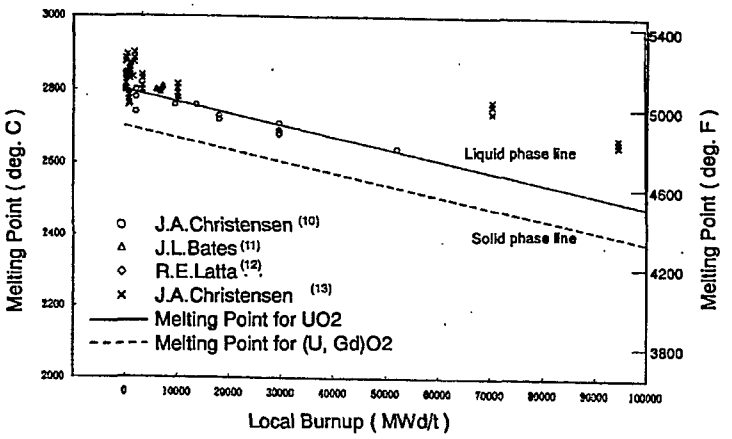

Figure B.2.1-4 Melting Point of Uranium Dioxide and Gd - Uranium Dioxide

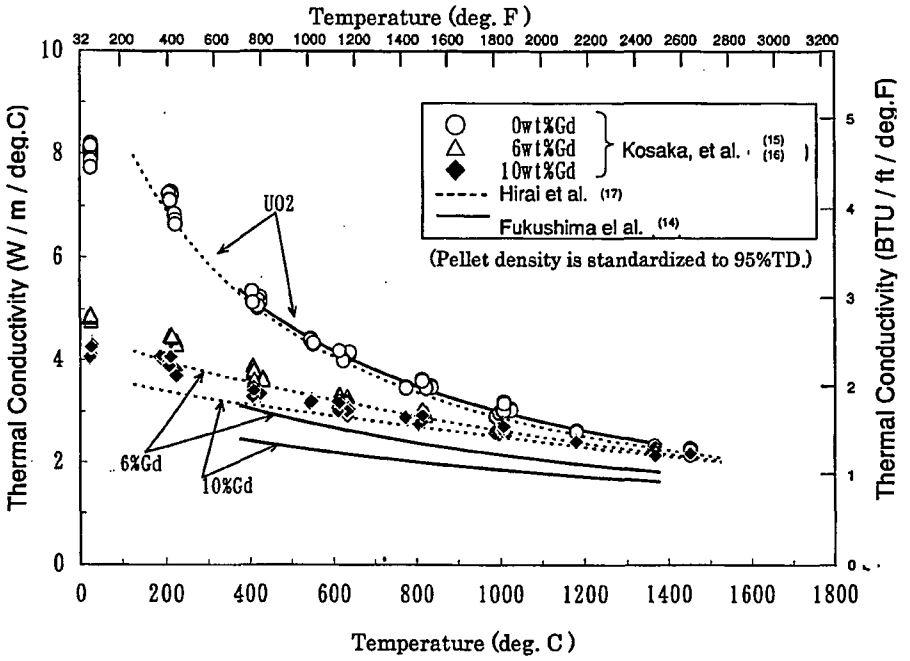

Figure B.2.1-5 Thermal Conductivity of Gd - Uranium Dioxide Pellets (14) - (17)

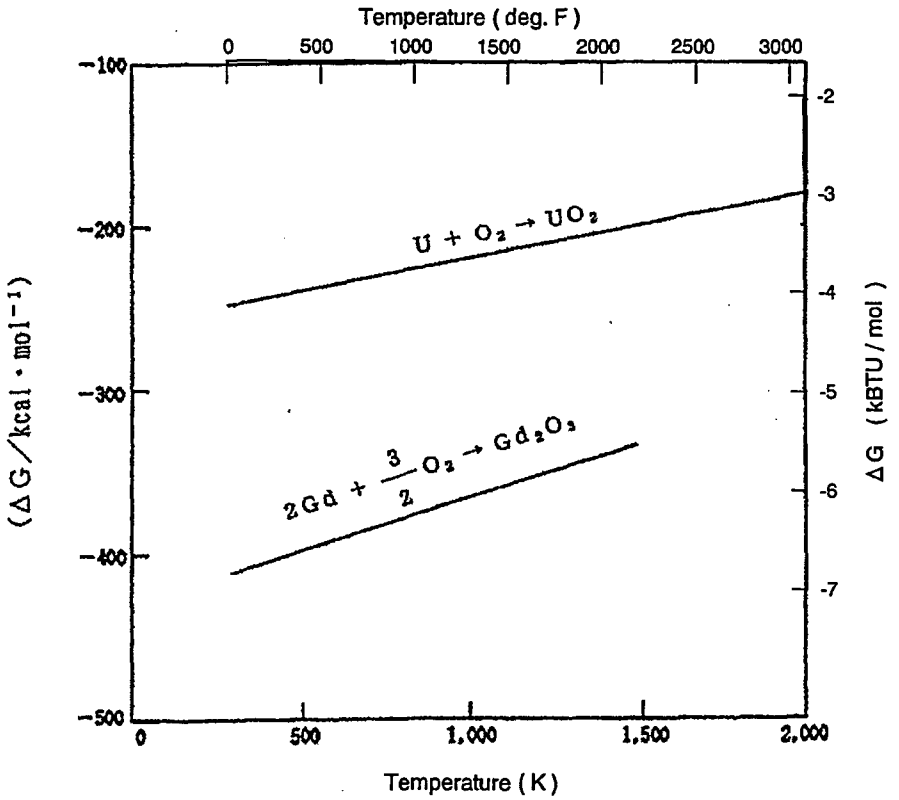

Figure B.2.2-1 Free Energy Generated by Uranium Dioxide and Gadolinia

B.3.0 ZIRLO™

B.3.1 Physical / Thermal Properties

B.3.1.1 Chemical Composition

ZIRLO is an alloy of improved corrosion resistances developed by Westinghouse Electric Corporation ("Westinghouse") , and may be regarded as the Zirconium-Niobium(Zr-Nb)alloy which is superior in corrosion resistances, added with tin (Sn) and iron(Fe)for the purpose of improving mechanical strength[1]·[3]. Alloy composition of ZIRLO is shown below.

Element	ZIRLO	(Reference) Zircaloy-4
Sn, wt%	[	1.20 ~ 1.70
Fe, wt%		0.18 ~ 0.24
Cr, wt%		0.07 ~ 0.13
Fe+Cr, wt%		0.28 ~ 0.37
Nb, wt%		-
O, wt%	]	[ ]
Zr	Balance	Balance

B.3.1.2 Lattice Parameter and Density

Concerning the addition of 5th element in the lattice parameter of Zr crystal (α phase), the following equations are available [4].

$$a_0=3.2317-0.276x \quad \text{-----(3-1)}$$
$$c_0=5.1476-0.44x+0.181xn-0.016x^2n \quad \text{-----(3-2)}$$
$$c/a=1.5923\pm0.056xn \quad \text{-----(3-3)}$$

Where x is atom fraction of solute and n is solute valence (taken as the Pauling valence = 2.44 for tin). In the addition of Sn of 1.5 wt%, the theoretical density of Zircaloy is 409 lb/ft^3(6.55 g/cm^3). This value is similar to the theoretical density 408 lb/ft^3(6.54 g/cm^3) calculated from lattice parameter, a_o= 3.230 angstrom and c_o= 5.150 angstrom recommended by ASTM.

For ZIRLO the lattice parameter is described below.

Changes of the lattice parameter of hcp Zr by added Sn are shown by the above equations (3-1), (3-2) and (3-3). Line (1) in Figure B.3.1.2-1 shows the changes of lattice parameter by added elements in Pauling valence= 2.44.

As for the changes of lattice parameter by added Nb, the data of up to 2.5 at% Nb is obtained. The linear approximation of these data is shown by line (2) in Figure B.3.1.2-1. Lattice parameter are measured for 2 at% Sn + 2 at% Nb, and the change widths from pure Zr are reported as a_o: -0.0136 angstrom and c_o: -0.0007 angstrom. Line (3) in Figure B.3.1.2-1 shows the changes of lattice parameter in case lattice parameter are linearly connected in pure Zr and 2 at% Sn + 2 at% Nb.

Line (3) is the change of lattice parameter for total addition in case that same amounts of Sn and Nb are added. Lattice parameter of ZIRLO is calculated based on lines (1), (2) and (3) in

Figure B.3.1.2-1. Table B.3.1.2-1shows the result of calculating lattice parameters by the method and the densities calculated from the values.

The theoretical density of ZIRLO is almost equal to the experimental value, and shall be 408 lb/ft^3(6.54 g/cm^3) by rounding to two decimals.

B.3.1.3 Thermal Expansion Coefficient

(1) Data in literature

As for the solid elements generally, simple relations are known to lie between linear expansion coefficient and melting point. As melting point is higher, linear expansion coefficient tends to be smaller.

Figure B.3.1.3-1[5] shows the data of axial direction thermal expansion of ZIRLO and Zircaloy-4. As shown in this figure, both almost match each other in up to 1112 deg.F (600 deg.C). If temperature rises further, ZIRLO is slightly smaller in thermal expansion coefficient, but the difference remains to be 8% or so even at 1472 deg.F (800 deg.C).

Melting points of ZIRLO and Zircaloy-4 measured at Mitsubishi are 3348 deg.F (1842 deg.C) and 3317 deg.F (1825 deg.C) respectively. The relation in which ZIRLO of higher melting point is slightly smaller in thermal expansion conforms to the relation seen generally in solid elements as described above. Judging from the difference of melting point being 18 deg.F (10 deg.C) and something and the actually measured values being matching up to 1112 deg.F (600 deg.C), however, result is that the same value of thermal expansion coefficient can be used for ZIRLO and Zircaloy-4.
As for Zircaloy-4 and CW-SR tube at 70 - 801 deg.F (21 - 427 deg.C), the following equations are specified[4].

$$\Delta L/L\ (\text{axial}) = \left(2.92 \times 10^{-6}\right)(T - 70) \qquad \text{-----(3-4)}$$

$$\Delta R/R(\text{radial}) = \left(3.22 \times 10^{-6}\right)(T - 70) \qquad \text{-----(3-5)}$$

Where T: Temperature (deg.F)

(2) Summary

ZIRLO and Zircaloy-4 are same in thermal expansion up to 1112 deg.F (600 deg.C), and the same value can be used in evaluation. Therefore, the equations (3-4) and (3-5) shall be used for the thermal expansion coefficient of ZIRLO.

B.3.1.4 Thermal Conductivity

Figure B.3.1.4-1 shows the temperature dependence of thermal conductivity. In the range from room temperature to 752 deg.F (400 deg.C), thermal conductivity of ZIRLO is about 5% higher than that of Zircaloy-4.

As ZIRLO has thermal conductivity slightly higher than Zircaloy-4, conservative evaluation is available by using the value of Zircaloy-4 in evaluation. For the thermal conductivity of ZIRLO, the same formula as Zircaloy-4[4] is applied.

K=[ ](Btu/h·ft·deg.F) ---(3-6)

T :Temperature (deg.F)
0 to 743 deg.F (395 deg.C)

B.3.1.5 Melting Point

For the melting point, actually measured data are available. In the melting point measurement, melting was checked in visual observation after temperature drop by once heating samples in inert gas atmosphere. In the results, the following values were given.

Zircaloy-4	3317 deg.F (1825 deg.C)
ZIRLO	3348 deg.F (1842 deg.C)

These values were given after temperature correction by regarding the melting point of pure Zr as 3317 deg.F (1852 deg.C).

In Zircaloy-4, 3360 deg.F (1849 deg.C) which is 5.4 deg.F (3 deg.C) lower than pure Zr is reported[4].

In the Zr-Nb binary system phase diagram, however, drop of melting point by added Sn seems to be larger. The value of Zircaloy-4, 3317 deg.F (1825 deg.C), measured actually by Mitsubishi is 48.6 deg.F (27 deg.C) lower than pure Zr, and better matches the drop tendency of liquid phase line in the phase diagram. This also matches the melting point of Zircaloy-4 3317 deg.F (1825 deg.C) in MATPRO, and the actually measured values look reliable.
Consequently, above values measured actually by Mitsubishi are applied as the melting point of ZIRLO.

The following value is applied as the melting point of ZIRLO.

ZIRLO	3348 deg.F (1842 deg.C)

B.3.1.6 Phase Transformation Temperatures

(1) Data in Literature

The following data have been reported as data in literature. α to β transformation point of pure Zr is 1584 deg.F (862 deg.C)[6] to 1585 deg.F (863 deg.C)[7] .

Materials	α to α+β	α+β to β
ZIRLO[5]	1382 deg.F (750 deg.C)	1724 deg.F (940 deg.C)
Zircaloy-4[5]	1499 deg.F (815 deg.C)	1778 deg.F (970 deg.C)
Zircaloy-2, -4[4]	1517±18 deg.F (825±10 deg.C)	1742±18 deg.F (950±10 deg.C)
Zircaloy[8]	1490 deg.F (810 deg.C)	1778 deg.F (970 deg.C)

Of the elements added to Zr, Sn is an α phase stabilizing element and Nb is α β phase stabilizing element. In ZIRLO which reduces Sn and adds Nb as compared with Zircaloy-4, therefore, the phase transformation temperature shifts to lower side.

Actually measured values of phase transformation temperature are as shown below. Phase

transformation temperatures were obtained from the singular points in phase transformation on differential thermal curve by heating the sample and standard specimen simultaneously by differential thermobalance in inert gas atmosphere at a constant rate and by obtaining the differential thermal curve representing the temperature differences of both specimens.

Materials	α to α+β	α+β to β
ZIRLO	1418 deg.F (770 deg.C)	1724 deg.F (940 deg.C)
Zircaloy-4	1508 deg.F (820 deg.C)	1778 deg.F (970 deg.C)

Sample materials are the ones used in density measurement and melting point measurement. Figure B.3.1.6-1 shows the relation between α to α+β phase transformation temperature and Sn amount[4],[5],[8].

Actually measured values of ZIRLO and Zircaloy-4 obtained at Mitsubishi: α to α+β phase transformation temperature is 1418 deg.F (770 deg.C) in ZIRLO and 1508 deg.F (820 deg.C) in Zircaloy-4, and α+β to β transformation temperature is 1724 deg.F (940 deg.C) in ZIRLO and 1778 deg.F (970 deg.C) in Zircaloy-4. These values almost match other data in literature. For the α to α+β phase transformation temperature of ZIRLO, therefore, 1418 deg.F (770 deg.C) would be adequate. For the α to α+β phase transformation temperature, 1724 deg.F (940 deg.C) would be appropriate.

(2) Summary

For ZIRLO, two values are mentioned for the α to α+β phase transformation temperature, such as the value 1382 deg.F (750 deg.C)[7] and the value 1418 deg.F (770 deg.C). For the a to a+ß phase transformation temperature, 1724 deg.F (940 deg.C) is given[5].

Of the two values of α to α+β phase transformation temperature, here, the lower temperature of 1382 deg.F (750 deg.C) shall be conservatively employed from the viewpoint of design/safety evaluation, and 1724 deg.F (940 deg.C) shall be employed for the α to α+β phase transformation temperature.

Phase transformation temperatures of ZIRLO

α to α+β	α+β to β
1382 deg.F (750 deg.C)	1724 deg.F (940 deg.C)

B.3.2 Chemical Properties

B.3.2.1 Compatibility With UO_2

If zircaloy cladding and UO_2 pellets come in contact with each other, oxygen in UO_2 becomes excessive by irradiation and diffuses into zircaloy, thus forming oxide layer (ZrO_2) in the cladding. When both come in close contact with each other, Zr oxide layer becomes (Zr, U)O_2 solid solution due to the diffusion of U into Zr oxide layer, thus forming a bonding layer which in turn causes a strong bonding of pellet-cladding[10]. These are suspected to corrode the cladding and affect PCI.

Similar to Zircaloy-4, ZIRLO cladding contains about 98wt% of Zr, and the behavior is similar to Zircaloy-4. Although oxidation and bonding of the inner surface of Zircaloy-4 and ZIRLO cladding irradiated to about 60,000 MWd/t has been found in commercial reactors, the reaction layer is at most only 0.47 mil (12 μm) thickness as shown in Fig 4.2.4.5-1, and has little effect on cladding stress.

B.3.2.2 Corrosion

In the outside of zircaloy cladding, oxide layer is formed by reaction with the hot primary cooling water under the operating conditions in the reactor. Corrosion rate of zircaloy shows the arrhenius type temperature dependence in the interface temperature between oxide layer and the zircaloy metal base material. As shown in Figure B.3.2.2-1[10], the amount of corrosion (increased weight for exposure time) increases by cubic rule (proportional to cubic root of time) in the initial stage, and increases linearly for time after the thickness of oxide layer exceeds 0.079 - 0.118mils(2 - 3μm) (transition point). In the reactor, interface temperature of the oxide layer so formed and the metal part increases as the thickness of oxide layer increases as time goes by. As shown in Figure B.3.2.2-2[2], [11] to [23], therefore, thickness of oxide layer tends to increase with burnup accumulation. If corrosion develops further, acceleration of corrosion is observed. Cause is said to be the corrosion of deposits when part of hydrogen produced by oxidation, which is absorbed into the cladding, precipitates on the outside of the cladding [24]. As shown in Figure B.3.2.2-2 on the zircaloy cladding, such corrosion behavior as described above has been confirmed in max burnup of fuel rod of 61,000 MWd/t (equivalent to fuel assembly average burnup 55,000 MWd/t) or more.

As shown in Figure B.3.2.2-3, ZIRLO is effective to reduce corrosion speed as compared with Zircaloy-4 in the out of pile tests. The corrosion behavior shows an acceleration of corrosion, similar to zircaloy cladding, as corrosion increases. This increase of corrosion in ZIRLO is also suspected to have been caused by the deposits of absorbed hydrogen. This has been confirmed in the out of pile corrosion test on hydrogen-absorbed cladding shown in Figure B.3.2.2-4. According to this figure, ZIRLO is effective to reduce corrosion up to 2000 ppm in the accelerated corrosion area by hydrides.

Judging from the above, the corrosion mechanism of ZIRLO is similar to Zircaloy-4 cladding and the effectiveness of improvement is also maintained similarly in the area of increased corrosion. Effectiveness to reduce corrosion is determined to persist in max burnup of fuel rod 61,000 MWd/t (equivalent to fuel assembly average burnup 55,000 MWd/t) as an actual combustion range of Zircaloy-4 cladding.
Recommended value of ZIRLO's effectiveness to reduce corrosion is 30% in design for the conventional tin Zircaloy-4 cladding.

Figure B.3.2.2-5 shows autoclave corrosion test data of Zircaloy-4 cladding in hot temperature steam. Three types of cladding lot materials satisfying the manufacturing specifications were exposed under the corrosion test conditions of maximum [ ] in hot temperature steam of [ ]. The result shows that the corrosion acceleration phenomenon is observed in the result at the temperature of [ ] [ ]. Therefore, to prevent an abnormal corrosion acceleration, it is decided to keep the cladding metal surface susceptible to oxidation below [ ] [ ]. This temperature limit is applied during Anticipated Operational Occurrences (AOOs) as a limit of the metal-oxide interface temperature. As the time of the power increase during AOOs is short, it is conservative to apply the result of the above test conducted at a constant temperature for [ ]. The same result is reported as below[25].

Steady State Operation ; [ ]
Transient : [ ]

And the result for ZIRLO is reported as below[5].

Steady State Operation ; [ ]
Transient : [ ]

The result for Zircaloy-4 is conservatively recommended.

3.2.3 Hydrogen Absorption

Hydrogen produced due to corrosion of cladding is partially absorbed into the cladding. Figure 4.2.4.2-1 [1], [16], [17], [19], [20], [26], [27] shows the oxide thickness and hydrogen absorption in the reactor. As shown in this figure, hydrogen absorption is proportional to the oxide thickness. This hydrogen absorption characteristic shows similar tendency in ZIRLO and Zircaloy-4. It is possible, thereby, to evaluate the hydrogen absorption by using the result of appropriate evaluation of corrosion. Figure 4.2.4.2-1 shows the line of hydrogen absorption as a reference. Concerning the hydrogen absorption in the reactor, however, there is no distinct difference among the types of cladding, which is about 11 ~ 17 %[27].

Recommended value of hydrogen absorption in design is 15%.

B.3.3 Mechanical Properties

B.3.3.1 Young's Modulus

(1) Examination

Table B.3.3.1-1 shows the axial young's moduli obtained from the load-displacement curve in the 725 deg.F (385 deg.C) uniaxial tensile test on zircaloy and ZIRLO cladding tubes.

In the load-displacement curve, the one with extensometer was used, and the Young's moduli was obtained for a range which seems to be an elastic area in startup.

Following formula is given thereby.

Zircaloy-4 ≥ ZIRLO

Concerning ZIRLO, the followings are given.

Zircaloy-4 average: [ ]
ZIRLO (std. ß): [ ]

About [ ] has dropped as shown above.

Another report shows Zr-1.0Nb was [ ] lower than pure Zr at room temperature. This matches the above result better comparatively. If Nb is added over solid solution limit, Young's modulus is estimated to drop.
Result is outlined below.

$E_{Zircaloy\text{-}4} : E_{ZIRLO} =$ [ ]

(2) Summary

Since ZIRLO and Zircaloy-4 have almost similar Young's module, both are treated similarly in evaluation for Zircaloy-4 [4] as below.

At 0 ~ 1200 deg.F (-18 ~ 649 deg.C);
E(psi)= [ ]
Where:
T: Temperature (deg.F)

B.3.3.2 Poisson's Ratio

(1) Examination

Poisson's ratio is shown by the following formula for isotropic materials.

$$\mu = \frac{E}{2G} - 1$$

Above formula cannot be applied to the anisotropic material such as Zircaloy-4. Concerning the value of μ for Zircaloy-4, therefore, the test method and the analysis, texture orientation should be effective in evaluation.

The measured values related to Zircaloy-2·Zr-Cr-Fe·Zr-2.5Nb alloys are variable in the range 0.33 ~ 0.38 [28], and seem to be contained in this range for ZIRLO.

The following formulae are applied to Zircaloy-4.

$\mu_r =$ { }
$\mu_z =$ { }

Where:
T: Temperature (deg.F)

An almost same formula is reported as below [4]. In other words, the data of Northwood [28] are extensive and smaller in deviation, and the reported items are reliable. Poisson's ratio is recommended as a function of temperature.

$\mu =$ [ ]

Where:
T: Temperature (deg.F), T < 1000 deg.F (538 deg.C)

According to the above formula, 0.367 is given at 68 deg.F (20 deg.C), and 0.332 is given at 932 deg.F (500 deg.C). These values are similar to the data in other literature, and can be applied to ZIRLO.

(2) Summary

Since the formula of Zircaloy-4 can be applied to ZIRLO, the following formulae are employed for Poisson's ratio.

Radial direction: $\mu =$ [ ]
Axial direction : $\mu =$ [ ]

Where;
T: Temperature (deg.F), T < 1000 deg.F (538 deg.C)

B.3.3.3 Yield Strength

(1) Examination

Measured yield strengths of ZIRLO and Zircaloy-4 are as shown below, and the yield strength

tends to be a bit higher in ZIRLO than Zircaloy-4.

	ZIRLO	Zircaloy-4
725 deg.F(385 deg.C)	[	]
RT	[	]

Yield strengths, UTS and elongation of Zircaloy-4 and ZIRLO are shown in Figure B.3.3.3-1. ZIRLO has almost same material properties with Zircaloy-4.

Figure B.3.3.3-2 shows the temperature dependency of the measured yield strengths of un-irradiated Zircaloy-4 and ZIRLO, and indicates that the measured values are slightly larger on the best estimated curve[4].

In other words, the best estimated curve for un-irradiated material [4] is somewhat smaller than the measured values, conservatively. Therefore, the prediction can be said to be in safe side of evaluation.

Consequently, the formula for Zircaloy-4 was found applicable as yield strength for ZIRLO.

(2) Summary

The formula for Zircaloy-4 [4] which is smaller than actually measured values shall be used for ZIRLO. Then, the following formula predicting an evaluation shall be applied for the best estimated curve. The lower bound at a 95 % probability at a 95 % confidence level should consider [ ] in the following formulas.

1) Un-irradiated uniaxial tensile yield strengths

SY= [ ] $T \leq 700$ deg.F (371 deg.C)
SY= [ ] 700 deg.F $< T \leq$ 900 deg.F (482 deg.C)

Where:
T: Temperature (deg.F)

2) Irradiated material uniaxial tensile yield strengths

SY= [ ] $T \leq 700$ deg.F (371 deg.C)
SY= [ ] 700 deg.F $< T \leq$ 900 deg.F (482 deg.C)

Where:
T: Temperature (deg.F)

B.3.3.4 Ultimate Tensile Strength

The ultimate strength (UTS) data as function of temperature are shown in Figure B.3.3.4-1 for Zircaloy-4 and ZIRLO. The UTS data of ZIRLO are included within the data scatter of Zircaloy-4. In other words, this figure shows that ZIRLO has almost same UTS property with Zircaloy-4. Consequently, the equations of Zircaloy-4 were found available as design UTS values of ZIRLO. Therefore following equations are used for the best estimated curve. The lower bound at a 95 % probability at a 95 % confidence level should consider [ ] in the following

formulas.

1) Un-irradiated uniaxial tensile ultimate strengths

UTS= [ ] T ≤ 700 deg.F (371 deg.C)
UTS= [ ] 700 deg.F < T ≤ 800.6 deg.F (427 deg.C)

Where:
T: Temperature (deg.F)

2) Irradiated material uniaxial tensile ultimate strengths

UTS= [ ] T ≤ 700 deg.F (371 deg.C)
UTS= [ ] 700 deg.F < T ≤ 800.6 deg.F (427 deg.C)

Where:
T: Temperature (deg.F)

B.3.3.5 Strain Criterion

1 % plastic strain as the criterion for maintaining fuel integrity is applied by considering the O'donnell's unstable strain theory. In this theory, it is necessary to keep the ductility in fuel cladding against the hydrogen absorption. Some un-irradiated data (680 deg.F / 360 deg.C) of Zircaloy-4 and ZIRLO have hydrogen content up to [ ] in Figure B.3.3.3-2 and Figure B.3.3.4-1 which show the yield strength and the ultimate strength, respectively. These figures indicate that data lie in the same range, regardless of hydrogen absorption, and that the hydrogen content of un-irradiated Zircaloy-4 and ZIRLO has no effects on the high-temperature mechanical property of the cladding. Figure B.3.3.5-1 shows the result of the high-temperature tensile test of irradiated cladding[27], [29]. While it shows the tendency that total elongation is reduced as the hydrogen absorption increases up to approximately [ ], the reduction tendency beyond this level is not seen and the elongation exceeds 1 % criterion sufficiently up to about [ ]. This demonstrates that 1 % plastic strain criterion is conservative up to about [ ], it can be confirmed that using this criterion up to high hydrogen content is valid.

B.3.3.6 Cladding Fatigue Property

As the result of fatigue test with irradiated fuel cladding shows consistency with Langer-O'Donnel best fit model, its design curve with the certain safety factor is applicable to high burnup fuel design as shown in Figure B.3.3.6-1[15], [27], [30].

B.3.3.7 Hydride Reorientation

The hydrogen absorbed in connection with oxidation is deposited as hydride if hydrogen is absorbed beyond the hydrogen solubility limit, causing reduction in the ductility of cladding. As the average temperature of cladding during plant operations is assumed at 570 deg.F to 750 deg.F (300 deg.C to 400 deg.C), the solubility limit of hydrogen of cladding is approximately 70 ppm to 200 ppm [31]. For this purpose, the hydrogen absorption is assessed and is confirmed to be below the limit. In the fuel cladding, these hydrides have characteristics to be oriented in the circumferential direction if circumferential stress is low, but be reoriented in the radial direction under the high circumferential stress. If hydrides are oriented in the radial direction, the cracks may occur along the hydrides. Therefore, it is necessary to prevent re-orientation of hydrides from the viewpoints of the integrity of fuel cladding.

The stress dependency of hydride reorientation in the case of Zircaloy-4 cladding is reported [32]. The reorientation of hydrides in the radial direction is significant at approximately 16000psi (110 MPa) or more. Likewise, the stress dependencies of hydride reorientation in the case of Zr-2.5Nb cladding are reported [33]. This indicates that the hydrogen reorientation tends to be greater with the increase in stress and the increase in temperature. If the temperature of the fuel cladding during normal operation is assumed at approximately 750 deg.F (400 deg.C), the hydrogen reorientation stress is approximately 11500psi (80 MPa).

The tensile stress in the circumferential direction of cladding due to the fuel rod internal pressure occurs when the internal pressure is higher than the external pressure. Figure B.3.3.7-1 shows an example where the circumferential stress of fuel cladding is assessed with the system pressure and 80 MPa as the inner stress. In this manner, the internal pressure should be below ~27MPa to avoid hydride reorientation.

B.3.4 References

(1) G.P.Sabol, et al., "Development of a Cladding Alloy for High Burnup", Zirconium in the Nuclear Industry : 8th International Symposium, ASTM STP 1023, 1989, pp.227-244

(2) G.R.Kilp, et al., "Corrosion Experience with Zircaloy and ZIRLO™ in Operation PWRs", ANS/ENS International Topical Meeting on LWR Fuel Performance, April 1991, Avignon, France

(3) M.G.Balfour, et al., "Westinghouse Fuel Operating Experience at High Burnup and with Advanced Fuel Features", ANS/ENS International Topical Meeting on LWR Fuel Performance, April 1991, Avignon, France

(4) P.J.Kuchirka, Beaumont, M. D., Iorii, J. A., "Properties of Fuel and Core Component Materials", WCAP 9179, 1978

(5) S. L.Davidson, and D. L.Nuhfer, "VANTAGE+ Fuel Assembly Reference Core Report", WCAP-12610, June 1990.

(6) B.Lustman, et al., "Merallurgy of Zirconium", McGraw-Hill, 1995

(7) Massalski et al., "Binary Alloy Phase Diagrams", ASM, 1986

(8) D.L.Hagrman, et al., "MATPRO-Version 11", NUREG/CR-0497 TREE-1280, 1979

(9) Nuclear Safety Research Association "Behavior of Light Water Reactor Fuels" Practice Text Series No. 3, Jul. 1998

(10) E.Hillner, "Corrosion of Zirconium-Base Alloys – An Overview", Zirconium in the Nuclear Industry : 3rd International Conference, ASTM STP 633, 1977, pp.211-235

(11) G.P.Sabol, et al., "In-Reactor Fuel Cladding Corrosion Performance at Higher Burnups and Higher Coolant Temperatures", ANS 1997 International Topical Meeting on LWR Fuel Performance, March 1997, Portland, Oregon

(12) S.Doi, et al., "Advanced Fuel Design and Performance for Burnup Extension ", ANS 2000 International Topical Meeting on LWR Fuel Performance, April 2000, Park City, Utah

(13) E.DeMatias, et al., "European Fuel Group's Fuel Performance", Top Fuel '97, BNES, 1997, pp.2.28-2.39

(14) J.Moon, "Farley Unit 1 EOC-7 ; 17×17 OFA Onsite Examinations Report", WCAP-11561, 1987

(15) Nuclear Power Engineering Corporation, Year 1997 Report on Light Water Reactor Modification Engineering Verification Test (related to high burnup fuels), March 1998

(16) M.G.Balfour, et al., Final Report "EP80-16, Hot Cell Examination of Zion Fuel Cycle 1 through 4, WCAP-10473", ESEERCO report, 1985

(17) U.P.Nayak, et al., Final Report "EP80-16, Hot Cell Examination of Zion Fuel Cycle 5, WCAP-10543", ESEERCO report, 1985

(18) M.G.Balfour, et al., "BR-3 High Burnup Fuel Rod Hot Cell Program, Volume 1: Final Report", WCAP-10238, Vol.1, DOE/ET 34073-1, 1982

(19) J. A.Kuszyk, "Hot Cell Examination of Surry Three- and Four-Cycle 17×17 Demonstration Fuel, Volume 1: Principal Results and Evaluation", WCAP-10514, Vol.1, DOE/ET 34014-14, 1984

(20) Nuclear Power Engineering Corporation, Year 1998 Report on Light Water Reactor Modification Engineering Verification Test (related to high burnup fuels), March 1999

(21) M.Yokote, et al., "PWR Fuel in Japan, Progress and Future Trends", Nuclear Engineering International, 1994, pp.24-29

(22) Nuclear Power Engineering Corporation, Year 1999 Report on Light Water Reactor Modification Engineering Verification Test (related to high burnup fuels), March 2000

(23) T.Takahashi, et al., "Advanced Fuel Development for Burnup Extension", ANS 1997 International Topical Meeting on LWR Fuel Performance, March 1997, Portland, Oregon

(24) J.Thomazet, et. al., "FRAGEMA Zirconium Alloy Corrosion Behavior and Development", ANS Topical Meeting on LWR Fuel Performance, April 1985, Orlando

(25) S.L.Davidson, (Ed.) et al., "Extended Burnup Evaluation of Westinghouse Fuel," WCAP-10125-P-A (Proprietary) and WCAP-10126-NP-A (Non-Proprietary), December 1985

(26) T.Kitagawa, et al., "Post irradiation examination of fuel rods in 55GWd/t lead use assembly", 2005 Water Reactor Fuel Performance Meeting, October 2005, Kyoto

(27) Nuclear Power Engineering Corporation, Year 2000 Report on High Burnup Fuels Verification Test, Jun. 2001

(28) D.O.Nothwood, I.M.London, and L.E.Bahen, "Elastic Constants of Zirconium Alloys", Journal of Nuclear Materials 55, 299-310(1975)

(29) Nuclear Power Engineering Corporation, 1994, Report on Verification Testing for Improved Light-water Reactor Technology (concerning high-burnup fuel, etc.), March 1995

(30) W.J.O'Donnel and B.F.Langer, "Fatigue Design Basis for Zircaloy Components", Nuclear Science and Engineering 20 pp.1-12, 1964

(31) C.E.Coleman, J.F.R.Ambler, "Scripta Metallurgica", 17 1983, p77

(32) H.Stehle, W.Kaden and R.Manzel, "External Corrosion of Cladding in PWRs", Nuclear Engineering and Design 33 (1975) 155-169

(33) D.Hardie and M.W.Shanahan, "Stress reorientation of hydrides in zirconium 2.5% niobium", Journal of Nuclear Materials 55 (1975) 1-13

Table B.3.1.2-1 Calculation Results of Lattice Parameters and Densities (Theoretical Values)

Alloy	Sn* (at%)	Nb* (at%)	a_0 (Å)	c_0 (Å)	Density ρ (lb/ft^3)	(g/cm^3)
ZIRLO	0.7706	0.9837	3.22628	5.14713	408.3	6.541
Zr	-	-	3.2317	5.1476	406.2	6.507
Zr'y-4	1.1552	-	3.22851	5.14761	407.5	6.528
Low Sn Zr'y-4	1.0007	-	3.22894	5.14761	407.2	6.523

*: Nominal value of wt% converted into at%

Table B.3.3.1-1 Young's Module Obtained from the Load-Displacement Curve of Uniaxial Tensile Tests (725 deg.F (385 deg.C))

Material	Sample No.		Composition	Young's Module : E $\times 10^6$ psi / kg/mm^2
Zircaloy-4	A1927W	HT-1	1.54Sn-0.31(Fe+Cr)	9.7167 $\times 10^6$ psi 6831.8kg/mm^2
		-2	-0.125 O	10.265 7217.6
				(9.9910) (7024.7)
	A1976W	HT-1	1.61Sn-0.32(Fe+Cr)	9.4228 6625.2
		-2	-0.125 O	9.7118 6828.4
				(9.5673) (6726.8)
Low C/W Zircaloy-4	RD-179	HT-1	1.52Sn-0.32(Fe+Cr)	10.314 7251.7
		-2	-0.13 O	10.108 7106.7
		-3		10.615 7469.5
				(10.346 (7274.0)
ZIRLO	8827W-1	HT-1	0.97Sn-0.106(Fe+Cr)-1.03Nb	9.5173 $\times 10^6$ psi 6691.6
		-2	-0.1108 O	9.5582 6720.4
		-3		9.5378 6706.0
				(9.5378) (6706.0)
β-quench ZIRLO	8828W-2	HT-1	〃	8.8187 6200.4
		-2	-0.1056 O	10.282 7229.1
		-3		9.7256 6838.1
				(9.6087) (6755.9)

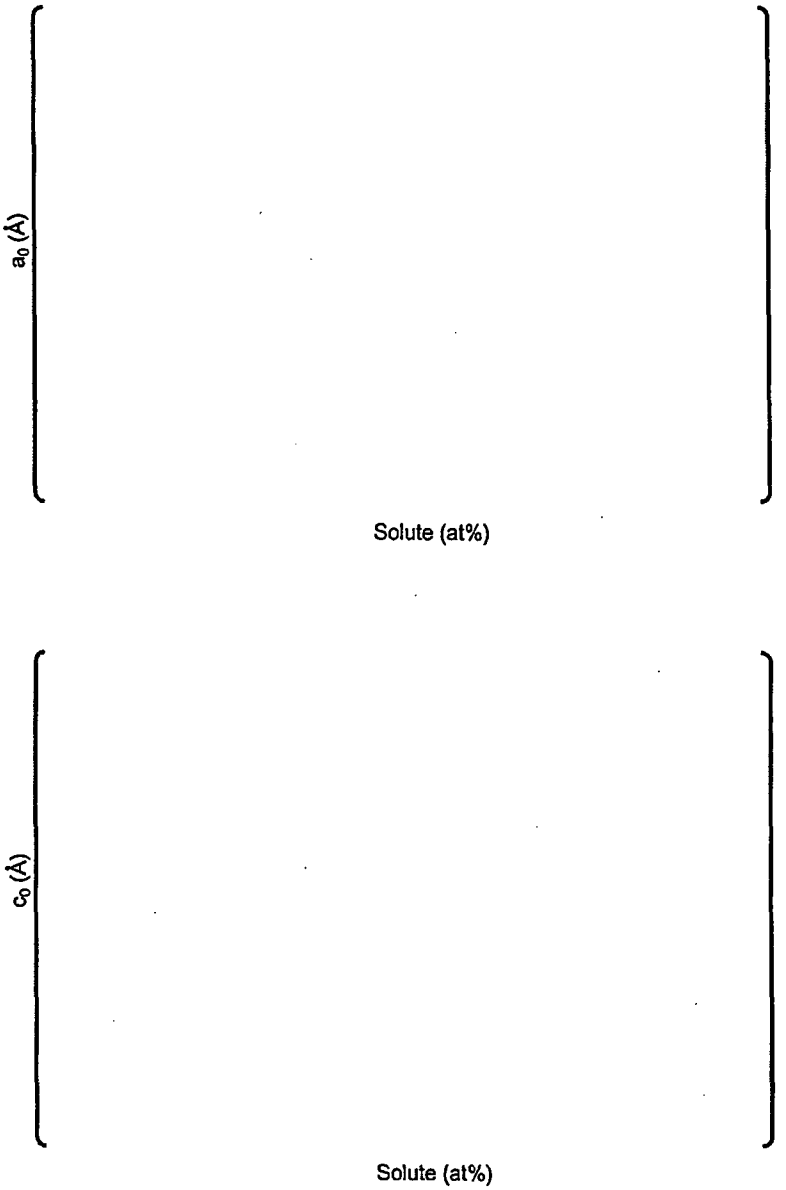

Figure B.3.1.2-1 Effects of Sn, Nb on the Lattice Parameters of α - Zr

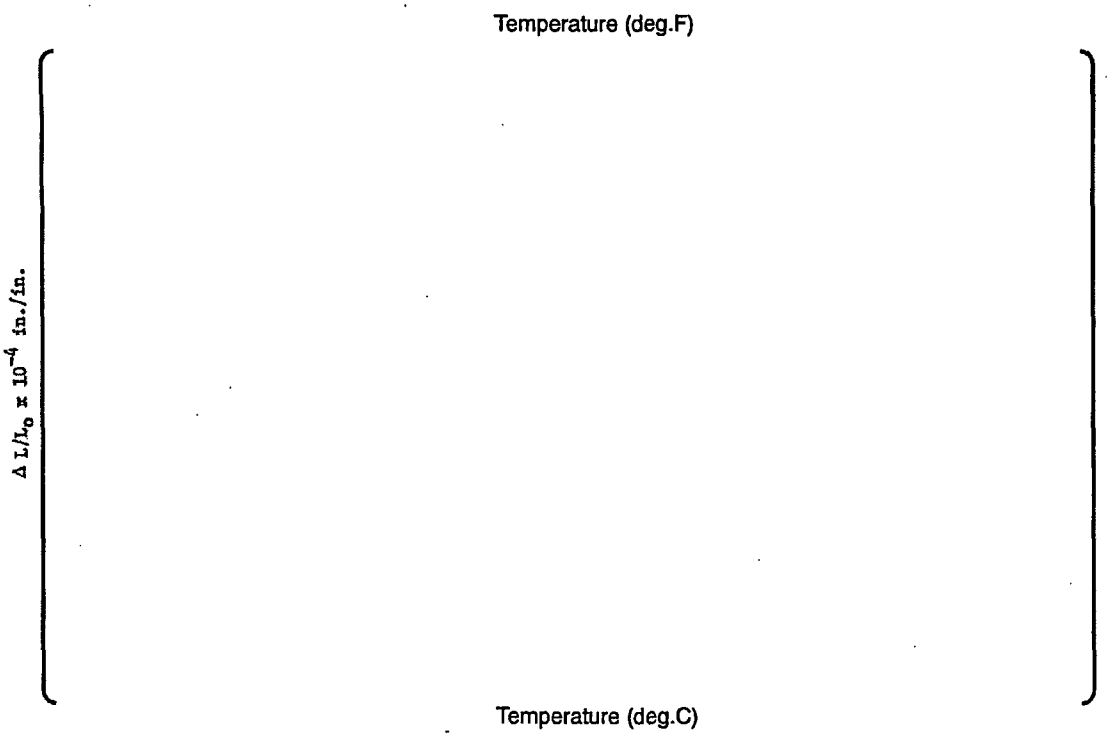

Figure B.3.1.3-1 Thermal Expansion of ZIRLO and Zircaloy-4 [5]

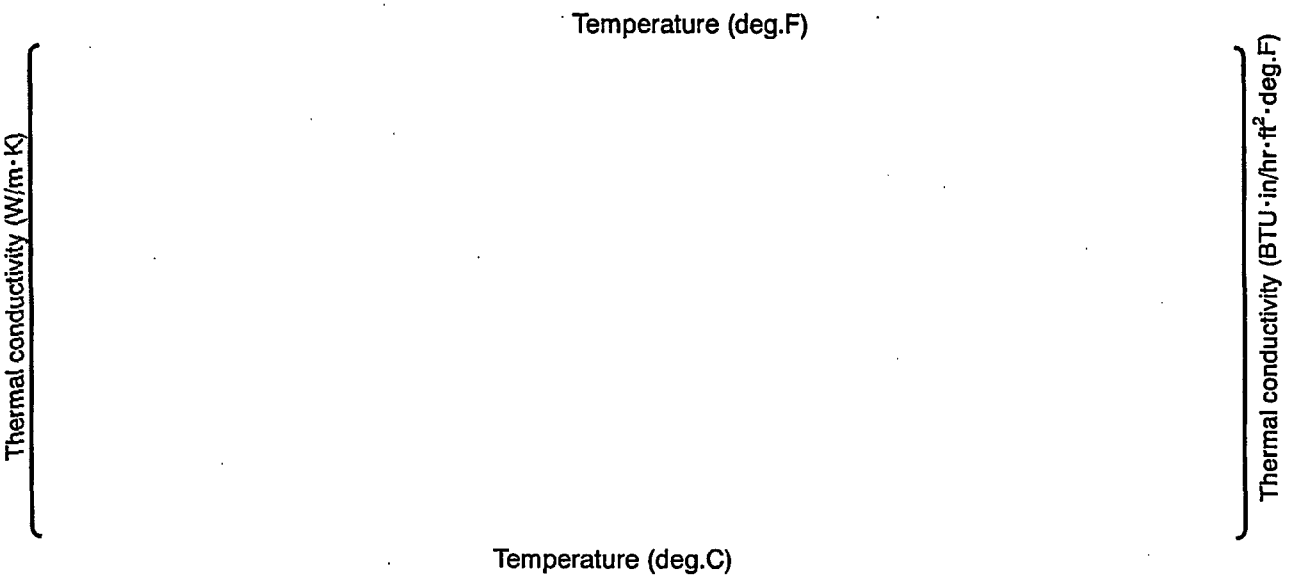

Figure B.3.1.4-1 Thermal Conductivity of ZIRLO and Zircaloy-4

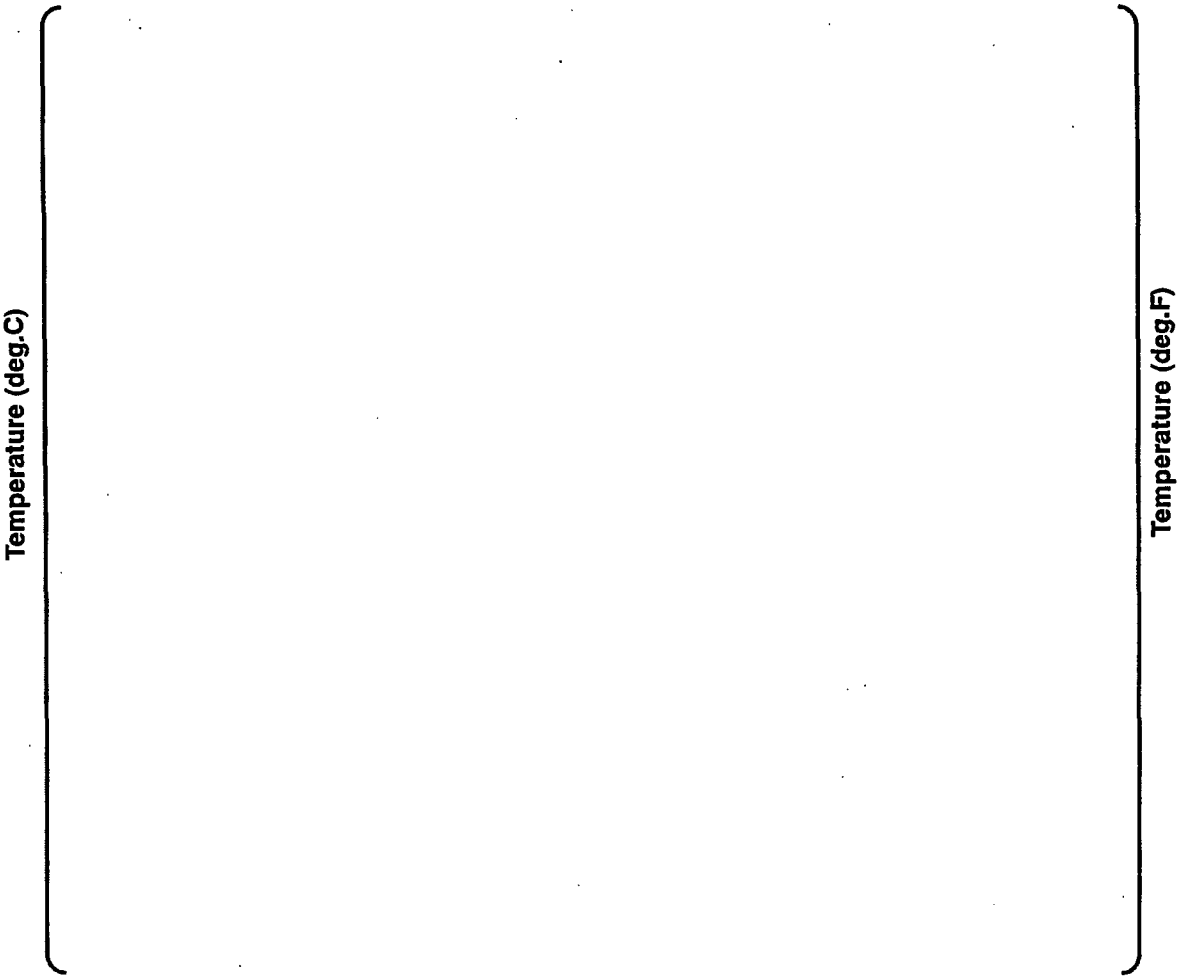

Figure B.3.1.6-1 Relationship Between α to α+β Phase Transformation Temperatures and Sn Content

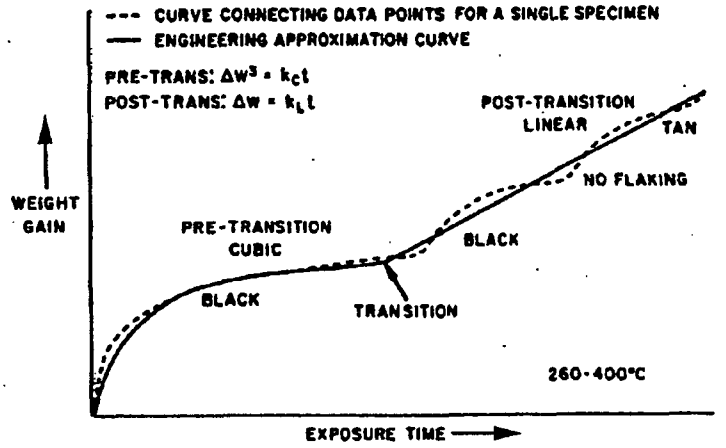

Figure B.3.2.2-1 Typical Corrosion Increase Curves from Out-of-Pile Corrosion Tests for Zircaloy-2 and Zircaloy-4[10]

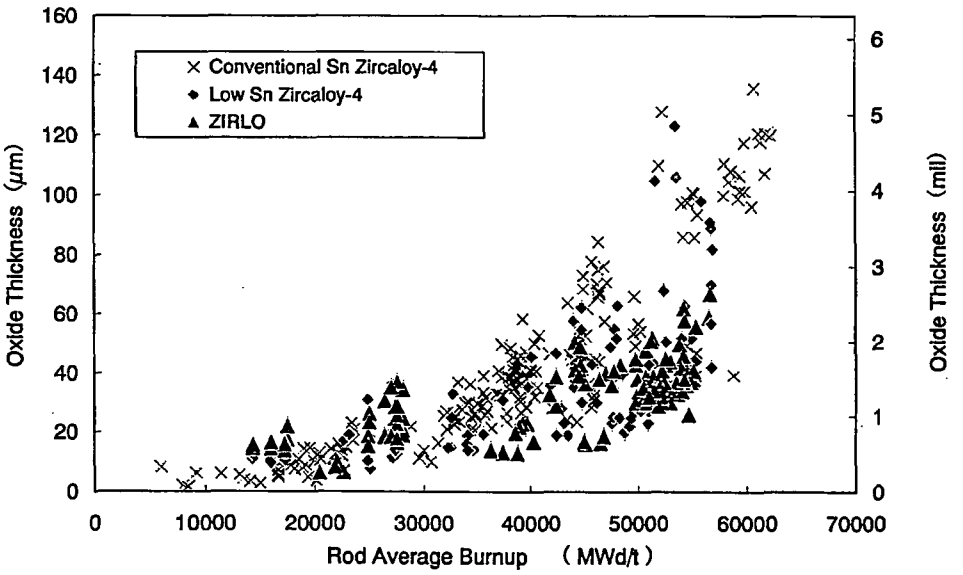

Figure B.3.2.2-2 In Pile Corrosion Behavior [1],[13] - [23]

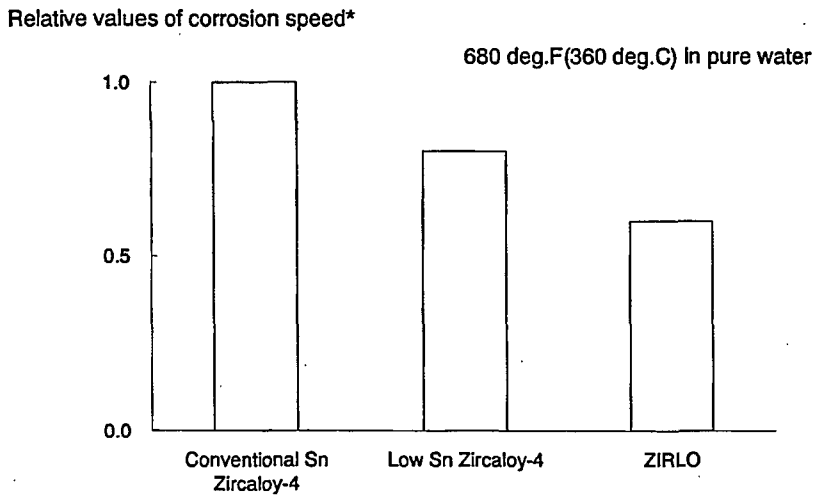

* Relative values of corrosion speed of each cladding material in case the corrosion rate of conventional Sn Zircaloy-4 is 1.0

Figure B.3.2.2-3 Comparison of Out-of-Pile Corrosion Rate between ZIRLO and Zircaloy-4

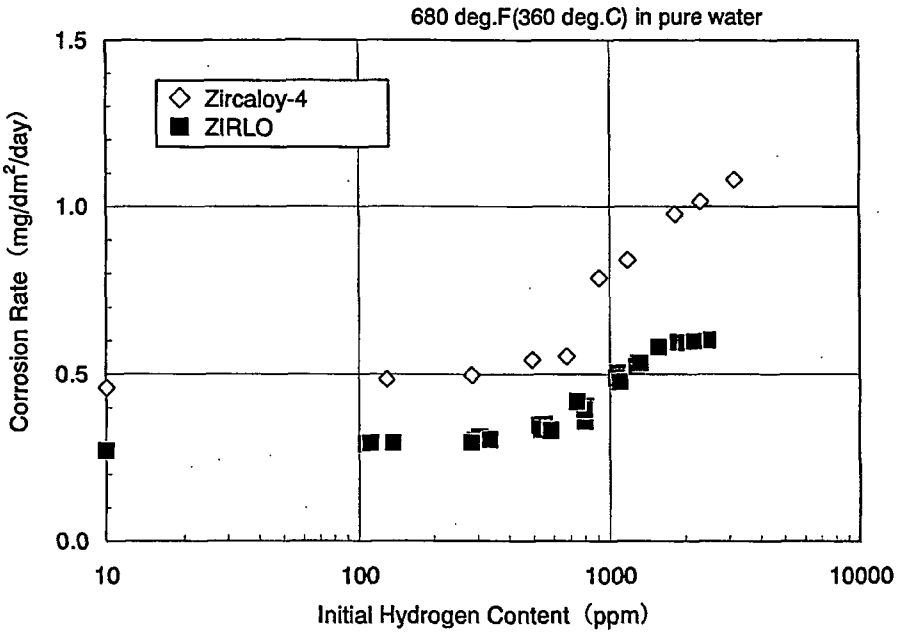

Figure B.3.2.2-4 Out-of-Pile Corrosion Rate of Pre-Hydrided Cladding

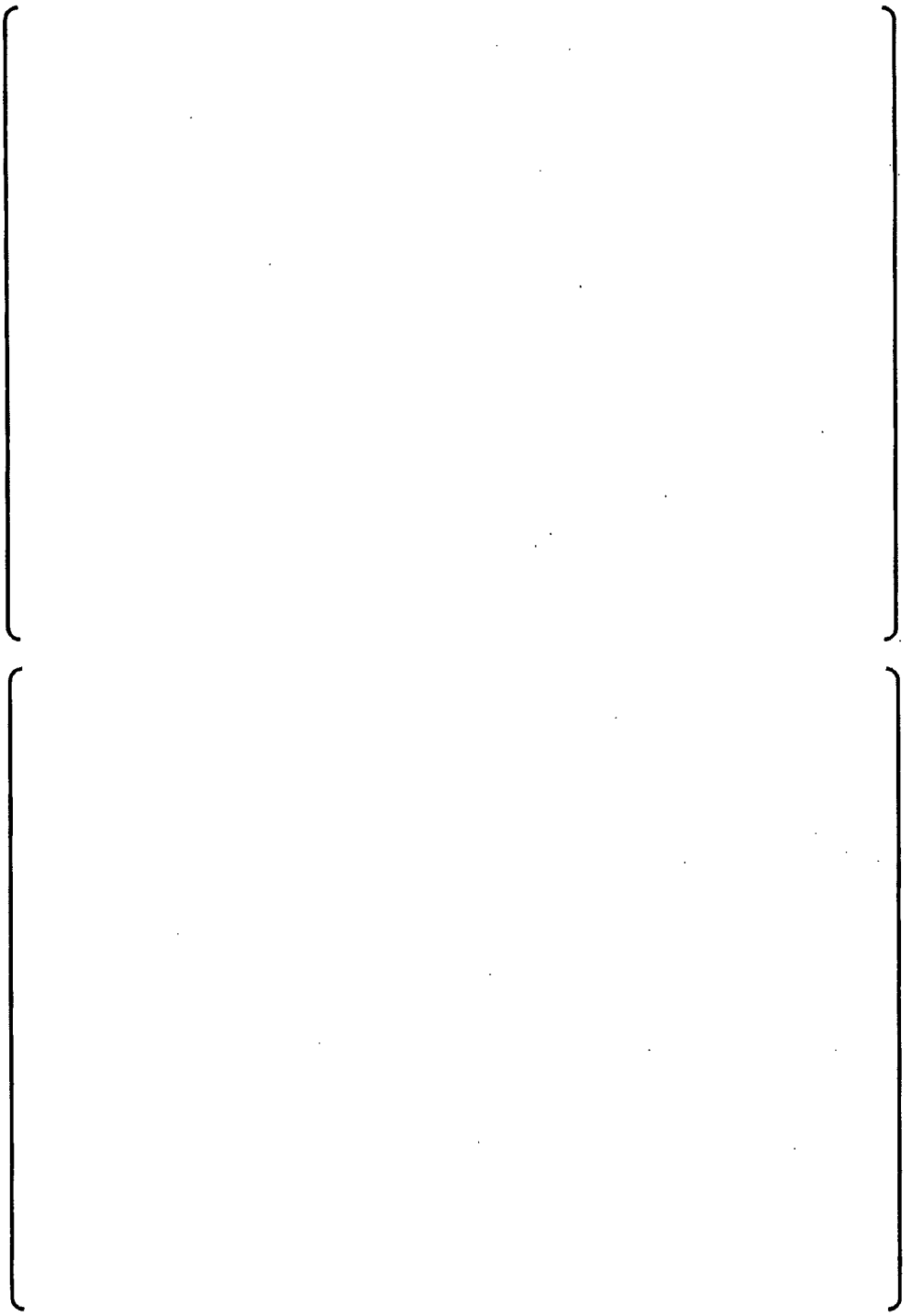

Figure B.3.2.2-5(1/2) Corrosion of Zircaloy-4 Over 752 deg.F (400 deg.C)

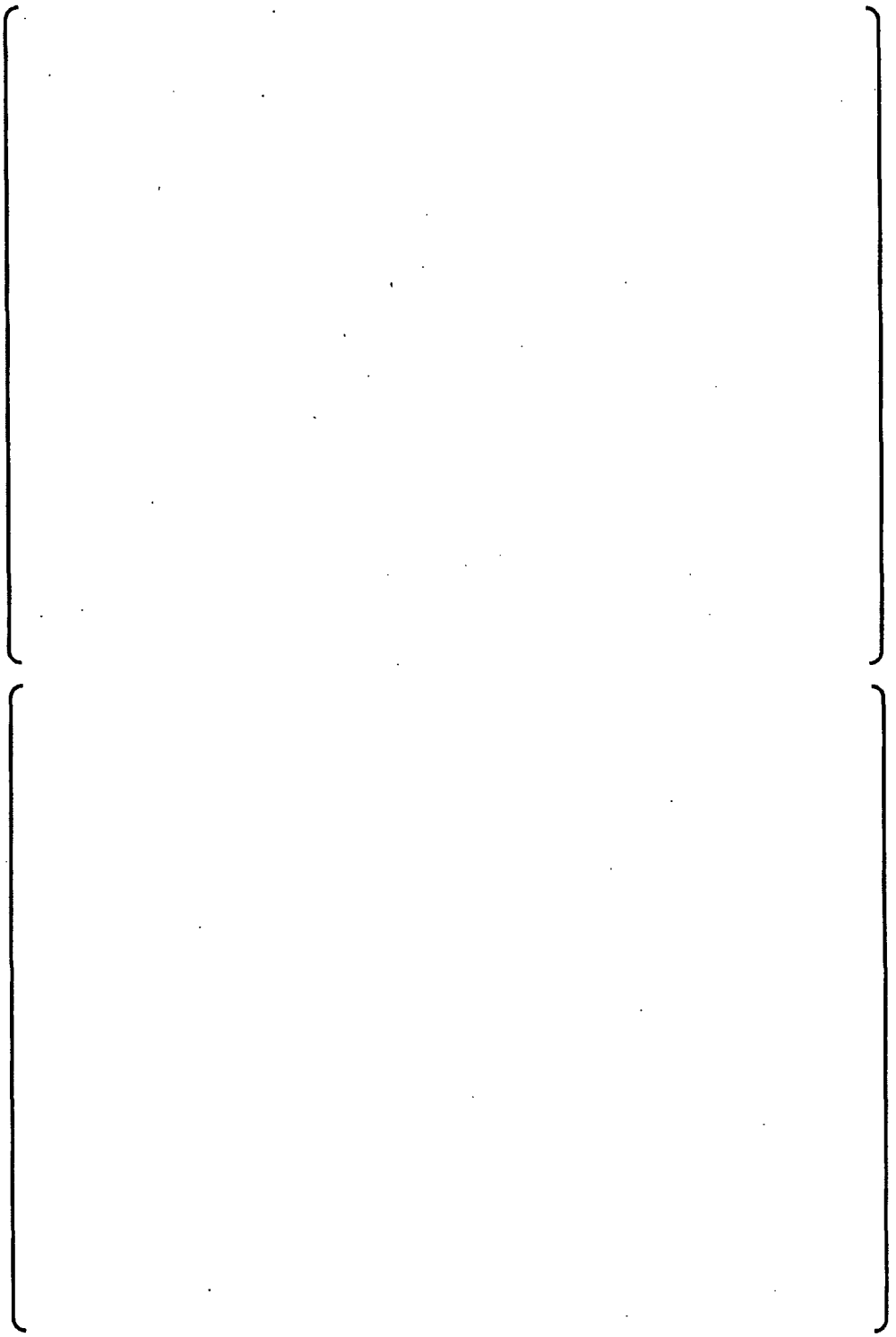

Figure B.3.2.2-5(2/2) Corrosion of Zircaloy-4 Over 752 deg.F (400 deg.C)

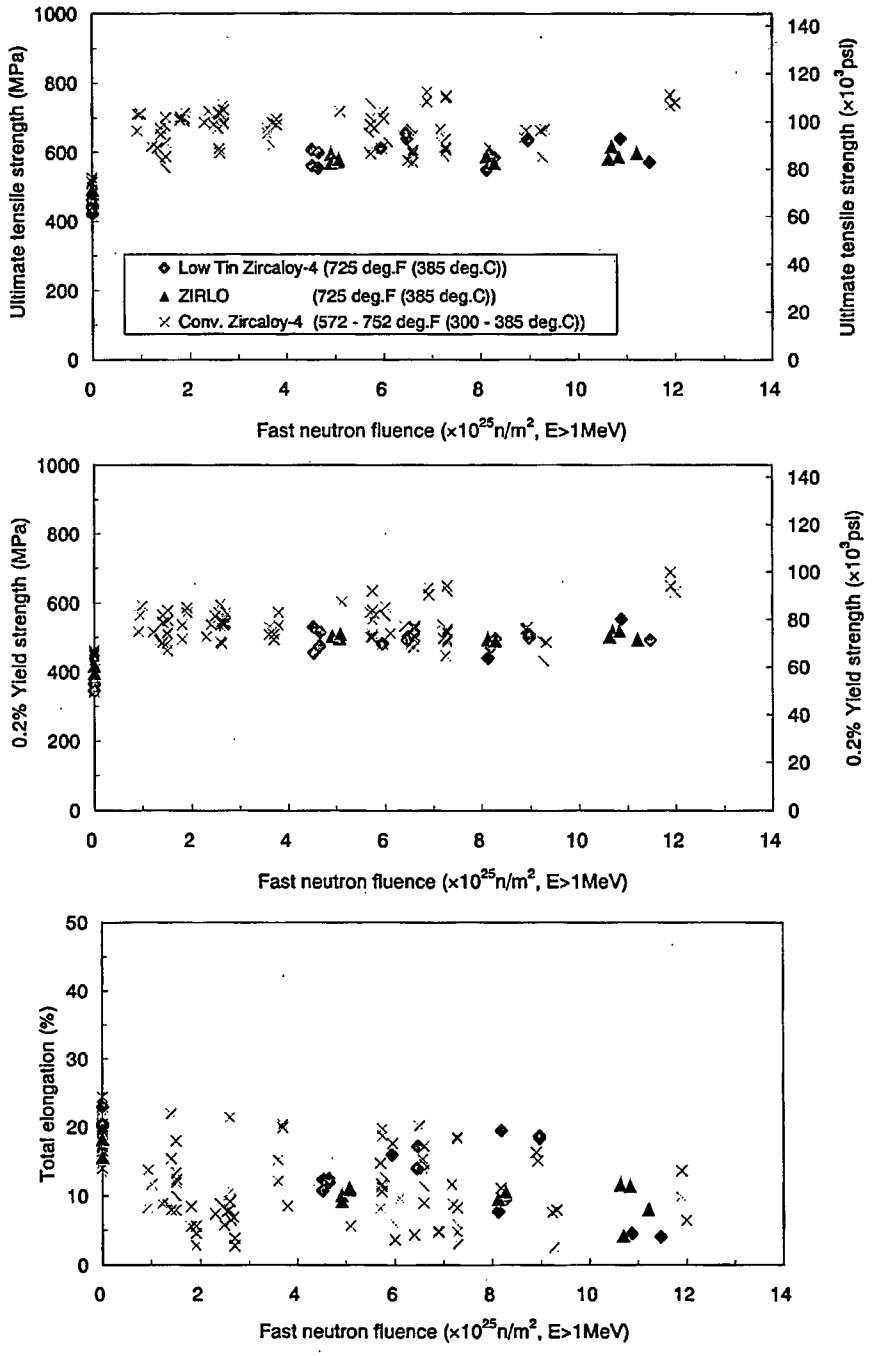

Figure B.3.3.3-1 Relationship between Mechanical Properties and Fast Neutron Fluence

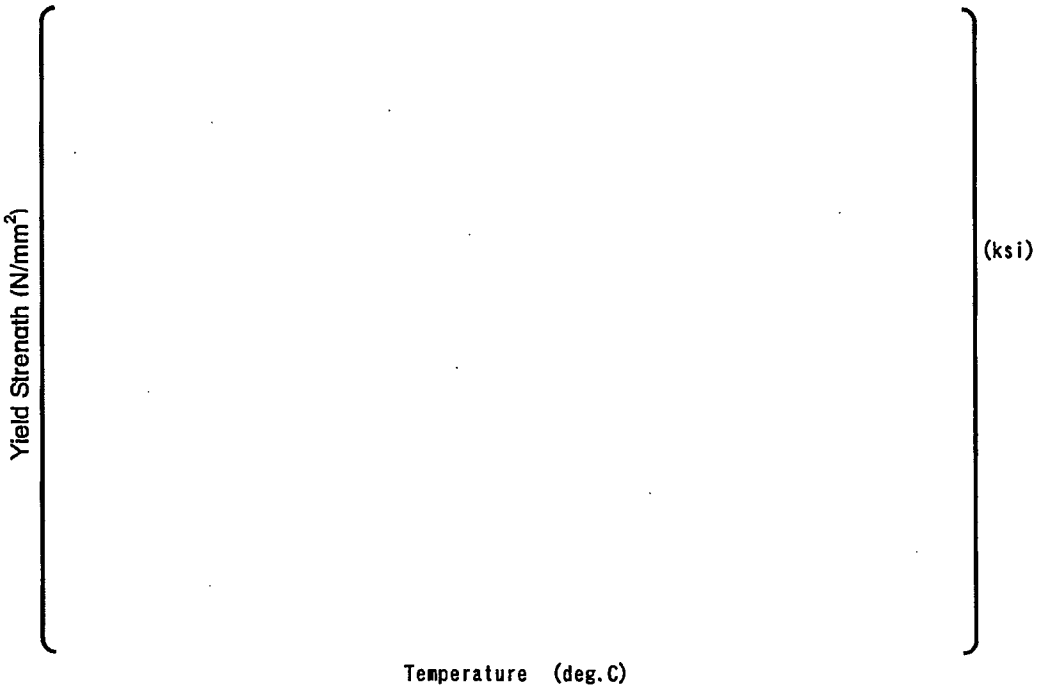

Figure B.3.3.3-2 Relationship between Yield Strength and Test Temperature

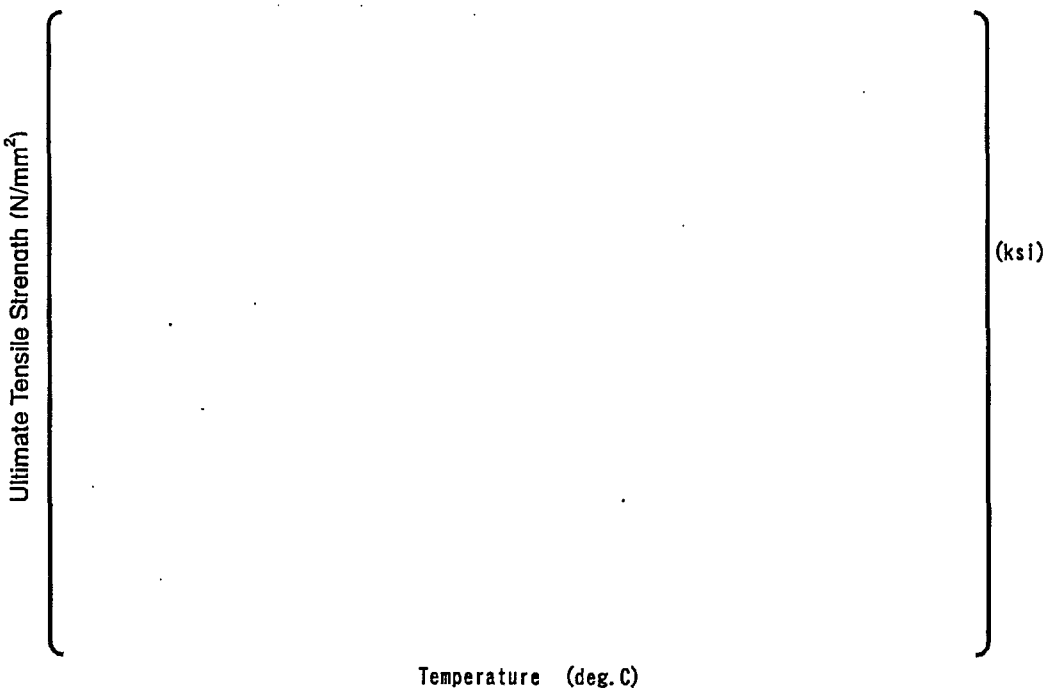

Figure B.3.3.4-1 Relationship between Ultimate Strength and Test Temperature

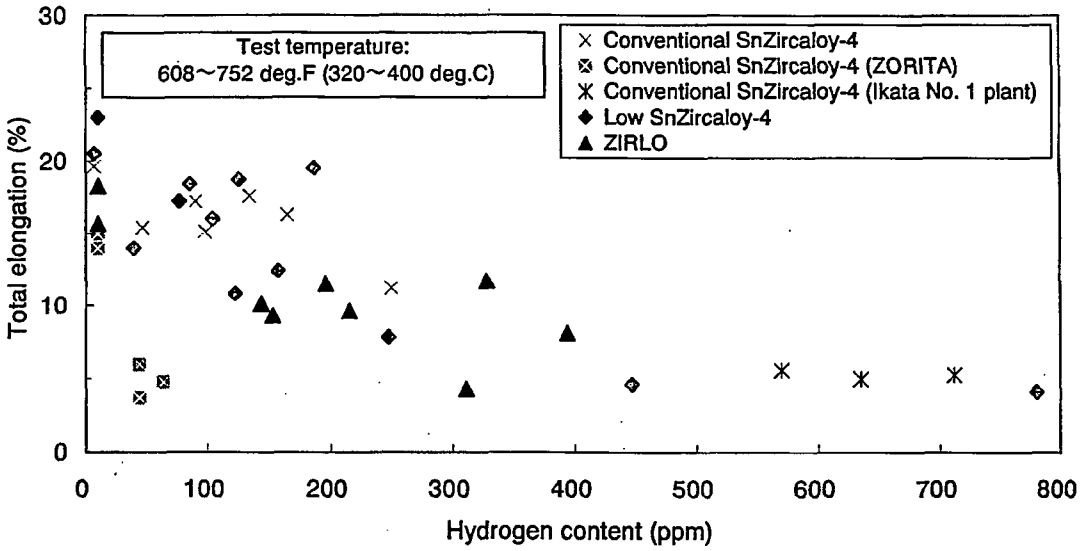

Figure B.3.3.5-1 Relationship Between Cladding Hydrogen Content and Total Elongation[30],[31]

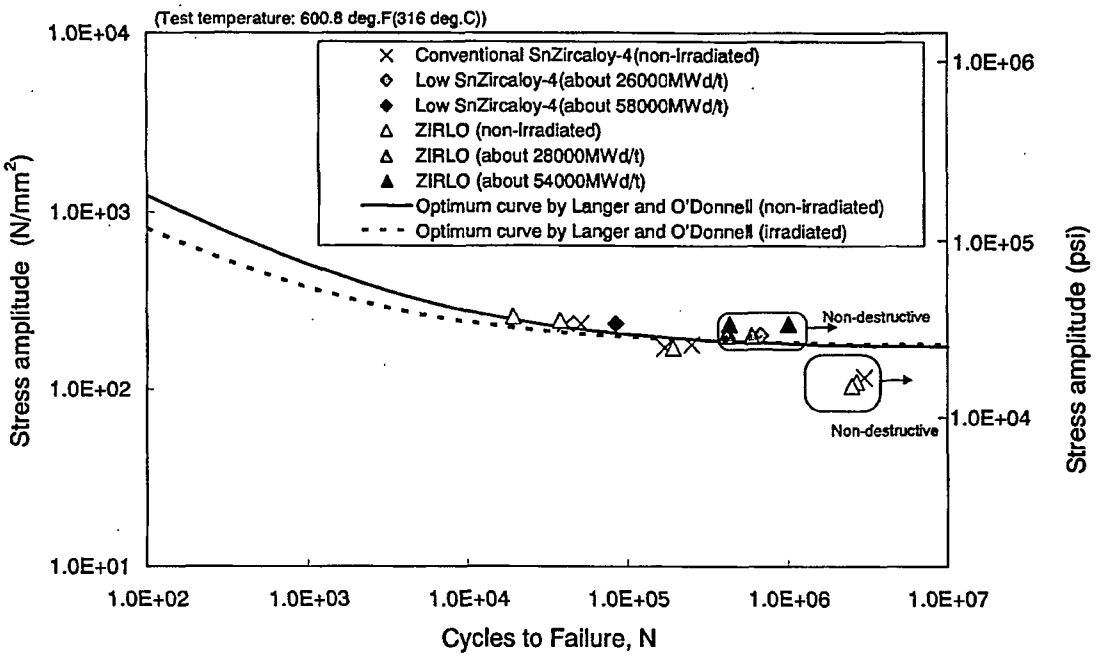

Figure B.3.3.6-1 Irradiation Data Comparing to Langer-O'Donnell Model

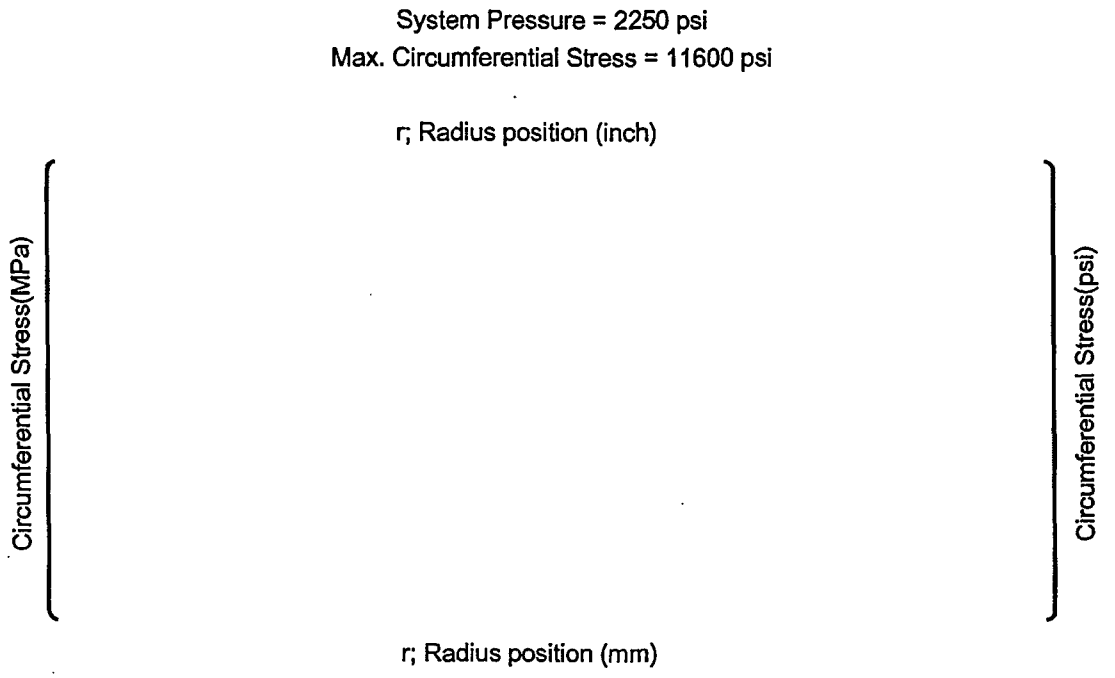

Figure B.3.3.7-1 Example of Circumferential Stress of Fuel Cladding

Appendix C

SAMPLE FINE CODE CALCULATION

May 2007

Table of Contents

List of Tables

List of Figures

Lists of Acronyms

FINE	Fuel rod INtegrity Evaluation
APWR	Advanced Pressurized Water Reactor
P/H	Power History
BOL	Beginning Of Life
EOL	End Of Life

C.1.0 INTRODUCTION

This appendix describes sample FINE code input and calculated results for a typical in normal operation for Mitsubishi fuel rod. The sample calculation is for a best estimate analysis. Section 2 and 3 provide descriptions of a sample input and output of fuel rod analysis.

C.2.0 SAMPLE FINE CODE INPUT

C.2.1 General

(1) Fuel Rod Geometry

17x17, 12 ft type PWR fuel rod geometry is used for sample FINE input. The fuel rod design provides fuel geometry information.

(2) Linear Heat Rate

The core average linear heat generation rate is another critical input to the fuel integrity analysis.

(3) Power History

The fuel rod power as a function of the irradiation time, called the power history (Power History: P/H), is an important parameter in the evaluation of fuel rod behavior. For this reason, the fuel integrity evaluation is performed based on the results of the core physics analyses for the fuel operating cycles. Figure C.2.1-1 shows the rod power history for sample FINE input.

(4) Axial Power Shape

The fuel irradiation conditions in the fuel rod integrity analysis are properly defined by considering the axial power distribution in the reactor core as well as the rod average power history based on the results of the core physics analyses. Figure C.2.1-2 shows the axial power distribution for sample FINE input.

(5) Fast Flux / Fluence

Since the cladding creep and irradiation growth depend on the fast flux and fast fluence, conversion factors relating the fast flux and fast fluence to the power and burnup, respectively, are provided by reactor core design.

(6) Primary Water Condition

The primary coolant flow rate, the primary coolant inlet temperature and the system pressure are required inputs for the fuel integrity analysis.

Figure C.2.1-1 Rod Power History

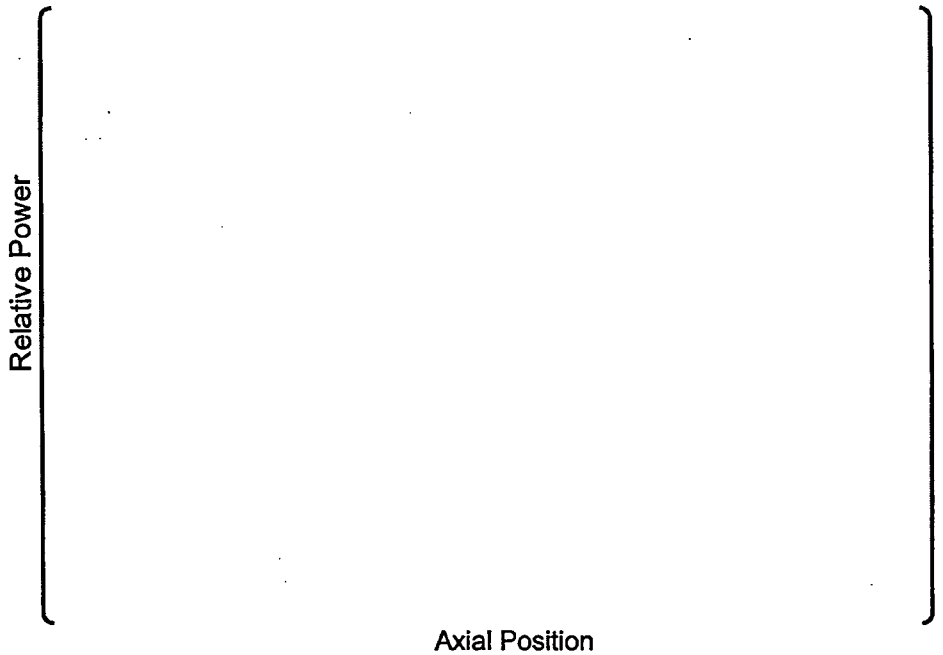

Figure C.2.1-2 Axial Power Distribution

C.2.2 Descriptions of Sample Input Parameters

The following table provides descriptions of the FINE code input parameters used in the sample calculation.

GROUP1

variable	Description	unit

GROUP2

variable	Description	unit

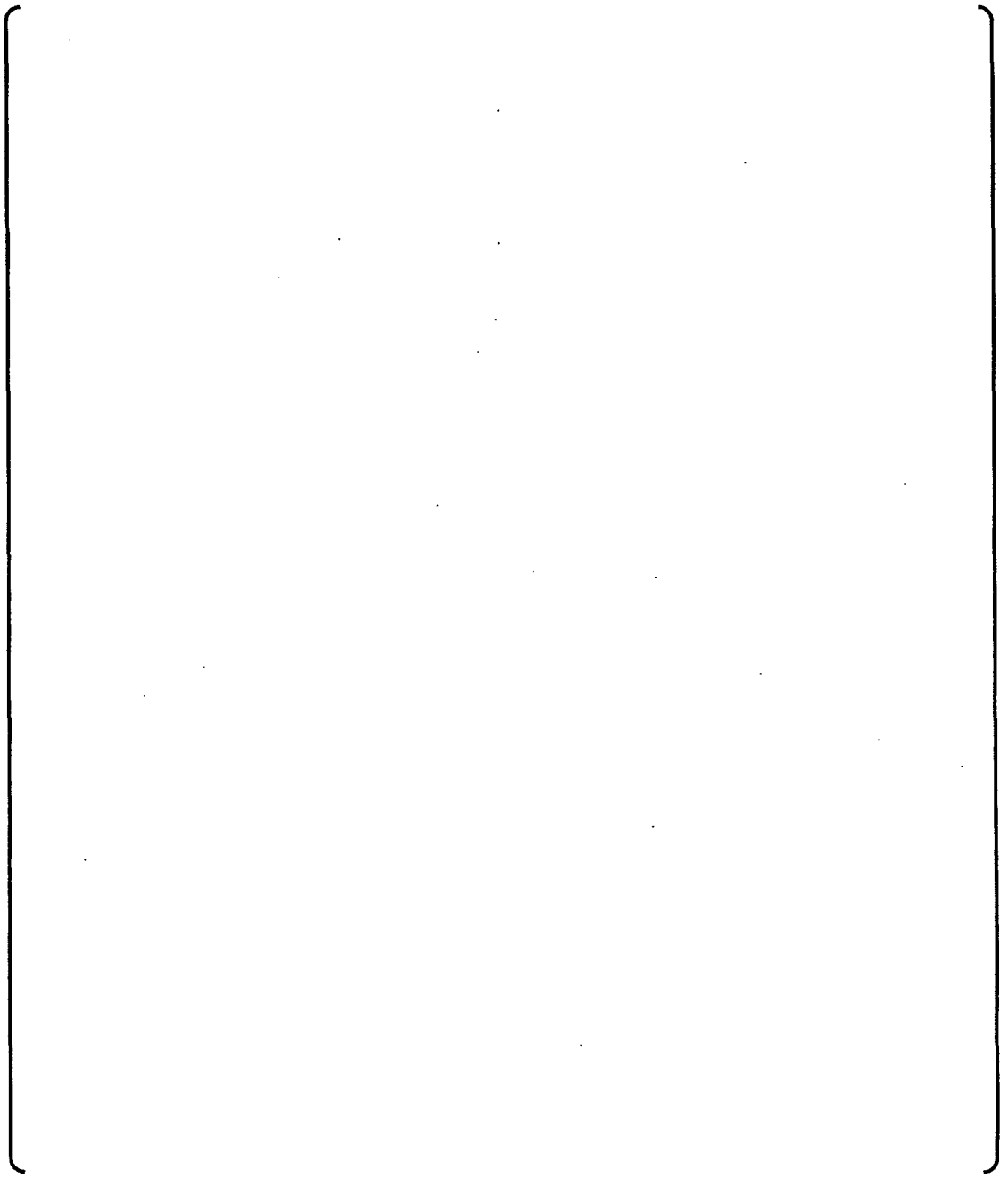

C.2.3 Sample FINE Code Input

FINE code input for this sample calculation is given below.

Sample input

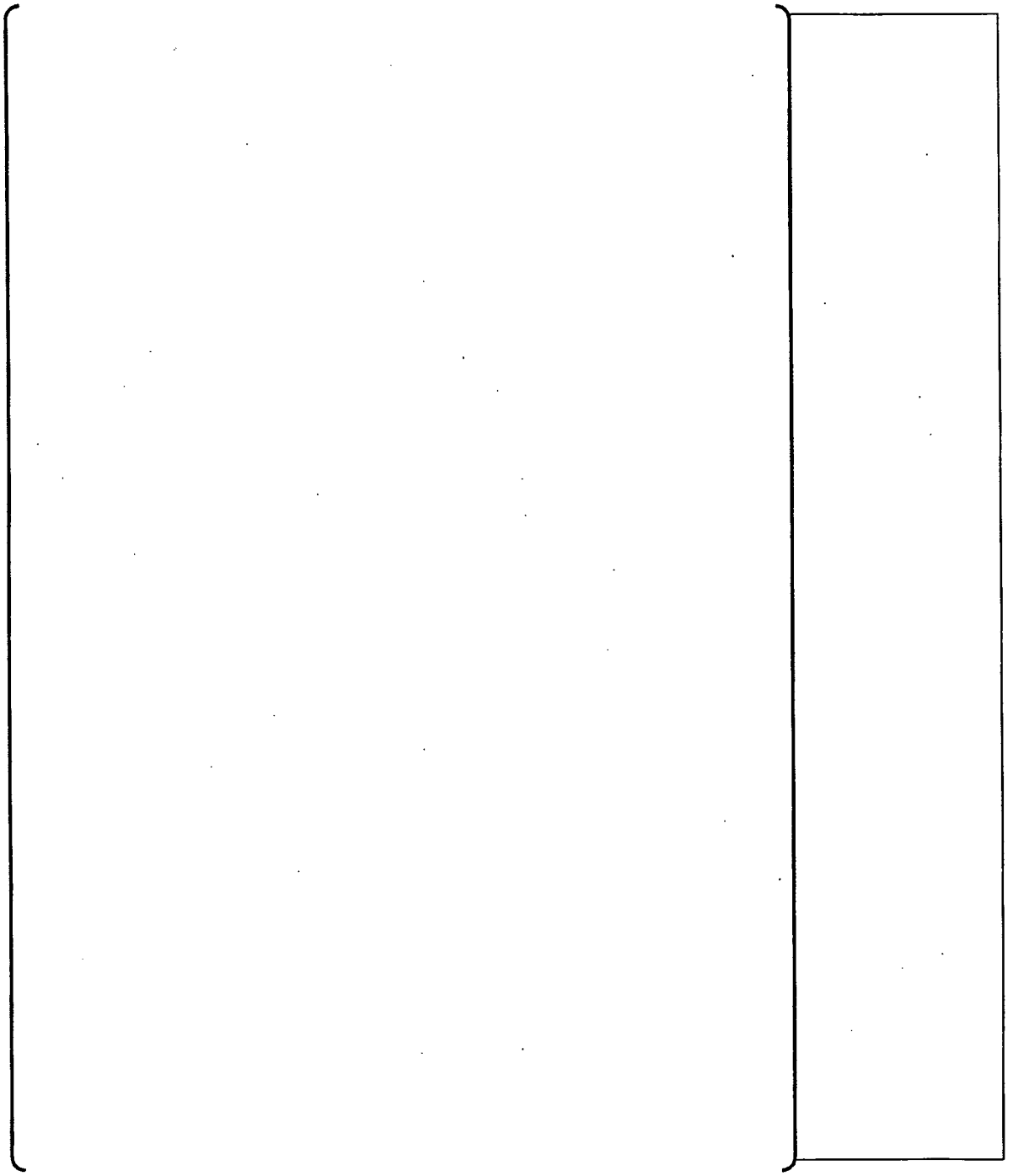

C.3.0 SAMPLE FINE CODE OUTPUT

C.3.1 Sample FINE Code Output

FINE code outputs at BOL (Beginning Of Life) and EOL (End Of Life) for this sample calculation are given in Table C.3.1-1.

C.3.2 The FINE Code Results for Sample Calculation

The FINE code results for this sample calculation are summarized in Figure C.3.2-1 to Figure C.3.2-8.

Table C.3.1-1(1/4) FINE Code Outputs for Sample Input at BOL and EOL

Sample Outputs

Table C.3.1-1(2/4) FINE Code Outputs for Sample Input at BOL and EOL

Sample Outputs		

Table C.3.1-1(3/4) FINE Code Outputs for Sample Input at BOL and EOL

Sample Outputs

Table C.3.1-1(4/4) FINE Code Outputs for Sample Input at BOL and EOL

Sample Outputs

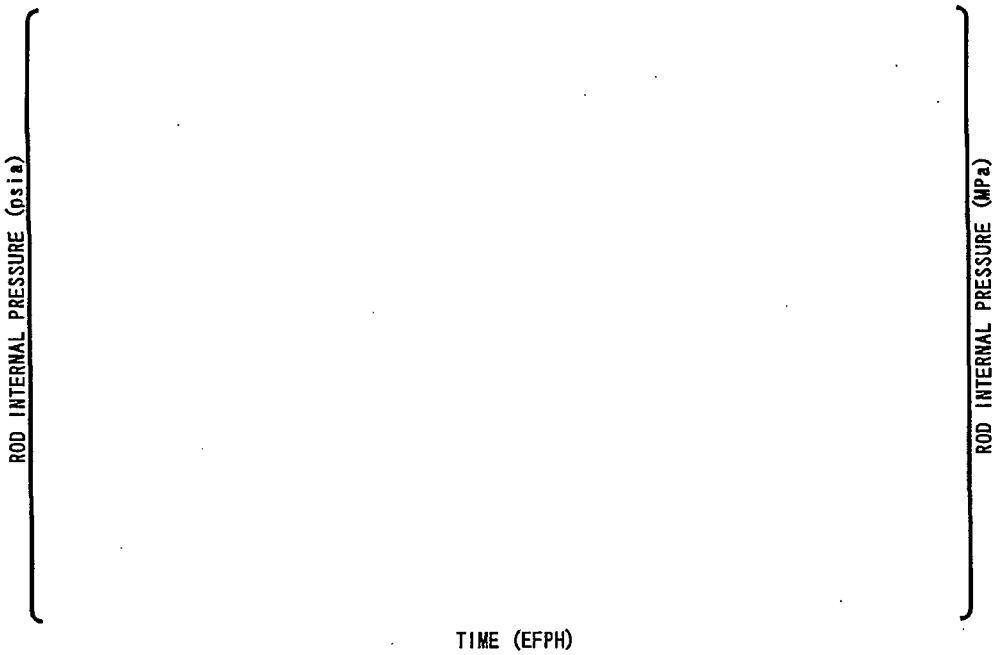

Rod Internal Pressure Performance

Figure C.3.2-1 Rod Internal Pressure

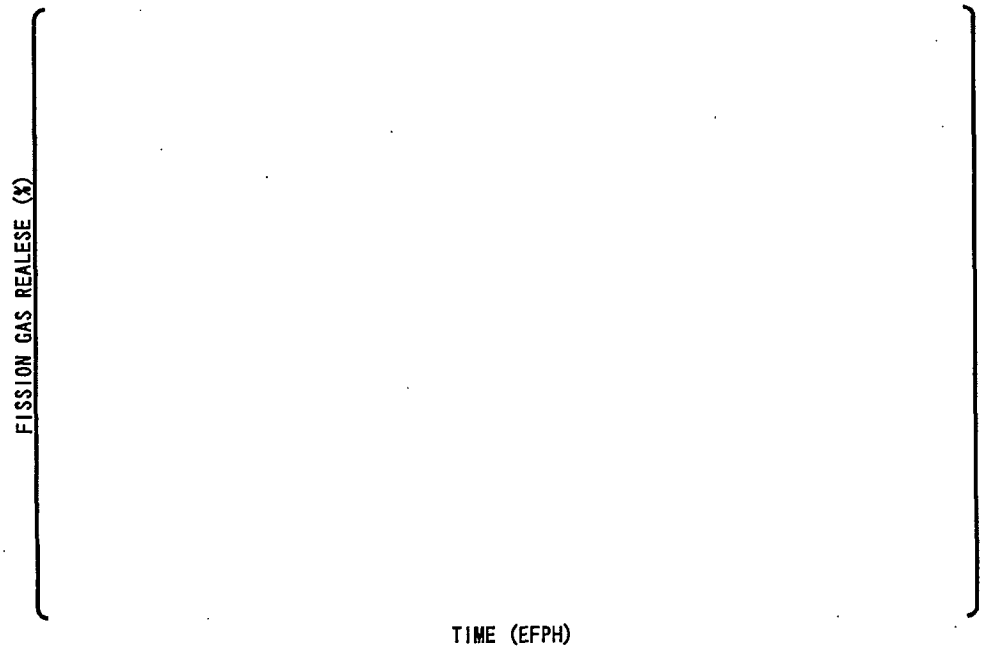

F.G.R Performance

Figure C.3.2-2 Fission Gas Release

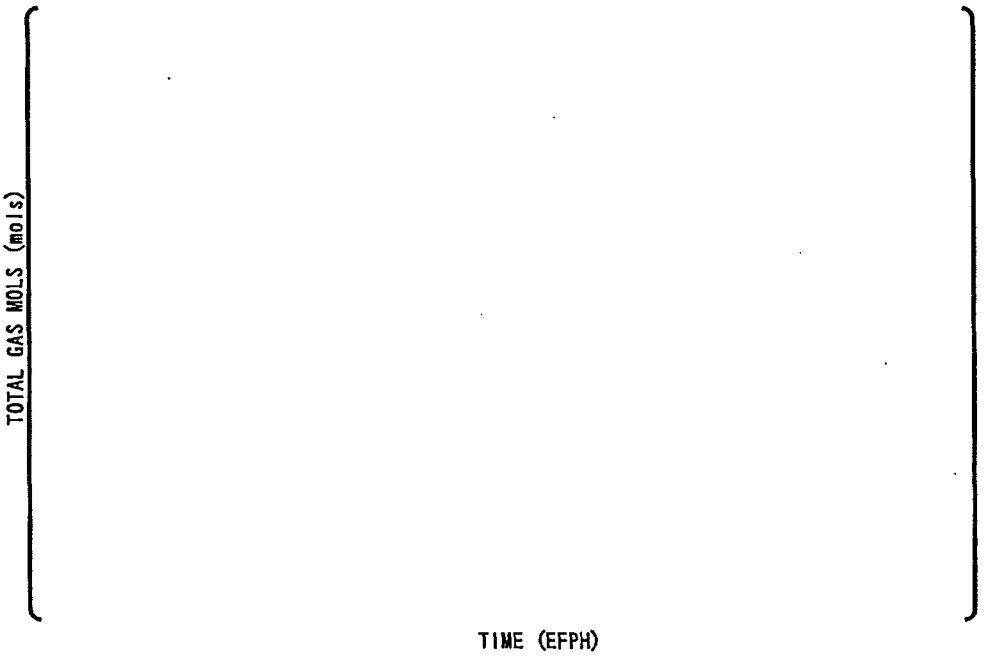

Total Gas Mol Performance

Figure C.3.2-3 Rod Total Gas Content

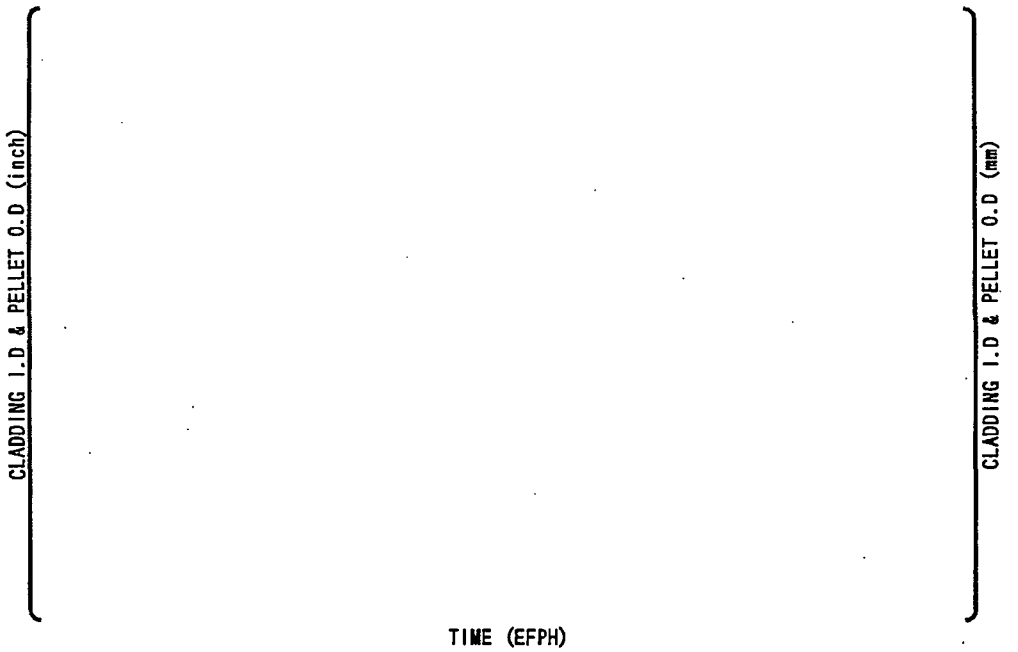

Figure C.3.2-4 Cladding Inner Diameter and Pellet Outer Diameter

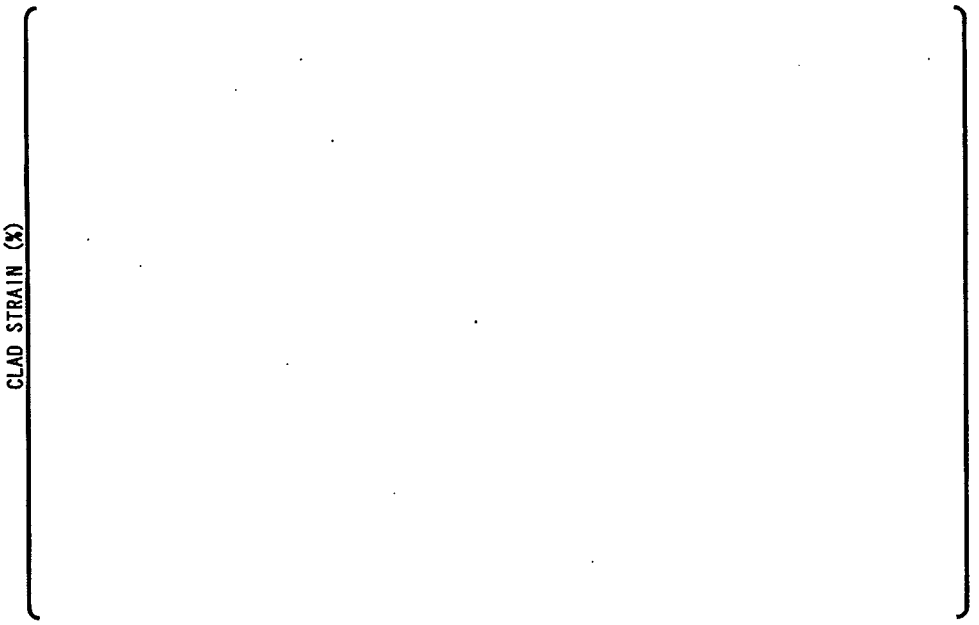

Clad Strain Performance

Figure C.3.2-5 Cladding Strain

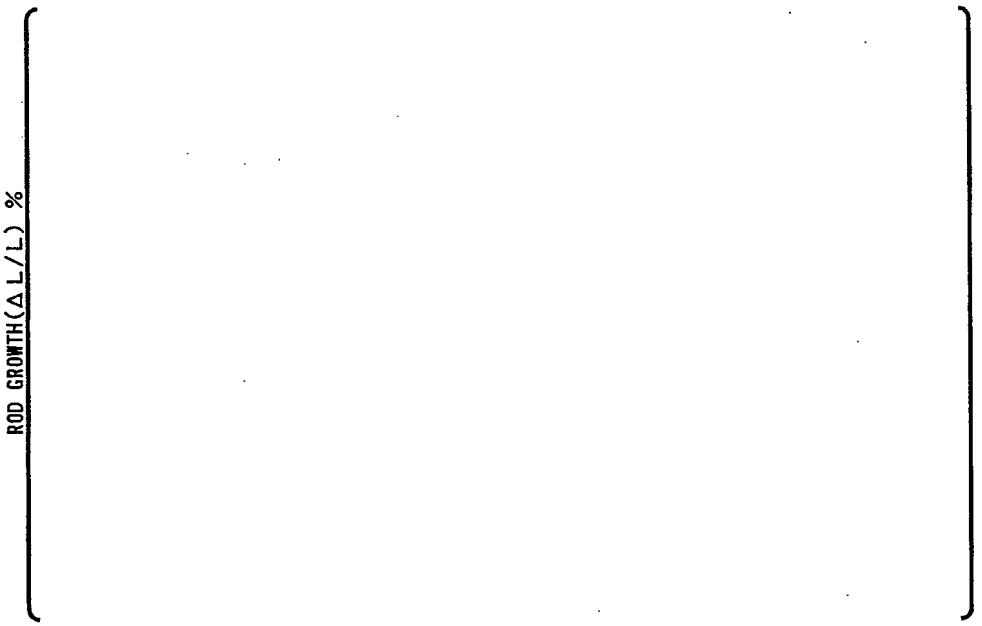

Rod Growth

Figure C.3.2-6 Rod Growth

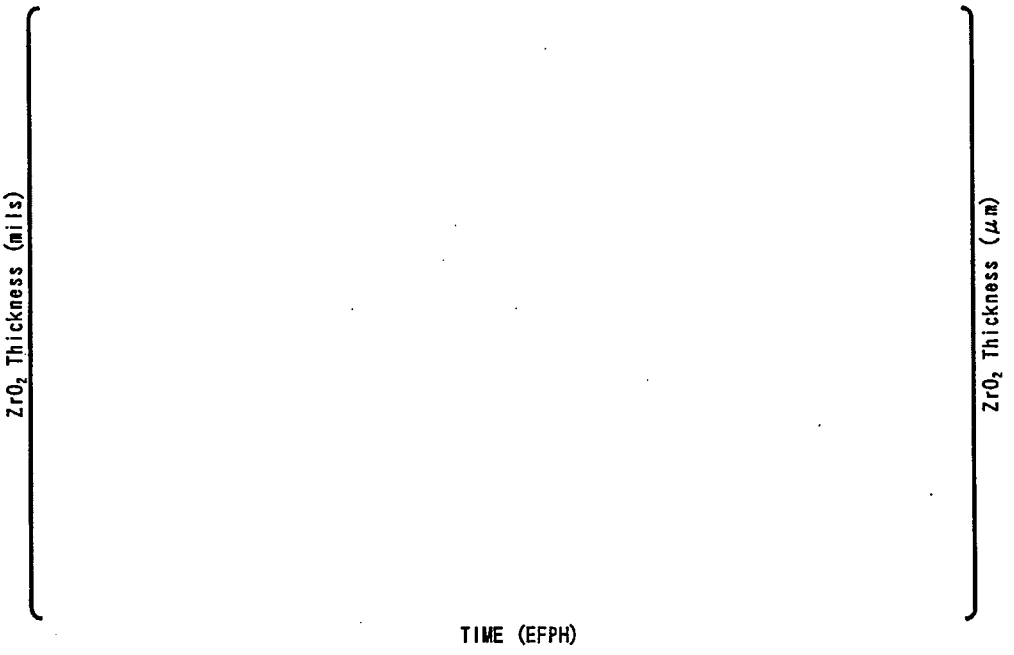

ZrO_2 Performance

Figure C.3.2-7 Cladding Corrosion

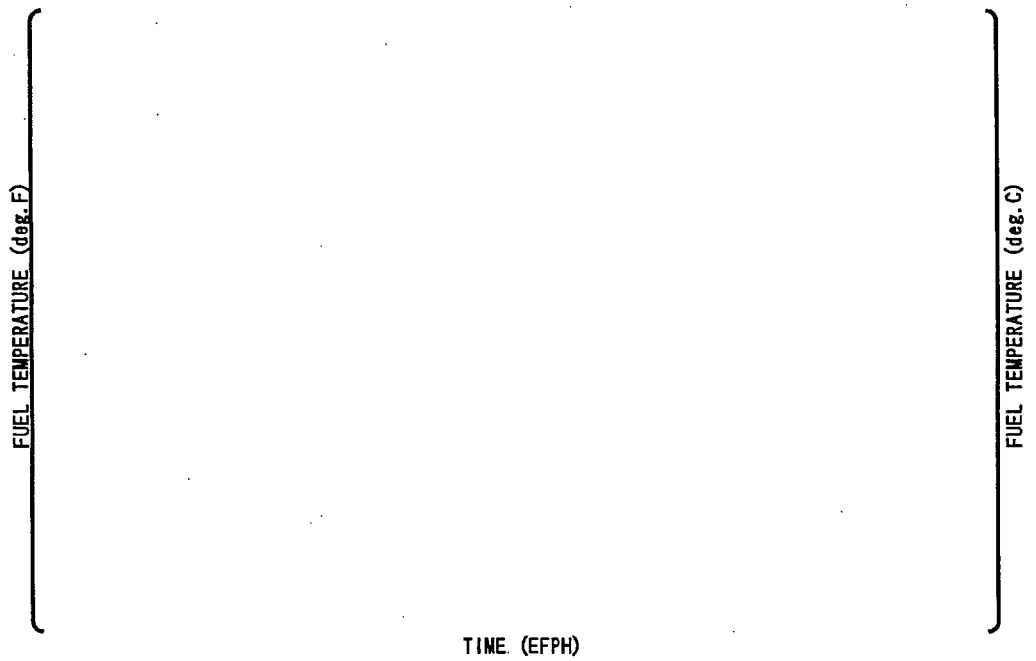

Fuel Rod Temperature Performance

Figure C.3.2-8 Fuel Temperature

Appendix D

ANALYSIS METHODOLOGY OF US-APWR FUEL ASSEMBLY FOR COMBINED SEISMIC AND LOSS-OF-COOLANT ACCIDENT

May 2007

Table of Contents

List of Tables

List of Figures

D.1.0 INTRODUCTION

The fuel assembly of US-APWR (referred to simply as 'fuel assembly' below), is an important structural component of the core. It is supported by a core support structure placed within the reactor vessel, and it is subjected to flowing coolant at high temperature and pressure during operation. With respect to Standard Review Plan Section 4.2 (NUREG-0800) [1], the fuel assembly must maintain the coolable geometry of the core during both seismic and loss of coolant accident (LOCA) events, and there must be no obstruction to the insertion of control rods for safe reactor shutdown. The fuel assembly must be designed to fulfill those functions. This appendix describes the functional requirement for the fuel assembly, the design philosophy, the acceptance criteria, and the evaluation methodologies to demonstrate that the functional requirements of the fuel assembly are maintained in the seismic and LOCA event.

D.2.0 FUEL ASSEMBLY STRUCTURE, FUNCTIONAL REQUIREMENTS AND ACCEPTANCE CRITERIA

D.2.1 Fuel Assembly Structure

The structure of the US-APWR fuel assembly is shown in Figure D.2.1-1. The fuel assembly is comprised of a 17 x 17 square array of 264 fuel rods, 24 control rod guide thimbles, and one guide tube for in-core instrumentation, as well as eleven grid spacers, one top nozzle and one bottom nozzle.

D.2.2 Functional Requirements for the Fuel Assembly

In accordance with SRP Section 4.2 [1], the fuel assembly must be designed to be capable to maintain coolable geometry of the core and to shut down the reactors safely during both seismic and LOCA states. The safety functions of the US-APWR fuel assembly components to ensure this capability are listed in Table D.2.2-1.

Table D.2.2-1 Functional Requirements for the Fuel Assembly

Component	Functional Requirements	Comments
Grid spacers, top and bottom nozzles	Maintaining coolable geometry of the core	These bundle the fuel cladding to prevent major damage to the fuel and maintain the structure of the fuel assembly.
Control rod guide thimbles	Maintaining coolable geometry of the core	Connect the top and bottom nozzles and the grid spacers; also maintain the core shape by supporting the fuel rods via the grid spacers.
	Safe reactor shutdown	Maintaining the path for insertion of the control rod into the fuel assembly.
Fuel cladding	Maintaining coolable geometry of the core	Fuel cladding fragmentation must not occur.

D.2.3 Design Philosophy and Acceptance Criteria

To maintain the functions listed in Table D.2.2-1, the control rod guide thimbles, fuel claddings, grid spacers, the top and bottom nozzles must be designed to meet the required strength. There are, however, no concrete specifications of acceptance criteria regarding strength for these components during the earthquake and LOCA in ASME Section III [2] or SRP Section 4.2[1] except for fuel claddings.

Therefore, the acceptance criteria defined in ASME Section III Subsection NG [2] for core support structures that are applied in the strength evaluation of the core support structure (described below), which has the same safety functions as the fuel assembly, are also applied to these components.

For the control rod guide thimbles, acceptance criteria related to buckling under vertical load is added as an evaluation item to confirm that there will be no obstruction to control rod insertion to prevent safe reactor shutdown during an accident. For the grid spacers, which bundles the control rod guide thimbles and fuel cladding together to maintain the structure of the fuel assembly, there are additional acceptance criteria with regard to maintaining the coolable geometry of the core.
The specified acceptance criteria are presented in Table D.2.3-1.

Table D.2.3-1 Acceptance Criteria

Structural Component	Acceptance Criteria	
	Primary General Membrane Stress	Primary Membrane Stress + Primary Bending Stress
Control Rod Guide Thimble Top and Bottom Nozzles	Min. (2.4 Sm, 2/3 Su) Note:	Min. (3.6 Sm, Su)
Fuel Cladding	90% of the irradiated yield stress at the appropriate temperature	
Control Rod Guide Thimble	Shall not buckle when subjected to vertical compressive load during an accident.	
Grid Spacer	No excessive deformation shall occur due to load during an accident.	

Note: Sm is the allowable stress intensity value; Su is ultimate tensile stress.

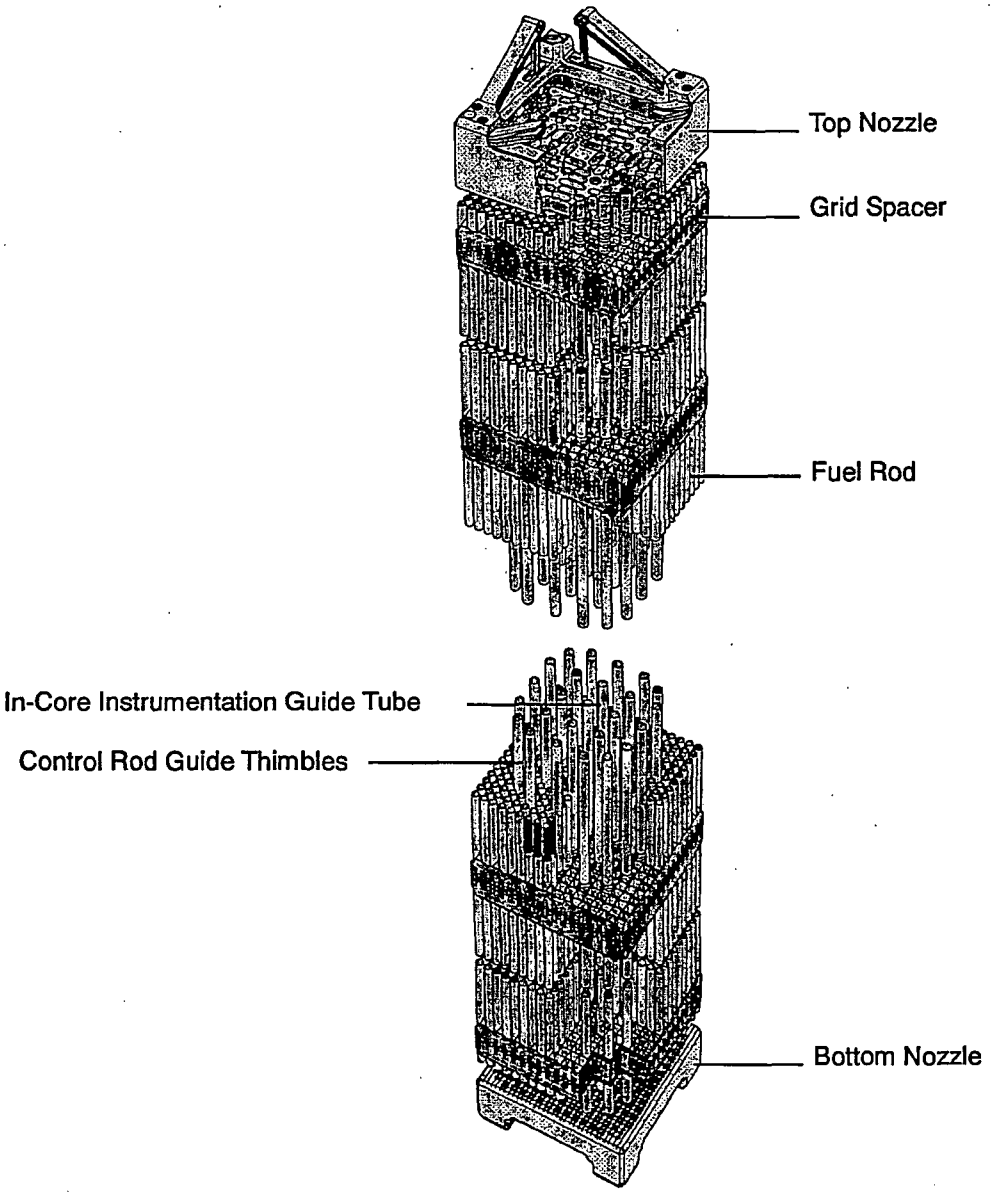

Figure D.2.1-1 Structural Schematic for the US-APWR Fuel Assembly

D.3.0 ENVIRONMENTAL CHANGES AROUND THE FUEL ASSEMBLY DURING EARTHQUAKE AND POSTULATED ACCIDENT

D.3.1 Structures Around the Fuel Assembly within the Reactor Vessel and Occurred Load

The fuel assembly is placed inside the reactor vessel as shown in Figure D.3.1-1. The reactor vessel also contains structures that serve to support the fuel assemblies, guide the control rods, and form paths for coolant flow. Of the core internal structures, the core plate, the core support plate, and the core support columns, and other such structures that support the fuel assemblies are particularly referred to as the core support structures. The fuel assembly is supported within the core barrel by the upper core plate and the lower support plates, and is fixed in place by pins attached to the upper core plate and the lower support plate. It is also surrounded by neutron reflectors that are placed in the core periphery.

During the plant operation, the hydraulic lift force, gravity and buoyant force act on the fuel assembly in addition to the mechanical force from the holddown spring for preventing liftoff of the fuel assembly. Once an earthquake happens, the loads caused by a motion of the reactor vessel act on the fuel assembly. On the other hand, the loads that accompany pressure fluctuations and hydraulic flow fluctuations in the reactor vessel act on the fuel assembly, when a postulated accident such as LOCA happens.

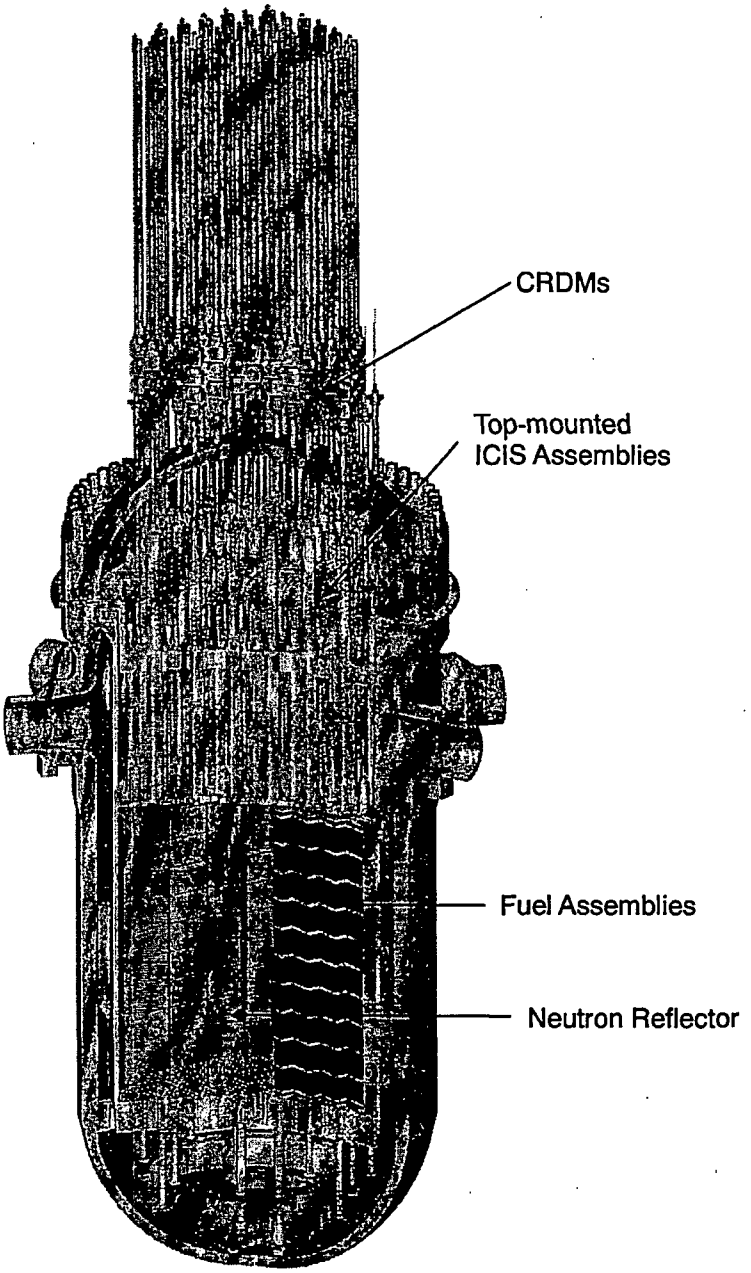

Figure D.3.1-1 Structures inside the US-APWR Reactor Vessel

D.3.2 Fuel Assembly Behavior during the Earthquake

The generation of stresses in the fuel assembly during the occurrence of an earthquake is described below.

- Vibration of the rector building caused by the earthquake leads to the vibration in the rector vessel.
- The vibration of the reactor vessel is accompanied by vibration of the upper core plate and the lower support plate that support the fuel assemblies.
- Because the upper core and the lower support plates vibrate in both vertical and horizontal directions, the accelerations vibrate the fuel assemblies supported by the plates.
- Magnitude and phase of the acceleration that act on the fuel assemblies due to the vibration of the upper and lower support points are the same as each other, because of the rigidity of the plates. Therefore, all of the fuel assemblies vibrate in synchrony. If the vibration is large, however, the displacement of the outermost fuel assemblies is limited by the neutron reflector, so collision may occur at the position of the grid spacers, the neutron reflectors or the adjacent fuel assemblies, which affects the horizontal vibration behavior of each fuel assembly.

D.3.3 Representative Postulated Accident

Of the postulated design bases accidents, LOCA involves a significant fluctuation of pressure and hydraulic flow inside the reactor, which are factors that affect the structural strength of the fuel assembly. In a LOCA caused by failure of a pipe, a decompression wave is generated at the point of failure which envelopes the core barrel vertically and circumferentially. That creates a time differential in the arrival of the decompression wave around the core that gives rise to loads, thus inducing vibration in the core. Therefore, LOCA is chosen as a representative event which affects on the fuel assembly's behavior in terms of causing significant vibration.

D.3.4 Fuel Assembly Behavior during LOCA

The fuel assembly behavior during LOCA is described below.

- Because the upper core plate and the lower support plate vibrate in both the horizontal and vertical directions due to the LOCA, the fuel assemblies supported by them are vibrated by the LOCA as well.
- The horizontal vibration of the upper core and the lower support plates during LOCA is at the fundamental frequency of the core barrel. Because the main vibration component is near 10 Hz, the fuel assemblies respond in a tertiary mode near their specific frequency. As with the seismic response in Section D.3.2, the magnitude and phase of the acceleration that act on the fuel assemblies due to the vibration of the upper and lower support points are the same, so all of the fuel assemblies vibrate in synchrony. If the vibration is large, however, the displacement of the outermost fuel assemblies is limited by the neutron reflector, so collision may occur at the position of the grid spacers, the neutron reflectors or the adjacent fuel assemblies, which affects the horizontal vibration behavior of each fuel assembly.

- Vertical vibration of the upper core plate and the lower support plate act on the fuel assembly as a form of the compressive load accompanied with distance variation between these plates where the fuel assembly is located. If that vertical acceleration of the lower support plate is large, it might cause the fuel assembly to rise up.

D.4.0 EVALUATION METHODOLOGY OF FUEL ASSEMBLY RESPONSE AND STRENGTH

D.4.1 Response Analysis of the Fuel Assembly in the Horizontal Direction

Horizontal responses to the earthquake and LOCA such as displacement of the fuel assembly and impact force at grid spacers among the fuel assemblies and neutron reflectors are independently analyzed by time-dependent response analysis code modeling a certain fuel assemblies array.
Obtained horizontal displacements are also independently provided to stress analyses of the fuel assembly. Resulting stresses are finally combined by Square Root of the Sum of the Square (SRSS) Method.
Procedure described above is schematically shown in Figure D.4.1-1.

D.4.1.1 Overview of the Response Analysis Code

For the analysis of the horizontal fuel assembly response, the FINDS code is used. The FINDS code is originally developed by MHI for seismic response analysis of the fuel assemblies array and can be also applied to LOCA response analysis. Vibration model of the fuel assembly in the FINDS code is based on empirically-confirmed models for not only 1st mode but also higher vibration modes in term of natural frequencies and vibration mode shapes. Concerning the collision characteristics of the grid spacers, the deformation characteristics obtained by grid spacer impact tests are reflected in the model.
Details and validity of the analytical model and procedures about the FINDS code are discussed in a paper [3] shown in reference.

D.4.1.2 Model of the Response Analysis

Of the fuel assemblies, which are placed at the center of the core, the time-dependent response analysis is performed so that the longest array of the fuel assemblies is chosen and vibrated to the direction where the fuel assemblies are lined up. The analytical models for the case with 17 fuel assemblies as maximum are shown in Figure D.4.1-2.
The individual fuel assembly is modeled with a beam element by the finite element method. Spring elements that correspond to the stiffness of the grid spacers and damping elements for modeling rebound characteristics are placed at the positions equivalent to the grid spacers to obtain the collision behavior. Because no collision occurs near the support points at the beam ends, the uppermost and lowest grid spacers are omitted. The upper and lower ends of the beam models are supported by the upper core and the lower support plates.
Rigid walls corresponding to neutron reflector are located on both sides of the outermost fuel assemblies.
The effect of the coolant inside the core is taken into account as an additional mass to the actual mass of the fuel assembly, and changes in the vibration characteristics (the specific frequency of the fuel assembly and the attenuation constant) are also considered.

D.4.1.3 Analytical Methodology

Displacements of the fuel assembly with vibration are analyzed by inputting the accelerations of upper core and lower support plates. The displacement varies according to the magnitude of the accelerations and collisions among the adjacent fuel assemblies and the peripheral neutron reflectors. The structures thus exhibit a group vibration behavior.

The fuel assembly response analysis model is two dimensional as previously shown in Figure D.4.1-2, while the response analysis of the reactor vessel is performed by 3-demensional model. Accordingly, the fuel assemblies' response analyses are independently done by using the acceleration of x and y direction obtained from the core internal's response analysis as inputs. The displacements of fuel assemblies are obtained from the result for x direction and y direction by the SRSS method.
Completely same procedure is applied to the horizontal response analysis for LOCA.

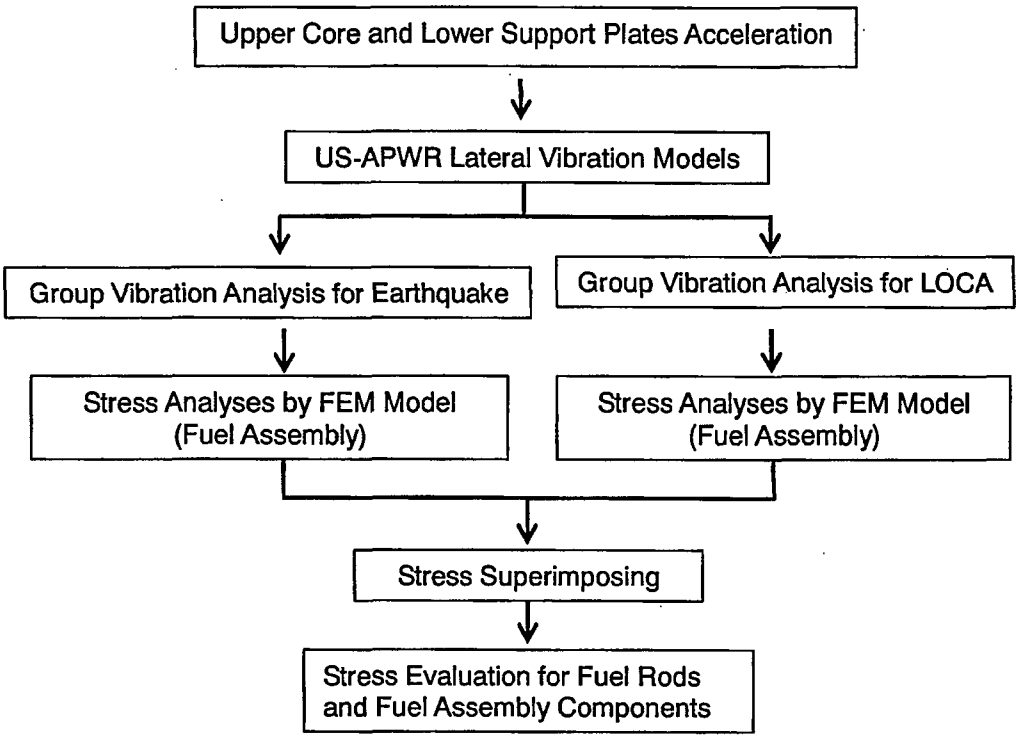

Figure D.4.1-1 Stress Evaluation for Seismic and LOCA Response in the Horizontal Direction

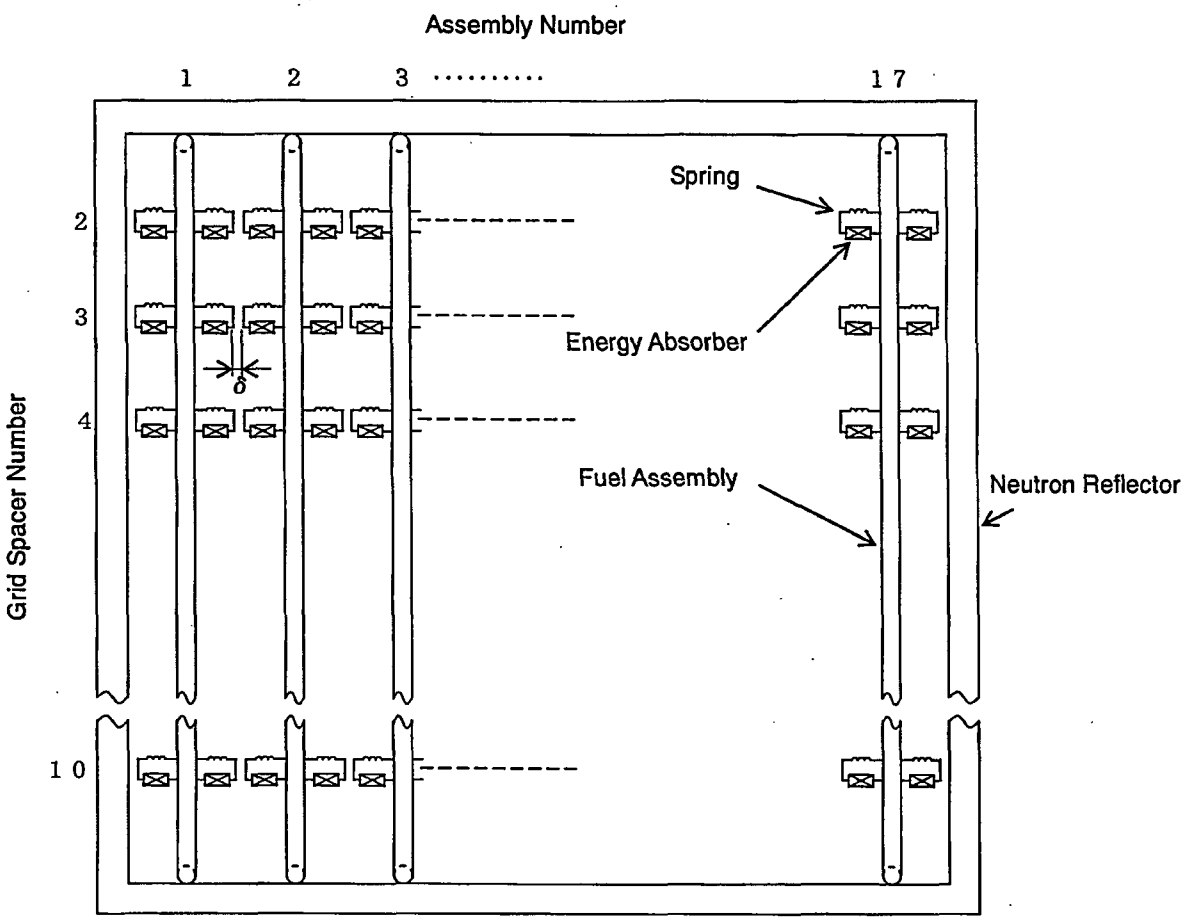

Figure D.4.1-2 Fuel Assembly Vibration Response Analysis Model in the Horizontal Direction

D.4.2 Fuel Assembly Stress Analysis to the Horizontal Response

D.4.2.1 Analytical Model

The fuel assembly stress analysis model in the horizontal direction is shown in Figure D.4.2-1.

[ ]

For the analysis, general FEM code, ANSYS is used for the analyses.

D.4.2.2 Verification of the Analytical Model

The stress analysis model for the US-APWR fuel assembly is based on conventional stress analysis model for the 12ft fuel assembly. Verification result for the 12ft fuel assembly model is summarized below.
Figure D.4.2-2 and Figure D.4.2-3 respectively show the comparison between experimental and analytical results about vertical strain distribution on control rod guide thimbles and fuel rods, when they are experimentally obtained and analytically simulated in horizontal forced vibration test of the 12ft fuel assembly.
It is confirmed that the analytical result gives good agreement with the test result with small difference.

D.4.2.3 Analytical Methodology

The stresses to the horizontal displacement by the earthquake and LOCA are individually analyzed by using the above model.

[ ]

Obtained stresses including the cladding and the control rod guide thimble by respective analyses for the earthquake and LOCA are superposed by the SRSS method.

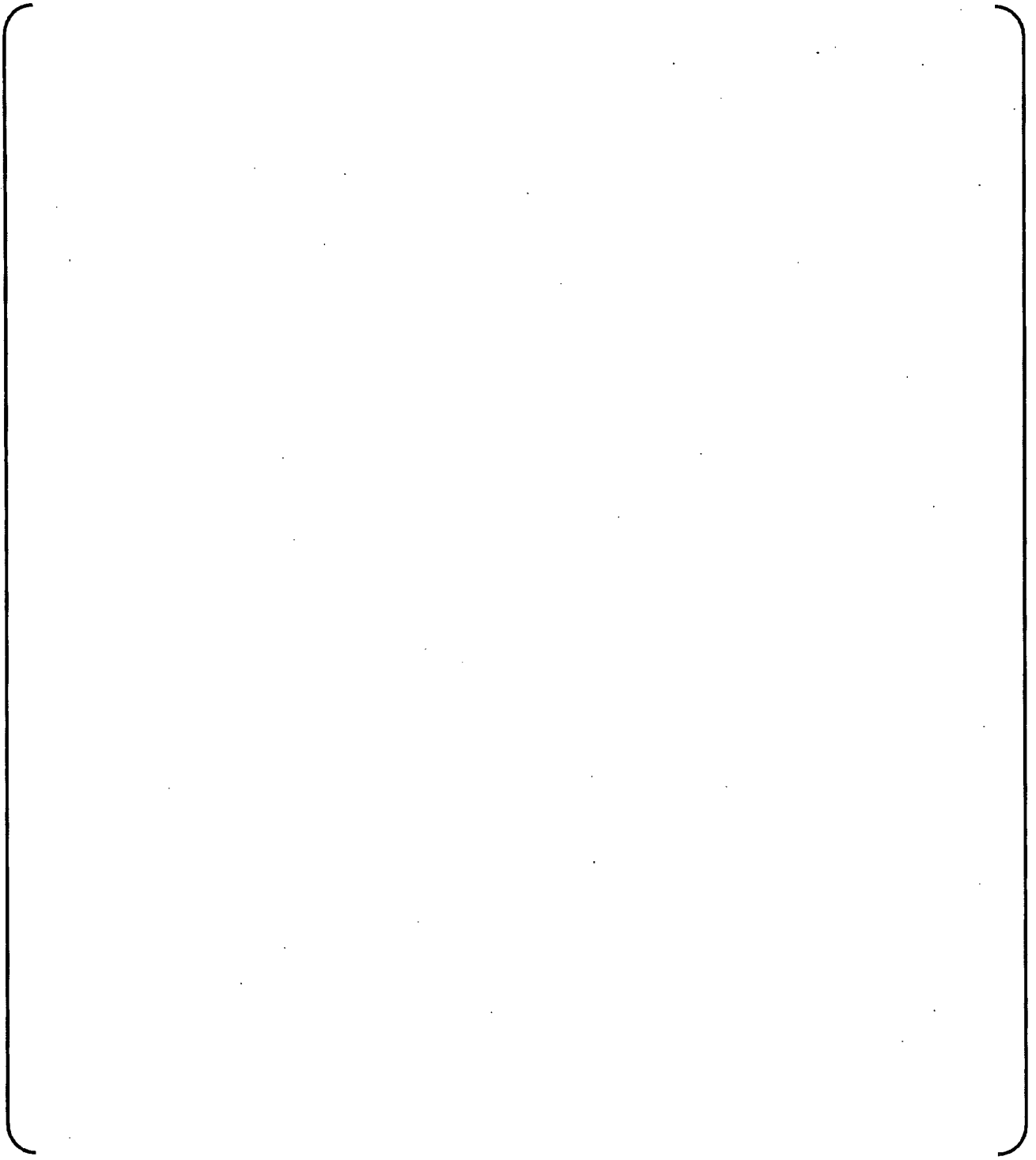

Figure D.4.2-1 Fuel Assembly Stress Analysis Model in the Horizontal Direction

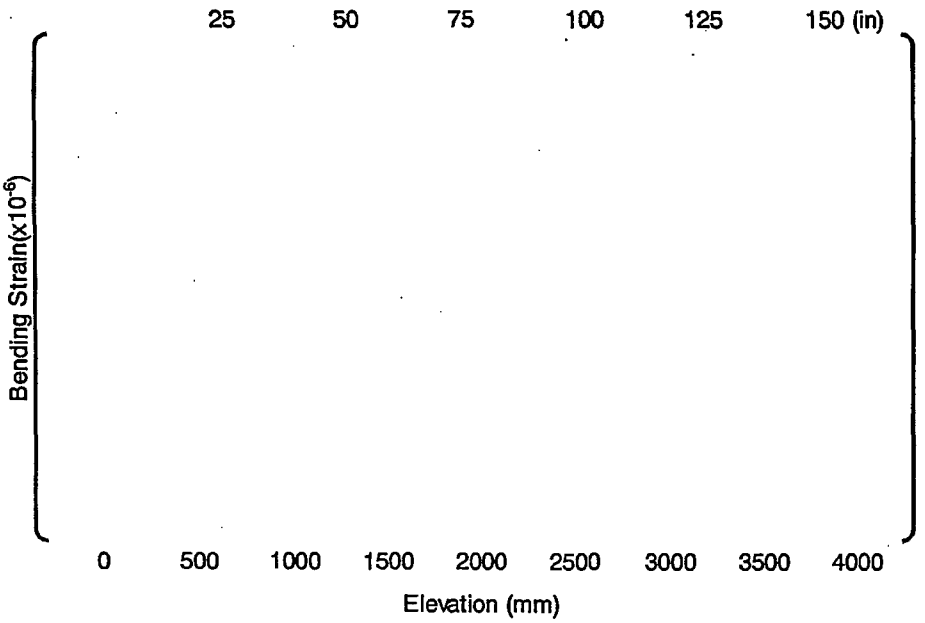

Figure D.4.2-2 Strain Distribution of Control Rod Guide Thimbles

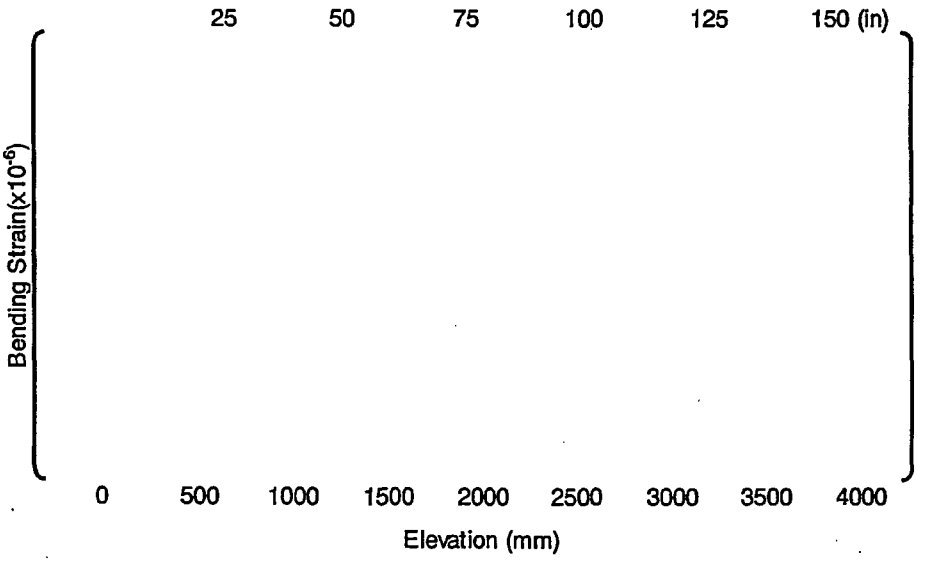

Figure D.4.2-3 Strain Distribution of Fuel Rods

D.4.3 Fuel Assembly Stress Analysis to the Vertical Response

For the stress evaluation in the vertical direction of the fuel assembly, stress analyses are followed by core internal response analyses but with less detailed than the fuel assembly response analyses performed for the horizontal direction.
The reason is that it is not necessary to consider interactions among the fuel assemblies and neutron reflectors as required in the horizontal direction and the performance of the fuel assembly can be dealt independently.
As the same with the horizontal direction, stress analyses for the earthquake and LOCA are individually carried out. Procedure is schematically shown in Figure D.4.3-1.

D.4.3.1 Analytical Models

The fuel assembly stress analysis model for the vertical response is shown in Figure D.4.3-2.

[ ]

In addition, for detailed stress analyses of the top and bottom nozzles, the models of the nozzles with three-dimensional solid elements are used.

D.4.3.2 Verification of the Analysis Models

(1) Fuel Assembly Stress Analysis Model

The stress analysis model for the US-APWR fuel assembly is based on conventional stress analysis model for the 12ft fuel assembly, as with the horizontal direction.
Verification result for the 12ft fuel assembly model is summarized below.
Distribution of the vertical displacement along the fuel assembly axis is shown in Figure D.4.3-3 which also indicates the comparison in between an experiment and an analysis. The distribution is obtained when 1860lb (40.2kN) corresponding to 6G of the fuel assembly's self-weight is compressively loaded on the top nozzle. It is confirmed that the analytical result gives good agreement with the test result by a narrow difference.
Regarding control rod guide thimbles and fuel rods, analytical obtained strain distributions are shown in Figure D.4.3-4 and Figure D.4.3-5 respectively with experimental results. Good agreement can be seen in the both figures.

(2) Analysis Models for the Top and Bottom Nozzles
Results of verification for the both nozzles applied by the 12ft fuel assembly are described below.
As the same with the fuel assembly model above, strain of the top and bottom nozzles are indicated as a form of measured versus predicted plot in Figure D.4.3-6 and 4.3-7 when vertical compressive load of 1860lb (40.2kN) is added on the nozzles. It is confirmed that the analytical results give good agreement with the test results by a narrow difference.

D.4.3.3 Analytical Method

The peak vertical load on the fuel assembly obtained by core internal response analyses is directly used as input for the stress analyses models for fuel assembly, the top and bottom nozzles.
In addition, for the control rod guide thimbles, the vertical load is also used for the buckling evaluation of the control rod guide thimbles.
The above stress analyses are individually carried out for the earthquake and LOCA.
Individually obtained stresses including the cladding and the control rod guide thimble to the seismic and LOCA responses are superposed by the SRSS method.

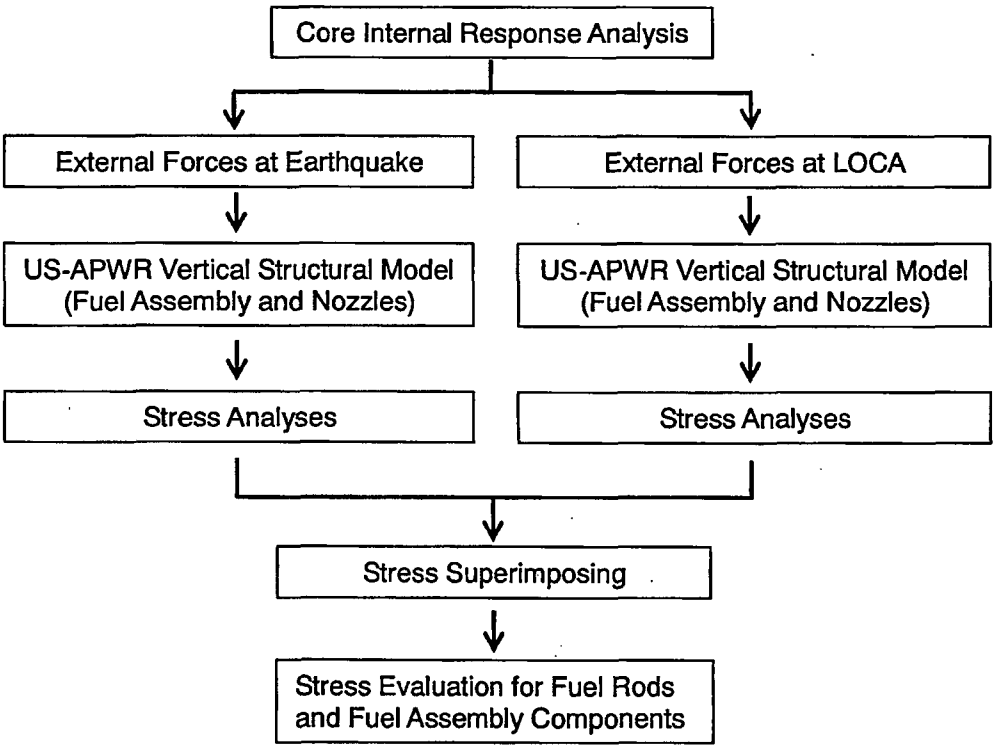

Figure D.4.3-1 Stress Evaluation for Seismic and LOCA Response in the Vertical Direction

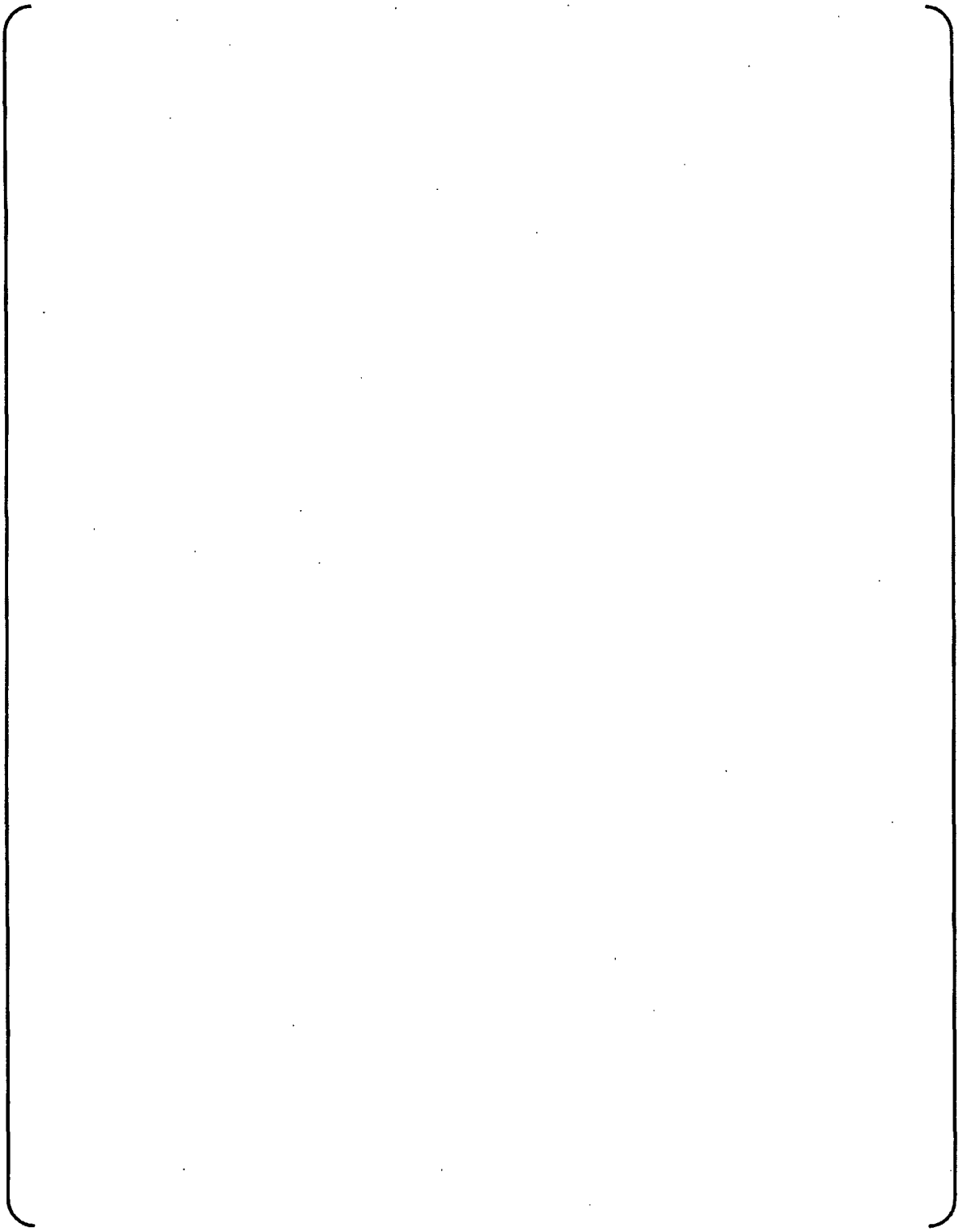

Figure D.4.3-2 Fuel Assembly Stress Analysis Model for Vertical Response

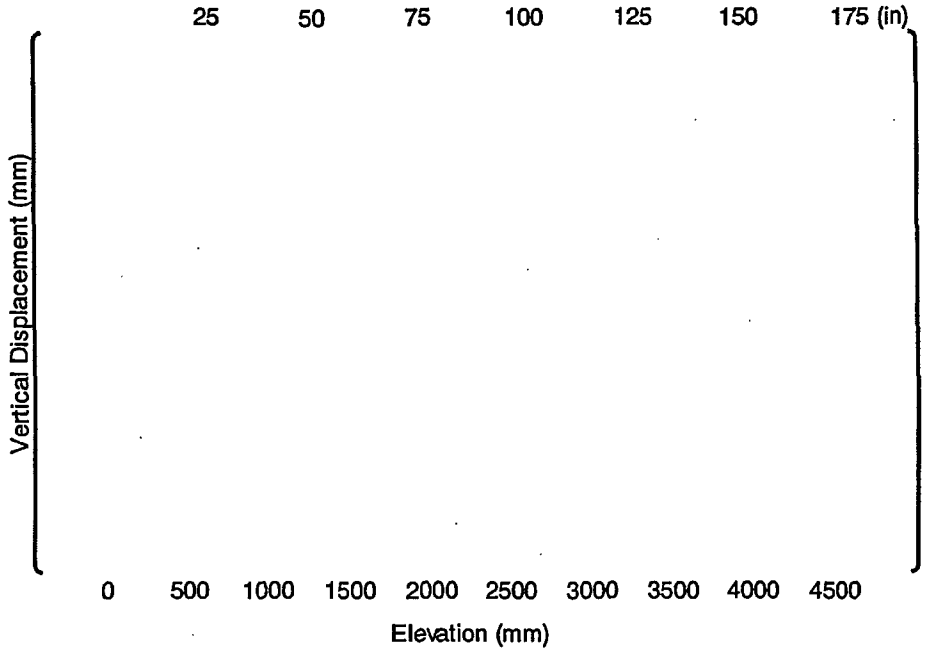

Figure D.4.3-3 Displacement Distribution of the Fuel Assembly under Axial Compression

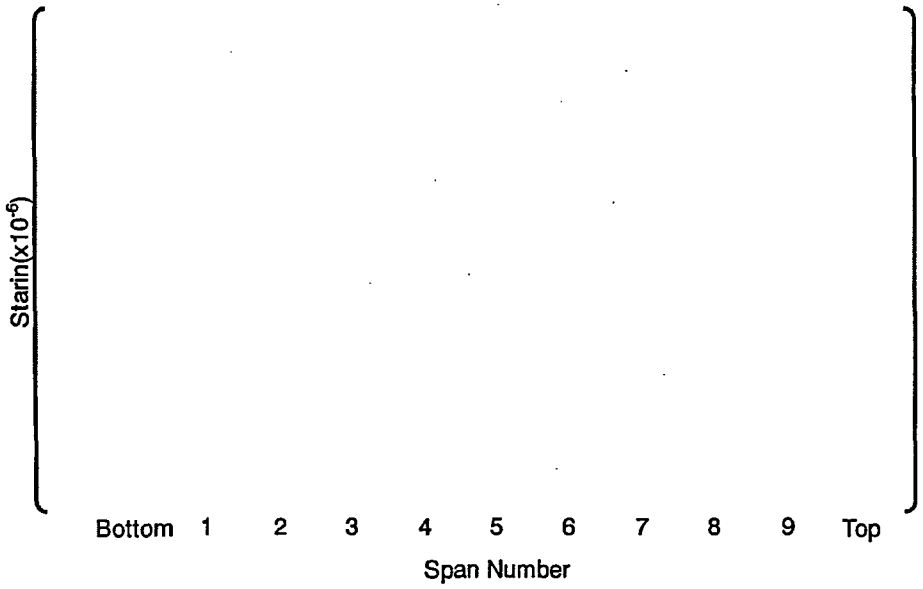

Figure D.4.3-4 Strain Distribution of the Distorted Control Rod Guide Thimbles

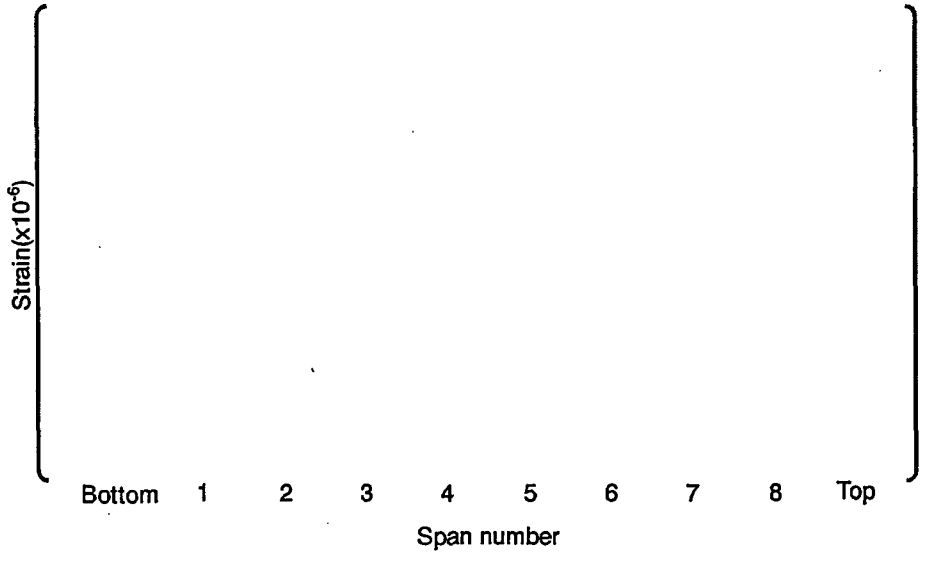

Figure D.4.3-5 Strain Distribution of the Distorted Fuel Rods

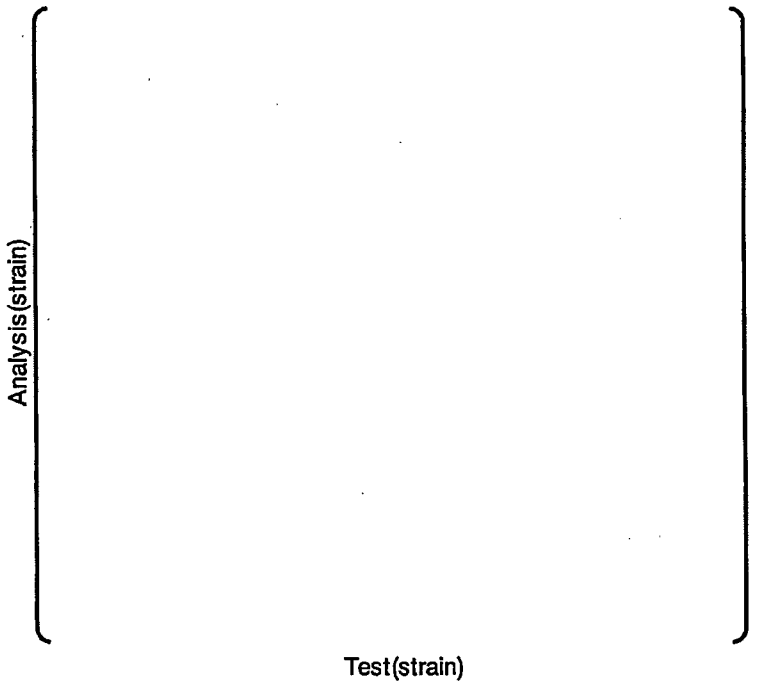

Figure D.4.3-6 Strain Distribution of the Top Nozzle under Compression

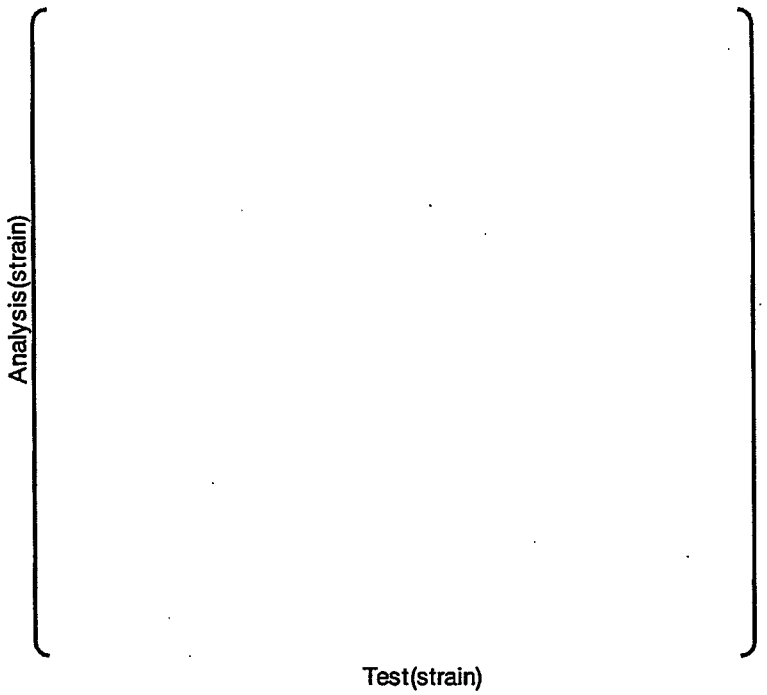

Figure D.4.3-7 Strain Distribution of the Bottom Nozzle under Compression

D.5.0 EVALUATION METHODOLOGY OF THE FUEL ASSEMBLY STRENGTH FOR COMBINED SEISMIC AND LOCA EVENTS

The stresses of the control rod guide thimble, the fuel cladding and the nozzles are obtained from the result of earthquake and LOCA by the SRSS method. In addition, the stress occurring under normal operation is added to these stresses.
Vertical and horizontal stresses are properly combined by SRSS method and compared to acceptance criteria such as primary general membrane stress and summation of primary membrane stress and primary bending stress.

D.6.0 CONCLUSION

A method for evaluating the strength of the US-APWR fuel assembly under earthquake and LOCA conditions has been developed.
Application of this method to the US-APWR fuel assembly demonstrates its capability to withstand earthquake and LOCA events.

D.7.0 REFERENCES

(1) U.S. Nuclear Regulatory Commission, Standard Review Plan (NUREG-0800) Section 4.2, March 2007
(2) American Society of Mechanical Engineers Boiler and Pressure Vessel Code Section III
(3) T.Sato et al., "PWR Fuel Seismic Analysis Method Considering Non-Linear Behavior", Japan Association for Wind Engineering, No.37 Octorber 1988